Hydrocode Modeling of Deflagration and Detonation with Dynamic Compaction of a Granular Explosive: Cyclotetramethylene-tetranitramine, HMX

by

Kelly Susan Mahon

A Dissertation Presented in Partial Fulfillment
of the Requirements for the Degree
Doctor of Philosophy

Approved August 2015 by the
Graduate Supervisory Committee:

Taewoo Lee, Chair
Kangping Chen
Marcus Herrmann
Huei-Ping Huang
Yang Jiao

ARIZONA STATE UNIVERSITY

December 2015

ABSTRACT

The study of deflagration to detonation transition (DDT) in explosives is of prime importance with regards to insensitive munitions (IM). Critical damage owing to thermal or shock stimuli could translate to significant loss of life and material. The present study models detonation and deflagration of a commonly used granular explosive: cyclotetramethylene-tetranitramine, HMX. A robust literature review is followed by computational modeling of gas gun and DDT tube test data using the Sandia National Lab three-dimensional multi-material Eulerian hydrocode CTH. This dissertation proposes new computational practices and models that aid in predicting shock stimulus IM response.

CTH was first used to model experimental data sets of DDT tubes from both Naval Surface Weapons Center and Los Alamos National Laboratory which were initiated by pyrogenic material and a piston, respectively. Analytical verification was performed, where possible, for detonation via empirical based equations at the Chapman Jouguet state with errors below 2.1%, and deflagration via pressure dependent burn rate equations. CTH simulations include inert, history variable reactive burn and Arrhenius models. The results are in excellent agreement with published HMX detonation velocities. Novel additions include accurate simulation of the pyrogenic material $BKNO_3$ and the inclusion of porosity in energetic materials.

The treatment of compaction is especially important in modeling precursory hotspots, caused by hydrodynamic collapse of void regions or grain interactions, prior to DDT of granular explosives. The CTH compaction model of HMX was verified within 11% error via a five pronged validation approach using gas gun data and employed use of a newly generated set of P-α parameters for granular HMX in a Mie-Gruneisen Equation

of State. Next, the additions of compaction were extended to a volumetric surface burning model of HMX and compare well to a set of empirical burn rates. Lastly, the compendium of detonation and deflagration models was applied to the aforementioned DDT tubes and demonstrate working functionalities of all models, albeit at the expense of significant computational resources. A robust hydrocode methodology is proposed to make use of the deflagration, compaction and detonation models as a means to predict IM response to shock stimulus of granular explosive materials.

To James, and of course, Mom and Dad.

Words are insufficient to convey the depth of my gratitude.

ACKNOWLEDGMENTS

The author gratefully acknowledges the technical advice provided by members of the computational mechanics group and energetics experts at Raytheon Missile Systems, most notably Henri, Greg and Kim.

Any opinions, findings, and conclusions or recommendations expressed in this material are those of the author and do not necessarily reflect the views of Raytheon Company.

Table of Contents

LIST OF TABLES

LIST OF FIGURES

Figure Page

CHAPTER 1

INTRODUCTION

Problem Statement

Deflagration to Detonation Transition (DDT) of granular secondary explosives has been an active field of research since the late 1950s. This challenging problem has been characterized in numerous experimental investigations and analytical models have been developed to describe pertinent physics. However, successful application of sufficiently accurate DDT models in hydrocode analysis tools has proven elusive due to the inherently complex nature of multi-phase physics and associated disparate timescales in the deflagration and detonation regimes. The aim of this dissertation is to successfully implement a model capable of simulating deflagration as a necessary component in the progress toward DDT simulation for practical use in the hydrocode CTH, developed and maintained by Sandia National Laboratory. The motivating factor behind this work is to be able to use the revised computational modeling approach, once effectively implemented, to account for Insensitive Munitions requirements in the design phase of energetic components. The fundamental premise of this work is "if we can model it, we can design for it."

Insensitive Munitions

Insensitive Munitions (IM) is a very real and important endeavor by the U.S. Armed Forces. There are no new waivers being granted for IM compliance. New rocket motor and warhead developments are now required to pass a certain series of tests that are designed to demonstrate a product's ability to withstand adverse stimuli. The

governing document for these IM tests and passing criteria is MIL-STD-2105: Department of Defense Test Method Standard Hazard Assessment Tests for Non-Nuclear Munitions. (MIL-STD-2105D: Hazard Assessment Tests for Non-Nuclear Munitions, 2011) These tests can be loosely grouped into two categories: thermal and shock stimulus. Thermal based tests include the two cook-off requirements, with the remaining tests falling into the shock stimulus category.

There is much interest in IM modeling capabilities, specifically being able to work it into the pre-design phase. This is currently not done. Designs in the recent past have used "best IM practices" or devices intended to aid in IM, but these are in no way an indicator of IM success and are not often enough to pass the gambit of tests. Redesigns are very costly, on the order of a redeveloping the entire rocket motor or warhead. It should be mentioned that the IM tests in themselves are very costly as they nominally require the products to be tested in the "all up round" configuration which includes the much more expensive forward missile assembly. This dissertation proposes new computational practices that can be used to predict shock stimulus IM response, and thusly can be used in lieu of a subset of the IM tests. A more detailed discussion of the history and relevance of Insensitive Munitions is included in the Appendix entitled INSENSITIVE MUNITIONS, page 235.

An Overview of HMX

Explosives are used in a variety of applications including warhead technology, initiators, boosters, demolition, mining, cutting charges, and explosive bolts, to name a few. Explosives are loosely grouped into two categories: either primary or secondary.

Primary explosives are more energetic and generally used in initiating changes; whereas secondary explosives are less energetic and safer for large quantity applications. According to (Carleone, 1993), the most common granular explosives with their respective acronyms are:

- Trinitrotoluene, TNT, $C_7H_5N_3O_6$
- Cyclotrimethylene-trinitamine, RDX, $C_3H_6N_6O_6$
- Cyclotetramethylene-tetranitramine, HMX, $C_4H_8N_8O_8$

TNT is the most commonly used of the three listed above, but is the least energetic. Numerous IM formulations of secondary explosives with RDX and HMX energetic bases and polymeric binders have been formulated in an attempt to address IM sensitivity issues. These polymeric binders are characterized by endothermic reactions which serve to absorb heat from the HMX crystalline reactions and delay the onset of adverse IM shock induced detonations. (Tarver & Tran, 2004) Such formulations commonly follow the naming convention Plastic Bonded Explosive (PBX) – formulation number.

RDX, also called cyclonite or hexogen, is one of the most frequently used high explosives and was first prepared by Henning in 1899, though its explosives properties were later discovered by von Herz in 1920. HMX, also called octogen and sometimes referred to as Her Majesty's Explosive or High Melting Explosive, has a higher detonation velocity than RDX and was originally a by-product of the Bachmann process used to synthesize RDX. Both RDX and HMX are thermally stable in storage with higher melting points than TNT and have desirable friction and impact insensitivities. Because of its higher detonation velocity over RDX, HMX was first

used as the prime energetic to crush fissionable material for long durations which increased yields in nuclear weapon development. HMX was therefore a technology transfer from the Atomic Energy Commission, with its first non-nuclear use in DARTs in 1952. Other well-known successors using HMX are TOW, M-28 Bazooka, LAW, Hellfire, and Viper. (Kennedy, 1993)

The cycloaliphatic structure of HMX is shown in Figure 1 along with an inverted microscope image of crystalline HMX (Grade II, Class A) in Figure 2. In a very general sense, HMX releases energy due to fuel oxidization reactions. Both oxidizer, provided by the Nitramine NO_2, and Carbon fuel reside within the cycloaliphatic structure of HMX. HMX has a fast reaction rate and this small reaction timescale directly corresponds to a high power output, which translates to high pressure and detonation velocity characteristics relative to other energetic material formulations. (Maienschein, 2014)

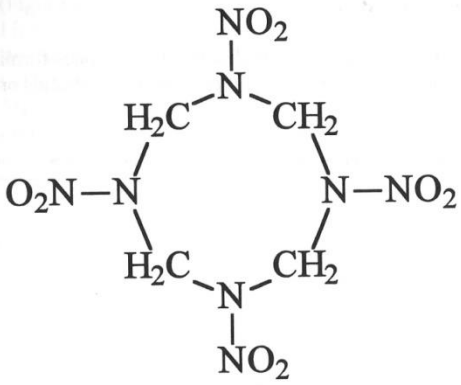

Figure 1: Molecular Structure of Cyclotetramethylene-tetranitramine, HMX. (Cooper, 1996, p.47)

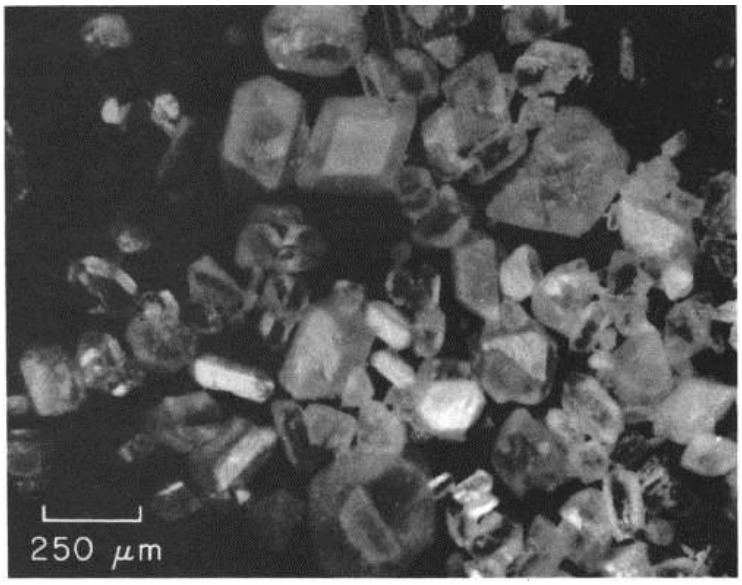

Figure 2: Inverted Microscope Image of Crystalline HMX (Grade II, Class A). (Dick, 1983, p. 123)

Both RDX and HMX belong to the aliphatic explosive group and are sub-divided into the Nitramines category as they are oxidized by NO_2. Heat is released during oxidation reactions of organic explosive formulations because the products have a lower internal energy than the reactants. A simple reaction product hierarchy guideline for organic explosives of the form $C_XH_YN_WO_Z$ exists based on the tendency toward the highest oxidation state (lowest internal energy state) and is summarized in the following flow diagram. There is some debate in the literature about whether CO or CO_2 formation should appear first in the product hierarchy. (Cooper, 1996)

Nitrogen tends to N_2

↳ Hydrogen burns to H_2O

↳ Most remaining Oxygen forms CO

↳ Still remaining Oxygen forms CO_2

↳ Any remaining Oxygen tends to O_2

↳ Trace amounts of NO_X form, (Cooper, 1996)

Applicability and Contribution to the Art

It is proposed that robust hydrocode modeling of rocket motors and warheads whilst still in the design phase can be a predictor for IM response. Such work in ongoing, in particular for thermal modeling of confined rocket propellants and high explosives. [(Yoh J. J., McClelland, Maienschein, Wardell, & Tarver, 2005), (Yoh J. J.-i., McClelland, Maienschein, & Tarver, 2005)] This dissertation is an addition to that new body of work, particularly focusing on the topic of IM shock stimulus of high explosive granular material.

CHAPTER 2

LITERATURE REVIEW

As discussed in the introduction, DDT is a research problem that has been in continuous study since the late 1950s. The aim of this literature review is to summarize key milestones and research approaches to DDT as it relates to granular secondary explosives, specifically HMX, both in terms of modeling and experiment. DDT can, in very simplified terms, be broken into three fundamental topics: deflagration, a transition mechanism from deflagration to detonation, and subsequent detonation. These topics will be briefly explored in the following sub-sections. ***The reader is strongly encouraged to review the Appendix entitled THOROUGH LITERATURE REVIEW, pages 207 through 235, for a much more detailed summary.***

Detonation and Deflagration of High Explosives

Given that the primary design intent behind the synthesis of granular explosives is to achieve detonation, of the three aforementioned DDT problem segments, detonation of granular secondary explosives is by far the best characterized. Only the implementation of numerical detonation models in existing hydrocodes will be discussed in this portion of the literature review as the aim of this dissertation is to develop a robust DDT model in an Eulerian hydrocode. Numerous detonation models of varying fidelity exist within the literature and are currently implemented in widely used hydrocodes today. The most commonly used hydrocode detonation models include: the Jones Wilkins Lee (JWL) model, Ignition and Growth model, History Variable Reactive Burn (HVRB) model, and the Arrhenius decomposition kinetics

based reactive burn model. These models were primarily developed at Sandia National Laboratory or Lawrence Livermore National Laboratory, with the notable exception of the Arrhenius rate equation. Hydrocode detonation models can be subdivided into two categories, either idealized detonation or reactive burn. The difference between the two modeling approaches is in the treatment of the detonation wave reaction zone and propagation mechanisms.

Idealized detonation models assume the detonation wave front is modeled as a jump discontinuity, reaction products are in chemical and thermodynamic equilibrium, a steady-state detonation condition exists, and the detonation velocity is constant. These assumptions imply that the detonation wave shape remains constant throughout propagation of the computational domain until boundary conditions, additional detonation waves, or rarefaction waves are encountered. The P-v plane Hugoniot curves from (Cooper, 1996, p. 254) in Figure 3 offer a graphical depiction of the jump discontinuity from unreacted to reacted states in a detonation. A model for steady state detonation conditions was developed by Chapman and Jouguet in the late 1800s and is commonly referred to as the CJ state. (Cooper, 1996) Alternatively, the CJ state is succinctly defined in (Kamlet & Jacobs, 1967) as the "minimum detonation velocity compatible with conservation conditions for sonic flow behind the discontinuity in a reference frame where the discontinuity is at rest."

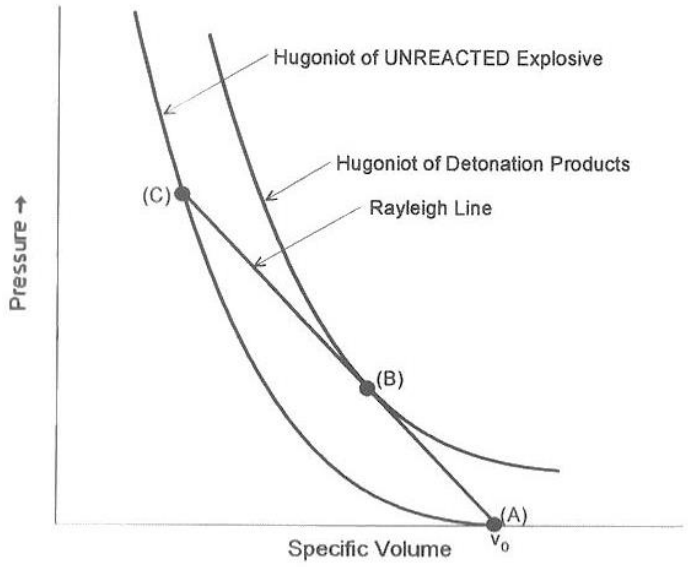

Figure 3: P-v Plane Hugoniot Curves of Detonation (Cooper, 1996, p. 254)

Simplified first order one-dimensional approaches to idealized detonation were simultaneously formulated by Zel'dovich, Von Neumann, and Deering in the 1940s. (Cooper, 1996, p. 253) Jones, Wilkins and Lee later developed one of the most widely implemented idealized detonation models while working at Lawrence Livermore National Laboratory. A version of the JWL equation with an additional λQ term added by the U.S. Navy's White Oaks Laboratory to account for the late energy release associated with aluminized explosives is given below in Equations [1] and [2]. The variables A and B are adjustable parameters, ω is the Gruneisen coefficient, and R_1 and R_2 are test cylinder radii. This equation is generally characterized with cylinder expansion data where cylinder expansion as a function of time are recorded and used to calibrate JWL parameters. [(Miller & Guirguis, 1993) , (Crawford, et al., 2012) , (Hertel E. S., 1998) , (Erikson, 2000)]

$$P = A\left(1 - \frac{\omega}{R_1 v}\right)e^{-R_1 v} + B\left(1 - \frac{\omega}{R_2 v}\right)e^{-R_2 v} + \frac{\omega}{v}(E + \lambda Q) \quad [1]$$

Where

$$\frac{d\lambda}{dt} = a(1-\lambda)^{1/2}\, p^{1/8} \quad [2]$$

Idealized detonation models such as the JWL model are useful when the exact point of initiation and general detonation wave shape are known or can be approximated.

Unlike idealized detonation models, reactive burn models are capable of modeling detonation in reaction to surrounding computational stimuli. These models take into account a leading shock front, also referred to as a detonation wave, with peak pressure known as the Von Neumann spike followed by a thin reaction zone with a corresponding pressure gradient prior to detonation products reaching steady state. [(Cooper, 1996) , (Zerilli, 1981), (Lee & Tarver, 1980)] The presence of a Von Neumann spike requires a finite reaction zone thickness and is not accounted for in idealized detonation models. A generalized plot of pressure versus distance for a detonation wave is included in Figure 4 for clarity.

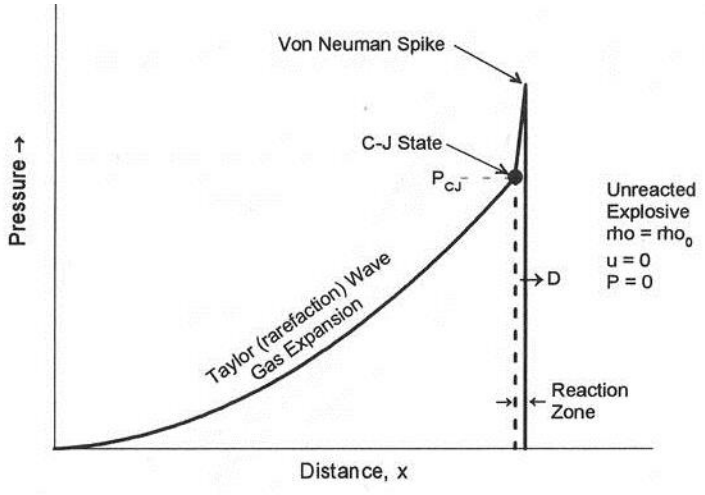

Figure 4: Pressure versus Distance CJ State Explanation. (Cooper, 1996, p. 256)

Arrhenius reactive burn is the oldest of the three most common reactive burn model types. This model is based on the Arrhenius equation developed by the Swedish chemist Svente Arrhenius in the early 1900s. The Arrhenius decomposition rate equation is given in its simplest form in Equation [3], where k is the reaction rate constant, A is the pre-exponential factor, E_a is activation energy, R is the universal gas constant, and T is temperature. (Yang, 2009)

$$k = Ae^{-E_a/RT} \quad [3]$$

This equation has been adapted, to varying degrees of complexity, for implementation in modern day hydrocodes. Arrhenius decomposition reactions can be written in terms of global reactions where the pre-exponential factor is scaled to account for the rate of molecular collisions and the activation energy threshold is reaction mechanism specific. *Yang's* 2009 paper provides a thorough examination of the pre-exponential frequency factor in terms of statistical mechanics. (Yang, 2009) In terms of detonation modeling, the Arrhenius reactive burn model can be used to model a one-step global reaction from unreacted to final states, as in reference (Mahon, 2014) for RDX detonation. Alternatively, detonation reactions can be broken into multi-step global reaction models, as in the work of [(Lee & Tarver, 1980), (Tarver & Tran, 2004)]

The Ignition and Growth reactive burn model was developed by Lee and Tarver of Lawrence Livermore National Laboratory in the late 1970s and is also referred to in the literature as the Lee-Tarver model. (Hertel E. S., 1998) Lee and Tarver's original Ignition and Growth model shown in Equation [4] from (Lee & Tarver, 1980) contained two reaction steps: an ignition phase and a subsequent growth phase. In this equation

F is the reacted explosive fraction, η is the relative compression of unreacted explosive, G is a surface area to volume ratio constant, V_0 is the explosive initial specific volume, V_1 is the shocked yet unreacted explosive specific volume, p is pressure and I, x, y, and r are constants.

$$\frac{\delta F}{\delta t} = I(1-F)^x \left(\frac{V_0}{V_1} - 1\right)^r + G(1-F)^x F^y p^z, \qquad \eta = \frac{V_0}{V_1} - 1 \qquad [4]$$

The first term in Equation [4] represents ignition of hot spots during void collapse or closure and the second term models growth of the reaction throughout the unreacted explosive. (Lee & Tarver, 1980) Subsequent work by *Lee and Tarver* modified their original Ignition and Growth model to account for short pulse duration shock initiation and further extend the applicability of the model beyond explosives to propellants. [(Hertel E. S., 1998), (Tarver, Hallquist, & Erickson, 1985), (Tarver & Green, 1989)]

The History Variable Reactive Burn (HVRB) model is specific to the hydrocode CTH and frequently used in the analysis field to model detonations. [(Hertel E. S., 1998), (Kerley G. , 1992)] HVRB calculates an extent of reaction, λ, given as a function of a pressure dependent history variable, φ, as shown in Equations [5] and [6]. (Starkenberg, 2002) Parameter sets for the HVRB model can be generated from and tuned with Pop-plot data. *Dudley's* 2010 International Detonation Symposium paper discusses HVRB parameter tuning in greater detail. (Dudley, Damm, & Welle, 2010)

$$\lambda = 1 - \left(1 - \frac{\varphi^{n_\varphi}}{n_\lambda}\right)^{n_\lambda} \qquad [5]$$

Where:

$$\phi = \int_0^t \left(\frac{p-p_i}{p_s}\right)^{n_p} \frac{d\tau}{\tau_s} \quad [6]$$

Deflagration of high explosives came into prominence as a field of study for two primary reasons. Further understanding of the deflagration properties of high explosives became desirable when explosives such as nitroglycerin, RDX, and HMX began being used in double base propellants to increase burn rate and energetic output. Additional concerns relating to explosive combustion are due to Insensitive Munitions issues and qualification testing requirements. Literature references for HMX deflagration begin in the 1970s and remain a popular area of publication.

In the interest of brevity, please refer to the Literature Review Appendix, specifically section DEFLAGRATION OF HIGH EXPLOSIVES beginning on page 214. Deflagration will later be revisited in the analytical verification section for the proposed test case experiments.

Deflagration to Detonation Transition

As previously noted, the field of deflagration to detonation transition has been active since the late 1950s. The literature review of this prolific field is subsequently divided into three sections as they relate to the present work: early experimental DDT with an emphasis on published HMX data, the Baer-Nunziato model and suggested modifications, and non-Baer-Nunziato based analytical formulations. All such sections are described in detail in the Literature Review Appendix with subsections entitled DDT Experimental beginning on page 218; Proposed Analytical Models Unrelated to

Baer-Nunziato beginning on page 222; and Baer-Nunziato Based Analytical DDT Models beginning on page 228. Numerous publications in the field contained both experimental data as well as proposed analytical models based on the collected data. These works will be divided into two categories: those based on the Baer-Nunziato DDT model and other proposed mechanisms, which are discussed in chronological order in the Appendix. In general, DDT in confined column type tests is thought to occur over four regimes: "conductive burning, convective burning, compressive burning, and detonation." (Baer & Nunziato, 1986) Discussions in the literature support varying dominance of reactions within these four regimes. Typical experimental configurations include a hollow metal tube filled with porous explosive initiated on one end.

In brief for this front-end literature review, the remainder of this chapter reviews the pivotal 1986 Baer-Nunziato multi-phase flow model for DDT formulated at Sandia National Laboratory and subsequent derived works. This model is one of the most referenced and well known of the multi-phase DDT models. Implementation of model improvements in an Eulerian hydrocode is one of the focuses of the present dissertation work.

The Baer-Nunziato (BN) model is based on the physical assumption of four regimes, including conductive burning, convective burning, compressive burning, and detonation as depicted in Figure 5. *Baer and Nunziato* emphasize the important coupling that occurs between thermal and mechanical processes during DDT, where the thermal process involves convective heating of upstream unreacted explosive material and mechanical processes involve compaction of the granular particles

upstream thereby increasing material density and inducing pressure build-up. Shock wave formation to full-fledged detonation is supported by "hot spot" regions. (Baer & Nunziato, 1986)

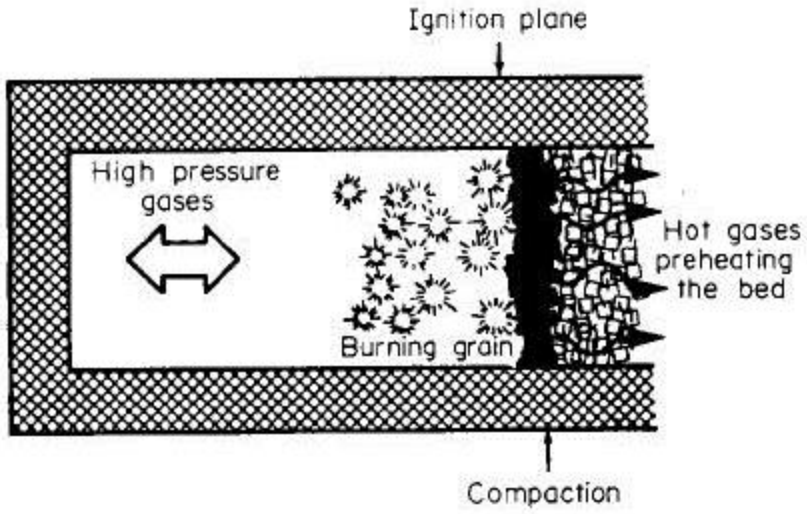

Figure 5: Baer-Nunziato Depiction of DDT Regimes. (Baer & Nunziato, 1986, p. 861)

Baer and Nunziato employ a continuum approach to the reactive two phase flow problem of HMX DDT in total non-equilibrium. They assert that the primary complication with the continuum approach in past solution attempts has been the problem of "closure" as it pertains to the volume fraction. For a one-dimensional two phase problem there are ten unknown variables: "pressure, temperature, density, velocity, and volume fraction" in each of the two phases. Mass, momentum and energy conservation in each phase solve for six variables with an additional two from phase based state relations, and one from a volume constraint. Thus, one equation is still needed in order for the problem to be fully determined. The BN model "proposes an

evolutionary equation for the volume fraction consistent with thermodynamics" to resolve the closure issue. (Baer & Nunziato, 1986)

Baer and Nunziato derive the following set of one dimensional governing equations, where the subscripts s and g denote solid and gas phases.

Conservation of mass:

$$\frac{\partial \rho_s}{\partial t} + \frac{\partial}{\partial x}(\rho_s v_s) = c_s^+ \quad [7]$$

and

$$\frac{\partial \rho_g}{\partial t} + \frac{\partial}{\partial x}(\rho_g v_g) = -c_s^+ \quad [8]$$

Conservation of momentum:

$$\rho_s\left[\frac{\partial v_s}{\partial t} + v_s\frac{\partial v_s}{\partial x}\right] = -\alpha_s\frac{\partial p_s}{\partial x} + (p_g - p_s)\frac{\partial \alpha_s}{\partial x} - \left(\delta + \frac{1}{2}c_s^+\right)(v_s - v_g) \quad [9]$$

and

$$\rho_g\left[\frac{\partial v_g}{\partial t} + v_g\frac{\partial v_g}{\partial x}\right] = -\alpha_g\frac{\partial p_g}{\partial x} - \left(\delta - \frac{1}{2}c_s^+\right)(v_g - v_s) \quad [10]$$

Conservation of energy:

$$\rho_s\left[\frac{\partial e_s}{\partial t} + v_s\frac{\partial e_s}{\partial x}\right] = -\alpha_s p_s\frac{\partial v_s}{\partial x} + \frac{\partial}{\partial x}\left(k_s\frac{\partial T_s}{\partial x}\right) + h(T_g - T_s) - (p_s - T\beta_s)\left(\alpha_s' - \frac{c_s^+}{\gamma_s}\right) \quad [11]$$

and

$$\rho_g\left[\frac{\partial e_g}{\partial t} + v_g\frac{\partial e_g}{\partial x}\right] = -\alpha_g p_g\frac{\partial v_g}{\partial x} + \frac{\partial}{\partial x}\left(k_g\frac{\partial T_g}{\partial x}\right) - h(T_g - T_s) - \left[p_g\frac{\partial \alpha_s}{\partial x} - \delta(v_s - v_g)\right](v_s - v_g) + (p_s - \beta_s)\left(\alpha_s' - \frac{c_s^+}{\gamma_s}\right) + c_s^+(e_g - e_s) \quad [12]$$

Compaction:

$$\frac{\partial \alpha_s}{\partial t} + v_s \frac{\partial \alpha_s}{\partial x} = \frac{\alpha_s \alpha_g}{\mu_c}\left[p_s - \left(p_g + \beta_s\right)\right] + \frac{c_s^+}{\gamma_s} \quad [13]$$

and

$$\alpha_g = 1 - \alpha_s \quad [14]$$

The BN model as applied to HMX DDT further utilizes a thermo-elastic variation of the Helmholtz free energy for the unreacted energetic material, a JWL Equation of State for the gaseous reaction products, a thermodynamic based equation for gas temperature, and a burn law given in the equation below. Theta is a function of both phases and epsilon is the kinetic shape factor.

$$c_{solid}^+ = -\epsilon\left(\theta + p_{gas}\right) \quad [15]$$

In the validation case of HMX DDT, a reflection boundary condition is used at the ignition end of the cylinder and an outflow boundary condition is applied at the opposite cylinder end. Initial conditions are consistent with the ignition of HMX. The aforementioned BN model equations are solved via application of the Method of Lines and yield results shown below in Figure 6. (Baer & Nunziato, 1986)

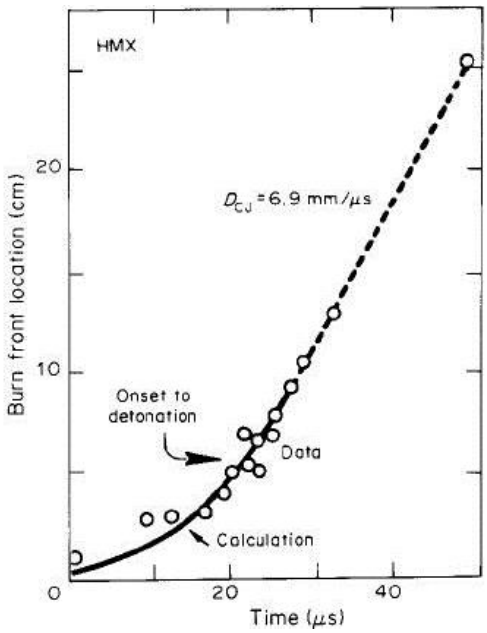

Figure 6: Baer-Nunziato Model Solution Ratio from 1986. (Baer & Nunziato, 1986, p. 877)

CHAPTER 3

RELEVANT TEST CASES AND VERIFICATION

Test Case Experiments

Two experimental test cases have been down-selected for verification and validation of the present hydrocode HMX DDT modeling research. These two experiments consist of vastly different apparatus setup and methodology and are included to increase fidelity of hydrocode model validation beyond reliance on a single set of data. Both experiments are referenced in numerous publications cited in the THOROUGH LITERATURE REVIEW within the Appendix and have therefore been peer reviewed within the research community.

Naval Surface Weapons Center Experimental Data

In the 1970s Richard Bernecker and Donna Price published numerous papers on experimental and analytical DDT research pertaining to waxed granular explosives. Experimental setup and procedure for the HMX DDT test data included in this sub-section are detailed in (Bernecker & Price, 1972). Figure 7 from this reference contains a diagram of the NSWC DDT tube experimental configuration. NSWC utilized seamless American Iron and Steel Institute (AISI) carbon mechanical steel, such as AISI 1015, for the main DDT tube mass. (Price & Bernecker, 1977) DDT tubes were sealed at both ends to contain pressure buildup and detonation products. *Bernecker and Price* indicate that the tube geometry of 16.27 ± 0.02 mm inner diameter, 50.95 ± 0.03 mm outer diameter, and 342.9 mm total length were selected in order to provide a large enough diameter to avoid convective burning and critical diameter interference for the intended granular explosive test articles. Furthermore, the wall thickness was sized to

contain high pressure gases during ignition and burning. Epoxy was used as a sealant to avoid air pockets or vent pathways where needed. An ignitor bolt with ignitor leads threaded through and sealed with epoxy caps the ignition end of the DDT tube. Directly following the ignitor bolt is a thermally resistant plastic ignitor cup containing approximately 0.33 grams of boron potassium nitrate, $BKNO_3$, with an imbedded bridgewire initiator. Explosive samples 295.4 mm in length were pressed into the DDT tube to the intended percentage of TMD. Test hardware was rigged with two types of instrumentation, Ionization Pins (IP) and Strain Gauges (SG), to capture burning and detonation wave speed, approximate length of pre-detonation run up region, and time durations for the burning and detonation intervals. A combination of commercially available IP and custom NSWC increased sensitivity copper based IP were imbedded 6.1 mm into the explosive charge and clocked around the length of the DDT tube. Commercially available strain gauges were mounted along the length of the DDT tube to capture pressure buildup. (Bernecker & Price, 1972) DDT test data from *Price and Bernecker* is cited in (Baer & Nunziato, 1986) among other publications.

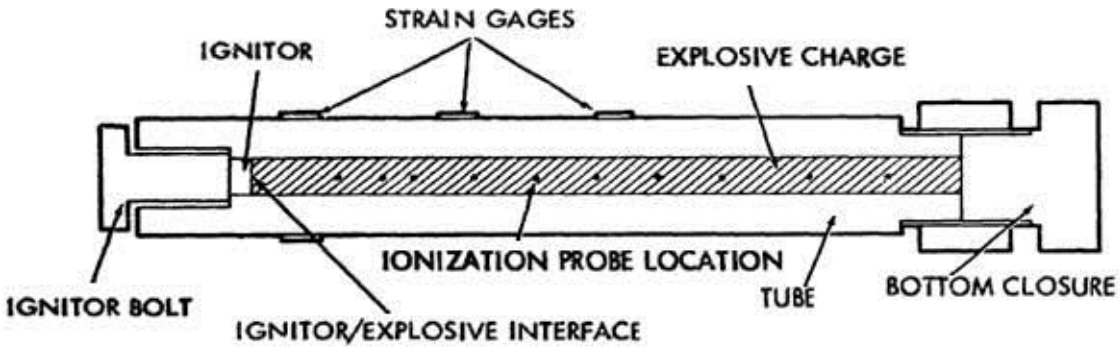

Figure 7: NSWC DDT Test Experimental Setup (Bernecker & Price, 1972, p. 3)

A compilation of test results utilizing the aforementioned experimental configuration are published in (Price & Bernecker, 1977). Experiments were conducted with Class A (approximately 200 μm) grain size samples as well as 115 μm sieve cut grain size samples at 70% TMD with wax content varying from 0-15%. Given the emphasis of the present research on the importance of porosity in run-up to DDT, only 0% wax content data will be used for comparison to computational results. Table 1 contains a summary of *Price and Bernecker's* HMX test data and Table 2 contains detailed data for the two 0% wax experimental shot numbers 1605 and 1616. Shot number 1605 is with Class A HMX data and shot number 1616 is with 115 μm HMX. In these tables V_{PC} is velocity of the post-convective (PC) wave, `l` is the pre-detonation column length $^{41}\Delta t_D$ indicates the "time from discharge of probe at x=41mm to onset of detonation, likewise $^{41}\Delta t_p$ indicates the "time from discharge of probe at x=41mm to passage of PC wave," and $^{41}\Delta t_E = {}^{41}\Delta t_D - {}^{41}\Delta t_p$. The post-convective wave is also referred to in the literature as the compressive wave.

Table 1: Data for 70% TMD HMX DDT Experiments. (Price & Bernecker, 1977, p. 20)

Shot No.	% Wax	ρ_0 g/cc	% TMD	b^f mm/μs	V_{PC} mm/μs	l mm	$^{41}\Delta t_D$ μs	$^{41}\Delta t_P$ μs	$^{41}\Delta t_E$ μs
				δ ~ 115μ					
1605	0	1.32	69.4	0.9	-	35	0	-	?
1610	3	1.31	70.7	0.51	1.14	67	22	0	22
1608	6	1.27	70.4	0.38	1.06	99	87	31	56
1611	9	1.23	69.9	0.38	0.7	143	197	80	117
1615	12	1.19	69.3	0.47	0.7	273	~569	~255	314
				δ ~ 200μ (Class A)					
1616	0	1.32	69.4	0.43	~1.3	45	1.7	1.2	0.5
1617	6	1.27	70.4	0.23	0.8	119	144	63	81
1618	9	1.23	69.9	0.23	1.1	210	395	216	179
1701	12	1.19	69.3	0.27	0.8	F	F	F	F

Table 2: HMX Prepared from Sieve Cut 115 and 200 Micron HMX (Price & Bernecker, 1977, pp. 45-46)

Shot Number: 1605			Shot Number: 1616		
Density	g/cc	1.322	Density	g/cc	1.322
	% TMD	69.4		% TMD	69.4
% Wax		0.0	% Wax		0.0
IP Data	x (mm)	t (μs)	IP Data	x (mm)	t (μs)
	16.1	0.0		16.0	0.0
	28.8	14.3		28.7	29.75
	41.5	18.25		41.4	39.6
	54.2	20.2		54.1	42.25
	66.9	21.95		66.9	43.8
	79.6	24.2		79.3	45.35
	92.2	25.85		92.3	47.1
	105.0	27.65		105.0	49.15
	130.4	31.25		130.4	52.45
	257.4	50.1		257.4	71.0
SG Data	x (mm)	t (μs)	SG Data	x (mm)	t (μs)
	12.2	4.6		12.3	21.1
	31.2	7.8		31.4	32.4-37.6
	50.3	20.7		50.4	40.5-44.5
	69.3	21.7		69.5	41.6-45.3
l (mm)		35±1	l (mm)		45±1
D (mm/μs)		6.80	D (mm/μs)		~6.9
σ (mm/μs)		0.04	σ (mm/μs)		-

Plots of distance versus time and strain versus time collected at specified ionization pin and strain gauge locations for shots 1605 and 1616 are included in Figure 8 through Figure 11 and will be referenced in subsequent chapters.

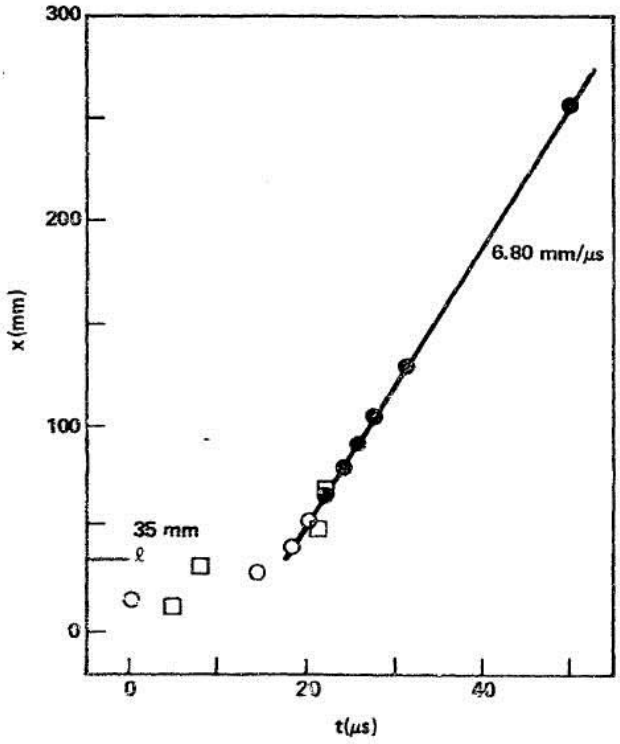

Figure 8: Shot No. 1605 Distance versus Time Data (Price & Bernecker, 1977, p. 52)

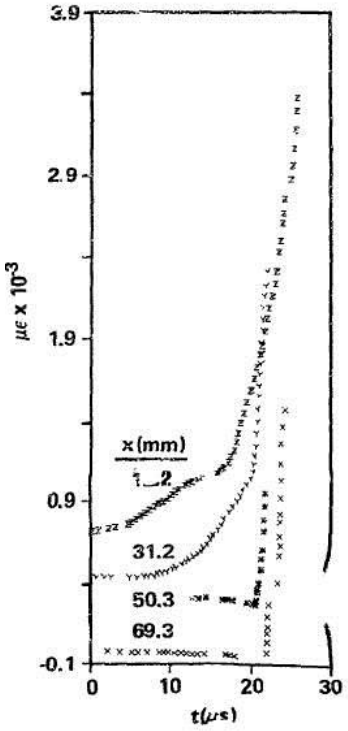

Figure 9: Shot No. 1605 Strain versus Time Data (Price & Bernecker, 1977, p. 52)

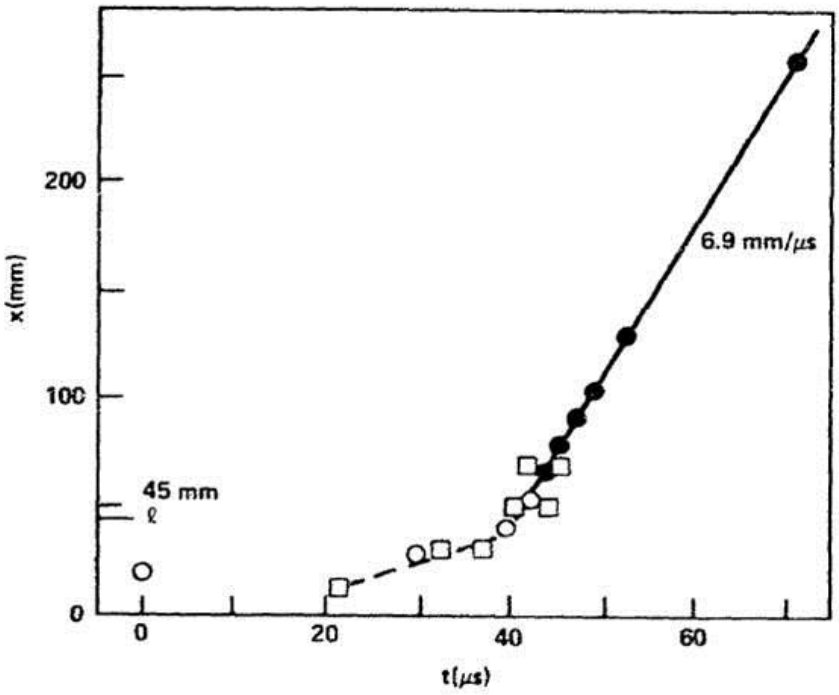

Figure 10: Shot No. 1616 Distance versus Time Data (Price & Bernecker, 1977, p. 57)

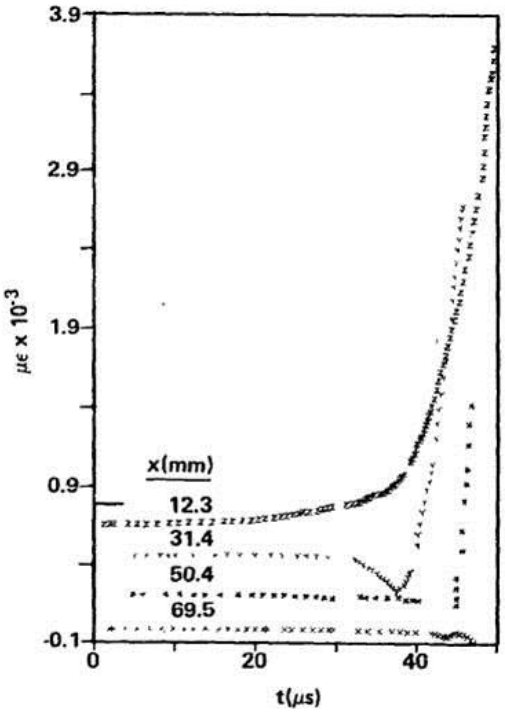

Figure 11: Shot No. 1616 Strain versus Time Data (Price & Bernecker, 1977, p. 57)

Los Alamos National Laboratory Experimental Data

The 1989 *McAfee* experimental DDT work out of Los Alamos National Laboratory (LANL) (McAfee, Asay, & Campbell, 1989) has been cited in numerous high density plug theoretical papers also out of LANL as well as external references including (Baer, Hertel, & Bell, 1996), (Stewart, Asay, & Prasad, 1994), (Xu & Stewart, 1997), and (Son, Kober, & Bdzil, 1997), among other publications.

The conceptual model of a high density plug in the DDT formation differs from the more traditional conduction, convection, and compressive burning followed by detonation schema generally assumed in DDT scenarios. *Stewart et al* describes the Los Alamos high density plug model in Figure 12.

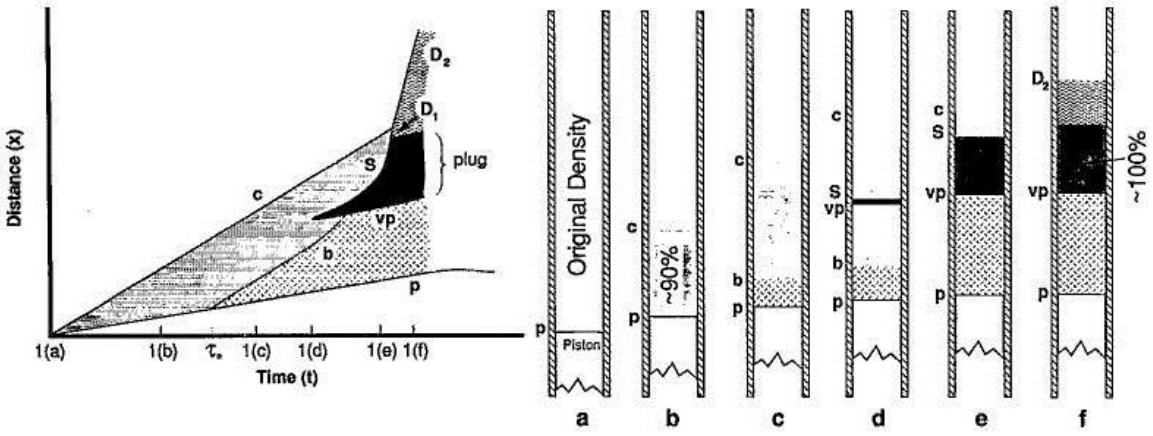

Figure 12: Los Alamos National Laboratory High Density Plug Model Description. (Stewart, Asay, & Prasad, 1994)

This model begins with a piston driven into an explosive sample during testing, denoted as (p) in Figure 12. Piston impact generates a leading compaction wave, labeled (c). This compaction wave increases test sample density from 70% of theoretical maximum and results in the formation of a reactive combustion wave,

labeled (b), near the trailing wave due to piston impact. The reactive combustion wave works its way forward and burns the compacted material. The reactive combustion front burn rate increase causes a shock, labeled (s), to coalesce in front of the combustion front and further compact the remaining unconsumed explosive to one hundred percent theoretical maximum density (TMD). This TMD "plug" region increases to consume all remaining unreacted material and then shock initiation occurs resulting in detonation of remaining material. The aft end of the plug is referred to as a "virtual piston" and labeled (vp). (Stewart, Asay, & Prasad, 1994)

Figure 13 from (Xu & Stewart, 1997) contains a diagram of the LANL DDT tube experimental configuration with additional annotations added to the original schematic in (McAfee, Asay, & Campbell, 1989) for clarity. *McAfee* utilized a gasless piston driven initiation system to avoid contamination of igniter gases within the sample test domain and non-planar effects of hotwire initiation mechanisms. This piston creates an initial compaction wave which is theorized to eventually form ahead of the burning front with the bridgewire initiation scheme in NSWC's experiments. In a follow-on paper *McAfee, Asay, and Bdzil* perform DDT experiments with direct hot gas ignition systems to quantify the influential region of convective burning which leads to compaction. This later work determined that pressure buildup occurs in the first approximately 10 mm of HMX column length and it is postulated that the dominant convective effects are limited to this sub-section. Based on further study McAfee concludes that "the boundary between the low-pressure convective region and the compact is equivalent to a combustion-driven mechanical piston." (McAfee, Asay,

& Bdzil, 1993) This assertion will be tested when comparing the NSWC direct-ignition results to the LANL piston impact experiments.

LANL's DDT tube is fabricated from Vascomax 250 steel with 12.7 mm inner diameter and 23.8 mm outer diameter. The DDT tube is caped on the far end with a steel plug and on the initiating end with an O-ring sealed piston mechanism and pressure transducer within the gauge holder assembly. The piston impacts HMX at an approximately steady state velocity of 100 m/s to induce burning. Class A or LX-04 grade HMX (approximately 170 μm mean and ≤ 60 μm) grain size at 65% and 75% TMD was hand packed in 8 mm segments into the DDT tube, with segments separated by 0.13 mm thick lead foil. Test hardware was rigged with a variety of instrumentation, including: self-shorting pins, ionization pins, optical fibers, Manganin gauge and x-radiographs focused on measuring lead foil location. Instrumentation in the experimental cavity is aligned with the interior chamber wall. As in the NSWC setup, epoxy was used as a sealant to avoid air pockets or vent pathways.

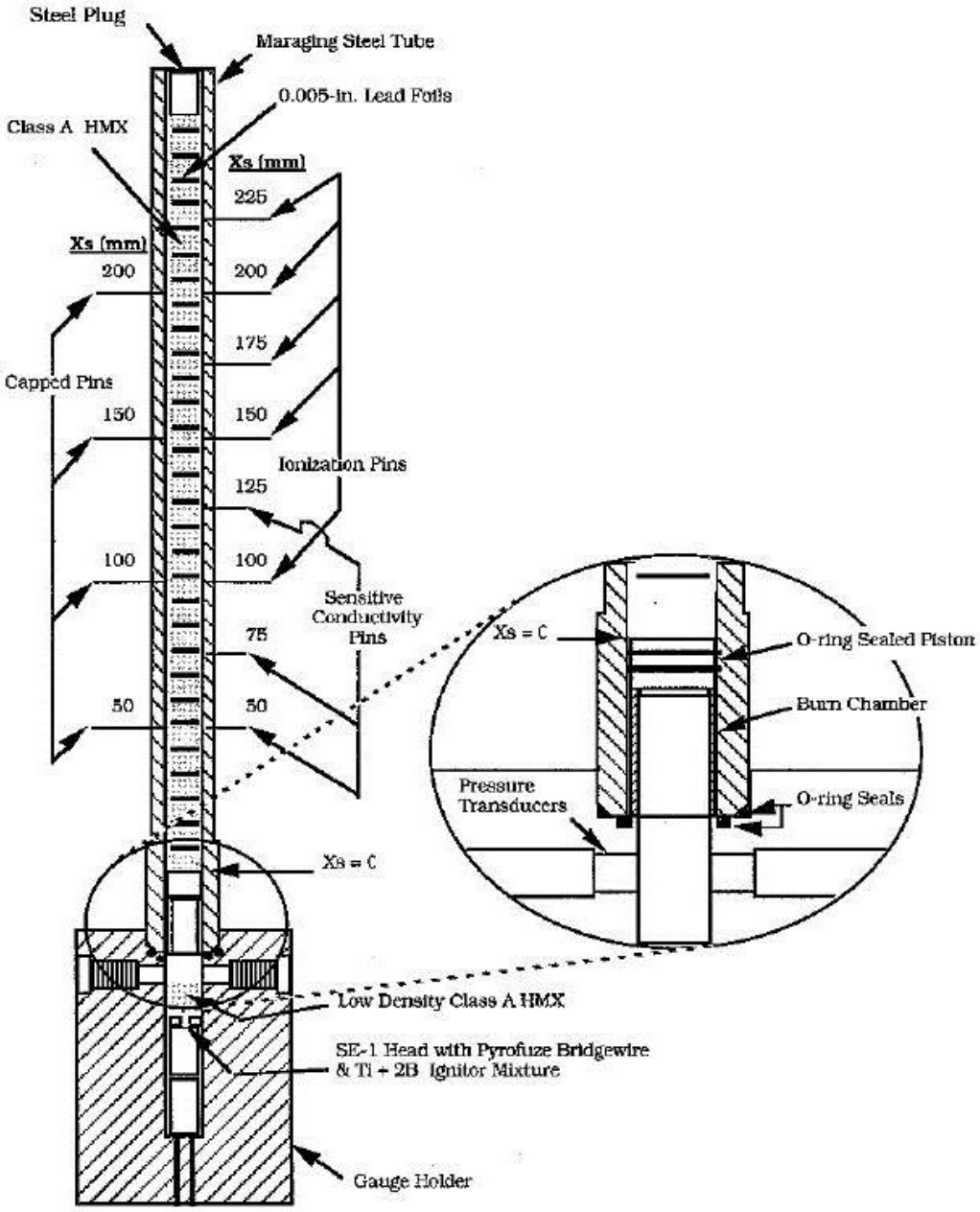

Figure 13: LANL DDT Test Experimental Setup (Xu & Stewart, 1997, p. 147)

Test results utilizing the aforementioned experimental configuration are also published in (McAfee, Asay, & Campbell, 1989). Figure 14 and Figure 15 contain plots of distance and chamber pressure versus time with the various instrumentation data sources noted on each plot. *McAfee* did not specify which shot numbers correspond to

65% or 75% TMD initial HMX sample density. While this reference contains plotted data for numerous experimental trials, the figures below for shot B-9036 are touted by *McAfee* as the "clearest observation of detonation in the compaction region."

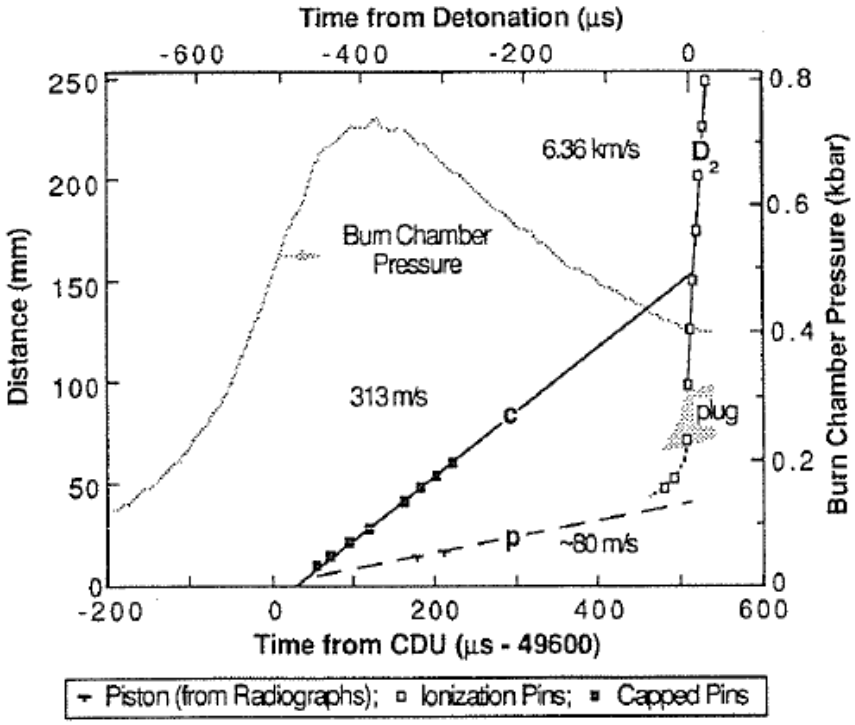

Figure 14: Reaction Front Distance and Chamber Pressure vs Time Data for Shot No. B-9036 During Entire Experimental Duration (McAfee, Asay, & Campbell, 1989, p. 272)

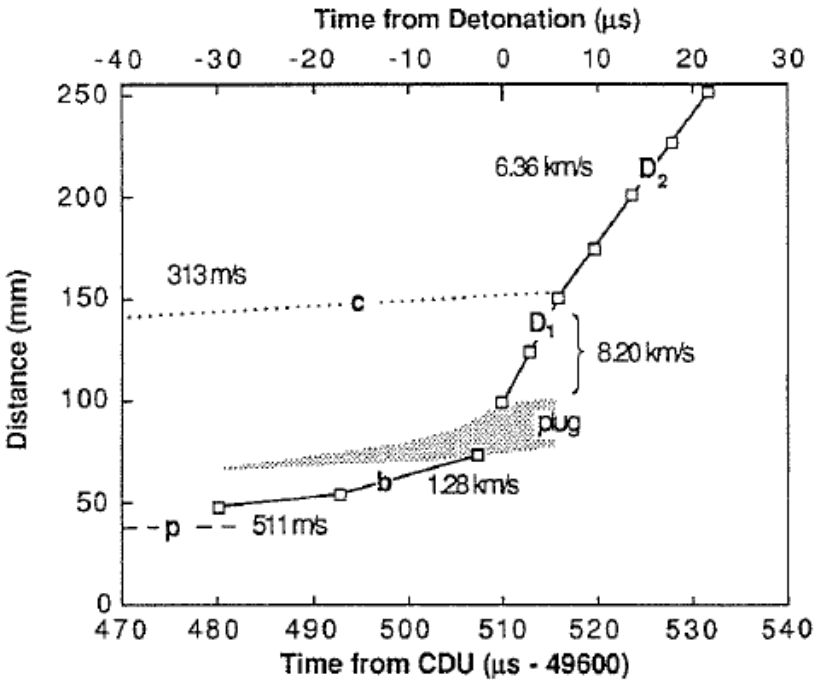

Figure 15: Reaction Front Distance vs Time Data for Shot No. B-9036 During DDT Event (McAfee, Asay, & Campbell, 1989, p. 272)

Analytical Verification

There is no straight forward method to analytically verify the complete LANL and NSWC DDT data sets due to the complex physics involved in the process of DDT. In order to determine if the experimental data is valid, the beginning and ending portions of the data can be approximated as solely burning/deflagration and pure detonation, respectively. Deflagration, which occurs over timescales in the 10^{-3} to 10^{-4} second range, is defined as high reaction propagation rate burning, though the terms deflagration and burning are ambiguous and no physical phenomenon occurs in the transition from burning to deflagration. Detonation, on the other hand, involves a shock wave with a thin trailing rapid reaction zone and occurs on the microsecond 10^{-6}

timescale. (Cooper, 1996) Thus, the presence of a shock wave at the reaction front is the defining distinction between deflagration and detonation.

Prior to the formation of a compressive shock wave and subsequent detonation, HMX deflagrates in a manner similar to solid rocket propellant. As with solid rocket propellant, the initial burning of HMX is largely a function of pressure, with secondary effects of initial temperature, according to the nominal burn rate law given below:

$$\dot{r} = ap^n \qquad [16]$$

The regression rate, normally measured in mm/sec or in/sec, is related to the operating pressure, p, by the coefficient "a" and exponent "n". These values are purely empirical in nature. There is no analytical treatment for predicting what the "a" and "n" values will be for any formulation, as they depend not only on composition and thermochemistry, but also on manufacturing and processing techniques. Therefore, to analytically verify the LANL and NSWC DDT experiments of interest, the author relies on the range of HMX burn rate data published in the literature to determine appropriate coefficients for Equation [16] above.

The pressure exponent or combustion index "n" value is of particular importance in determination of the burn rate. The pressure exponent for solid rocket motors is below 0.6 for most cases. High values of n, for example n > 0.8, are sensitive to any changes in pressure and are not common in solid rocket motors. (Sutton & Biblarz, 2010) If n > 1, the burning rate and pressure become irreversibly sensitive to each other and can lead to a runaway reaction and over-pressurization. This is to be avoided in solid rocket motors, but is inherent in detonation of HMX and other

explosives. This burning to deflagration behavior can be clearly observed at the beginning of Figure 8, Figure 10, and Figure 14.

Knowledge of the burning rate is important to the DDT process. Gas production from HMX combustion continuously increases the pressure and thus the burn rate, and dynamically compacts the HMX bed. The gas production continues until it has exceeded the flame front's ability to permeate through the porous grain, which is increasing in density because of compaction driven by the deflagrating material. This leads to a runaway reaction due to the high combustion indices. Subsequently, a compressive shock wave forms and begins the transition to detonation.

Several notable sources exist for burning rate data of HMX. At low pressures, below 100 MPa (14.5kpsi), (Sinditskii, Egorshev, Berezin, & Serushkin, 2009) summarize the HMX combustion data of American and Russian sources in a consolidated burning rate versus pressure plot given in Figure 16. A slope break (common in propellants for a large range of pressures) is apparent in this data at approximately 10MPa. The combustion index is very high in this data and over unity above 10MPa.

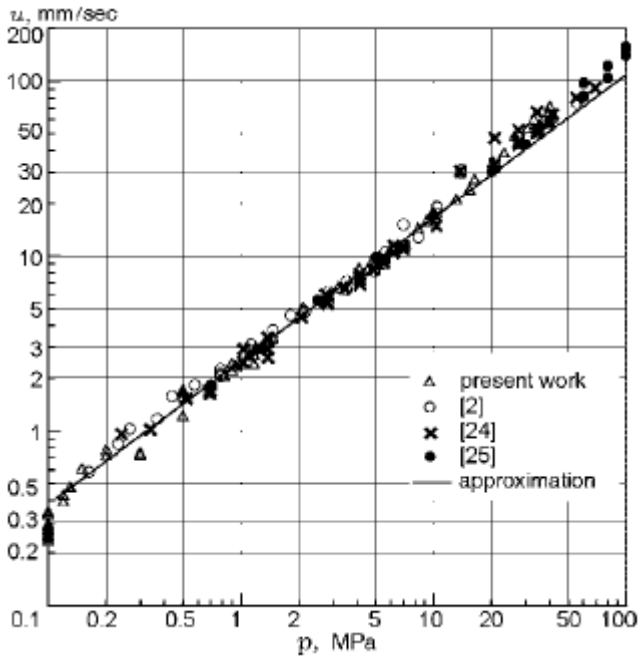

Figure 16: HMX Burning Rate Data for Low Pressures (Sinditskii, Egorshev, Berezin, & Serushkin, 2009)

(Esposito, Farber, Reaugh, & Zaug, 2003) of Lawrence Livermore National Laboratory published burn rate data for HMX at higher pressures, with a combustion index again above unity (n = 1.27) for small grain HMX operating above 5GPa (725kpsi) in Figure 17. Near the theoretical maximum density of HMX the detonation threshold can be generally approximated between roughly 3-8 GPa, depending on the penetration distance of the compressive shock wave into the energetic material.

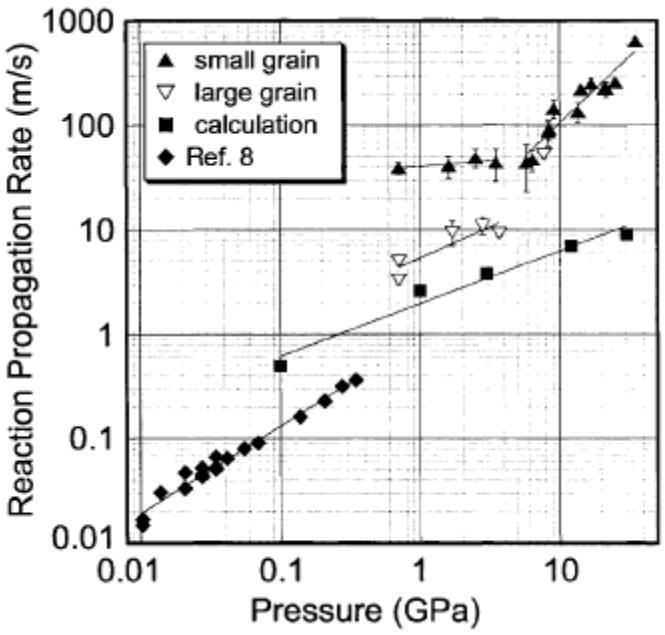

Figure 17: HMX Burning Rate Data for High Pressures

(Esposito, Farber, Reaugh, & Zaug, 2003)

For ease of reference, the combustion indices for the above two data sets are tabulated below.

Table 3: HMX Combustion Indices for a Range of Pressures

Source	Pressure (MPa)	Combustion Index "n"
Sinditskii, et al	0.2 - 10	0.77-0.82
Sinditskii, et al	10 - 100	0.9-1.1
Esposito, et al	>5,000	1.27

The above data would be particularly useful if instrumentation could resolve these instantaneous pressures of the flame front during the deflagration phase of HMX, which happens very early in the DDT process. This is beyond the capabilities of current

pressure transducers, hence the use of ionization pins to locate the shock front and estimate the burning rate and detonation velocity. Figure 14 shows a burn chamber pressure, which is the initial pressure rise from the igniter. The peak of 0.07 MPa would be considered the low-pressure limit of HMX, as HMX does not burn below atmospheric pressure according to (Sinditskii, Egorshev, Berezin, & Serushkin, 2009). Moreover, the pressure data does not capture the flame front propagation, which is instead marked by ionization pins. As such, this data is not useful to analytically calculate the burning rate of HMX as it transitions through the DDT tube.

As discussed in the detailed Literature Review, the remarkable progress of fiber optic measurements has recently (2011) been able to resolve the pressures during burning, deflagration, and detonation. Figure 82 can be used to correlate burning of the explosive to fundamental equations. According to the pressure measurements on this plot and previous HMX burn rate data discussed above, the burning-to-deflagration pressure increase from 1.86 GPa to 6.3GPa would roughly equate to a maximum burning rate of 58 m/s according to the HMX burn rate data from (Esposito, Farber, Reaugh, & Zaug, 2003). Shown mathematically, $r = 5.6 \times 6.3^{1.27} =$ **58 m/sec**. This estimation agrees relatively well with the **80 m/sec** LANL shot B-9036 HMX ionization pin rate listed on Figure 14. It should be noted that this is not a one-to-one comparison as (Udd, Dunaway, Biegert, & Johnson, 2011) used a 97% RDX and 3% wax composition in this experiment, which is less energetic than HMX (detonation velocity of RDX is 8.59 vs 9.1 km/sec for HMX with a molecular weight ratio of 0.75). (Cooper, 1996) The underestimated burning rate calculated as 58 m/s vs measured 80 m/sec is thusly expected. NSWC did not capture data at a high enough frequency to

adequately resolve the early deflagration regime as their experiments were configured to force relatively quick DDT.

Calculation of detonation parameters at the Chapman-Jouguet (CJ) state also rely on a mixture of experimental data and empirically derived equations. Table 4 contains experimental data for the CJ State of HMX at TMD listed in (Cooper, 1996). It is noteworthy to mention that references in the literature contain a range of TMD for HMX crystal density between 1.89-1.905 grams/cm^3 and thus stated percentages of TMD in this dissertation are an approximation depending on the assumed TMD of the specific reference. NSWC assumes a TMD of 1.902 grams/cm^3 and LANL use a TMD of 1.89 grams/cm^3.

Table 4: Experimentally Obtained HMX Detonation Parameters at TMD (Cooper, 1996, p. 258)

Variable	HMX
% TMD	100
ρ_0 $[g/cm^3]$	1.89
D $[km/sec]$	9.11
ρ_{CJ} $[g/cm^3]$	2.515
P_{CJ} $[GPa]$	39

Knowing detonation velocity at TMD allows for straight-forward calculation of detonation velocity for a granular explosive containing air filled voids at a correspondingly lower density. *Cooper's* text describes how Manny Urizer of then Los Alamos Scientific Laboratory (LASL) derived an equation to determine detonation velocity of energetic mixtures as a function of partial volume and individual constituent

detonation velocities. For an air filled void equivalent detonation velocity of 1.5 km/s, the detonation velocity of a less than TMD granular explosive can be calculated according to Equation [17]. (Cooper, 1996)

$$D = 1.5 + \rho\left(\frac{D' - 1.5}{\rho_{TMD}}\right) \quad [17]$$

By plotting experimentally obtained unreacted material density versus density at the CJ State for dozens of explosive variants, *Cooper* obtains a logarithmic relationship between unreacted explosive density and density at the CJ state given in Equation [18]. Subsequently, by rearranging mass and momentum equations for the Hugoniot jump discontinuity briefly discussed in the detonation section of the Literature Review, *Cooper* obtains Equations [19] and [20] for pressure and velocity in the CJ State. (Cooper, 1996)

$$\rho_{CJ} = 1.386{\rho_0}^{0.96} \quad [18]$$

$$P_{CJ} = \rho_0 D^2\left(1 - \frac{\rho_0}{\rho_{CJ}}\right) \quad [19]$$

$$u_{CJ} = \frac{P_{CJ}}{\rho_0 D} \quad [20]$$

An alternative empirically based calculation for CJ pressure as a function of gamma, the ratio of specific heats, was derived by *Kamlet and Short* at NSWC. The authors utilize experimentally observed data trends to develop Equation [21] for gamma as a function of unreacted material density. *Kamlet* further derives Equation [22] for pressure at the CJ State from conservation of mass and momentum as well as definitions of the CJ State and speed of sound. (Kamlet & Short, 1980) In the absence of an equation for gamma, typical energetic material calculations assume gamma

equals three. However, the data in Table 5 shows that three is only valid near TMD and in not appropriate for comparison to the NSWC and LANL experiments.

$$\gamma_{CJ} = \frac{0.655}{\rho_0} + 0.702 + 1.107\rho_0 \quad [21]$$

$$P_{CJ} = \frac{\rho_0 D^2}{\gamma_{CJ} + 1} \quad [22]$$

Table 5 contains the hand calculated values obtained by applying Equations [18] to [22] to the specific densities of HMX used in NSWC shot number 1605 and 1616 as well as LANL shot number B-9036. Note that the DDT tube diameters in both of these experiments were sufficiently large such that they are above the critical diameter of HMX. At energetic material cylindrical sample diameters below the critical diameter detonation velocity decreases with decreasing diameter until the detonation wave is no longer sustainable due to edge interaction effects with tube walls. One noteworthy assumption pertains to the density of HMX in LANL shot B-9036. *McAfee* states that all experiments are conducted with either 65% or 75% TMD granular HMX; however; *McAfee* does not specify the density used for each individual shot data record. Thus, the assumption that shot B-9036 occurred with 65% TMD HMX is based on comparison of the calculated detonation velocity of 6.45 km/s to the experimentally recorded value of 6.36 km/s. Table 5 shows excellent agreement between the NSWC and LANL experimental detonation velocity data as compared to values calculated with Equation [17], with experimental error ranging from 0.3% to 1.4%. Both *Cooper* and *Kamlet's* independently derived empirical approaches to calculating pressure at the CJ State are included for completeness to demonstrate the validity of each method.

Cooper and *Kamlet's* treatment of pressure at the CJ State only differed by 1.4% error for NSWC and 2.1% error for LANL data.

Table 5: Analytical Calculation of NSWC and LANL Detonation Parameters

Variable	NSWC	LANL
% TMD	69.4	65
ρ_0 $[g/cm^3]$	1.32	1.23
D $[km/sec]$	6.82	6.45
ρ_{CJ} $[g/cm^3]$	1.81	1.69
P_{CJ} $[GPa]$	16.58	13.91
u_{CJ} $[km/sec]$	1.84	1.76
γ_{CJ}	2.66	2.60
Rule of γ P_{CJ} $[GPa]$	16.81	14.20
% Diff P_{CJ}	1.4	2.1
Test Data D $[km/sec]$	Shot 1605: 6.8 Shot 1616: 6.9	Shot B-9036: 6.36
Experimental Error % D	Shot 1605: **0.3** Shot 1616: **1.1**	Shot B-9036: **1.4**

Based on the above Analytical Verification section calculations of burn rate, where possible, and detonation velocity, as compared to data for NSWC shots 1605 and 1616 as well as LANL shot B-9036 the author concludes that the experimental data in these references is suitable for further use in computational validation. Additional detonation parameters at the CJ State are included in Table 5 for comparison with CTH results in Chapters 4 and 5.

CHAPTER 4

CTH HYDROCODE: RESEARCH GAP IDENTIFICATION

Background on CTH

The term hydrocode refers to an analysis field focused primarily on material and shock dynamics behavior in the very high strain rate regime. Figure 18 below graphically demonstrates this assertion. In Figure 18, the region between σ_0 and σ_1 represents elastic material behavior, between σ_1 and σ_2 is the elastic-plastic material behavior region, and beyond σ_2 is the plastic (fluid-like) behavior region. It is above σ_2 in the very high strain rate region where hydrocodes are designed to operate. In this region materials exert hydrodynamic behavior where material strength does not dominate a solution; indeed, early hydrocodes did not even include material strength to compensate for computational resource limitations. Given their operation primarily in the hydrodynamic regime, the field of analysis is termed "hydrocode."

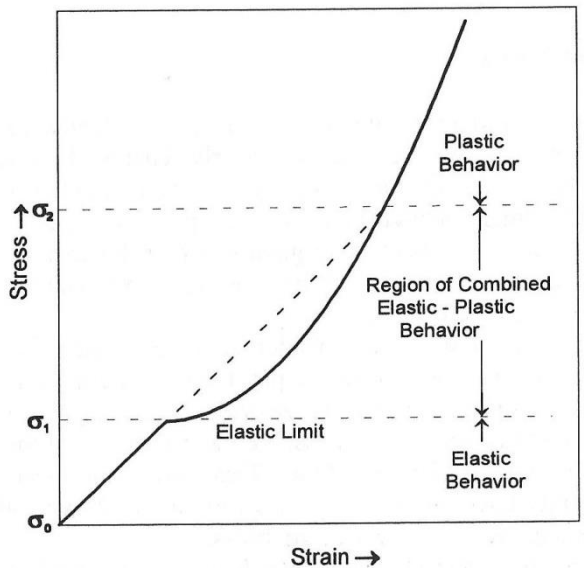

Figure 18: Compressive Stress-Strain Curve to Very High Stress Level. (Cooper, 1996, p. 168)

CTH is the hydrocode utilized for implementing the research contained within this dissertation. CTH was developed and is maintained by Sandia National Laboratory and is currently designated as a Defense Article. The code name CTH is not truly an acronym, but more of a math pun of sorts. What would become CTH began in 1969 as the Coupled Hydrodynamic and Radiation Transport Diffusion (CHART-D) one dimensional hydrocode. In 1975, CHART-D was upgraded to a two-dimensional hydrocode and the name was changed to CSQ, or CHART-D Squared ($CHART\text{-}D^2$), to signify the addition of a second dimension to the analysis domain. Lastly, in 1980 CSQ was re-christened CTH, or CSQ to the Three-Halves ($CSQ^{3/2} = (CHART\text{-}D^2)^{3/2}$) to keep the math correct while denoting the addition of a third spatial dimension to the analysis domain. (Crawford D. , 2011)

CTH version 10.2 is utilized for the present analyses. CTH is a three-dimensional multi-material Eulerian hydrocode capable of modeling high strain rates characterized by high velocity impact, shock wave transmission through dissimilar materials and shock wave coalescence. The user interface for CTH is rooted in its national laboratory research code beginnings and the code is still intended to operate on massively parallel Linux computing systems with “input decks”. Though the days of punch cards are history, the code utilizes a text format input deck arranged into various cards to define pertinent physics and geometry. Post-processing can be accomplished both manually using the output text and binary files or in conjunction with the build-in SpyMaster code whose commands can be added as a card to the input deck to generate plot images as the code is running. Both post-processing methods are utilized in this dissertation.

The code inputs are loosely arranged in terms of geometric input, definition of initial conditions and boundary conditions, as well as EOS, strength models and fracture criteria. CTH has a fairly extensive library of EOS and strength models for numerous materials of interest in common energetics analyses. However, the user can define material properties for existing equations of state and this option is largely exercised for the subsequent analyses in this dissertation to include complex material behaviors and properties not listed in the standard library inputs. An overview of early EOS formulation and requirements for implementation in hydrocodes is provided in (Hubbard & Johnson, 1959). The base units of CTH are time in seconds, distance in centimeters, temperature in electron volt, pressure in dynes/cm^2, and energy in ergs. Additional details on CTH input structure, solvers, EOS, geometry input, strength models, fracture criteria, and many more relevant complex physical phenomenon within the code capability are described in the following references: [(Crawford, et al., 2012), (Hertel E. S., 1998), (Hertel & Kerley, 1999), (Hertel & Kerley, 1998), (Silling, 1996), (Taylor, 1992)]

Characteristics of Shock Physics

Before delving into the computational outputs of CTH modeled with existing EOS for the above two NSWC and LANL test cases, it is instructional to first define some fundamental shock wave interaction effects that one can observe in the computational results. Three basic types of shock interactions, as described by *Cooper*, are: (1) the impact of two different materials at high velocity, (2) behavior at the interface of two different materials and (3) colliding shockwaves. (Cooper, 1996)

High velocity material impacts are common in the field of energetics both as an initiation mechanism, in the case of high velocity flyer plates, and as an insensitive munitions design concern in the instances of bullet or fragments impacting a component filled with energetic material. High velocity flyer plates can be used to begin an initiation train. In general, flyers begin initiation via shock transfer which occurs when a thin disk-like component impacts an energetic material at very high velocity (on the order of km/s). Upon impact, a shock wave travels from the site of impact into the energetic material and another wave travels back into the flyer plate. Conservation equations dictate that the pressure and particle velocities in the energetic material and flyer plate are equivalent at the impact site. (Cooper, 1996) This means of initiation is demonstrated in the subsequent section in order to force a detonation in the LANL experiment. Detonation in the LANL DDT experimental setup is forcibly achieved by replacing the slow moving (100 m/s) piston with a thin layer of steel moving at very high speed (5 km/s).

When a shock moves through one material to an adjacent contacting material the pressure wave changes according to the shock impedance, Z, defined in the below equation. In this equation ρ is the initial (un-shocked) material density and U is the shock speed.

$$Z = \rho_0 U \qquad [23]$$

Transitioning from lower shock impedance material to higher shock impedance material results in an increase in pressure. Alternatively, passing from higher shock impedance material to lower shock impedance material results in a lower pressure.

Hugoniot curves, introduced in Figure 3 for the pressure-specific volume plane, are useful in determining the corresponding pressure change in an adjacent material due to shock transfer. For a given material, all shock solutions (including the CJ point) lie along the material specific Hugoniot curve. Generally, the pressure-particle velocity plane form of the Hugoniot curves is utilized in this type of calculation as the particle velocity and pressure are equivalent at the material interface. Thus the Hugoniot equations can be solved for the unknown pressure of the wave traveling into the adjacent material or located on a Hugoniot curve for the adjacent material. (Cooper, 1996) Reference (Mahon & Paine, 2014) details the shock impedance study of the shock damping capabilities of several materials when positioned adjacent to an HMX based energetic material.

The pressure-particle velocity plane Hugoniot curves for HMX detonation reaction products at the LANL experimental configuration density of 1.23 g/cm^3 and the NSWC experimental configuration density of 1.32 g/cm^3 are presented in Figure 19 below. *Cooper* obtained the empirically derived pressure ratio versus velocity ratio equation used to calculate the curves in this figure by plotting pressure-to-CJ pressure ratios versus particle velocity-to-CJ particle velocity experimental data for numerous explosive variants. Equation [24] contains *Cooper's* empirical relation valid in the range of pressure-to-CJ pressure ratios greater than 0.08. (Cooper, 1996)

$$\frac{P}{P_{CJ}} = 2.412 - 1.7315\left(\frac{u}{u_{CJ}}\right) + 0.3195\left(\frac{u}{u_{CJ}}\right)^2 \qquad [24]$$

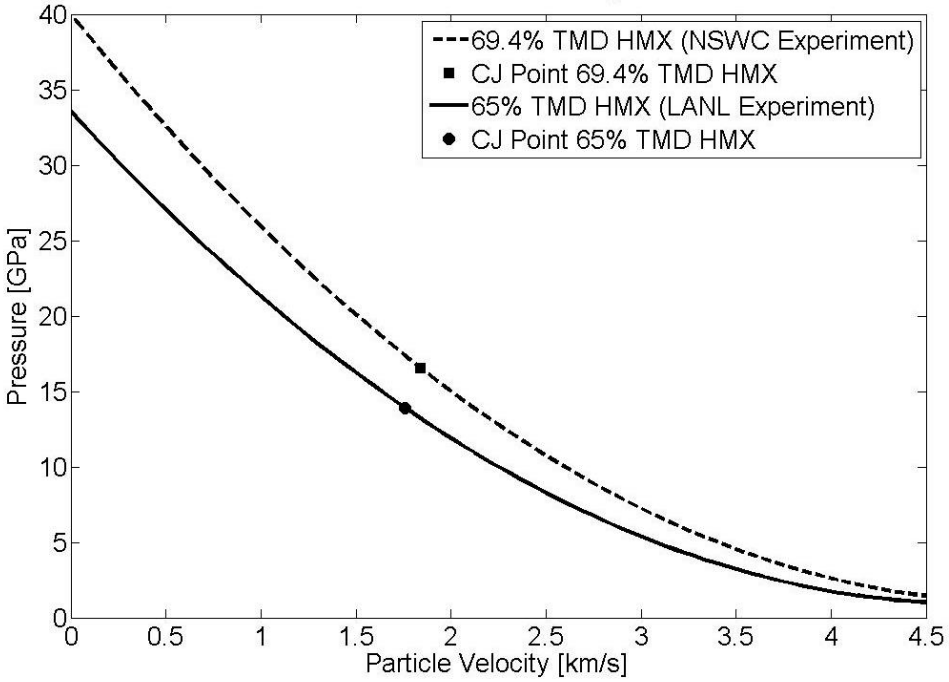

Figure 19: Detonation Reaction Products P-u Plane Hugoniot for HMX

Colliding shock waves represent the third standard shock interaction scenarios in detonation physics. As expected, when two shock waves collide, the collision results in shock waves which reflect backward relative to the original direction of travel. Interestingly, the pressure of the reflected waves is higher than the sum of the pressures of the original two coalescing waves due to the Hugoniot curves (i.e. not linear relationships). (Cooper, 1996)

A useful tool in the analysis of high velocity impact, shock transmission through dissimilar materials, and colliding shock physics is known as a *Pop-Plot*, named after its' creator Alfonse Popalato of Los Alamos National Laboratory. Pop-plots are a graphical representation of experimentally obtained run distance into an explosive that a shock wave of known pressure travels before resulting in detonation of the energetic material. These plots provide useful comparisons to hydrocode analytical results as

impacted explosives do not immediately detonate upon contact with a shock wave; rather the wave travels a finite distance into the material before inducing detonation. The higher the pressure of the incoming shock wave, the shorter the run-up distance to detonation. Furthermore, Pop-plots indicate pressure thresholds below which detonation has not been experimentally observed (though DDT is still a possibility depending on confinement, hardware configuration, and environmental conditions). Figure 20 contains a Pop-plot for HMX at 65% TMD and will be utilized for comparison to CTH computational results in subsequent sections and chapters. A Pop-plot closer to the NSWC experimental HMX density of 70% TMD could not be located in the literature. There is one noteworthy pressure distinction: the CJ pressure represents the minimum steady state pressure trailing the detonation wave while the Pop-plotted pressure is the detonation initiation threshold.

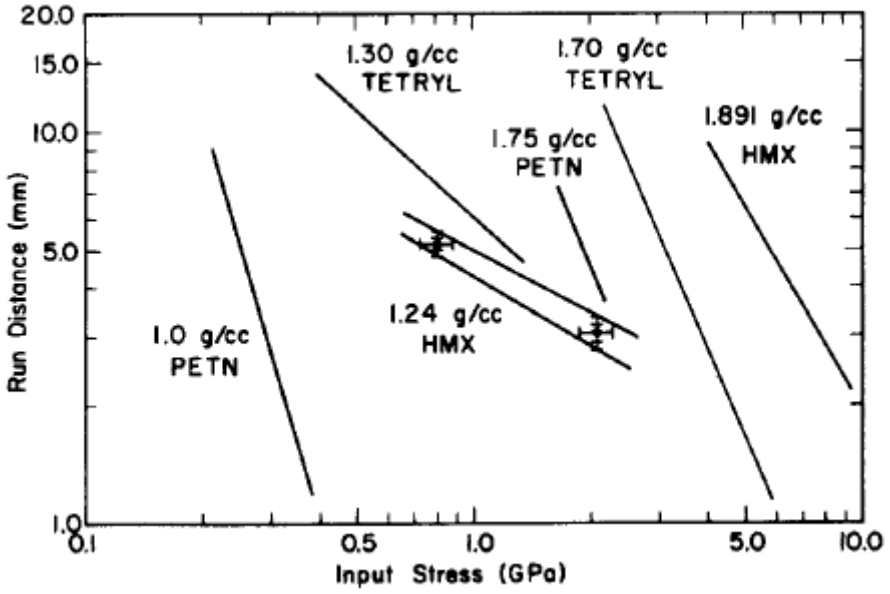

Figure 20: HMX Pop-Plot at Approximately 65% TMD (Dick, 1983)

Research Gap Identification

The remainder of this chapter contains a description of the model set-up, pertinent physics and results obtained for 22 simulations total (11 each for the NSWC and LANL test configurations presented in Chapter 3) which have been formulated to fully characterize the existing inability of CTH to model DDT due to shock initiation. For clarity, these 11 different variants of simulations utilized to study the research gap are listed below in bullet points.

- Inert simulations utilizing the Mie-Gruneisen (MGR) equation of state for HMX to characterize the contribution and differences between NSWC and LANL initiation mechanisms (piston versus $BKNO_3$ pellet).
  - (1) HMX at 100% TMD with baseline mesh spacing
  - (2) HMX at NSWC and LANL densities (69.4% and 65% TMD, respectively) with baseline mesh spacing
  - (3) HMX at NSWC and LANL densities (69.4% and 65% TMD, respectively) with refined mesh spacing
  - (4) HMX at NSWC and LANL densities (69.4% and 65% TMD, respectively) with non-uniform mesh spacing
- History Variable Reactive Burn (HVRB) simulations with modified initiation mechanisms to force detonation of HMX.
  - (5) HMX at 100% TMD with baseline mesh spacing
  - (6) HMX at NSWC and LANL densities (69.4% and 65% TMD, respectively) with baseline mesh spacing

        - (7) HMX at NSWC and LANL densities (69.4% and 65% TMD, respectively) with refined mesh spacing
        - (8) HMX at NSWC and LANL densities (69.4% and 65% TMD, respectively) with non-uniform mesh spacing
    - (9) History Variable Reactive Burn (HVRB) simulations with refined mesh spacing and representative test case initiation mechanisms to model attempted DDT of HMX.
    - (10) Arrhenius Reactive Burn (ARB) simulations run on a non-uniform mesh with representative test case initiation mechanisms and Arrhenius equation parameters tailored to HMX *deflagration* rates to model initial deflagration of HMX.
    - (11) Arrhenius Reactive Burn (ARB) simulations run on a non-uniform mesh with representative test case initiation mechanisms and Arrhenius equation parameters tailored to HMX *detonation* rates to model detonation regime of HMX run on a non-uniform mesh.

Hydrocode Model Descriptions

Simulations in this chapter ran on an HP Z800 workstation with 12 cores, 64 Gigabytes of RAM, and 2 Terabytes of disk space. Details of the mesh cell counts for the three mesh size variations are listed in Table 6. The mesh size for NSWC simulations is comparatively larger than for LANL simulations due to larger experimental apparatus dimensions requiring a larger computational domain. Non-uniform mesh spacing was utilized with the Arrhenius Reactive Burn simulations to

reduce mesh spacing, where appropriate, and optimize use of computational resources. Uniform mesh dimensions were determined based on the minimum material thickness within the LANL and NSWC geometric inputs. In NSWC and LANL models the driving thin features are the DDT tube wall thicknesses of 1.734 and 0.555 centimeters, respectively. A general guideline for simulation robustness and stability is to have a minimum of two to five cells across the minimum thickness in a mesh. The reason for this recommendation is because CTH is an Eulerian hydrocode and as such computes shared volume fractions as materials move through fixed mesh cells. Consequently, if a thin material is not defined by a sufficient number of computational cells across a thickness the shared volume fractions can be incorrectly calculated in addition to mass movement and material characteristics.

All simulations were performed in three-dimensional space with quarter symmetry boundary conditions. Specifically, boundary conditions at the bottom of the X and Y axes were set to symmetry and boundary conditions at the bottom and top of the Z axis as well as the top of the X and Y axes were set to an outflow boundary condition such that mass is allowed to exit (but not re-enter) the mesh.

Table 6: CTH Simulation 3-D Quarter Symmetry Mesh Cell Counts

Test Cases	**Baseline Mesh** *[Number of Cells]*	**Refined Mesh** *[Number of Cells]*	**Non-uniform Mesh** *[Number of Cells]*
NSWC	1,361,250 ΔX=ΔY=ΔZ=0.1cm	10,890,000 ΔX=ΔY=ΔZ=0.05cm	16,720,000 ΔX,Y,Z: 0.02-0.2cm
LANL	496,000 ΔX=ΔY=ΔZ=0.1cm	3,968,000 ΔX=ΔY=ΔZ=0.05cm	7,723,125 ΔX,Y,Z: 0.02-0.2cm

Figure 21 shows a 3-D isometric cross section of the NSWC materials plot as well as a 2-D close-up cross-section near the initiating end of the experimental set-up. Table 8 contains detailed information on the material number, component name, component material, EOS, strength model and fracture criteria references for the NSWC geometry. In this figure, A indicates Material 4 and 5, the bottom lug and closure, modeled as 4340 steel in the absence of specific alloy information beyond the indication of "heavy end closure". The ignitor bolt shown in F and listed as Material 3 is similarly modeled as 4340 steel. All three materials are defined with a SESAME EOS CTH library set of parameters for 4340 steel, a CTH library set of Johnson Cook strength model parameters and a CTH library fracture pressure.

B shows Material 1, the DDT tube modeled as 1045 steel in keeping with the NSWC reference to carbon mechanical steel with a tensile strength of 80 ksi, yield

strength of 65 ksi, and ultimate tensile strength of 90 ksi. (Bernecker & Price, 1972) Matweb lists the yield strength of cold drawn AISI 1045 round steel as 76.9 ksi and the ultimate strength as 90 ksi. (Matweb, 2014) The selection of 1045 steel with a slightly higher yield strength than the steel quoted by NSWC translates to greater confinement and should assist with simulating DDT. Steel with lower yield strength would equate to less confinement and therefore make the task of modeling DDT more challenging. The 1045 steel alloy was the closest alloy to yield and ultimate stress identified during an extensive literature review of available carbon mechanical steel Johnson Cook parameters. The EOS is set to CTH library parameters for a SESAME Iron model because 1045 steel is composed of 98.51 - 98.98 % Iron. (Matweb, 2014) Material 3, indicator E, is assigned a programmed burn EOS, which utilizes Jones-Wilkins-Lee (JWL) model parameters. These parameters are not available in the CTH library and were calculated by the author in the LLNL code CHEETAH and formulated into a CTH user defined EOS. Air is assigned as Material 7 and occupies the remainder of the domain not assigned to other materials in previous geometry definitions. Air is modeled with a CTH library SESAME EOS table, an elastic-perfectly-plastic Von Mises strength model and a very low fracture pressure. Marker D indicates the presence of tracer points. In CTH, tracers are discrete user defined points for collecting and recording specified local variable data. Tracers can be input as Lagrangian and move with a material, or Eulerian and fixed to the mesh. Both variants are utilized in this analysis.

Table 8 lists HMX, denoted as marker C and Material 6, with multiple EOS. The selection of EOS is based on the simulations listed in the beginning of the Research

Gap Identification section. A Mie-Gruneisen EOS is utilized for inert simulations. This EOS has been compiled by the author from a variety of sources and entered into CTH as a user defined material with a P-α porosity model when running with NSWC and LANL HMX densities. The P-α porosity model introduces porosity by assigning solid material density, porous material density, start and end compaction pressures as well as various other optional criteria. The Mie-Gruneisen parameters utilized in this user defined model were selected after an extensive review of available literature on granular HMX. Additional discussion of the Mie-Gruneisen EOS and p-α porosity model is included in the chapter entitled MODEL IMPROVEMENTS IN CTH. Throughout this work, it is assumed that the HMX modeled herein is based on material characterization studies or validation experiments conducted with high quality pure HMX granular samples. Inclusion of HMX material impurities would require re-definition and validation of EOS model parameters.

An HVRB EOS was input for HMX when running both modified forced detonation and representative test case DDT simulations. The HVRB model is a composite EOS, meaning it is defined from two other primary EOS along with additional parameters controlling calculation of reactivity, propagation, and mixing. This HVRB model utilized the CTH library reactivity parameters in conjunction with the appropriate variation of user defined Mie-Gruneisen EOS for unreacted material and CTH library SESAME HMX detonation products. SESAME and Mie-Gruneisen EOS are both primary EOS. Variations in Mie-Gruneisen parameters are included in simulations with no porosity or porosity scaled to NSWC and LANL densities.

Lastly, an Arrhenius Reactive Burn (ARB) model was used in Arrhenius equation based simulations for both models of HMX deflagration and detonation. As with the other HMX equations of state in this dissertation study, ARB parameters in Table 7 were identified in a thorough literature review and formulated into a user defined ARB EOS. Both deflagration and detonation parameter define one-step zero-order Arrhenius rate reactions. The ARB EOS is also a composite EOS with user defined frequency factor, reformulated activation energy and reaction threshold temperature. The appropriate user-defined Mie-Gruniesen model was again input for unreacted HMX as well as the CTH library SESAME table for HMX detonation products. The differentiating features between Arrhenius deflagration and detonation parameter sets are that the deflagration model has a lower activation energy and frequency factor (as expected). The author identified well over a dozen Arrhenius detonation parameter sets for HMX at various states (solid, liquid, and/or gas) and across a broad temperature range. Therefore, the HMX detonation ARB parameters were selected for consistency with the single deflagration Arrhenius parameter found in the literature. Deflagration frequency factor is on the order of 10^{15} and detonation frequency factor is on the order of 10^{19}. This particular set of Arrhenius HMX detonation parameters was selected because it is valid in the solid-liquid state range near HMX melting, was obtained via experiment with high heating rates (as is appropriate in DDT scenarios), (Yang, 2008) and compared well with 10^{18} order of magnitude frequency factor data for the less energetic explosive RDX (Cooper, 1996). The same set of Arrhenius parameter data is used in NSWC and LANL CTH simulations. Both experimental test scenarios were run on a non-uniform mesh for

Arrhenius HMX analyses because past work by the author, presented in (Mahon, 2014) has shown that the CTH implementation of the Arrhenius EOS requires very fine mesh spacing in an energetic material to run successfully and output valid results. Computational resource limitations drive the need for non-uniform mesh spacing in the computational domain beyond the energetic material. HVRB and Mie-Gruneisen EOS are much less sensitive to mesh density and therefore a uniform mesh was appropriate in these types of simulations.

Table 7: HMX Arrhenius Parameters

Reaction Type	**Activation Energy [kcal/mol]**	**Frequency Factor [s^{-1}]**	**Threshold Reaction Temperature [K]**
Deflagration	46.2 (Mitani & Williams, 1986)	$5.0*10^{15}$ (Mitani & Williams, 1986)	531.15 (Cooper, 1996)
Detonation	52.7 (Yang, 2008)	$5.0*10^{19}$ (Yang, 2008)	531.15 (Cooper, 1996)

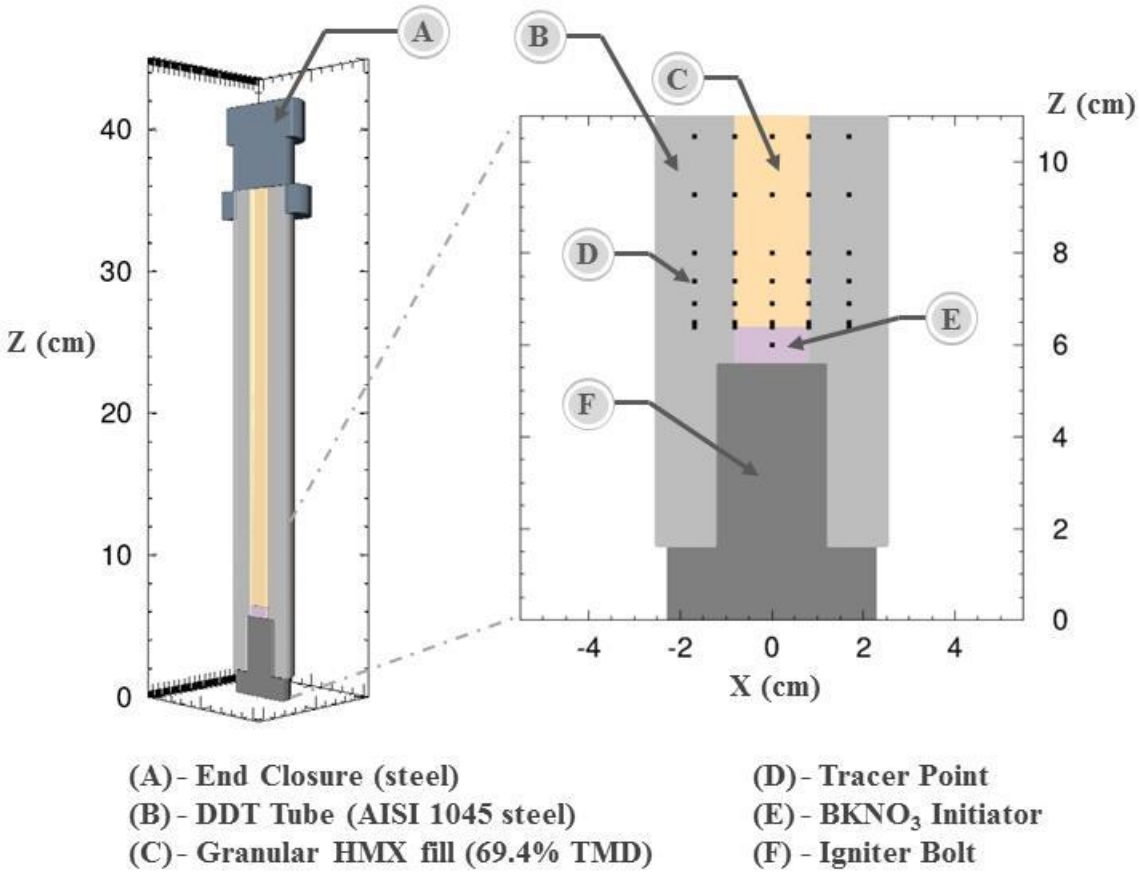

Figure 21: CTH Material Cross Section for NSWC Model

Table 8: NSWC CTH Model Parameter References

Mat'l #	Compo-nent	Material Type	EOS Model & Ref.	Strength Models & Ref.	Fracture Criteria & Ref.
1	DDT Tube	AISI 1045 Steel	SESAME: (Sandia, 2006)	Johnson Cook: (Jaspers & Dautzenberg, 2001), (Matweb, 2014)	(Matweb, 2014)
2	Ignitor Bolt	4340 Steel	SESAME: (Sandia, 2006)	Johnson Cook: (Sandia, 1995), (Silling, 1996)	(Sandia, 1995)
3	BKNO3 Ignitor	BKNO3	Programmed Burn: (Lawrence Livermore, 2012), (Crawford, et al., 2012), (Hertel E. S., 1998)	Von Mises: (Crawford, et al., 2012)	(Crawford, et al., 2012)
4	Bottom Lug	4340 Steel	SESAME: (Sandia, 2006)	Johnson Cook: (Sandia, 1995), (Silling, 1996)	(Sandia, 1995)
5	Bottom Closure	4340 Steel	SESAME: (Sandia, 2006)	Johnson Cook: (Sandia, 1995), (Silling, 1996)	(Sandia, 1995)
6	HMX	HMX	MGR: (Baer, Kipp, & van Swol, 1998) , (Marsh, 1980), (Hall & Holden, 1988), (Menikoff R. , 2001), (Crawford, et al., 2012) HVRB: (Sandia, CTH 10.2: Equation of State Data File, 2006), (Crawford, et al., 2012) ARB: (Mitani & Williams, 1986), (Yang, 2008), (Dobratz & Crawford, 1985), (Crawford, et al., 2012)	Von Mises: (Baer, Kipp, & van Swol, 1998)	(Crawford, et al., 2012), (Baer, Kipp, & van Swol, 1998)
7	Air	Air	SESAME: (Sandia, 2006)	Von Mises: (Crawford, et al., 2012)	(Crawford, et al., 2012)

Figure 22 shows a 3-D isometric cross section of the LANL materials plot as well as a 2-D close-up cross-section near the initiating end of the experimental set-up. Table 9 contains detailed information on the material number, component name, component material, EOS, strength model and fracture criteria references for the LANL geometry. In Figure 22, markers E and A denote Material 2 and 3, the piston initiation mechanism and end plug, modeled as 4340 steel. As with the NSWC experiment, the alloy type of the steel plug was not indicated and the piston material was undefined. Thus, these two components are also modeled as 4340 steel for consistency with the NSWC CTH model. Both materials are defined with a SESAME EOS CTH library set of parameters for 4340 steel, a CTH library set of Johnson Cook strength model parameters and a CTH library fracture pressure.

B shows Material 1, the DDT tube modeled with Vascomax 250 steel as defined in the LANL experimental set-up description. In CTH, the EOS is defined by an existing CTH library EOS for a SESAME Vascomax 250 table, in conjunction with a CTH library Steinberg-Guinan-Lund Vascomax 250 strength model and fracture pressure from material properties listed in (Matweb, 2014). Air, Material 5, is modeled with a CTH library SESAME EOS table, an elastic-perfectly-plastic Von Mises strength model and a very low fracture pressure. Table 9 lists HMX, denoted as marker C and Material 4, with multiple EOS. The aforementioned EOS explanation in the NSWC model description is also valid for HMX EOS parameters in the LANL CTH model. Marker D in the subsequent figure again points to tracers within the model. As in the NSWC model, both Lagrangian and Eulerian tracers are utilized in the various LANL geometry based CTH analyses.

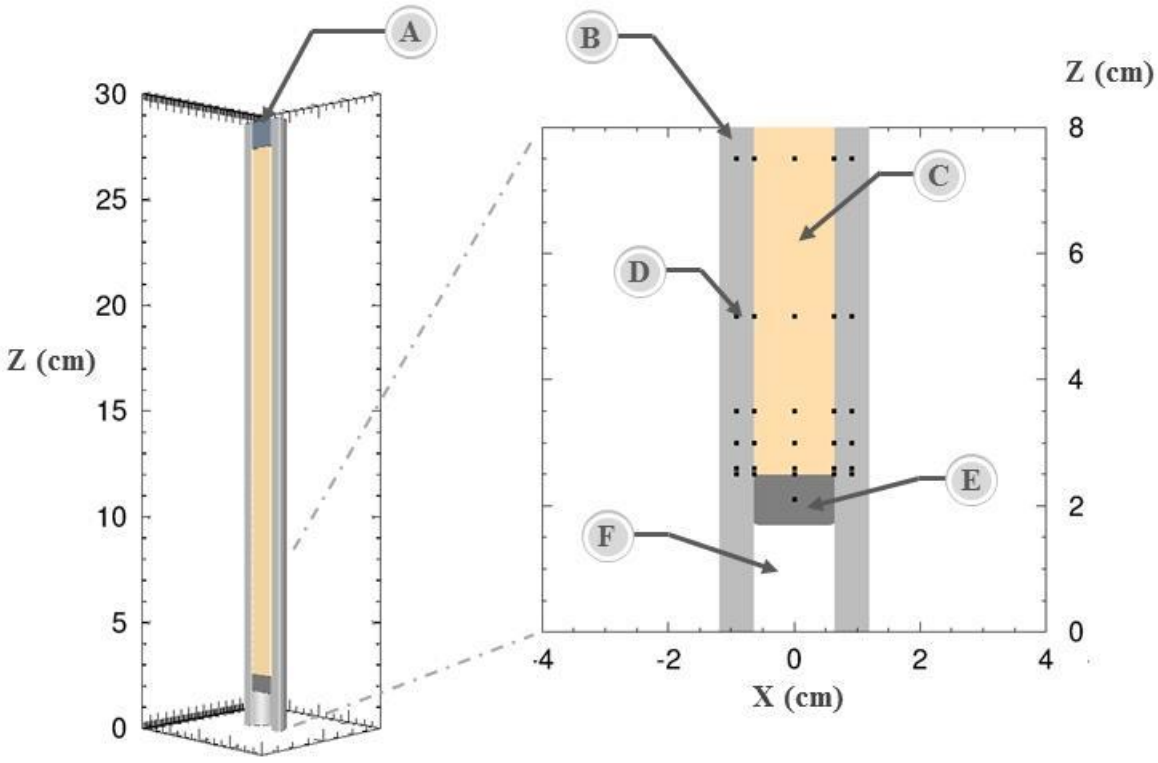

(A) - Plug (steel)
(B) - DDT Tube (Vascomax 250 steel)
(C) - Granular HMX fill (65% TMD)
(D) - Tracer Point
(E) - Piston
(F) - Ignitor Burn Chamber

Figure 22: CTH Material Cross Section for LANL Model

Table 9: LANL CTH Model Parameter References

Mat'l #	Compo-nent	Material Type	EOS Model & Ref.	Strength Models & Ref.	Fracture Criteria & Ref.
1	DDT Tube	Vasco-max 250 Steel	SESAME: (Sandia, 2006)	Johnson Cook: (Taylor, 1992), (Sandia, 1995)	(Matweb, 2014)
2	Piston	4340 Steel	SESAME: (Sandia, 2006)	Johnson Cook: (Sandia, 1995), (Silling, 1996)	(Sandia, 1995)
3	End Plug	4340 Steel	SESAME: (Sandia, 2006)	Johnson Cook: (Sandia, 1995), (Silling, 1996)	(Sandia, 1995)
4	HMX	HMX	MGR: (Baer, Kipp, & van Swol, 1998), (Marsh, 1980), (Hall & Holden, 1988), (Menikoff R. , 2001), (Crawford, et al., 2012) HVRB: (Sandia, CTH 10.2: Equation of State Data File, 2006), (Crawford, et al., 2012) ARB: (Mitani & Williams, 1986), (Yang, 2008), (Dobratz & Crawford, 1985), (Crawford, et al., 2012)	Von Mises: (Baer, Kipp, & van Swol, 1998)	(Crawford, et al., 2012), (Baer, Kipp, & van Swol, 1998)
5	Air	Air	SESAME: (Sandia, 2006)	Von Mises: (Crawford, et al., 2012)	(Crawford, et al., 2012)

Inert HMX: Initiation Mechanism Characterization

The discussion of results defining the DDT research gap in CTH begins with a simulation of the test case initiation mechanisms where the HMX DDT tube fill is defined as inert. By rendering the primary DDT charge inert, important characteristics about the initiation train and subsequent energy deposition into the explosive can be gleaned. Two variations of initiation mechanisms are represented by the NSWC and LANL test cases, and are the primary reason these frequently referenced experimental sources were down-selected for validation of the present modeling improvements effort.

The LANL experiment is initiated via impact of a piston traveling at a steady state speed of 100 m/s when contacting the granular HMX charge. Note: a 100 m/s velocity initial condition was imposed on the piston such that CTH modeling of the earlier explosive events to move the piston were not necessary. Once the piston impacts the granular HMX, a low amplitude impact wave is imparted on the energetic material and a substantial delay (approximately 40 μs from Figure 14) is observed.

NSWC, on the other hand, utilized a $BKNO_3$ charge to begin their DDT test events. $BKNO_3$ is a common pyrogen, meaning it deflagrates and does not detonate, ignitor formulation used for its gas generation properties. Deflagration of $BKNO_3$ adjacent to the granular HMX results in high amplitude wave transfer which causes HMX deflagration and subsequent DDT to occur much more rapidly, as observed in Figure 8 and Figure 10. Note that LANL and NSWC define time zero in two different manners. LANL sets time equal to zero at the first signal from the capacitance discharge

unit, whereas NSWC defines time zero when the first ionization pin triggers at approximately 1.6 cm measured from the HMX initiating end.

Of the pertinent physics modeled in this inert simulation section, two noteworthy accomplishments are represented. First, the author formulated a user defined programmed burn model for $BKNO_3$. Second, the author was able to successfully formulate an inert Mie-Gruneisen (also used as the unreacted material model in the composite HVRB and ARB reactive models) user defined EOS for granular HMX from multiple references with a working p-α porosity model. The successful implementation of porosity is evidenced in subsequent density plots showing compaction wave propagation through granular HMX and further bolstered by comparison with 100% TMD HMX simulations. Details on the granular HMX Mie-Gruneisen EOS and p-α porosity model are included in the subsequent chapter.

Figure 23 below contains a time sequence of pressure contours from 0.5 to 2 μs in 0.5 μs increments. This figure is included to confirm the successful pyrogenic behavior modeling of $BKNO_3$, as evidenced by the fact that the $BKNO_3$ pellet has a wave front pressure less than the CJ pressure of $BKNO_3$. Also noteworthy in this figure is the wave front shape change at the interface of the DDT tube and granular HMX. Steel has a higher sound speed than HMX and therefore the pressure wave generated by BKNO3 propagates and expands more quickly though the steel DDT tube than the energetic material. Note that pressure in the subsequent CTH contour plots is given in Bars, where 1 GPa is equivalent to 10 kBar for reference.

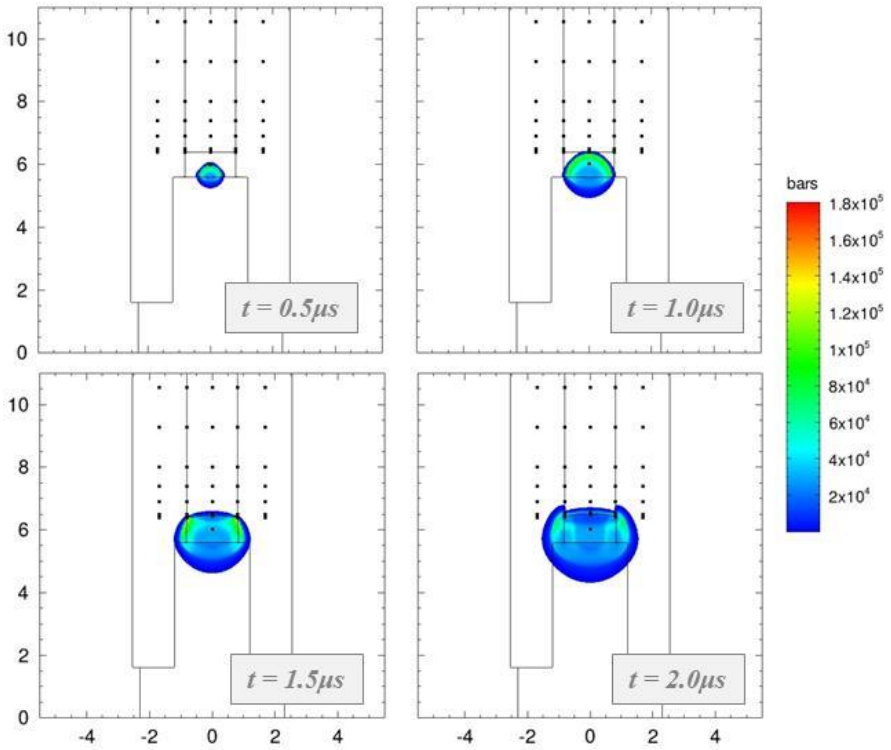

Figure 23: NSWC BKNO3 Pressure Contours

Figure 24 further demonstrates the relationship between wave front shape, wave speed propagation, and material density. This figure contains a side-by-side comparison of NSWC simulations with 100% TMD and 65% TMD (porous) HMX. Again, note that the pressure wave imparted into the HMX travels faster through the higher density 100% TMD HMX than the 65% TMD HMX because the higher density material has a higher sound speed.

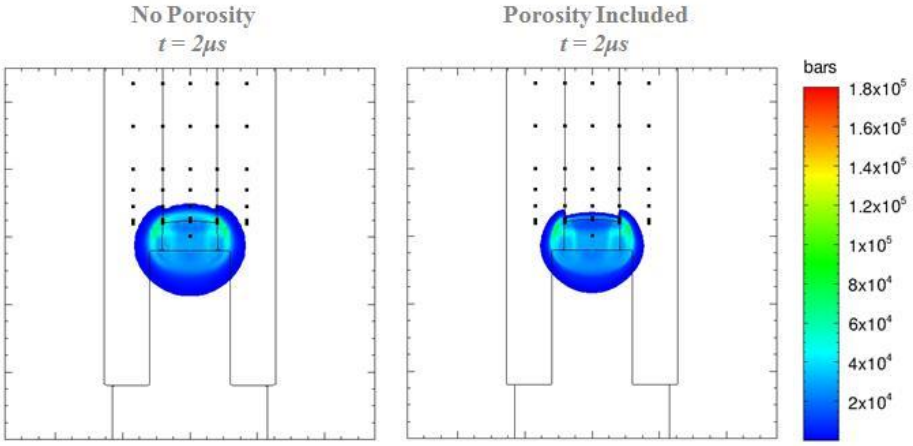

Figure 24: NSWC BKNO3 Pressure Contour Comparison between Porosity

Lagrangian tracer data at an initial position of one centimeter within the HMX are plotted in Figure 25. The tabulated data on this plot show a difference of approximately 8% between the baseline and refined mesh density and 14.5% difference between refined and non-uniform mesh results. Additionally, a 300% increase in pressure is observed when comparing the porous versus 100% TMD maximum pressure values demonstrating the effect of the porosity model. Unfortunately the run distance data on the Pop-plot for 65% TMD HMX in Figure 20, is outside the bounds of the data plotted below such that a comparison would not be valid.

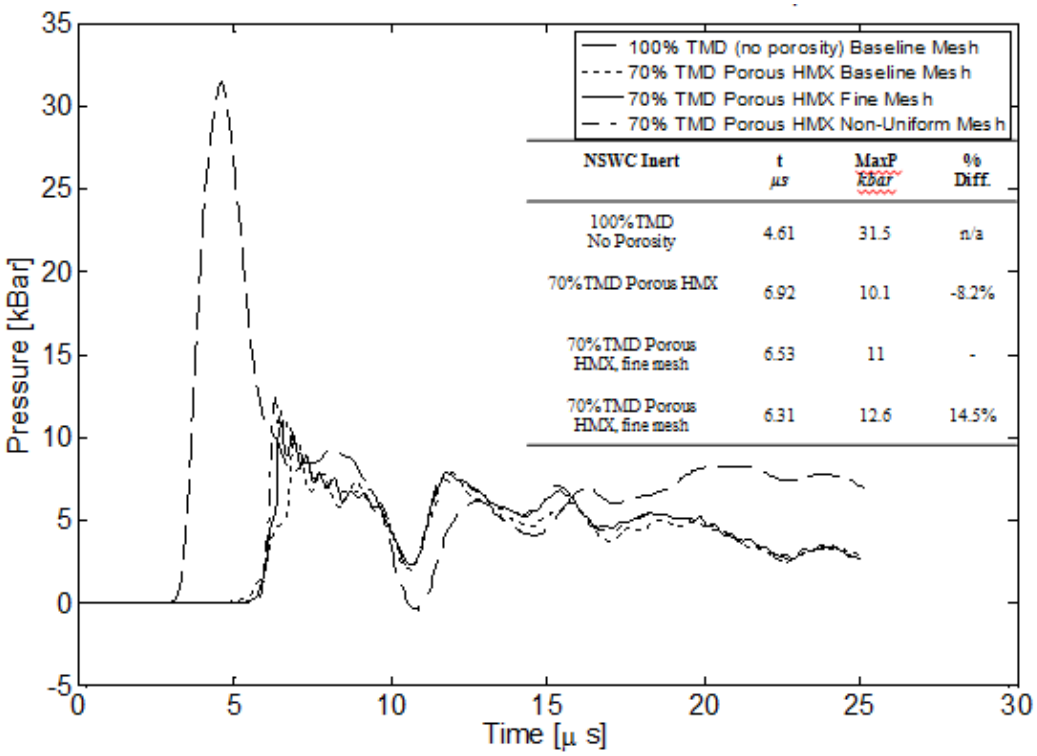

NSWC Inert	t μs	MaxP kbar	% Diff.
100% TMD No Porosity	4.61	31.5	n/a
70% TMD Porous HMX	6.92	10.1	-8.2%
70% TMD Porous HMX, fine mesh	6.53	11	-
70% TMD Porous HMX, fine mesh	6.31	12.6	14.5%

Figure 25: NSWC Inert Pressure Comparison at 1 cm in HMX

Figure 26 shows time sequences of density contour plots for inert HMX simulations with porosity (65% TMD), refined mesh and porosity, as well as 100% TMD HMX. Once again, the successful implementation of porosity is evidenced in subsequent density plots showing compaction wave propagation through granular HMX and further supported by comparison with 100% TMD HMX simulations. In the figure below, it can be observed that the density of the fully compacted material goes slightly beyond 100% TMD of HMX (1.9 g/cm^3) due to the addition of heavier $BKNO_3$ contaminant constituents in the compacting material composition. Moreover, as the compaction wave propagates upward the wave front becomes increasingly contoured.

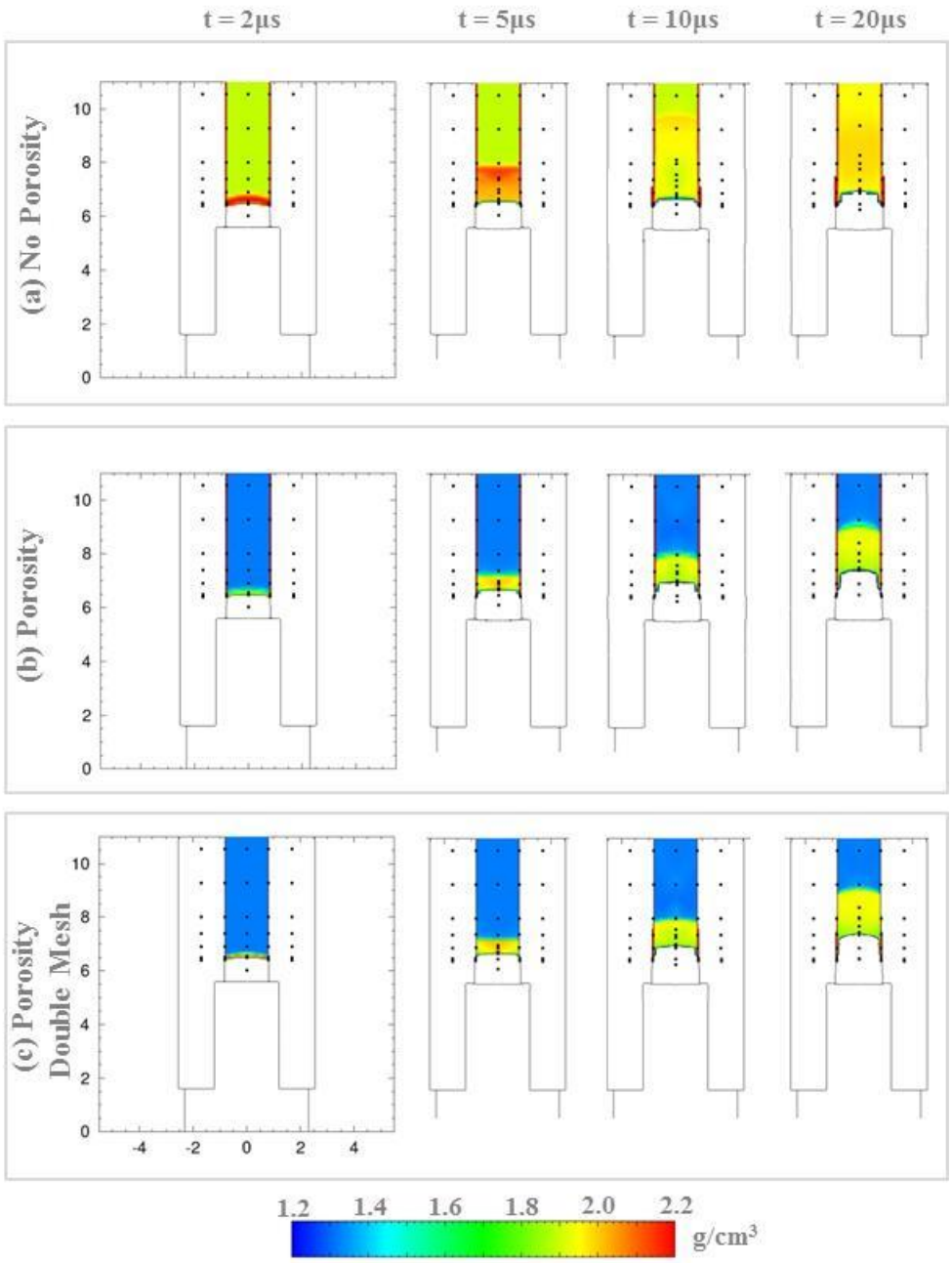

Figure 26: NSWC Inert Compaction Wave Comparisons Contours of Density.

LANL DDT experiments are initiated by piston impact and as such pressure contours of the moment of contact are not included as the low amplitude wave pressures are far below those of the pyrogenic $BKNO_3$ initiation event. Figure 27 contains a plot of Lagrangian tracer data at an initial position of one centimeter within the HMX. The

tabulated data on this plot show a difference of approximately 10.5% between the baseline and refined mesh density and a difference of nearly 29% between the refined and non-uniform meshes. High error percentages are postulated to exist for two reasons. Firstly, CTH is an Eulerian hydrocode that computes shared volume fractions as materials move through fixed mesh cells. If there are an insufficient number of computational cells across the thickness in which compaction occurs, the shared volume fractions can be incorrectly calculated in addition to mass movement and material characteristics. Secondly, these results are for the inert simulation results at low pressures compared to CTH's standard operating regime of detonation level pressures and thus higher error is to be expected. Detonation pressures are on the order of hundreds of kBars, roughly 10,000 times higher than the inert low amplitude impact pressures plotted below. Further mesh refinement is likely required to resolve wave propagation in such a low pressure regime. A roughly 250% increase in pressure is observed when comparing the porous versus 100% TMD maximum pressure values demonstrating the effect of the porosity model.

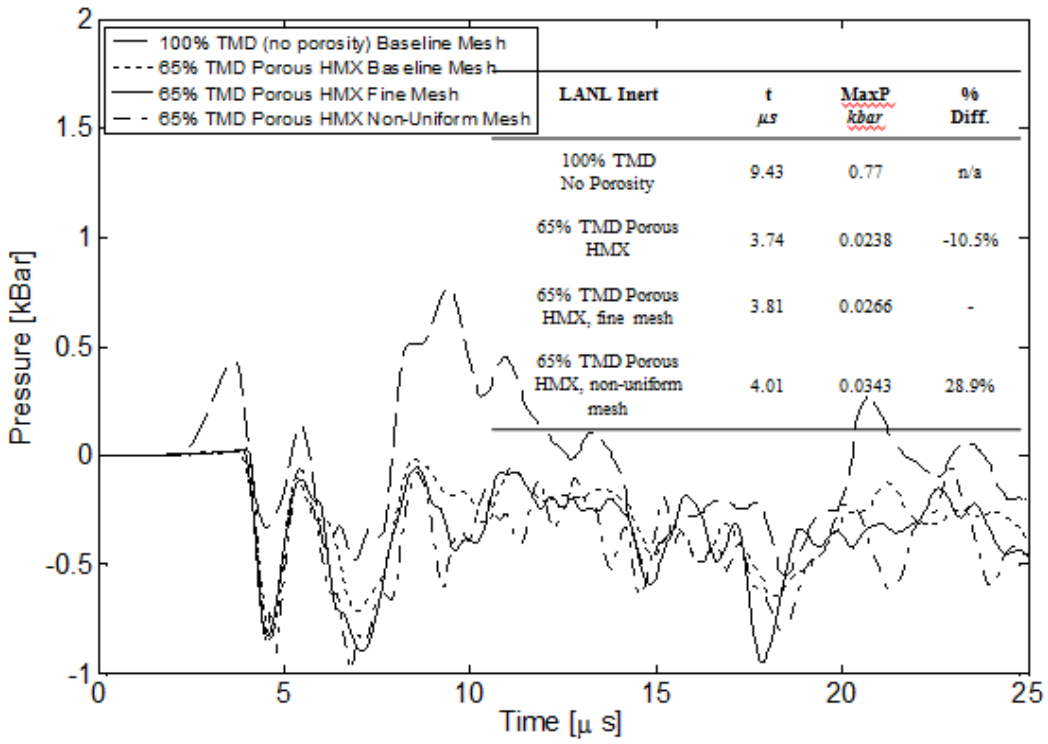

Figure 27: LANL Inert Pressure Comparison at 1 cm in HMX

Contours of density for the three inert LANL simulations are given in Figure 28. Due to the nature of the low amplitude wave initiation mechanism employed by LANL in their DDT testing, very little compaction wave motion is observed solely from the piston impact event, as described in (McAfee, Asay, & Bdzil, 1993). The results in Figure 28 are at odds with the *McAfee's* assertion that "the boundary between the low-pressure convective region and the compact is equivalent to a combustion-driven mechanical piston." (McAfee, Asay, & Bdzil, 1993) Though the results presented in Figure 26 and Figure 28 are for inert results (and do not contain convective burning regions) it is evident that compaction due to the piston versus pyrogenic initiation mechanisms are very different. *McAfee's* conclusion that pressure build-up

occurs in the first 10 mm of the HMX column for the piston initiation mechanism were accurate.

Mesh size dependence is evident in Figure 28, specifically parts (a) and (b). In this figure only HMX density contours are colored, and in subplots (a) and (b) thick red lines are located at the piston-HMX boundary indicating density well above the theoretical maximum for HMX and very little material motion is observed. This is an example of the previously noted issue with shared volume fraction computation on coarse meshes in Eulerian hydrocodes. The piston material, modeled as 4340 steel with a density of approximately 7.9 grams/cm^3 (Matweb, 2014), is incorrectly impinging on the volume occupied by HMX. Thus, an artificially high density is output for HMX on the coarse meshes. Subplot (c) of Figure 28 shows that the thick red density contour at the piston-HMX interface is reduced on the refined mesh and compaction is more readily observed in the refined mesh results, specifically at two microseconds. One further note of importance is that compaction wave speeds referenced in the LANL test data include the contribution of deflagration reactions and are therefore not referred to in this inert results section.

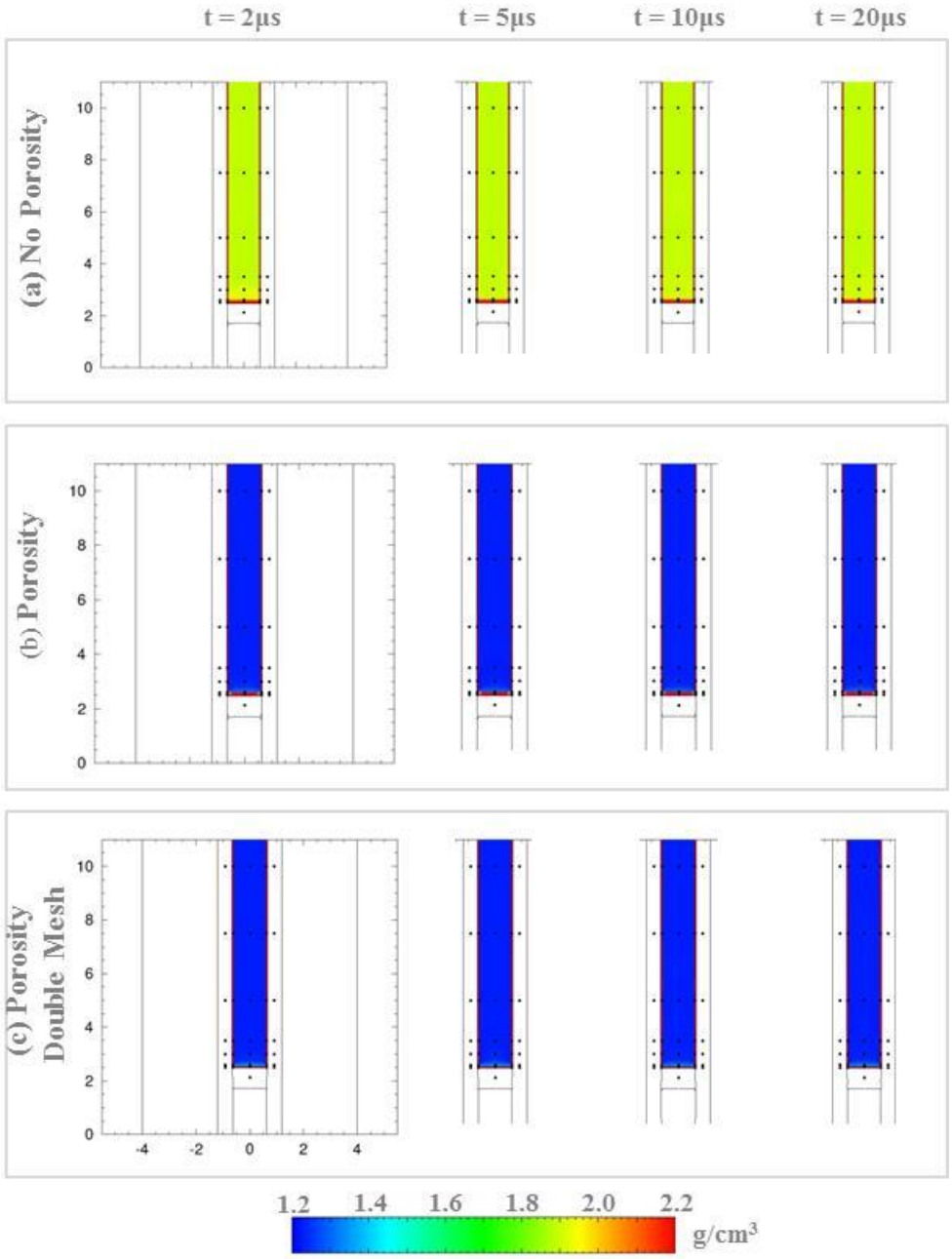

Figure 28: LANL Inert Compaction Wave Comparisons - Contours of Density.

HMX Forced Detonation with HVRB

Simulations in which HMX was forced to detonate by increasing the amount of energy imparted during the test case specific initiation train events were included in this research study in order to demonstrate that CTH is capable of adequately modeling the detonation regime. Success criteria for replication of the pertinent physics are defined as exceeding the CJ pressure in the steady state post-detonation wave region and approximately matching the expected detonation velocity. In the four different forced detonation simulations in this sub-section (with HMX at 100% TMD, and granular HMX run on the baseline mesh, refined mesh, and non-uniform mesh) the NSWC initiation mechanism was altered by exchanging the $BKNO_3$ initiator pellet with a common booster pellet energetic formulation comprised mostly of HMX and detonated via programmed burn settings. Additionally, the LANL experimental configuration was modified by changing the 100 m/s piston into a 5 km/s thin flyer.

In Figure 29, a time sequence of forced detonation pressure contours run on the refined mesh are shown. Note that the maximum pressure scale value is set to the CJ pressure for 69.4% TMD HMX calculated in the Analytical Verification section (16.6 GPa = 160 kBar = $1.6*10^5$ Bar). The earliest snapshot of pressure contours shows the replacement booster pellet material detonating. As time progresses, the high amplitude wave from the booster pellet detonation is transferred to the adjacent HMX and a detonation wave front forms. The detonation wave continues to propagate upward through unreacted HMX and outward into the DDT tube side walls resulting in shock reflection and tube expansion until all HMX is reacted and forms detonation products. DDT test scenarios in the literature observe onset of detonation near the location where

a thick walled DDT tube begins radial expansion. This deformation is observed very near the site of booster pellet initiation and is therefore consistent with experimental observations noted in the literature.

NSWC instrumented their experimental apparatus set-up with ionization pins along the cylinder length at the HMX-interior DDT tube diameter interface. These ionization pins are replicated throughout this dissertation by Lagrangian tracers positioned at the HMX-1045 steel tube wall interface at coordinates specified by NSWC. Lagrangian tracers were selected to move with the tube side wall radial expansion. Figure 30 contains pressure versus time histories of tracers at the NSWC ionization pin locations. Similar plots for all other research gap characterization scenarios (both NSWC and LANL configurations) are included for reference in Appendix C. Pressure traces in Figure 30 indicate the arrival time of the detonation wave by a sharp peak. The tracer closest to the base of the DDT tube at the $BKNO_3$ initiator end is represented by the left most pressure vs time trace. Tracer locations further up the tube progress from left to right. Data in this plot was reduced from a large CTH output file and post-processed in a Matlab script written by the author. The maximum pressures observed at the detonation wave front in Figure 30 are in excess of 150 kBar.

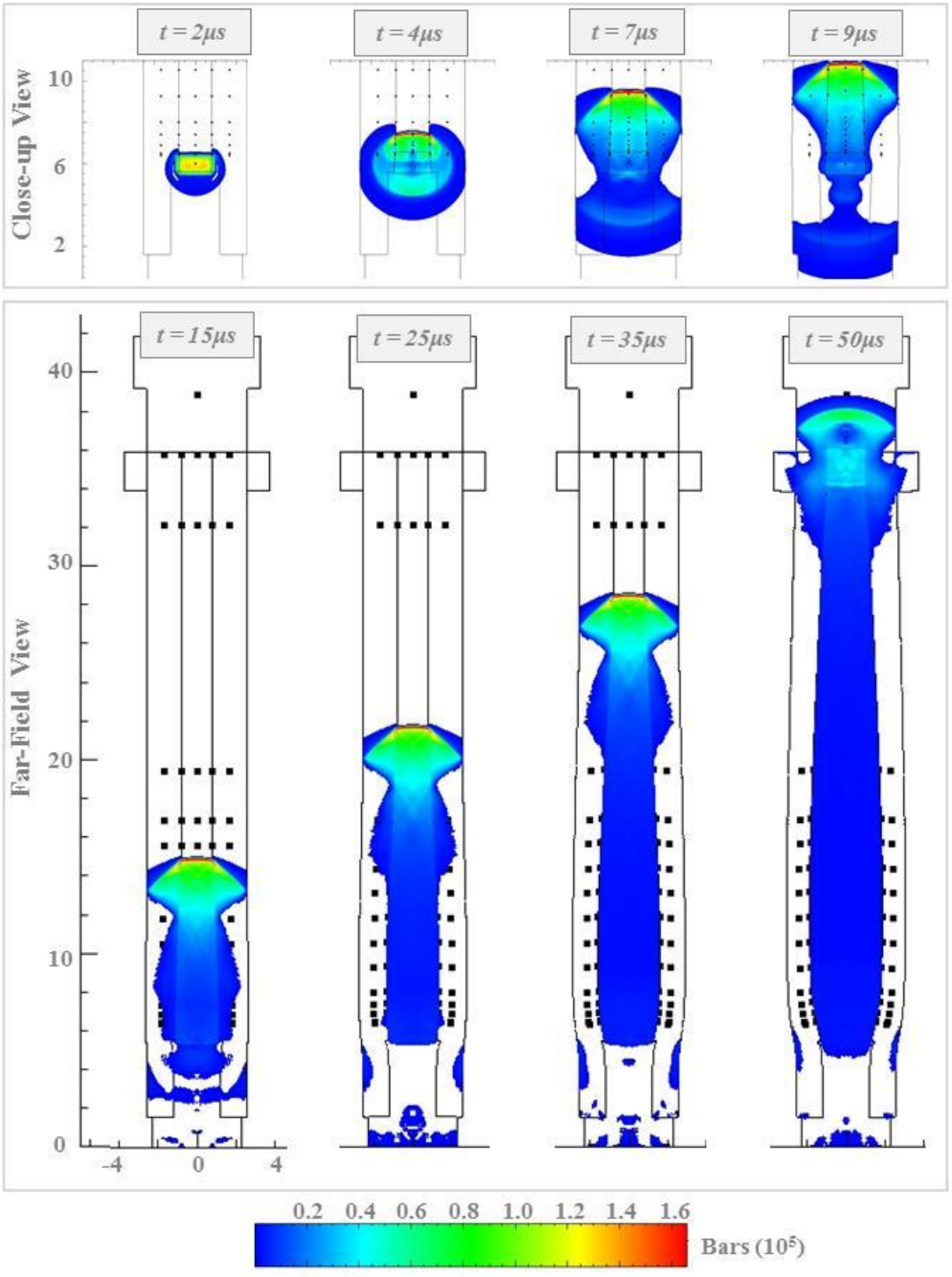

Figure 29: NSWC HMX Forced Detonation with HVRB; Fine Mesh with Porosity.

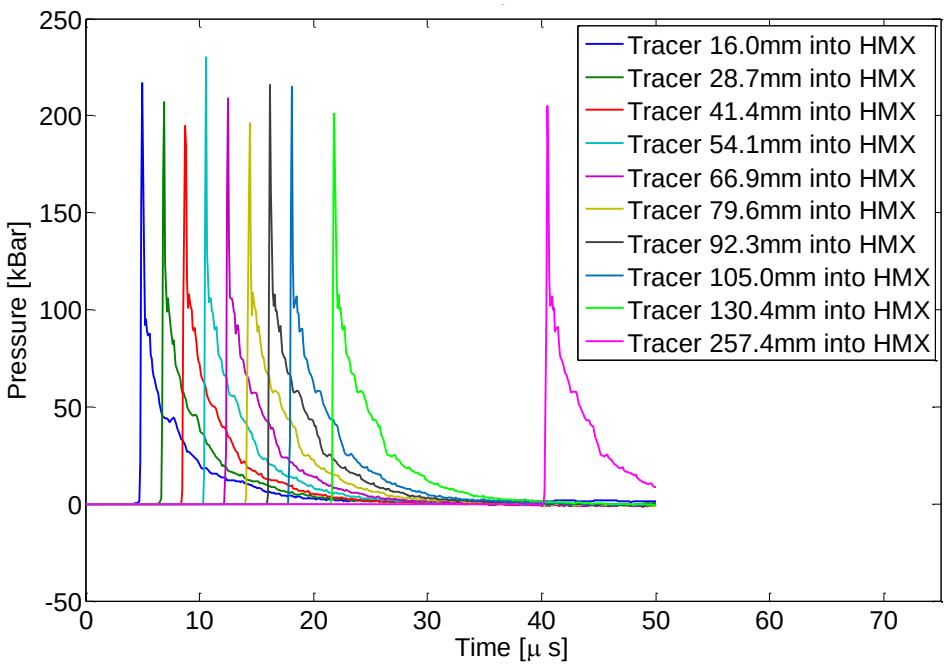

Figure 30: NSWC HVRB Forced Detonation 69.4% TMD HMX Pressure Tracer Data at Experimental Ionization Pin Locations.

Figure 31 contains pressure versus time tracer data at Eulerian tracers positioned near the cylinder length center in the center of the HMX core fill. As compared to the data plotted in Figure 30 the central HMX pressure tracer locations yield a higher pressure, which is expected as the sidewall interference while the detonation wave passes from HMX to steel will dampen the observed pressure trace peak. Pressure values in the figure below are greater than the CJ pressure of 69.4% TMD and 100% TMD HMX. Exceeding the CJ pressure when employing the HVRB EOS for energetic materials is expected as the HVRB model captures the von Neumann spike in the reaction front. The von Neumann spike occurs at the shock front and is followed by a finite reaction zone in which the minimum pressure gradient value is that of the CJ pressure at the location when all reactants have been converted to products.

(Lee & Tarver, 1980) This phenomenon is evident in Figure 31 when comparing porous HMX peak widths for the baseline, fine, and non-uniform meshes. As the minimum cell width decreases (increasing total mesh cell count) the width of the peaks capped by the Von Neumann spike narrows in direct relation to the mesh spacing, which is indicative of the reaction zone thickness calculated by CTH. Because of this important reaction zone capturing observation and the tabulated percent pressure differences of ±10% from fine mesh results, all simulations in the following chapter entitled MODEL IMPROVEMENTS IN CTH will be run on the fine or non-uniform mesh. Subsequent oscillations downstream of the pressure spike indicate shock wave reflections.

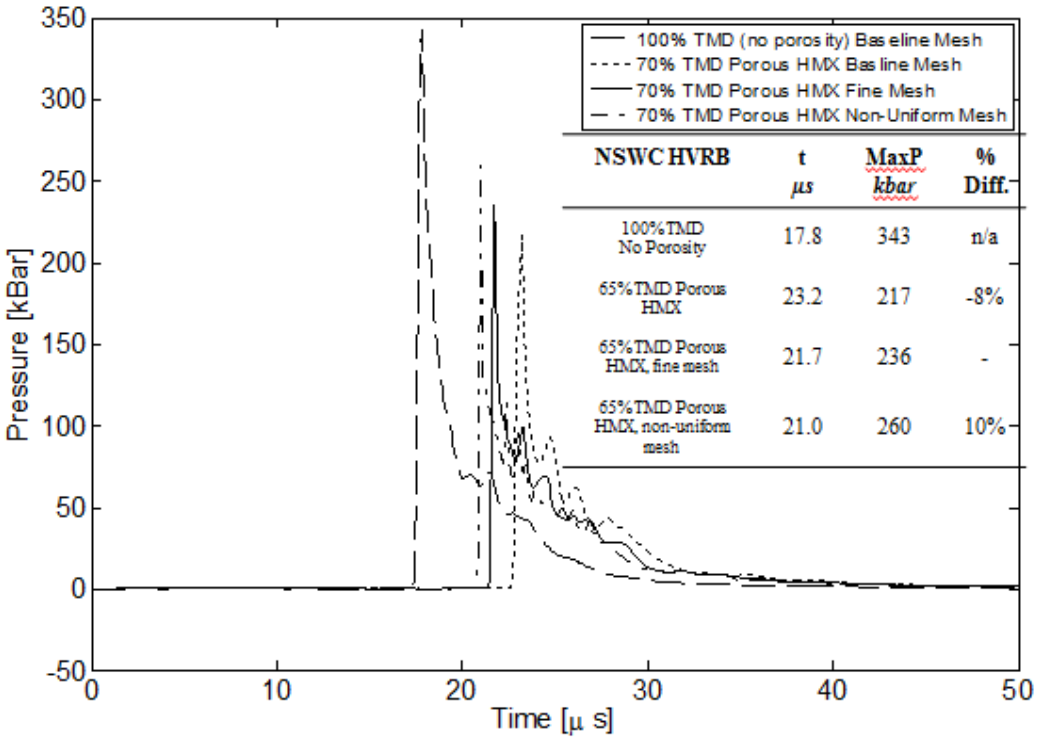

NSWC HVRB	t μs	MaxP kbar	% Diff.
100% TMD No Porosity	17.8	343	n/a
65% TMD Porous HMX	23.2	217	-8%
65% TMD Porous HMX, fine mesh	21.7	236	-
65% TMD Porous HMX, non-uniform mesh	21.0	260	10%

Figure 31: NSWC HVRB Forced Detonation HMX near Center Pressure Comparison

In Figure 32, a time sequence of forced detonation pressure contours run on the refined mesh are shown for the LANL case. Note that the maximum pressure scale

value is set to the CJ pressure for 65% TMD HMX calculated in the Analytical Verification section (13.9 GPa = 139 kBar = $1.39*10^5$ Bar). The earliest snapshot of pressure contours shows the replacement high speed flyer impacting the HMX and causing detonation via shock transfer. The detonation wave continues to propagate upward through unreacted HMX and outward into the DDT tube side walls resulting in shock reflection and tube expansion until all HMX is reacted and forms detonation products. Side wall tube expansion is observed very near the high velocity flyer impact site. Pressure traces for sidewall data points are included in the Appendix entitled EXISTING EOS: TRACER PRESSURE OUTPUT. The detonation wave shape in this simulation can be approximated as quasi-1D. For this reason, piston impact experiments are at times touted in the literature as better for computational comparison than experiments with energetic shock initiation which introduce non-planar three-dimensional effects and contaminant products.

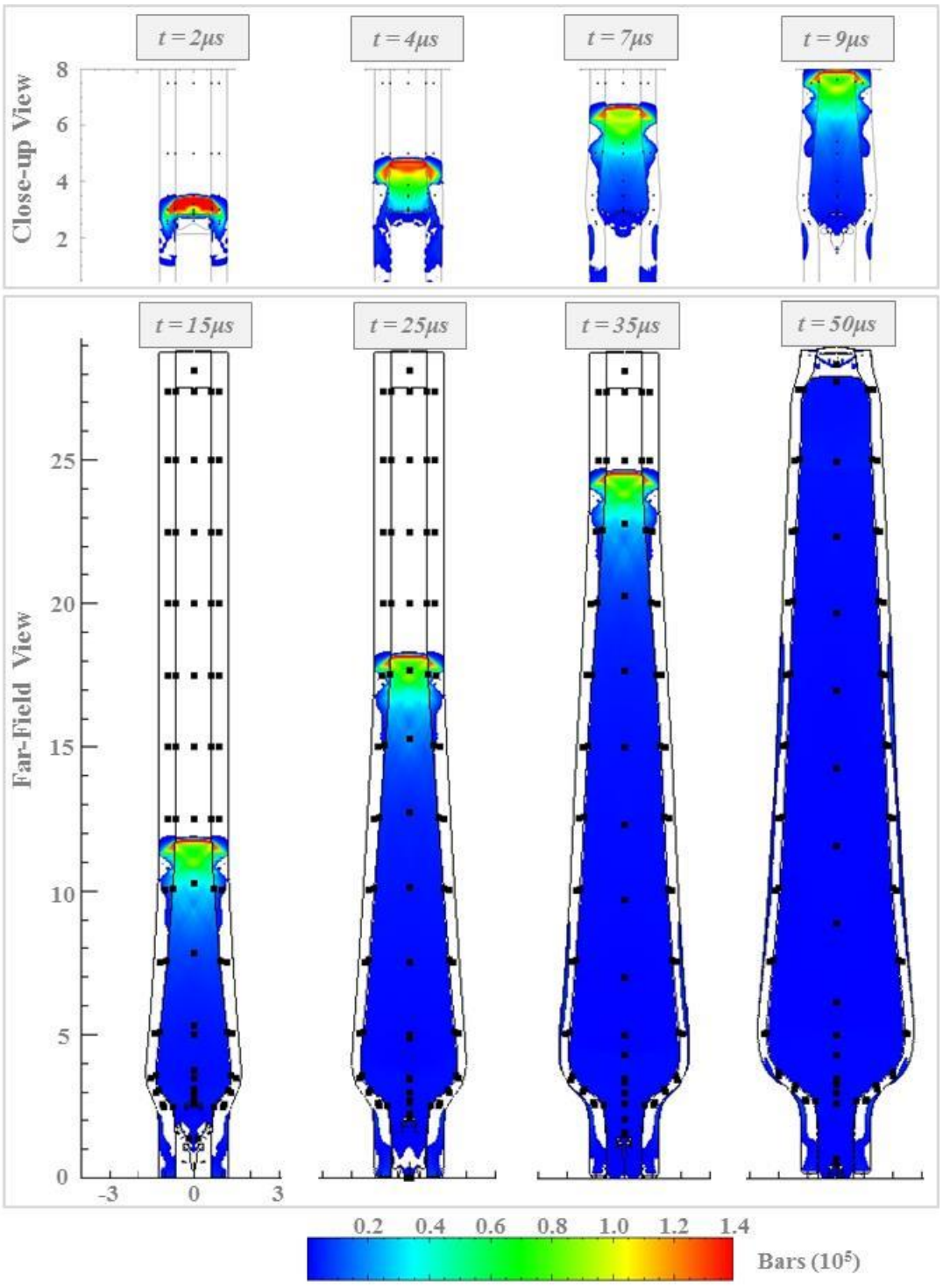

Figure 32: LANL HMX Forced Detonation with HVRB; Fine Mesh with Porosity.

Figure 33 also contains pressure versus time tracer data at Eulerian tracers positioned near the cylinder length center in the center of the HMX core fill. Maximum pressure values in the figure below are greater than the CJ pressure of 65% TMD and 100% TMD HMX. As noted above, exceeding the CJ pressure is expected with the HVRB model and subsequent oscillations downstream of the pressure spike indicate shock wave reflections. Previously discussed influences of mesh spacing on pressure spike peak width can also be observed in the plot below. Mesh independence comparisons of maximum pressure are also approximately within ±10%, and are therefore consistent with NSWC forced detonation simulation results.

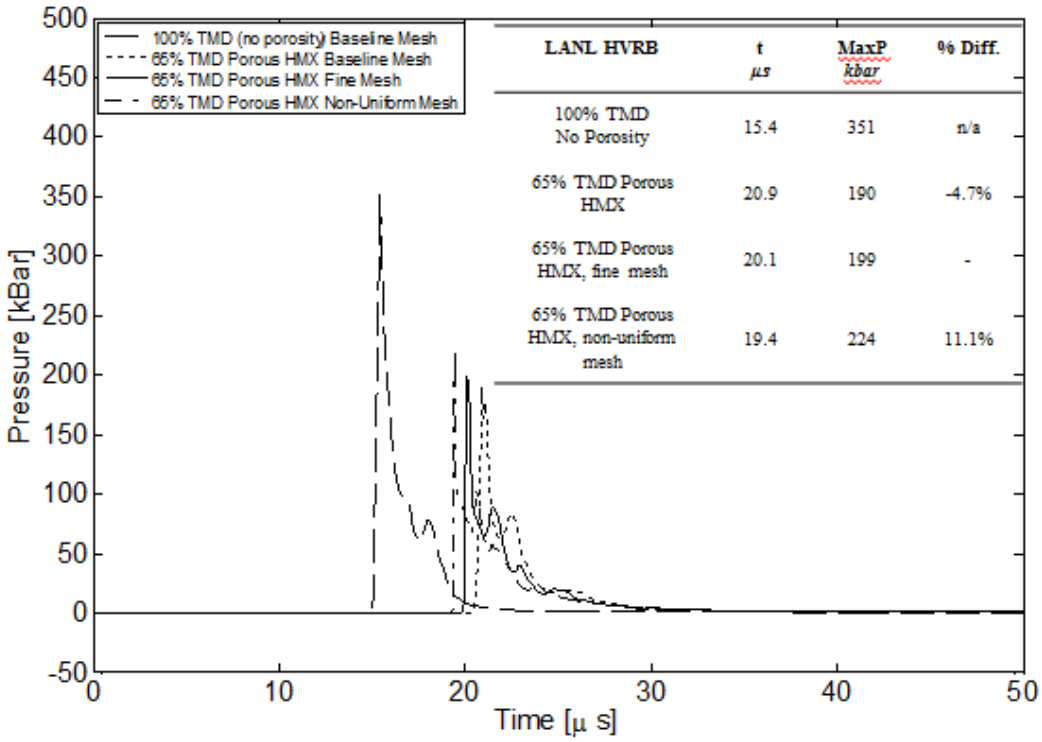

LANL HVRB	t μs	MaxP kbar	% Diff.
100% TMD No Porosity	15.4	351	n/a
65% TMD Porous HMX	20.9	190	-4.7%
65% TMD Porous HMX, fine mesh	20.1	199	-
65% TMD Porous HMX, non-uniform mesh	19.4	224	11.1%

Figure 33: LANL HVRB Forced Detonation HMX near Center Pressure Comparison

Representative Test Cases with Various EOS

Results in this sub-section were obtained for representative test cases where the NSWC configuration is initiated with a $BKNO_3$ pyrogenic pellet and the LANL test cases are once again initiated with a piston traveling at 100 m/s. Simulations were performed for HMX, with appropriate porosity, modeled with an HVRB equation of state as well as porous HMX with Arrhenius EOS parameters scaled for deflagration and detonation reactions. The HVRB simulations ran on the refined mesh and ARB simulations ran on the non-uniform mesh described in Table 6.

Figure 34 contains time sequence contours of pressure for the representative (unaltered) NSWC experimental configuration with a porous HMX EOS set to HVRB. Likewise, Figure 35 contains similar pressure contour time sequence images for the unaltered LANL test case with an HVRB EOS for granular HMX. In both instances simulations were run to 50 μs, beyond the time deflagration should have begun, and the HVRB EOS is unable to model early deflagration reactions. This inability to model early deflagration reactions is evidenced by pressure from initiation mechanisms dissipating throughout the DDT tube structure with no energetic component reactions. The HVRB model is incapable of modeling deflagration because this pressure dependent EOS is formulated to start detonation reactions when reaction pressure thresholds are exceeded. These pressure thresholds are indicated in the Pop-plot in Figure 20. Because pressures transmitted into the HMX at the piston and $BKNO_3$ interfaces are below this threshold pressure, little to no reaction occurs.

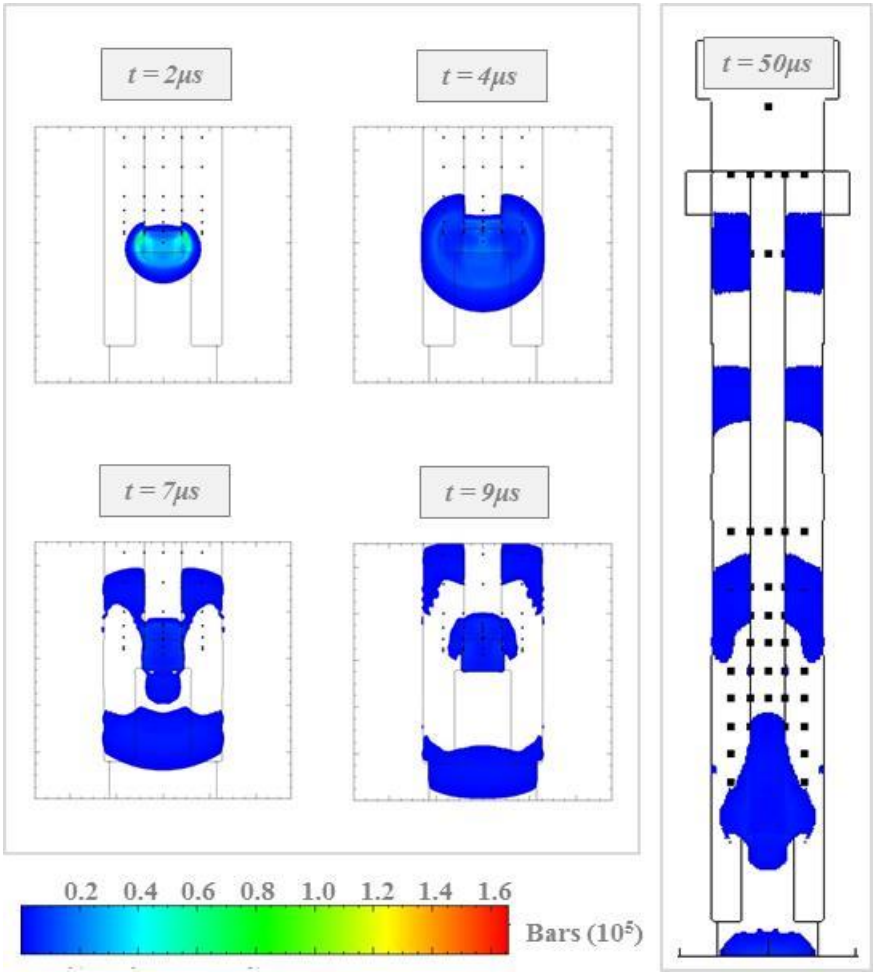

Figure 34: NSWC HVRB Representative Test Case Simulation

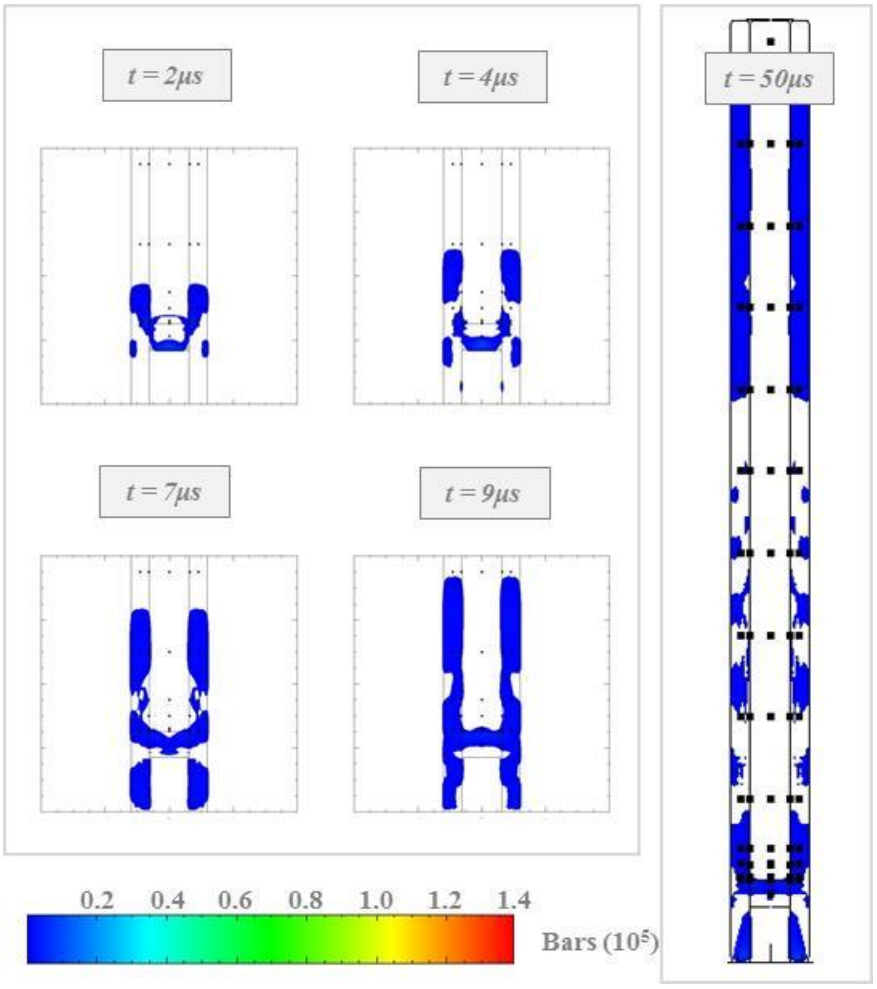

Figure 35: LANL HVRB Representative Test Case Simulation

The next several figures show pressure contour time sequence results of simulations for NSWC and LANL run with the Arrhenius Reactive Burn EOS with parameters tuned for deflagration and then detonation in separate simulations. The ARB model functions through implementation of the Arrhenius rate law, given in Equation 3, into CTH. Arrhenius parameters for deflagration and detonation are included in Table 7 and discussed in the Hydrocode Model Descriptions section of this chapter. In this temperature dependent EOS, if the initiation threshold temperature of a reaction is exceeded the reaction rate is calculated as a function of activation energy, temperature and frequency factor according to the Arrhenius rate law.

Figure 36 contains time sequence pressure contours for the NSWC test case with an ARB deflagration tuned EOS for granular HMX and Figure 37 shows pressure contours for the NSWC set-up with ARB detonation tuned EOS parameters. In these two figures it is evident that reactions of maximum pressures at the reaction wave front occur. The high amplitude wave imparted by $BKNO_3$ deflagration adjacent to the granular HMX yields a temperature above the reaction temperature threshold and the deflagration ARB model produces reaction results with peak pressures exceeding the CJ pressure of 69.4% TMD HMX, which would be expected for detonation but not deflagration. However, the wave shape is flat (despite the 3-D wave imparted by $BKNO_3$) and the reaction layer is non-uniform, rather clustered towards the center of the energetic fill column. On the other hand, in the NSWC results for ARB EOS with detonation parameters the reaction wave pressures do not reach that of the CJ pressure, implying that detonation is not occurring. Yet, the wave speed of the simulation with detonation tuned parameter is higher: 7.6 km/s for detonation parameters and 7.1 km/s

or deflagration parameters. Interestingly, the extent of reaction variable maximum for the detonation parameter simulation reaches one showing that the all HMX has been reacted and converted to products. Thus, the ARB deflagration simulations appear to detonate and the ARB detonation simulations appear to deflagrate when looking at maximum pressure data, but have a higher wave velocity than the deflagration tuned simulations with correspondingly higher pressures. Certainly further study is needed to understand and correct this phenomenon.

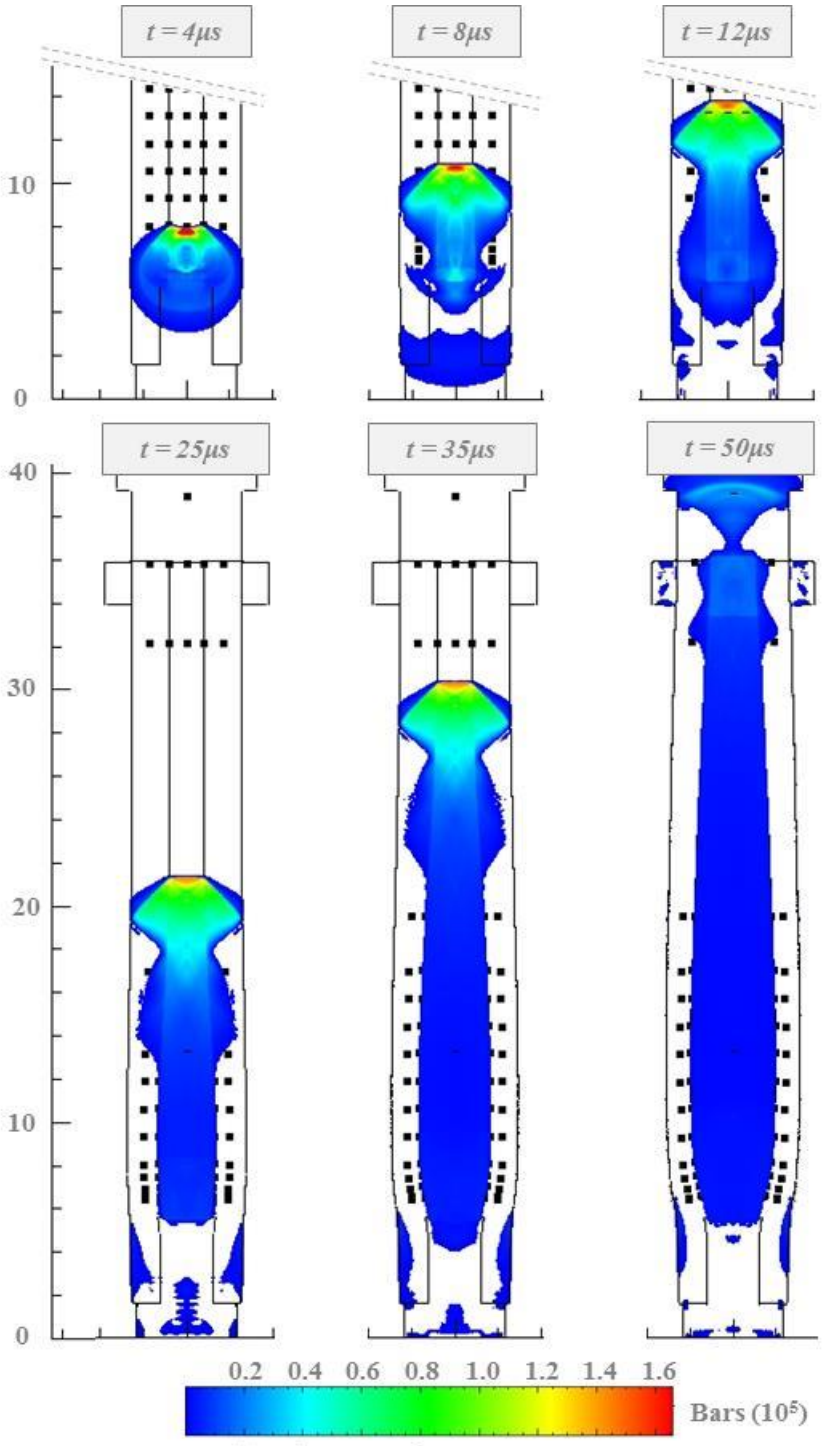

Figure 36: NSWC ARB Deflagration Simulation

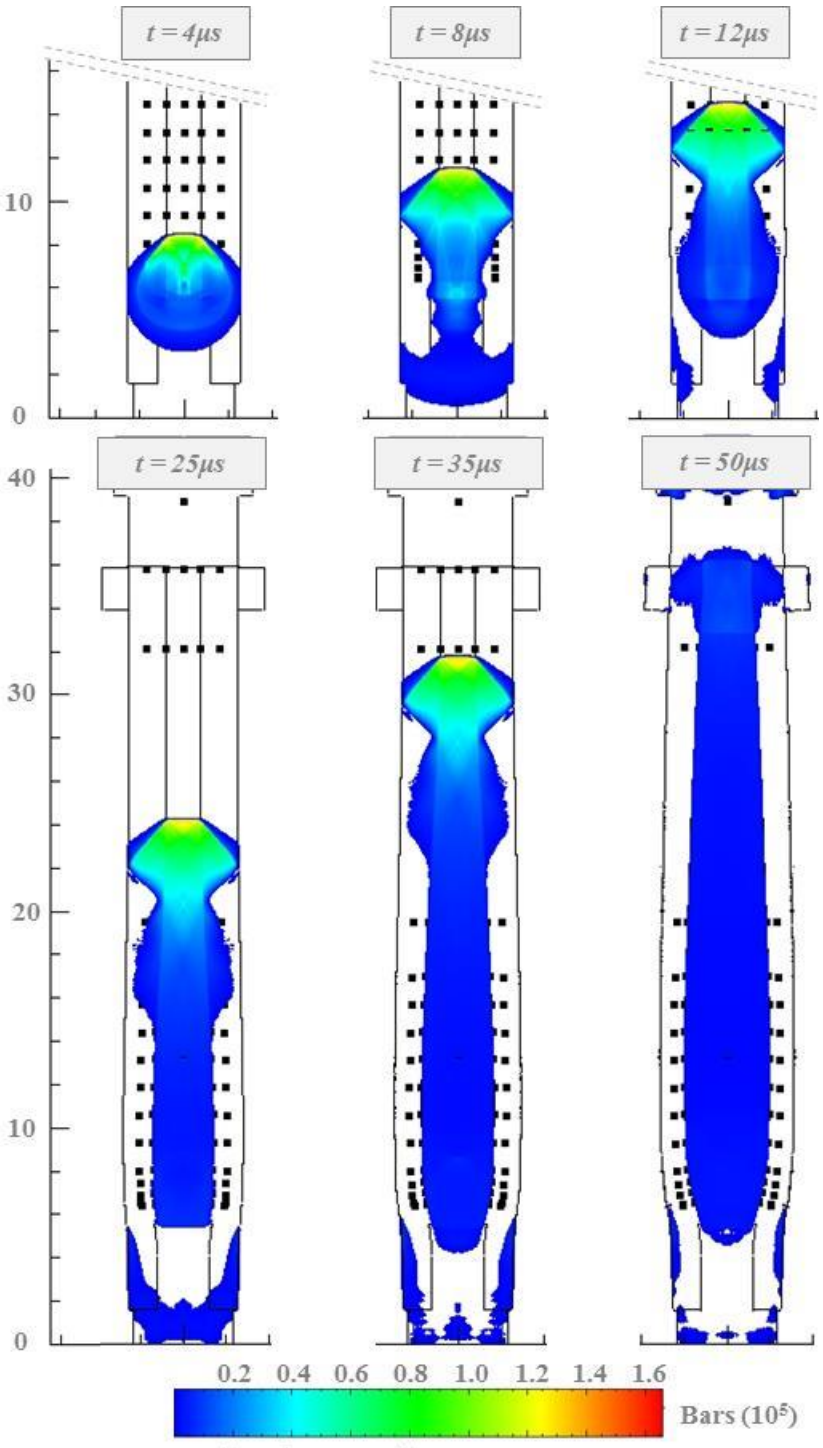

Figure 37: NSWC ARB Detonation Simulation

Figure 38 contains time sequence pressure contours for the LANL test case with an ARB deflagration tuned EOS for granular HMX and Figure 39 shows pressure contours for the LANL set-up with ARB detonation tuned EOS parameters. In these two figures it is evident that no reactions occur and the pressure wave imparted by the piston dissipates through the DDT test apparatus structure. Result in the following two plots are only shown to 17.5 μs to show close-up views of no reaction occurring as a result of the piston impact, though simulations were run for a full 50 μs. The lack of observed reaction as of 50 μs indicates that the initiation threshold temperature is not exceeded in the granular HMX. In reality, the low amplitude wave should eventually cause pore collapse and localized hot spot initiation resulting in a delayed onset deflagration (transitioning to detonation due to steel DDT tube and plugged end confinement). This theory is consistent with the approximately 40 μs delayed reaction recorded in LANL's experimental results in Figure 14 and Figure 15. It can be concluded that the current implementation of the Arrhenius Reactive Burn EOS does not account for low amplitude initiation mechanisms via localized hot spots.

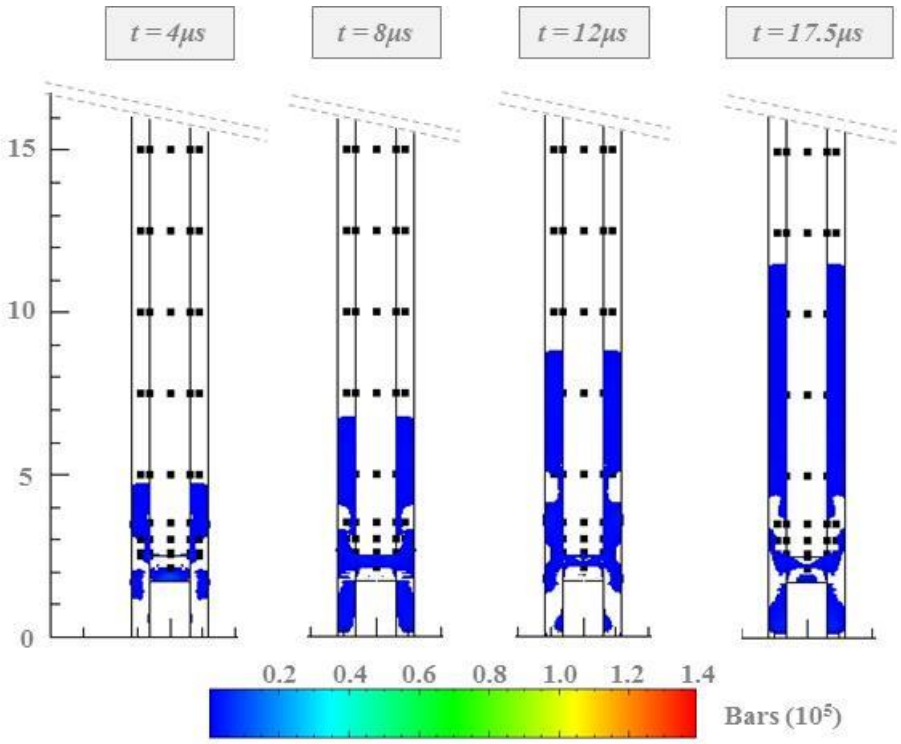

Figure 38: LANL ARB Deflagration Simulation

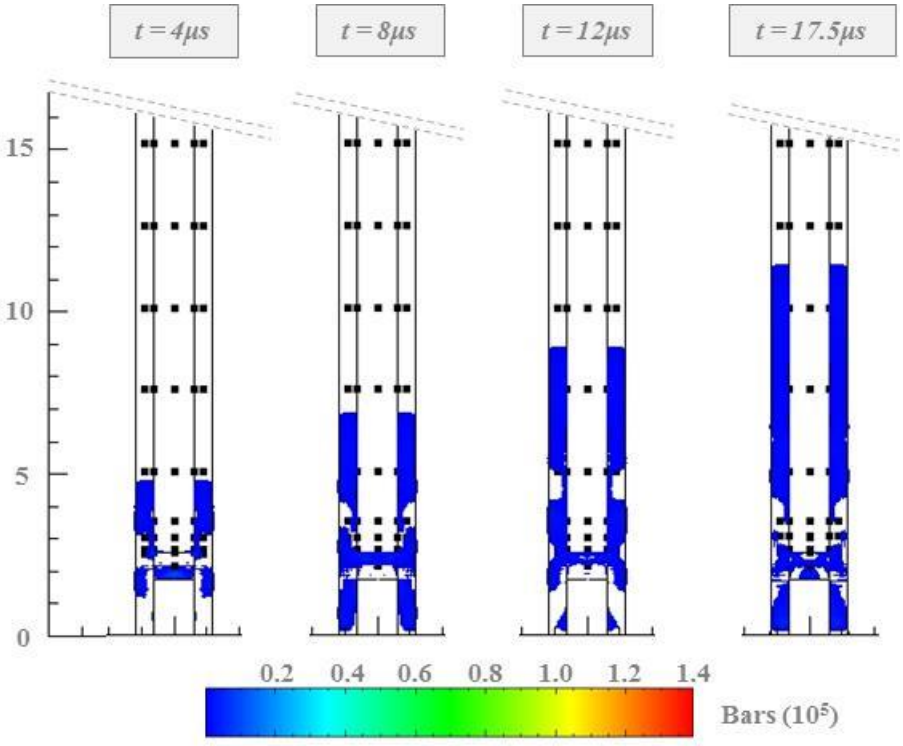

Figure 39: LANL ARB Detonation Simulation

Summary and Discussion of Research Gap

Results of the research gap study are summarized in this section along with a discussion of the path forward based on analysis assessments. Figure 40 contains a compilation of burn front versus time data, as presented in the NSWC experimental results, for comparison of the research gap simulations with granular HMX at 69.4% TMD that yielded reacting energetic responses. In this figure, black points are the published NSWC experimental results for fine-sieved and approximately 200 micron grain size HMX trials. The space between the black points therefore represents the region of possible reactive solutions based on HMX grain size and distribution. CTH results are plotted with various grey points. Success in modeling detonation of granular HMX is evidenced by the matching slopes of all grey points with the experiment black points. Experimental and computational values for the detonation velocity (slope of the distance versus time plots in the linear detonation region) are included in the plot legend. A shift to the left on the time axis indicates that CTH simulations run with HVRB, ARB deflagration or detonation EOS are able to model detonation, but this detonation occurs with no prior burning.

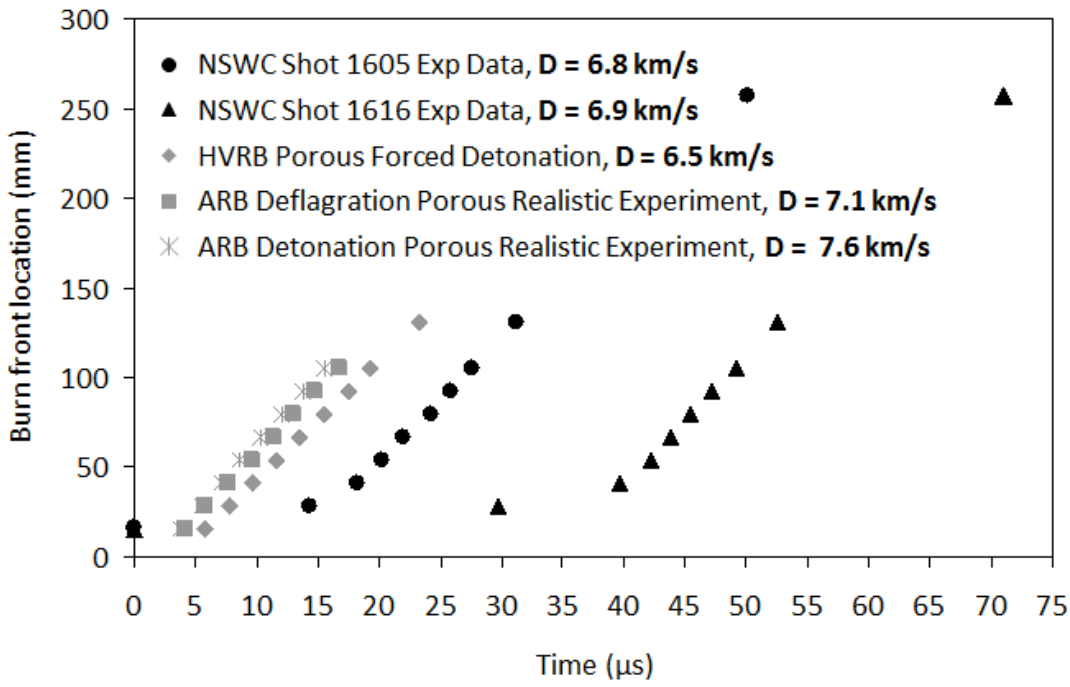

Figure 40: NSWC Data. Experimental vs Computational x-t Burn Front Trajectory.

Figure 41 contains a compilation of burn front versus time data, as presented in the LANL experimental results, for comparison of the research gap simulations with granular HMX at 65% TMD that yielded reacting energetic responses. In this figure, black points are the published LANL experimental results. Success in modeling detonation of granular HMX is once more evidenced by the matching slopes of all CTH points (grey) with the experiment black data points. The severe left shift on the time axis further supports the proposed explanation that CTH simulations are able to model detonation, but detonation occurs with no prior burning and this region is of considerable duration in the piston impact experiment.

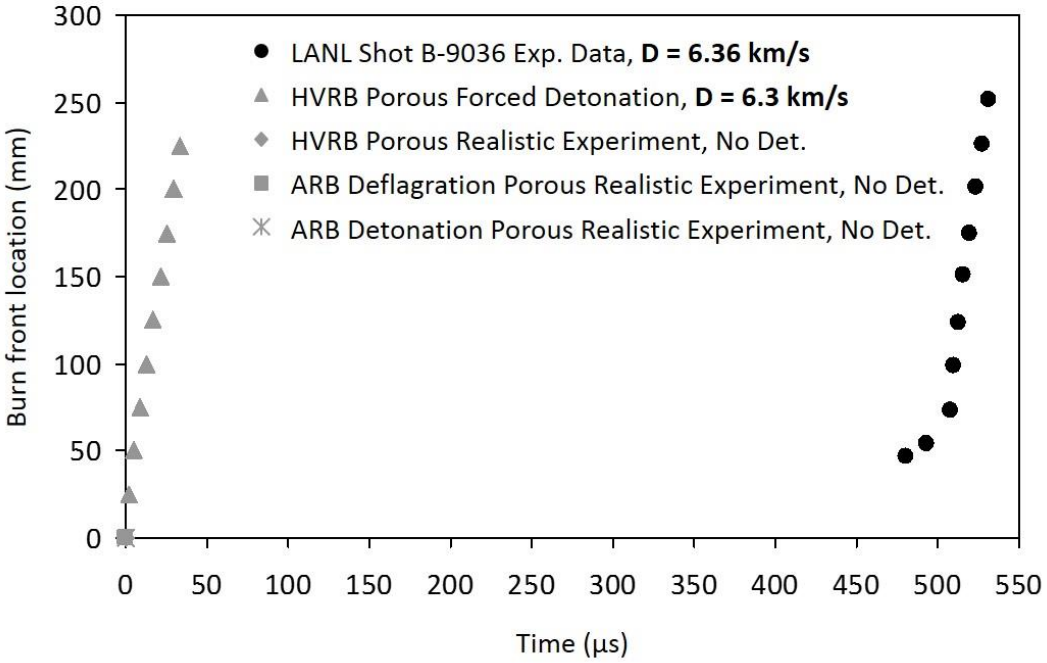

Figure 41: LANL Data. Experimental vs Computational x-t Burn Front Trajectory.

Table 10 summarizes the energetic response of all 22 simulations performed to characterize the research gap. In this table, XRN denotes the Extent of Reaction variable calculated for each energetic material EOS in CTH. XRN values range from zero to one, where zero means no reaction has occurred and one signifies that all reactants have been converted to products. A number between zero and one indicates that a reaction is on-going. Maximum values of XRN at Lagrangian tracers spaced 0.1, 0.5 and 1 centimeter within the HMX core center on the initiating end of the DDT tube are tabulated below. As expected, XRN values for inert cases are all equal to zero and XRN for all forced detonation simulations are equal to one. XRN data for the Arrhenius EOS simulations further supports the discussion above, where XRN is zero for the LANL cases and one for the NSWC cases. The only non-zero or one value of XRN

occurred for the representative experimental setup simulation with HVRB EOS for NSWC geometry. This XRN value of 0.0366 indicates that the HVRB model initiates minimal reactions, but is not formulated to sustain this type of reaction propagation.

Table 10: CTH Existing EOS DDT Responses

		NSWC Response			**LANL Response**		
		No Reaction	*Burn /Def.*	*Det.*	*No Reaction*	*Burn /Def.*	*Det.*
Inert	Inert 100% TMD No Porosity Baseline Mesh	XRN=0			XRN=0		
	65/69.4% TMD Porous Baseline Mesh	XRN=0			XRN=0		
	65/69.4% TMD Porous Fine Mesh	XRN=0			XRN=0		
	65/69.4% TMD Porous Non-Uniform Mesh	XRN=0			XRN=0		
HVRB	Forced Detonation 100% TMD No Porosity Baseline Mesh			XRN=1			XRN=1
	Forced Detonation 65/69.4% TMD Porous Baseline Mesh			XRN=1			XRN=1
	Forced Detonation 65/69.4% TMD Porous Fine Mesh			XRN=1			XRN=1
	Forced Detonation 65/69.4% TMD Porous F Non-Uniform Mesh			XRN=1			XRN=1
	Realistic Exp. Setup 65/69.4% TMD Porous Fine Mesh		XRN= 0.0366		XRN=0		
ARB	Reaction Rates for Deflagration			XRN=1	XRN=0		
	Reaction Rates for Detonation			XRN=1	XRN=0		

Based on this research gap characterization the following conclusions are reached:

- Inert: Accurate simulation of the pyrogenic material $BKNO_3$ is possible and porous energetic material compaction has been modeled
- HVRB forced detonation: CTH is able to approximately match the slopes of the detonating portion of LANL and NSWC data with porous compaction represented in the composite pressure dependent EOS
- HVRB representative test cases: minimal reaction observed, EOS not suited to sustain burning
- ARB: CTH is able to initiate reactions for high amplitude pressure wave impulses, but not for low amplitude piston driven mechanisms (likely due to lack of hot spot physics within the model)

Figure 42 contains a bar chart of run time for each of the 22 simulations presented in this Chapter. This chart is intended to demonstrate the computational expense of mesh spacing from baseline, to refined, to non-uniform and graphically depict the response output of each simulation. In total, approximately 965 CPU hours (40 CPU days or over 5 CPU weeks) of computational time have been spent and 400 gigabytes of data generated in characterizing the existing inability of CTH to model DDT of granular HMX. The author's path forward is to investigate two possible solutions: modification of the existing B-N multiphase model or formulation of discrete burning/deflagration model.

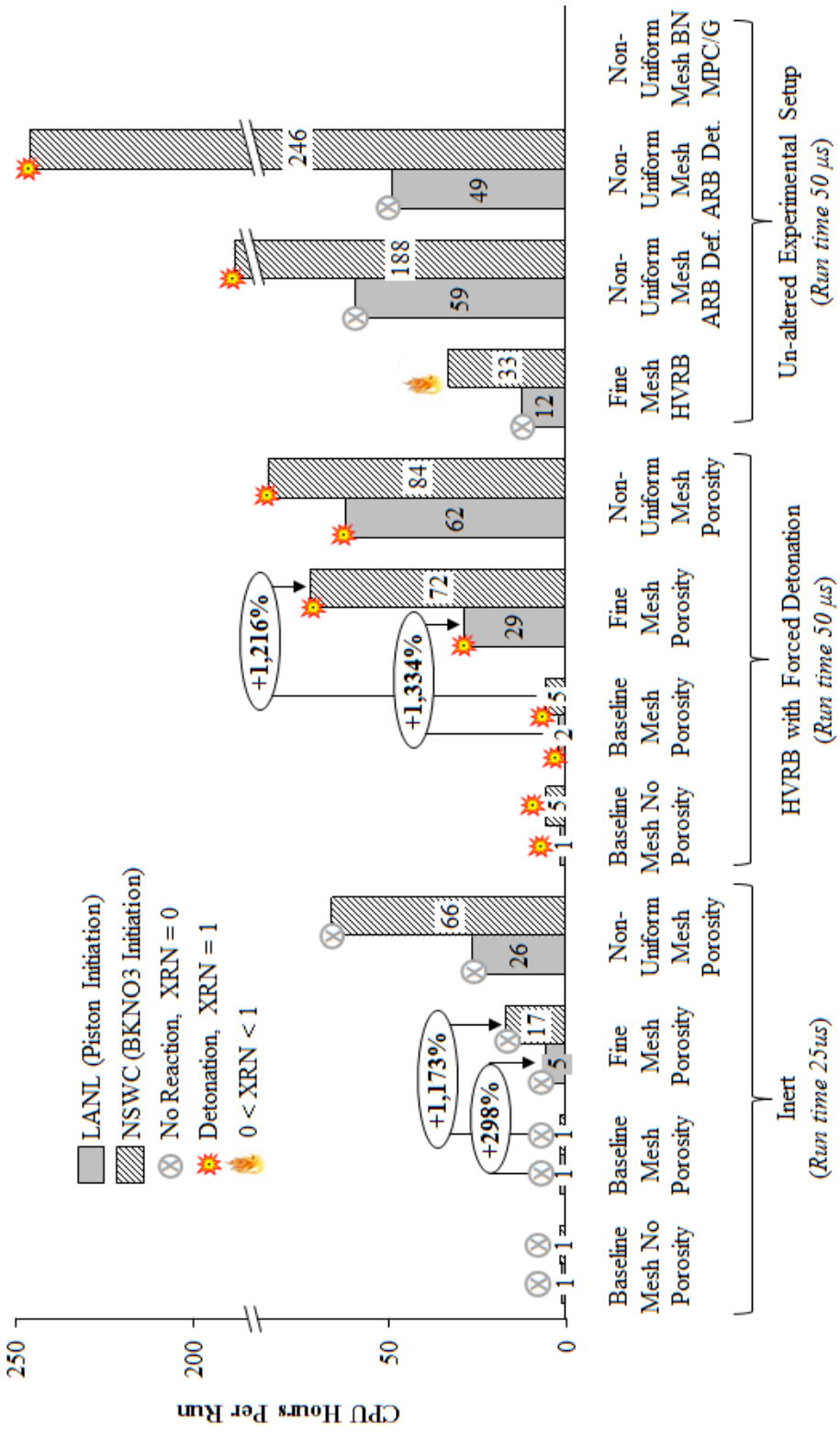

Figure 42: Run Time Plot of Simulations

CHAPTER 5

MODEL IMPROVEMENTS IN CTH

CTH Current Implementation

CTH Version 10.2, utilized in this dissertation research, contains an existing implementation of the Baer-Nunziato multi-phase reactive flow model discussed in detail in Appendix A. This is currently the only EOS in CTH capable of modeling the complex multi-phase physics and disparate time-scales associate with DDT phenomenon. The following bulleted quotes extracted from text in reference (Baer, Hertel, & Bell, 1996) describe implementation of the Baer-Nunziato multi-phase reactive flow model in CTH circa 1996:

- "Conservation of mass, momentum and energy is preserved
  - Relative flow effects: phase diffusion due to velocity difference between individual phase particle velocities and mixture mass-averaged velocity
  - Phase interactions (mass exchange, drag, heat transfer) are cell volume-averaged quantities
- All multi-phase conservation equations have both source and phase diffusion terms
  - Eulerian step: phase diffusion effects and cell-surface forces incorporated via operator splitting

        - Phase quantities are transported in or out of cells: Flux-Corrected-Transport method used to include phase diffusion and internal boundary conditions
        - No artificial smearing at material interfaces is introduced
    - Lagrangian step: remaining cell volume source quantities are resolved
    - After Lagrangian step, volume fractions of single mixed phase material are remapped to Eulerian mesh
    - Parameters are then reassembled for EOS calculation at the beginning of the next time-step
    - Sound speed constraint called for Courant condition assessment
- Phase interactions are resolved with an algorithm based on asymptotic semi-analytical solutions to account for inaccuracy of explicit time difference methods"

Limitations of BN Execution in CTH

The existing multi-phase reactive flow model implementation in CTH, based on the work introduced in (Baer & Nunziato, 1986), is challenging to implement due to the use of dozens of input parameters. Once a correct input parameter set is established, Reference (Baer, Hertel, & Bell, 1996) notes that the "interaction of phases occurring with greatly disparate time-scale leads to the solution of equations that are mathematically stiff." The author made multiple unsuccessful attempts at modeling a one dimensional multi-phase reactive flow simulation with granular HMX. Each

simulation crashed with an error indicating stiff solver issues. Subsequent personal communications with the CTH development group at Sandia National Laboratory indicated that stiff solver problems are a known issues and attempted modification of the associate sub-routines pertaining to the scope of the present research is inadvisable.

Path Forward

Given the unanticipated and out of scope complexity associated with updating stiff solver related issues in the CTH implementation of the 1986 Baer-Nunziato multi-phase reactive flow model, an alternative path forward is pursued in the remaining dissertation sections.

The author's current methodology for creating a hydrocode model of a scenario where DDT is suspected to occur in the run-up to detonation consists of first modeling the problem utilizing a reactive burn composite EOS for the energetic material. If initiation occurs in this model no further analysis is required. However, if detonation is not achieved directly from a reactive burn composite EOS, the author re-runs the simulation employing an inert Mie-Gruneisen primary EOS for the energetic material. Results in the form of pressure as a function of penetration distance into the energetic material recorded at specified tracer points are compared to a Pop-plot. As explained in the Literature Review, Pop-plot is the name given to plots of input stress versus penetration distance into an energetic material to achieve prompt initiation of the explosive. The term Pop-plot was coined in honor of Alphonse Popolato. Data plotted on a Pop-plot are obtained from empirical wedge test results and are influenced by density and therefore porosity of an explosive. If inert simulation results at specified

penetration depths into the energetic material are relatively close to the initiation line on a Pop-plot, DDT is deemed to potentially play a role in initiation and experimental testing is required to prove this hypothesis. If CTH pressure results are far below the Pop-plot initiation thresholds then DDT is less likely to occur, depending on the specific energetic material, though it is still a distinct possibility due to hot spot initiation.

Based on the aforementioned existing DDT investigation CTH simulation methodology, it is evident that one primary component in Deflagration to Detonation Transition modeling, namely deflagration, is not currently modeled. The remainder of this dissertation seeks to generate a computational model capable of simulating granular HMX deflagration in CTH. The hydrocode method for DDT can then be revised to include an approach simulating deflagration to increase simulation result reliability and decrease the need for DDT experimental testing in projectile impact scenarios. One advantage of this approach, in contrast to the Baer-Nunziato multi-phase reactive flow model, is the ability to conduct straight forward testing to obtain model parameters. The Baer-Nunziato multi-phase reactive flow implementation in CTH contains *dozens* of adjustable parameters that require tuning to correctly model behavior (once stiff solver issues are overcome). Deflagration followed by a separate detonation simulation is advantageous in that model parameters can be obtained from straight forward testing mechanisms. For deflagration parameters, Crawford bomb testing provides a means to calculate burn rate as a function of pressure. With the HVRB model, parameters can be tuned from wedge test data. Likewise, Arrhenius parameters can be obtained from DSC testing for a known ramp rate, temperature

range, and material state. The compendium of these approaches will yield a robust practical and applicable methodology to determine if granular HMX will undergo DDT.

Novel Additions to CTH

In order to achieve the goal of successfully modeling granular HMX deflagration in CTH as a vital component of the DDT methodology several novel contributions to the field are necessary. Porosity in granular energetic materials governs reactivity thresholds and thus influences the sensitivity of an explosive. Accurate modeling of porosity is therefore important to predict the explosive reactivity in either deflagration or detonation regimes. A set of P-α porosity model parameters for granular HMX was not found after an extensive literature review. Therefore, validation of a set of P-α porosity parameters for granular HMX is the first step in simulating deflagration or detonation. Once a complete set of parameters is established, CTH equation reformulations are required to create a deflagration model specifically intended for explosives.

In assessing the research gap, discussed in detail in Chapter 4, several novel contributions to the field were made. First, a set of parameters for the pyrogenic initiator $BKNO_3$ were established to model NSWC experimental conditions. Second, Arrhenius Reactive Burn (ARB) simulations with separate sets of parameters tuned to granular HMX deflagration or detonation were performed as follow-on to work presented in (Mahon, 2014) for RDX. Lastly, an initial porosity model for granular HMX was presented to approximate energetic material compaction as a function of

input stress in both LANL and NSWC DDT tube experiments. Parameters in this set were obtained from numerous references and assembled into an initial approximation of HMX porosity. Iterative refinement and validation of this set of P-α porosity parameters is the subject of the subsequent section.

Mie-Gruneisen EOS & P-α Porosity of Granular HMX

As discussed in the inert results section of the chapter entitled CTH HYRDROCODE: RESEARCH GAP IDENTIFICATION, one notable accomplishment of the present work is the formulation of an inert Mie-Gruneisen user defined EOS for granular HMX from multiple references with a working P-α porosity model. This porous Mie-Gruneisen EOS was utilized both as a standalone inert material as well as the unreacted material model in composite HVRB and ARB reactive EOS. Details on the granular HMX Mie-Gruneisen EOS and P-α porosity model and validation are included within this sub-section.

The Mie-Gruneisen EOS is a pressure dependent primary EOS based on material specific Hugoniot curve data, an example of which is Figure 3. As *Segletes* explains, an EOS is generally utilized to characterize material pressure in terms of density and temperature which are needed to solve the conservation of mass, momentum and energy equations. However, scenarios often modeled in hydrocodes occur at such rapid rates that heat transfer is of little concern and governing equations can be solved in terms of internal energy, rather than temperature, for a known pressure and density. (Segletes, 1991) Variations of the Mie-Gruneisen EOS exist depending on the Hugoniot plane referenced in derivations. One form of the Mie-Gruneisen EOS is

included in the equation directly below from (Segletes, 1991, p. 19). In this equation, P is pressure, E is specific internal energy, Γ is the Gruneisen coefficient which is a function of density, and μ is a compression coefficient. Subscript h denotes reference Hugoniot states and subscript 0 indicates ambient conditions.

$$P = P_h(1 - \Gamma\mu/2) + \rho_0\Gamma(1 + \mu)[E - E_0] - P_0\Gamma\mu/2 \quad [25]$$

CTH's implementation of the Mie-Gruneisen EOS has the option to include porosity via a P-α model described in greater detail in (Hertel E. S., 1998). The P-α model that was originally formulated by *Herrmann* and published in 1968 was intended to accurately model porous compaction in a thermodynamically consistent manner at high stresses and approximate compaction at lower stresses. In *Herrmann's* porosity model the distention parameter, α, is defined as the ratio of specific volume of a porous material, v, to the specific volume of a solid matrix material, v_s.

$$\alpha = \frac{v}{v_s} \quad [26]$$

A fundamental assumption of *Herrmann's* model is that the specific internal energy is equivalent for the porous material and solid matrix material when at the same temperature and pressure conditions. From this relation it is evident that α is greater than one for a porous material and equal to one when the material reaches a fully compacted state. The primary function of α is to distinguish the volume change of the solid matrix material due to material compression from the volume change of the porous material due to void collapse (compaction). (Herrmann, 1969) *Herrmann's* P-α model recasts an EOS where pressure is a function of specific volume of a solid matrix material and internal energy to include porous effects by making pressure a function of

porous material specific volume divided by α as well as internal energy. The equation below demonstrates this relationship:

$$P = f(v_{s,}\, E) \xrightarrow{porosity\ added\ to\ EOS} P = f\left(\frac{v}{\alpha}, E\right) \quad [27]$$

Herrmann separates the effects of compaction into two regimes: elastic and plastic, as shown in Figure 43 below. Assuming that shear strength is negligible and consequently sound speed can be appropriately represented by only the bulk sound speed, the porosity term α_p can be expressed in the form included in the equation below. In this equation, Equation (24) from *Herrmann's* original 1969 publication, subscript p denotes the plastic deformation regime, p_s is the pressure at which compaction is complete and α=1, p_e is the elastic compaction region pressure threshold, and α_0 is the initial porous material distention parameter. (Herrmann, 1969)

$$(\alpha_0 - 1)/(\alpha_p - 1) = [(p_s - p)/(p_s - p_e)]^2 \quad [28]$$

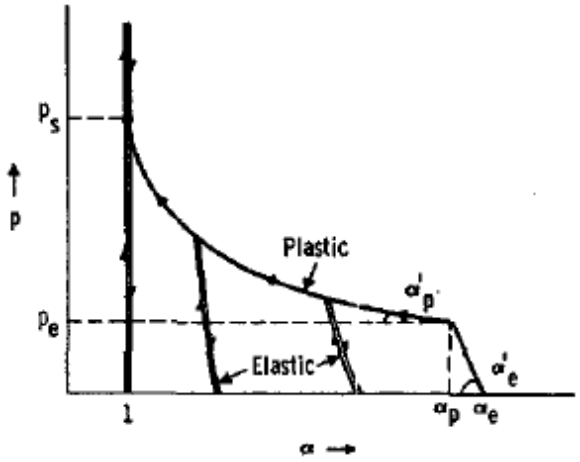

Figure 43: Pressure versus Porosity, α, in Elastic and Plastic Compaction Regimes (Herrmann, 1969, p. 2491)

In 1971, Carroll and Holt of Lawrence Livermore National Laboratory published a notable augmentation of the original formulation of the P-α model. *Carroll and Holt* modified the pressure dependent EOS relation in the above equation to include a factor of 1/α, as shown in the equation directly below, to correct for the observation that the pressure in the porous material is approximately equivalent to 1/α times the solid matrix material average pressure value. (Carroll & Holt, 1971)

$$P = f\left(\frac{v}{\alpha}, E\right)/\alpha \qquad [29]$$

Mie-Gruneisen EOS with P-α porosity parameters implemented in CTH to model porous granular HMX in NSWC and LANL DDT experiments were based on a compilation of parameters published in the following references: (Baer, Kipp, & van Swol, 1998), (Marsh, 1980), (Hall & Holden, 1988), (Menikoff R. , 2001), and (Crawford, et al., 2012). Based on recommendations in (Kerley G. I., 2006), porous HMX was accurately modeled by inputting Mie-Gruneisen parameters for HMX at 100% TMD in conjunction with P-α porosity model parameters at the porous density to replicate validation simulation experimental conditions. Within the P-α model, initial pressure at which compaction occurs in the elastic region is assumed to begin above 1 Bar (approximately 1 atmosphere).

The pressure limit at which compaction is complete, α=1, compelled further study. The value of pressure at which compaction is complete input in CTH simulation results presented in the above chapter entitled RESEARCH GAP IDENTIFICATION is 2.3 kBar. This parameter was obtained by digitizing granular HMX experimental data and corresponding computational simulation results published in (Menikoff R. ,

2001). *Menikoff's* strength based porosity calculations in an Eulerian hydrocode consist of mesoscale simulations of granular HMX gas gun data published in (Sheffield, Gustavsen, & Anderson, 1997). Unlike the present work which models porosity as a function of pressure via the P-α model, *Menikoff's* Eulerian simulations calculated porosity effects from elastic-plastic interactions as a function of yield strength of HMX grains in mesoscale calculations. *Menikoff's* strength based model is analogous to the P-α model in that it relates the average material stress to the stress of the solid matrix material. (Menikoff & Kober, 1999) *Sheffield's* experimental setup is simulated in CTH with macroscale porous (P-α model) granular HMX parameters from the aforementioned reference list to validate the modeling methodology employed in the present work.

Setup/Implementation

Sheffield et al. conducted gas gun experiments at Los Alamos National Laboratory to characterize compaction behavior of multiple porous granular energetic materials. Given the motivation of this dissertation, only experimental results with granular HMX are considered and subsequently simulated in CTH. The LANL gas gun experiments were configured such that a polychlorotrifluoroethylene (Kel-F) projectile traveling between 270-700 m/s (depending on the experimental trial) impacted a layered stack of Kel-F, followed by a 3.9 mm thick layer of coarse or fine granular HMX at 65-74% TMD, followed by either a poly-4-methyl-1-pentene (TPX) or polymethylmethacrylate (PMMA) backing disk. Test hardware was rigged with magnetic particle velocity or polyvinylidene diflouride (PVDF) stress gauges to capture velocity or stress data both at the Kel-F to HMX front interface and HMX to TPX or

PMMA back interface. (Sheffield, Gustavsen, & Anderson, 1997) Wave profile time delays for the known HMX thickness of 3.9 mm enable calculation of the average compaction wave speed. (Menikoff R. , 2001)

Figure 44 below illustrates the experimental setup diagram from Figure 2.6 in *Sheffield*. This schematic was digitized by the author to obtain CTH geometry measurements for replication of compaction experiments in CTH. Based on this Matlab digitization of the image in Figure 44, the following material thicknesses were modeled in CTH: Kel-F impactor thickness 11.5 mm, Kel-F front disk thickness 4.8 mm, HMX thickness stated in *Sheffield* 3.9 mm, and TPX or PMMA back disk thickness 12.2 mm.

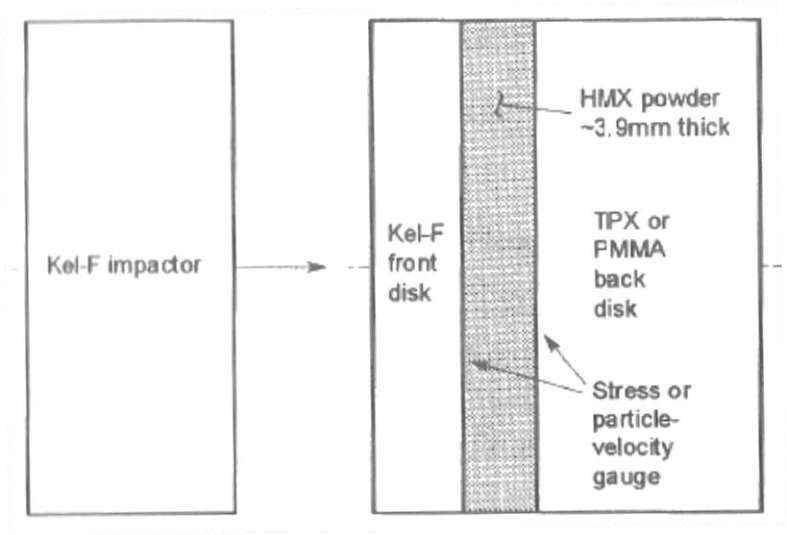

Figure 44: LANL HMX Compaction Gas Gun Experimental Setup (Sheffield, Gustavsen, & Anderson, 1997, p. 36)

Data from multiple LANL gas gun shots were down-selected for simulation in CTH to validate P-α porosity settings for granular HMX. Gas gun experiments were instrumented to obtain either velocity or stress data, though not both at the same time, which necessitated the selection of multiple shot results. Selected data were chosen for

several key reasons. First, the influence of grain size was taken into consideration by comparing CTH simulations to experimental results corresponding to both "coarse" 120 μm mean particle size and "fine" 10-15 μm mean particle size tests to determine which data set CTH more closely replicates. For comparison, HMX mean particle size in the LANL DDT test case is 170 μm and 115 or 200 μm in the NSWC test cases referenced in the previous chapters.

A second selection criteria involved impactor velocity range. Though *Sheffield* reports that the LANL gas gun experiments were conducted for impactor velocities in the range of 270-700 m/s, only back plate velocity versus time traces for experimental trials with impactor velocities of 270-288 m/s and 596-601 m/s are reported in his compilation book chapter. Given that the LANL DDT tube experimental piston velocity is 100 m/s the lower impactor velocity range is more appropriate for comparison of lower amplitude impact waves. Furthermore, *Menikoff* and *Sheffield* both note reactivity within the granular HMX sample at the higher impactor velocity range above 500 m/s, which influences back plate data by producing higher velocity readings as compared to inert samples. HMX reactivity for impactor velocities above 500 m/s is supported by calculations indicating the likelihood of HMX reaction due to the presence of hot spots above impact wave pressures greater than 0.5 GPa (5 kBar). Input pressure at the impactor range of 596-601 m/s is approximately 0.72 GPa (7.2 kBar). [(Menikoff & Kober, 1999) , (Sheffield, Gustavsen, & Anderson, 1997)]

The CTH simulations in this chapter ran on an HP Z800 workstation with 12 cores, 64 Gigabytes of RAM, and 2 Terabytes of disk space as well as a high speed massively parallel cluster on up to 128 processors. Mesh sizes with uniform spacing of

0.02 cm (200 μm) were utilized as the baseline coarse mesh as this spacing is the aforementioned LANL and NSWC DDT tube test case non-uniform mesh minima. The problem domain for porosity validation was much smaller, 3 by 6 centimeters, compared to the larger NSWC domain of 5.5 by 5.5 by 45 centimeters, enabling and ultimately necessitating much finer meshing. Smaller uniform mesh spacing down to 0.001 cm (10 μm) was utilized for comparison because this is the mesh spacing employed by *Menikoff* in his mesoscale hydrocode simulations. Mesh size iterative simulations were performed between 200 μm and 10 μm to determine the minimum mesh utilization for acceptable comparison to experimental data. The largest uniform mesh spacing allowable was determined to be 30 μm. The driving thin feature in the LANL gas gun model is the 0.39 cm thick granular HMX sample. With the baseline coarse mesh this material was modeled with 19.5 cells across the HMX thickness. Generally, the guideline for Eulerian hydrocodes is two to five cells minimum across the minimum thickness to resolve shared volume fraction calculation errors. Though the baseline coarse mesh is well above this guideline, the author was unable to find information in the literature advising on acceptable meshing practices with P-α porosity models of macroscale granular energetic material and consequently decided on a conservative meshing scheme. Given the large variations in 2D axisymmetric total mesh cell count, from 45,000 cells for the 200 μm uniform mesh up to 18,000,000 for the 10 μm uniform mesh, correspondingly pronounced differences in run time were encountered. The 200 μm mesh ran in less than 1 CPU hour while the 10 μm mesh required closer to 1,000 CPU hours per input deck.

All simulations were performed in a two-dimensional cylindrical coordinates system with a symmetry boundary condition at the axis of symmetry. Specifically, the boundary condition at the bottom of the X axis was set to symmetry and boundary conditions at the bottom and top of the Y axis as well as the top of the X axis were set to an outflow boundary condition such that mass is allowed to exit (but not re-enter) the mesh.

Figure 45 contains a 2D image of the LANL gas gun materials plot with mirroring across the axis of symmetry, the Y axis. In this figure, A indicates the back plate, modeled as PMMA or TPX depending on the experimental configuration. HMX is identified with marker B. The front plate, shown in C, and flyer plate, shown in D, are both composed of Kel-F. Air is included in the white region filling the remainder of the computational domain. All solid materials are defined with a Mie-Gruneisen EOS, and air is modeled with a SESAME tabular EOS. EOS parameters were obtained from the following references for KEL-F, TPX, and PMMA: [(Sandia, CTH 10.2: Equation of State Data File, 2006), (Menikoff R. , 2001), (Matweb, 2014), and (Marsh, 1980)] Inert granular HMX Mie-Gruneisen EOS parameters were compiled from the references listed in Table 8 and Table 9 with the notable exception of parameters for the pressures at which compaction begins and ends. These parameters were iteratively determined by the author based on comparison of CTH simulations with experimental data and expanded upon further in both the subsequent data analysis discuss and in (Mahon, 2015). All material strength models were assigned as Elastic Perfectly Plastic Von Mises models with yield strength, Poisson ratio, and fracture pressure obtained from (Matweb, 2014). The Kel-F flyer was initially positioned at a standoff distance of

0.02 cm, one baseline coarse mesh cell, away from the Kel-F front plate and assigned a Y velocity equivalent to the experimental gas gun velocity for a specific trial.

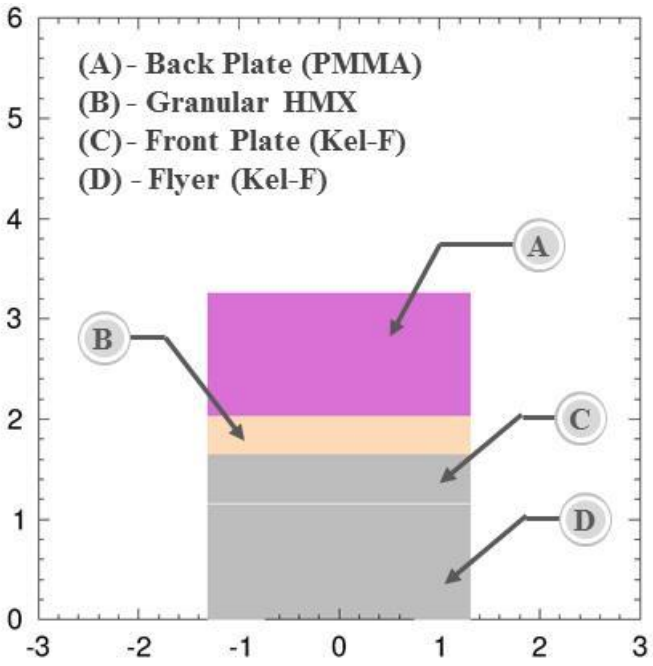

Figure 45: CTH 2-Dimensional Cylindrical Coordinates Gas Gun Experimental Model.

Validation Schema

Both Lagrangian and Eulerian discrete user defined tracer points were defined in the CTH porosity model validation simulations to record local pressure (stress), velocity, and density data as a function of time. The LANL gas gun experimental configuration replicated in CTH contained magnetic particle velocity or polyvinyllidene diflouride (PVDF) stress gauges. Similar to the configuration modeled in (Menikoff R. , 2001), the present simulations utilized rows of approximately 50

tracers one baseline coarse mesh cell distance into the interface boundaries spaced 0.01cm apart linearly to collect and replicate experimental data in (Sheffield, Gustavsen, & Anderson, 1997). A Matlab script was written by the author to reduce, post-process, time-shift, and average tracer data. Tracers intended to replicate the experimental configuration were modeled as Lagrangian, allowed to move with the originally assigned material, and specific variable quantities were averaged at each time, recorded in 0.1 microsecond increments, to accurately model experimental data.

Validation of the P-α porosity model in CTH followed a five-pronged multi-parameter validation approach. Specifically, this approach included comparison of experimental data or analytical calculations (where noted) to CTH in terms of:

Approach 1: PDVF gauge stress data at the Kel-F front plate (when available)

Approach 2: Magnetic particle velocity data velocity vs time traces at the front plate (when available) and back plate, specifically focused on rise time and wave profile

Approach 3: Magnetic particle velocity data arrival time of the plastic compaction wave, specifically instantaneous velocity at the back plate. Plastic compaction wave velocity changes as a function of distance in granular compaction.

Approach 4: Analytical comparison of elastic compaction wave speed at the back plate to longitudinal sound speed

Approach 5: Analytical Hugoniot comparison to final compacted density at the average shock velocity

The P-α porosity model is controlled by several input parameters, shown in the calculation of the porous distention parameter, α_p, from *Herrmann's* original journal article in Equation 28. Input parameters include the pressure at which compaction begins, p_e, the pressure at which compaction is complete corresponding to $\alpha_p=1$, p_s, the initial porosity of the material, as well as the corresponding inputs for the Mie-Grunesien EOS in which P-α porosity is implemented. Throughout this validation approach the author explored parameter sensitivities. By iterative computational analysis it was determined that the minimum pressure at which compaction begins parameter, p_e, influenced the wave front shape. A p_e parameter value of 1 Bar (approximately 1 atmosphere) result in a planar wave front. Higher values of this parameter p_e result in an increasingly pronounced non-planar curved wave front. CTH simulation results were quite sensitive to the value assigned to the pressure at which compaction is complete. Consequently, a majority of time in this validation effort was required to correctly adjust this parameter. Mesh independent CTH results for the LANL gas gun experimental configuration showed that decreasing the pressure at which compaction is complete increased the final compacted %TMD, increased transmission time of the compaction wave through the granular energetic material, and lowered back plate average velocity. Likewise, increasing the pressure at which compaction is complete resulted in lower final %TMD compaction values, decreased compaction wave transmission times, and higher back plate average velocity. Setting p_s to 3 kBar produces CTH results with excellent agreement with experimental data and is consistent with calculations in (Baer & Nunziato, 1989).

Before delving into results and validation of the aforementioned Approaches 1-5, it is instructional to review time sequences of pressure and density contour plots contained in Figure 46 for a general overview of pertinent physical phenomena and P-α porosity modeling implementation. This figure contains CTH simulation results for a simulated LANL gas gun experiment with granular HMX density of 1.24 g/cm^3, 65% TMD, and piston velocity of 279 m/s run on the finest mesh spacing of 10 μm. Plots in the left column are pressure contours and plots in the right column are density contours. Progress of the compaction wave through granular HMX is evident in the images from three to six microseconds given in one microsecond intervals. In this CTH simulation configuration the planar wave reaches the beginning of the HMX sample at 2.8 μs. Piston impact imparts a plastic compaction planar wave of approximately 2.3 kBar into the granular HMX. Plastic compaction wave pressure (as well as wave front velocity) decreases as a function of time as the compaction wave travels through the granular energetic material sample. An elastic precursor compaction wave traveling at approximately the sound speed of granular HMX leads the planar compaction wave. Edge effects minimally influence the wave shape in HMX at later times, shown below at six microseconds by rounding of the planar wave edges due to rarefaction waves impinging at the granular HMX to air interface. Edge effects are more pronounced in the pressure contour plots within the region of the Kel-F front flyer and plate. Kel-F to HMX boundary occurs at the solid orange horizontal line and edge effects are evident as a function of time with the narrowing orange region. The finite plastic compaction wave thickness in HMX shown in the pressure contour plots supports *Sheffield's* assertion that "porous materials do not propagate sharp shock waves. Instead, the waves

are spatially and temporally diffuse or spread out." (Sheffield, Gustavsen, & Anderson, 1997) Focusing now on the right column of density contours, a plastic compaction wave progresses through granular HMX and the gradually increasing influence of edge effects are also evident. According to the density scale, HMX in this experimental configuration compacts to below 100% TMD.

LANL experimental gas gun data for both "coarse" 120 μm mean particle size and "fine" 10-15 μm mean particle size tests were compared to CTH simulation results on a broad range of mesh spacing, ranging from 10 to 200 micrometers, in order to determine which grain size distribution CTH more closely replicates. Using appropriately tuned P-α inputs CTH data compares very well to back plate experimental velocity versus time traces for fine mean particle size HMX and significantly underestimates back plate velocity for experimental data collected with coarse grain HMX particle distributions. This observation makes sense when one considers the physical representation of the P-α porosity model in an Eulerian hydrocode. The P-α porosity model assumes a uniform distribution of porosity throughout a matrix material and does not consider statistical particle distribution and packing. Uniform porous distribution is therefore more closely replicated in samples with consistent and small interstitial spaces, referred to as void regions in the study of granular energetic materials, more characteristic of fine grain samples. Large variations in void size throughout a coarse grain sample do not match the simplifying assumptions inherent in the P-α porosity model. Subsequent validation cases are only compared to fine grain, 10-15 μm mean particle size, experimental granular HMX data.

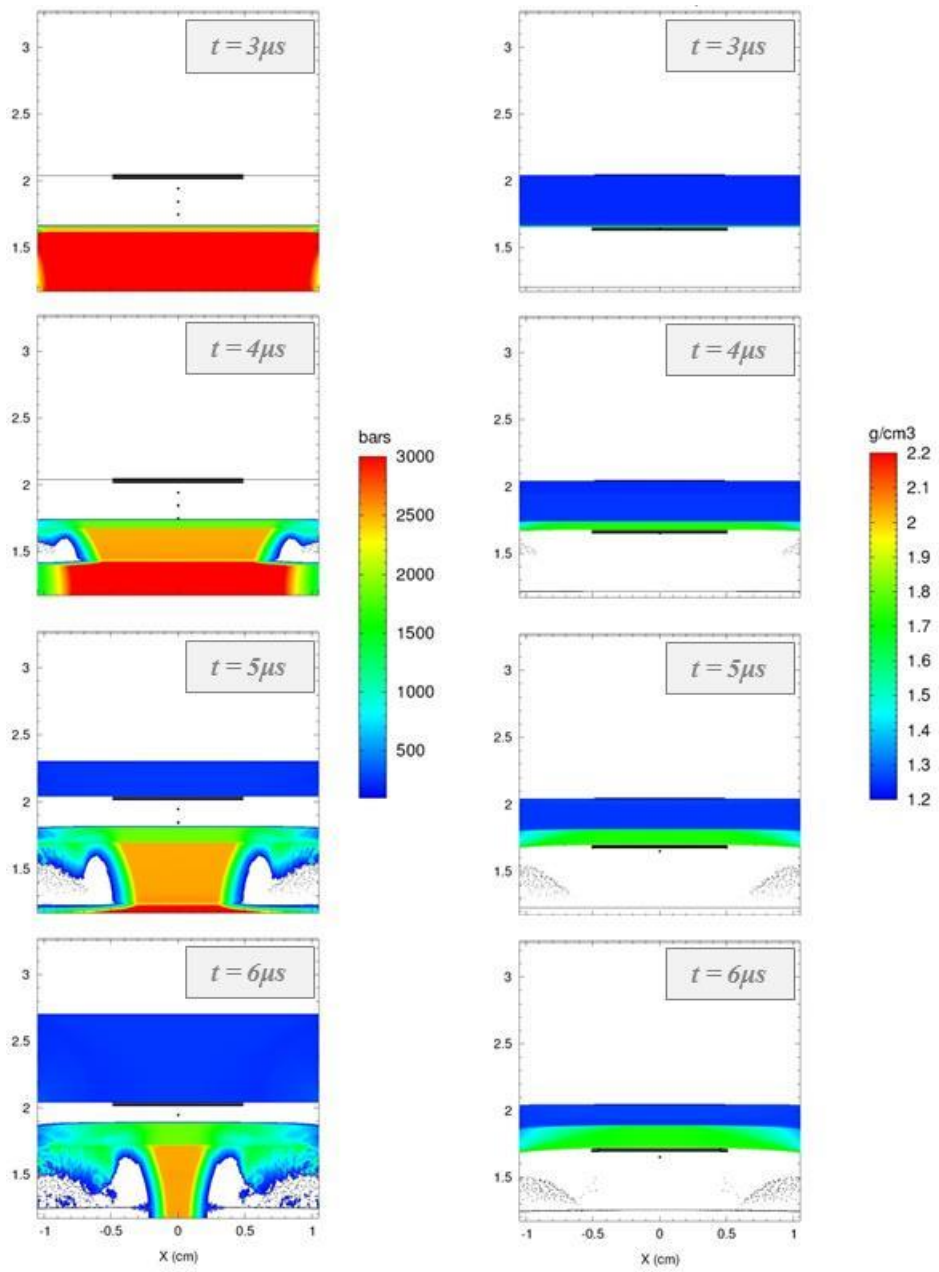

Figure 46: LANL Gas Gun Simulation Density and Pressure Contours at ρ = 1.24 g/cm^3

Results 1: LANL Gas Gun at 1.24 g/cm³

Validation *Approach 1* compares the *Sheffield* experimental PDVF gauge stress data at the Kel-F front plate to approximately 50 CTH Lagrangian tracer values spaced 0.01 cm apart linearly and positioned one baseline coarse mesh cell distance from the interface boundary. Figure 47 contains a plot of experimental PDVF Kel-F front plate input wave pressure versus time along with corresponding CTH results post-processed in Matlab. The CTH results have been shifted in time to facilitate comparison with experimental results. Time zero occurs when the input wave reaches the Lagrangian tracers of interest. This time shift is consistently employed in subsequent plots.

Sheffield data plotted in the figure below correspond to experimental shot number 2477 with a piston velocity of 285 m/s, coarse grain HMX, and a TPX back plate. This is the only input stress data provided in *Sheffield*. CTH simulations replicated *Sheffield* experiments with fine grain distribution 1.24 g/cm^3 HMX samples (unknown shot number) with a piston velocity of 279 m/s and a PMMA back plate. However, it is appropriate to compare the results of this experiment as only the front gauge data is being used for comparison purposes and waves traveling at material sound speed are not aware of upstream disturbances.

Finer mesh CTH results and experimental data in Figure 47 compare well near time zero when the input wave reaches the granular HMX sample after traveling though the Kel-F front plate. The slight dip at the beginning of the experimental data set is not evident in CTH results. This dip may be due to impedance mismatch at the gauge interface position between the Kel-F front plate and HMX sample. CTH tracers were

imbedded one cell away from the interface to avoid shared volume fraction calculation and impedance issues.

CTH results from the 200 μm mesh contain large pressure fluctuations across the averaged tracer values indicating the need for finer mesh spacing. On the 30 μm mesh these fluctuations decrease dramatically and are nearly gone on the 10 μm mesh. Similarly, comparison between trend lines of the experimental data, 30 μm, and 10 μm mesh results are qualitatively similar at times near zero. CTH results break away from the experimental trend at 2.2 μs, likely due to impingement of rarefaction waves at tracers positioned closet to the edge. At the crest of the initial empirical dip in digitized results, occurring at 0.39 μs, CTH results at the nearest data capture point of 0.4 μs are within 11% of the experimental data. Differences between CTH results from the 30 μm and 10 μm mesh simulations remain within 10% of the experimental results until the slope break away point at 2.2 μs. Part of the difference in CTH and empirical input wave data can be attributed to slight differences in simulation versus experimental conditions. The CTH simulations were intended to replicate fine grain HMX back plate velocity data. Available front plate data piston velocities are 2% higher (285 m/s for coarse HMX Shot 2477 versus 279 m/s for fine grain HMX) leading to slightly higher input wave pressure. CTH baseline mesh results are not quantitatively compared due to large pressure fluctuations. An additional reason for plot deviations beginning at 2.2 μs is due to simulation setup assumptions. CTH simulations assume the PDVF and magnetic particle velocity gauges are positioned in the geometric center of the front plate to HMX interface and HMX to back plate interface. Furthermore, CTH tracers are spaced 0.01cm apart linearly over 0.5 cm beginning at the axis of symmetry, thus

assuming the experimental gauge is 1 cm in diameter. Gauge size and positional differences in the experimental trials can influence the output stress profile. The author concludes that front plate input wave pressure calculated in CTH compares well on finer meshes with experimental data published in (Sheffield, Gustavsen, & Anderson, 1997) and yield strength based porosity model hydrocode results published in (Menikoff R. , 2001).

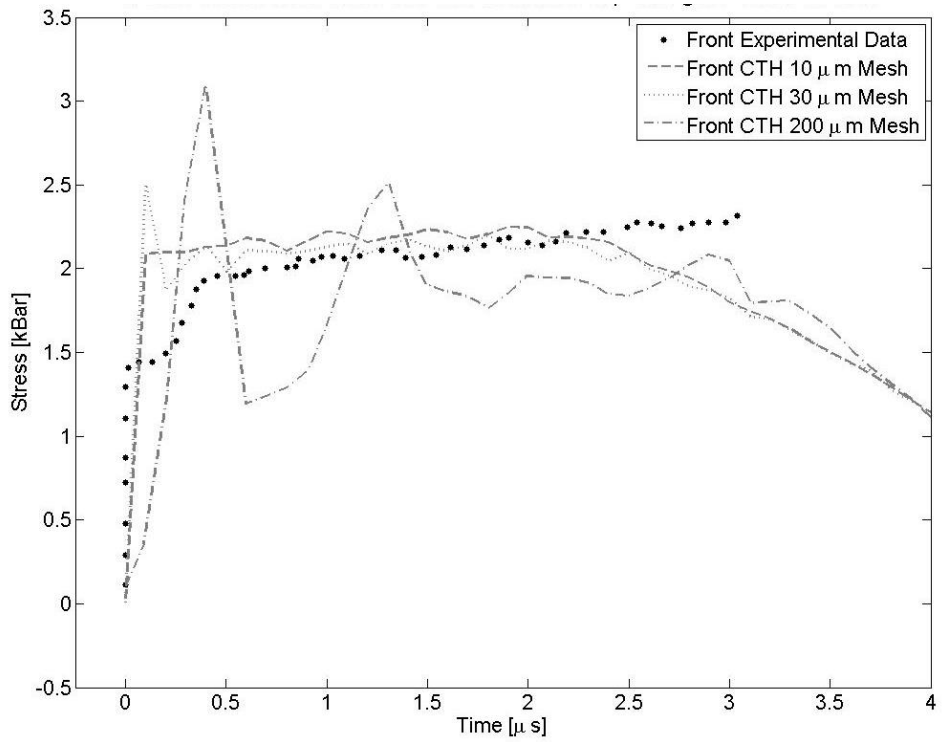

Figure 47: LANL Front Interface Stress Gas Gun Simulations at ρ = 1.24 g/cm3 and V = 279 m/s.

Validation *Approach 2* concerns the comparison of velocity versus time traces at the front Kel-F plate and back PMMA plate for the same CTH simulation scenario of fine grain HMX at a density of 1.24 g/cm^3 and a piston velocity of 279 m/s. As with

front plate input wave PDVF stress gauge data, magnetic particle velocity data at the Kel-F to granular HMX interface were only available for *Sheffield* Shot 912 configured with 1.24 g/cm^3 coarse grain HMX with a piston velocity of 285 m/s and a TPX back plate. Though it is appropriate to compare upstream input wave front plate profiles despite the differences in HMX coarse and fine grain samples, slightly higher input wave velocity profiles are expected due to the 2% higher piston velocity in available input wave front plate velocity data.

Figure 48 contains subplots of front and back plate velocity versus time profiles. CTH results have been shifted in time to facilitate comparison with experimental results. The left subplot contains front tracer data compared to experimental results from Shot 912. As in the input pressure wave profile comparison, CTH results on the 30 μm and 10 μm meshes compare quite well to digitized experimental data at early times and baseline mesh results yield an underestimation with large oscillations. A break away in data trends is evident again around 2.2 μs. Prior to this trend line break away, which is likely due to rarefaction wave impingement, CTH results on the two finer meshes are within 6% of experimental results from 0 to 2.2 μs. A portion of the CTH under-predicted velocities can be attributed to the 2% lower piston velocity in CTH. Velocity spikes at the wave front in the computational results were also observed in yield strength based porosity model hydrocode calculates in reference (Menikoff & Kober, 1999). *Menikoff and Kober* attribute this velocity spike to the "blow-off velocity at the free surface and is a consequence of the pores between grains." They further note that the velocity spike magnitude above piston velocity increases with increasing piston velocity.

Though the experimental data do not capture time from piston impact to arrival of the input wave at the Kel-F front plate to HMX interface, mesh dependent input wave arrival times were observed in CTH. These results are not visible in Matlab plotted results due to time shifting for consistency with experimental results. In all CTH simulations of 1.24 g/cm^3 fine grain HMX the piston is positioned one baseline mesh cell thickness of 0.02 cm from the Kel-F front plate with an initial velocity of 279 m/s. Thus, the piston impacts the front plate at 0.7 μs. An input wave then reaches the Kel-F to granular HMX interface at the following times in CTH: 2 μs on the 200 μm mesh, 2.7 μs on the 30 μm mesh and 2.8 μs on the 10 μm mesh. The sound speed of Kel-F published in (Menikoff R. , 2001) is 2,030 m/s. For a 0.48 cm thick front plate the corresponding calculated CTH wave speeds through Kel-F are: 3,692 m/s on the 200 μm mesh, 2,400 m/s on the 30 μm mesh, and 2,285 m/s on the 10 μm mesh. Some error may be attributed to the data write interval of 0.1 μs. However, these results serve to emphasize the importance of mesh size on result accuracy.

Once the input wave begins transmission through and compaction of granular HMX two separate waves propagate through the CTH simulated HMX sample. This phenomenon is consistent with the distinction of elastic and plastic compaction regimes in the P-α model. (Herrmann, 1969) The concept of a discontinuity propagating through a solid material at a speed less than the sound speed is explained in detail in (Power, Stewart, & Krier, 1989). *Powers et al* assert that subsonic or supersonic compaction waves can exist depending on piston impact velocity and a critical piston velocity threshold separates the two regimes. Subsonic compaction waves are "characterized by a smooth rise in pressure from ambient to a higher pressure equal to the static pore

collapse stress level" while supersonic compaction wave behavior is that of "a discontinuous shock leads a relaxation zone where the pressure adjusts to its equilibrium static pore collapse value." Subsonic compaction has been experimentally documented while supersonic compaction wave existence is purely theoretical. (Power, Stewart, & Krier, 1989) In the piston velocity range of interest for this study, approximately 280 m/s, subsonic compaction waves occur. The average compaction wave velocity is substantially lower than the bulk sound speed of HMX, 2,740 m/s [(Baer, Kipp, & van Swol, 1998), (Cooper, 1996)]. Note that the cited sound speed value is for solid matrix HMX crystals at a theoretical maximum density of 1.903 g/cm^3. Porosity in a granular energetic material is theoretically postulated to lower the bulk sound speed because the wave is transmitted through contacting grains and therefore has a longer path to travel in granular materials. (Menikoff & Kober, 1999)

Validation *Approaches 2* and *3* distinguish between the rise time (more generally the velocity versus time curve profile) and the arrival time of the transmitted plastic wave through the granular HMX as two separate validation criteria. This distinction has been made to differentiate between the finite rise time at a single geometric location characteristic of subsonic compaction waves and the arrival time of the wave. Shock velocity, U_s, changes as a compaction wave traverses a granular compact and thus obtaining an accurate arrival time represents accurate modeling of the average plastic compaction wave transmission throughout the thickness of granular HMX.

The right subplot in Figure 48 is a comparison of empirical magnetic particle velocity gauge data for a 1.24 g/cm^3 fine grain HMX experimental configuration with

piston impact velocity of 279 m/s and a PMMA back plate. CTH simulation input conditions for the three uniform mesh variations replicate the known experimental conditions. Approximately 50 CTH Lagrangian tracer values spaced 0.01 cm apart linearly and positioned one baseline coarse mesh cell distance from the interface boundary are utilized to capture data adjacent to the HMX to PMMA back plate interface. A smooth transition and 0.1 μs rise time is observed in the experimental data. (Sheffield, Gustavsen, & Anderson, 1997) CTH results on both the 10 μm and 30 μm meshes contain a slope change 0.1 μs into the wave arrival. Measuring the rise time from only the single sharp slope region the calculated rise times are 0.4 μs for the 30 μm mesh and 0.2 μs for the 10 μm mesh. These results are indicative of the need for very fine mesh spacing to accurately resolve inert porous granular energetic material behavior. Back plate velocity values at the peak of the arrival wave are within +5% on the 10 μm mesh and -2% on the 30 μm mesh. The baseline 200 μm mesh results completely diffuse the arrival wave profile, with a rise time of approximately 2 μs, and underestimate the back plate interface velocity by nearly 50%.

In validation *Approach 3* the transmitted wave arrival times are of primary focus. As previously stated, good comparison between arrival times implies that compaction behavior throughout the granular sample has been accurately approximated due to the degradation of shock velocity as a function of penetration distance into the granular compact. Transmitted wave arrival occurs at 5.12 microseconds in the digitized experimental data. Comparing the start of upward velocity trend in the right subplot CTH results of Figure 48 the 30 μm mesh has an arrival time of 4.8 μs, within 6% of experiment, and the 10 μm mesh calculates an arrival time of 4.9 μs, within 4%

of empirical data. While the rise time in the baseline mesh is highly diffuse, near the center of the waveform does overlap with experimental data.

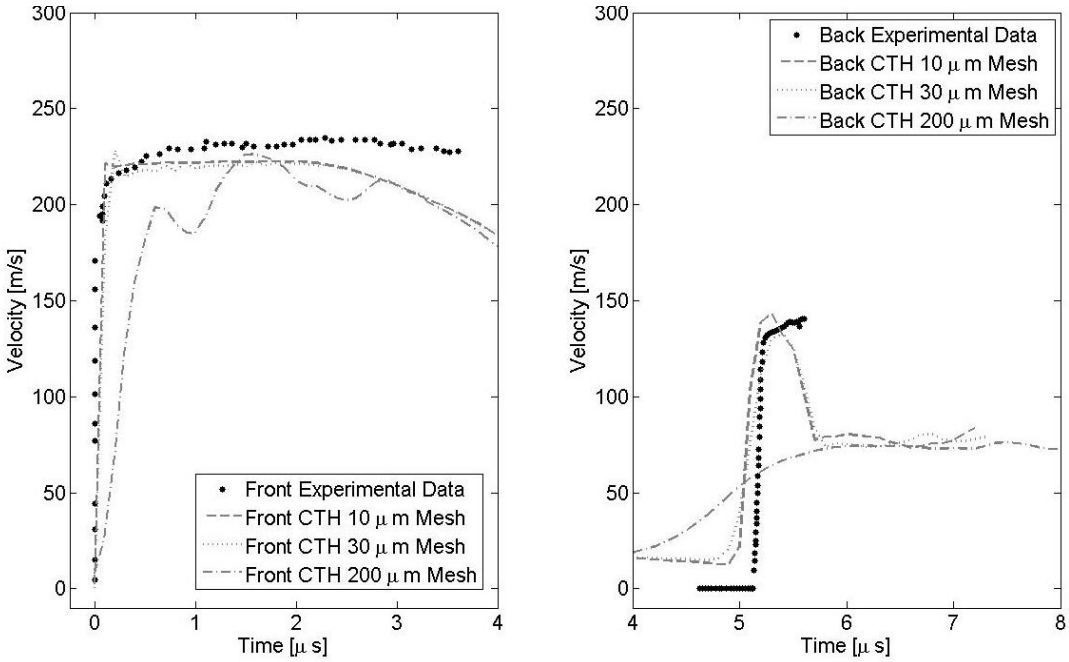

Figure 48: LANL Velocity Magnitude in Gas Gun Simulations with Fine HMX ρ = 1.24 g/cm^3 and V = 279 m/s.

Validation *Approach 4* is a comparison of published HMX longitudinal sound speed to the elastic precursor wave speed calculated in CTH. The elastic wave speed is calculated at the same tracer locations as the back plate velocity profiles to avoid impedance matching issues with adjacent plate. For a granular HMX sample thickness of 0.39 cm, the elastic precursor arrival times in CTH are as follows: 1.2 μs on the 200 μm mesh, and 1.4 μs on the 30 μm and 10 μm meshes. These transmission times correspond to shock velocities of 3,250 m/s and 2,785 m/s, respectively. For the previously cited longitudinal sound speed value of 2,740 m/s for crystalline HMX,

calculation errors of 19% and 2%, respectively, are obtained. These results further validate the excellent agreement between CTH and the p-α porosity model at higher mesh densities. Lower sound speeds theorized to exist for granular energetic materials are not observed due to simplifying assumptions inherent in the P-α porosity model.

The final validation point, *Approach 5*, is a comparison of analytical final compaction density calculations as well as additional experimental results to CTH results at the center thickness of the HMX sample. A plot of density versus time of an Eulerian fixed tracer particle positioned at the granular HMX center is provided in Figure 49. Final compaction density can be derived from Hugoniot jump conditions for pressure and density as a function of shock and particle velocity, as detailed in Reference (Sandusky & Liddiard, 1985). The resultant non-dimensional equation is given below in Equation [30]. In this equation, φ is the percent density ratio equal to 100*(density/TMD). Subscript 0 denotes initial granular material state and subscript h denotes the Hugoniot jump condition state. TMD is assumed to be the previously cited HMX crystal density of 1.903 g/cm^3. Shock velocity, U_s, changes as a function of time and position in the granular material during compaction. The particle velocity, u_p, levels off to a steady-state value following attenuation of the input shock from transmission through the front plate.

$$\varphi_h = \frac{\varphi_o \cdot U_s}{U_s - u_p} \qquad [30]$$

In the present calculation shock velocity is calculated via the arrival time of the plastic compaction wave at the granular HMX center thickness, 0.39 cm / 2 = 0.195 cm. For an arrival time of 2.5 μs, the corresponding shock velocity is 780 m/s. Particle

velocity is initially equal to the piston velocity of 279 m/s and decreases as the compaction wave traverses the granular material. Particle velocity at the HMX sample center is measured from a Lagrangian tracer and equal to 220 m/s. This particle velocity compares well with the steady state experimental front plate velocity oscillations in the range of 230-235 m/s in the right subplot of Figure 48. Further particle velocity degradation is expected by the time the plastic compaction wave reaches the granular HMX center. With the known values of initial density as well as shock and particle velocity, the corresponding final compaction density is calculated via Equation [30] as 1.73 g/cm^3, 91% TMD, and plotted on Figure 49 to facilitate comparison to CTH results. Excellent agreement, within 1%, is achieved between the Hugoniot theoretical compaction density and CTH results on finer meshes.

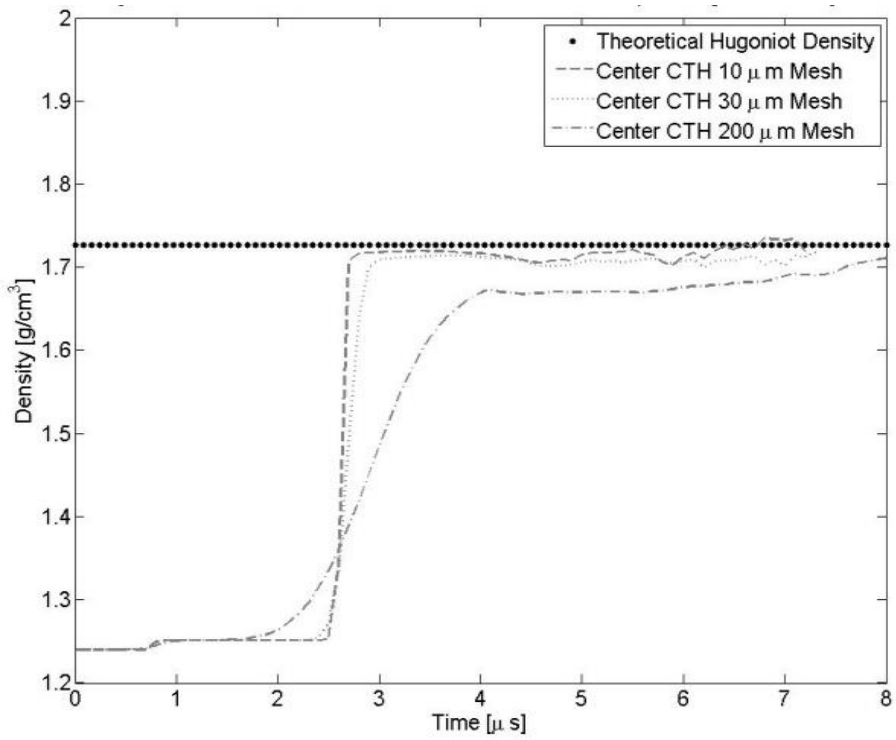

Figure 49: Geometric Center HMX Density vs Time of LANL Gas Gun Simulation at $\rho = 1.24 g/cm^3$

A brief literature review was also conducted to determine if supporting experimental results intended to measure final compaction density have been published. According to (Sandusky & Liddiard, 1985), there are four different experimental techniques to test dynamic compaction of granular energetic material. These four experimental methods include: gas driven, piston driven, ramp loaded, and shock driven compaction experiments. Results with the ramp loaded technique are reported in (Elban & Chiarito, 1986) for 64.6% TMD, or 1.23 g/cm^3. Ramp loaded experimental results are reported in the final compaction range of 86.5% - 97.3% TMD for 64% HMX at maximum stresses in the range of 18.7 to 227 MPa, or 0.187 to 2.27

kBar. Variations in results as compared to the present gas driven compaction mechanism are expected given the differences in experimental approach.

Results 2: LANL Gas Gun at 1.40 g/cm³

In order to extend the results of the porosity analysis beyond the aforementioned 1.24 g/cm^3 results, the author conducted iterative simulations to replicate experimental results at 1.4 g/cm^3 as the NSWC test case HMX density is between 1.24-1.4 g/cm^3 at 1.322 g/cm^3. Figure 50 contains time sequences of pressure, left column, and density, right column, contour plots for a simulated LANL gas gun experiment with granular HMX density of 1.4 g/cm^3, 74% TMD, a piston velocity of 270 m/s, and PMMA back plate run on the finest mesh spacing of 10 μm. As in the previous simulation with granular HMX at 1.24 g/cm^3, the planar wave reaches the beginning of the HMX sample at 2.8 μs and impact imparts a plastic compaction planar wave of approximately 2.3 kBar into the granular HMX. The planar compaction wave is led by an elastic precursor compaction wave traveling at approximately the sound speed of granular HMX. Plastic compaction wave pressure and velocity decrease as a function of time as the compaction wave travels through the granular energetic material sample. Final granular HMX densification is again slightly below TMD in keeping with Hugoniot theoretical estimations.

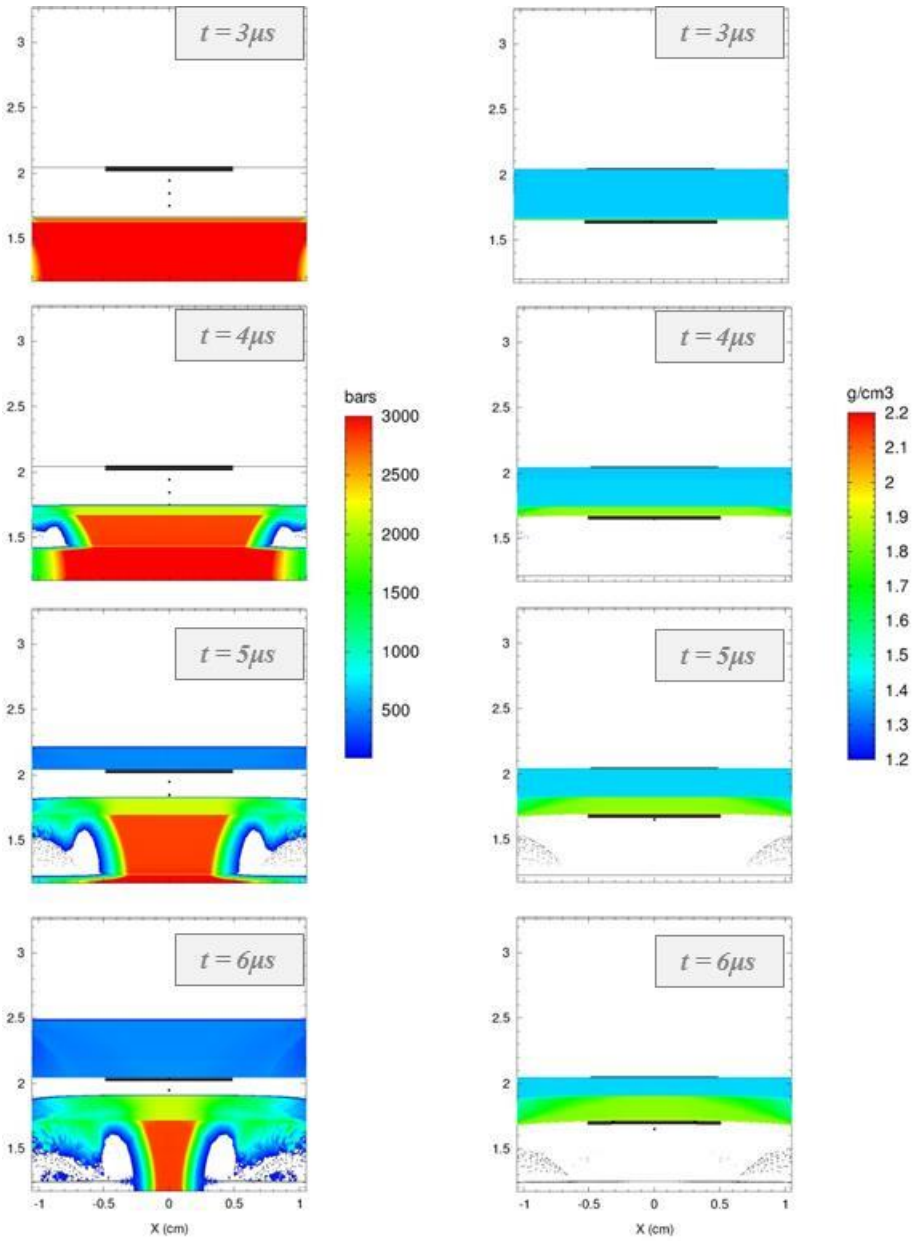

Figure 50: LANL Gas Gun Simulation Density and Pressure Contours at Density = 1.40 g/cm^3

The subsequent discussion will briefly review the five validation approaches as applied to the 1.4 g/cm^3 granular HMX CTH simulation results. Regarding validation *Approach 1*, to compare the *Sheffield* experimental PDVF gauge stress data at the Kel-F front plate to CTH Lagrangian tracer values near the interface boundary, *Sheffield*

did not publish input pressure results with 1.4 g/cm^3 HMX samples. Figure 51 contains a plot of CTH results for front plate input wave pressure versus time post-processed in Matlab for relative comparison. Again, the CTH results have been shifted in time and time zero occurs when the input wave reaches the Lagrangian tracers of interest.

CTH results on the 30 μm and 10 μm meshes follow approximately the same trend indicating mesh independence in results. CTH results from the baseline 200 μm mesh contain large pressure fluctuations across the averaged tracer values further supporting the need for finer mesh spacing observed in previous porosity validation simulation results. Minor pressure fluctuations are present in the 30 μm mesh results and are not readily observed in the 10 μm mesh front plate pressure trace. Impingement of rarefaction waves and sample edge effects are postulated to cause drop in the pressure versus time contours after 2.2 μs.

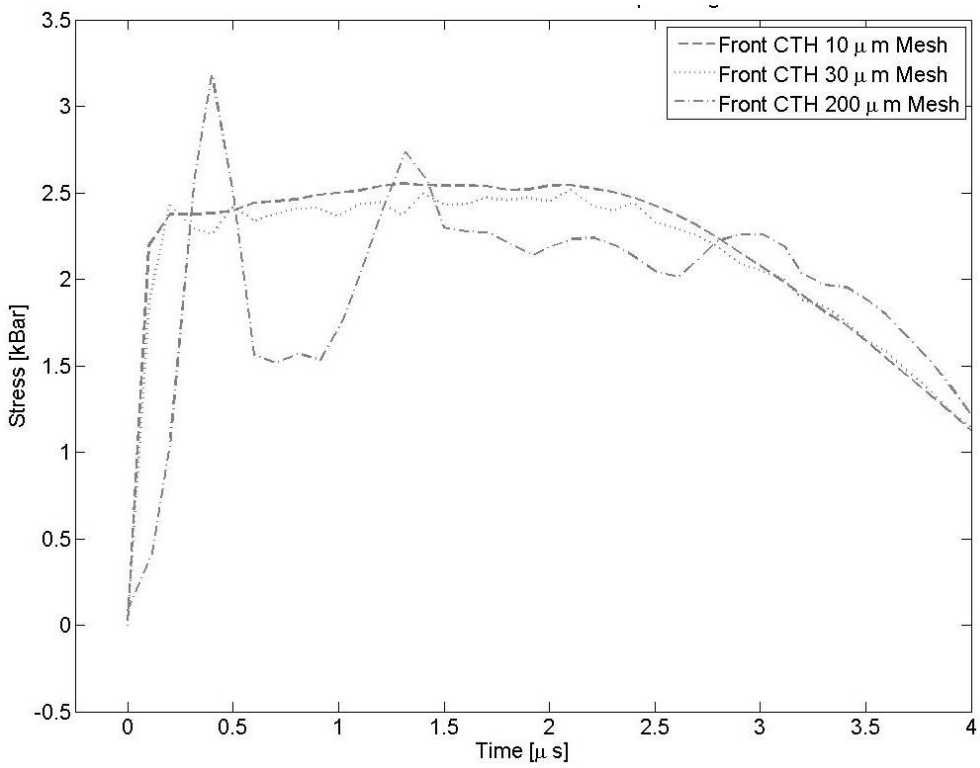

Figure 51: LANL Front Interface Stress Gas Gun Simulations at $\rho = 1.40$ g/cm^3 and V = 270 m/s.

Front plate magnetic particle velocity data for the first part of validation *Approach 2*, comparison of velocity versus time traces at the front Kel-F plate, were not published in (Sheffield, Gustavsen, & Anderson, 1997). Consequently, the front plate velocity traces in the left subplot of Figure 52 are included only for comparison purposes. As expected, input velocity wave profiles are attenuated from the initial piston impact velocity of 270 m/s as the input wave transmits through the Kel-F front plate and decrease to a particle velocity closer to 205 m/s. A small blow-off velocity spike is present at the crest of the input waveform.

Experimental data is available for the second portion of validation *Approach 2*, comparison of back plate velocity versus time profiles, and is included in the right subplot in Figure 52. CTH simulations were modeled to replicate the LANL gas gun experiment configured with granular HMX at a density of 1.4 g/cm^3, a piston velocity of 270 m/s, and PMMA back plate. Approximately 50 CTH Lagrangian tracer values spaced 0.01 cm apart linearly and positioned one baseline coarse mesh cell distance from the interface boundary are utilized to capture data adjacent to the HMX to PMMA back plate interface. As in the past scenario, a 0.1 μs rise time is observed in the experimental data. (Sheffield, Gustavsen, & Anderson, 1997) CTH results on the 30 μm meshes contain a slope change 0.1 μs into the wave arrival. This slope change is minimal in results run on the 10 μm mesh. For consistency, measuring the rise time from only the single sharp slope region the calculated rise times are 0.3 μs for the 30 μm mesh and 0.2 μs for the 10 μm mesh, further supporting the need for very fine mesh spacing to accurately resolve inert porous granular energetic material behavior. Back plate velocity values at the peak of the arrival wave are within +7% on the 10 μm mesh and +5% on the 30 μm mesh. Baseline 200 μm mesh results completely diffuse the arrival wave profile, with a rise time of over 1 μs, and under estimate the back plate interface velocity by 35%.

Validation *Approach 3* compares hydrocode calculated transmitted wave arrival times to empirical results to assess global compaction behavior throughout the granular HMX. Transmitted wave arrival occurs at 4.7 microseconds in the digitized experimental data. The shorter transmission time in results with HMX at 1.4 g/cm^3 compared to results at 1.24 g/cm^3 is to be expected given that HMX has a higher sound

speed than the void region. Comparing the start of upward velocity trend in the right subplot CTH results of Figure 52 the 30 μm mesh has an arrival time of 4.5 μs, within 4% of experiment, and the 10 μm mesh calculates an arrival time of 4.6 μs, within 2% of empirical data. As in the previous simulations, diffuse baseline mesh results overlap with experimental data near the waveform center. Based on the presented arrival time results comparison, the author concludes that CTH is capable of accurately modeling global behavior of shock velocity degradation as a function of penetration distance into the granular compaction region.

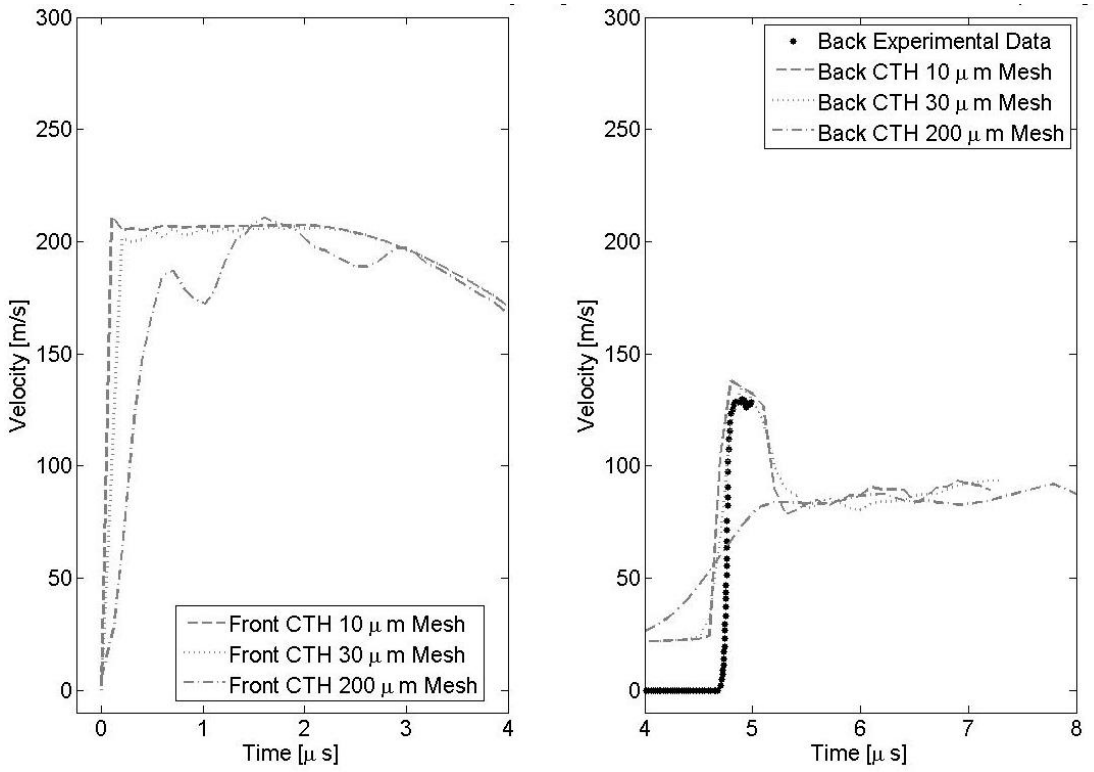

Figure 52: LANL Velocity Magnitude in Gas Gun Simulations with Fine HMX ρ = 1.40 g/cm3 and V = 270 m/s.

Validation *Approach 4* compares published HMX longitudinal sound speed to the elastic precursor wave speed calculated in CTH at the same tracer locations as the back plate velocity profiles. For a granular HMX sample thickness of 0.39 cm, the elastic precursor arrival times in CTH are 1.2 μs on the 200 μm mesh, and 1.4 μs on the 30 μm and 10 μm meshes corresponding to shock velocities of 3,250 m/s and 2,785 m/s, respectively. The reported shock velocities correspond to 19% and 2% error, respectively, when compared to the sound speed of crystalline HMX. These results are identical to the results obtained for 1.24 g/cm^3 granular HMX simulations, thereby implying that the elastic precursor wave is transmitted at the solid material sound speed regardless of porosity (within the porosity range analyzed).

Validation *Approach 5* compares analytical final compaction density calculations as well as additional experimental results to CTH results at the center thickness of the HMX sample. A plot of density versus time of an Eulerian fixed tracer particle positioned at the granular HMX center is provided in Figure 53. Equation [30] is utilized to calculate the Hugoniot state final compaction density at the granular HMX center thickness, 0.39 cm/2 = 0.195 cm, as a function of the known plastic compaction wave arrival time and steady state particle velocity obtained from Lagrangian tracer data. For an arrival time of 2.0 μs, the corresponding shock velocity is 848 m/s. Particle velocity is initially equal to the piston velocity of 270 m/s and decreases as the compaction wave traverses the granular material. Particle velocity at the HMX sample center is 205 m/s. With these values the corresponding final compaction density is calculated as 1.85 g/cm^3, 97% TMD, and plotted in Figure 53 to facilitate comparison

to CTH results. As in the previous simulations, CTH simulation results are within 1% of the Hugoniot theoretical compaction density.

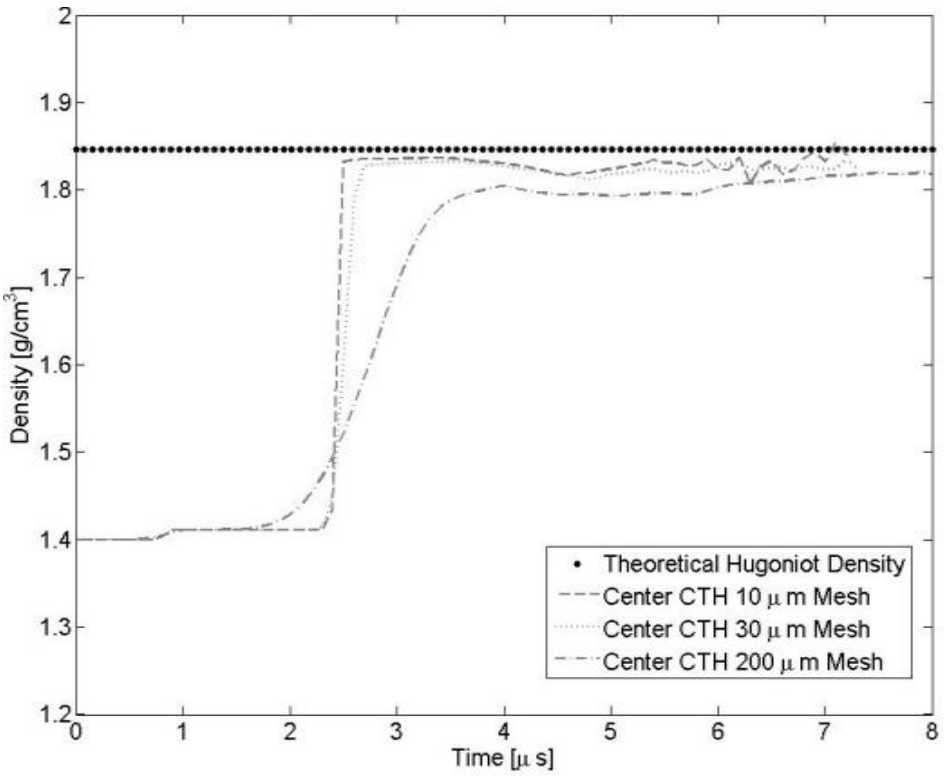

Figure 53: Geometric Center HMX Density vs Time of LANL Gas Gun Simulation at Density = 1.40 g/cm^3

Experimental results with the piston driven technique are reported in (Sandusky & Bernecker, 1985) for 73%, 1.39 g/cm^3, Class D coarse HMX with an average particle size of 870 μm. At a piston velocity of 267 m/s (Sandusky & Bernecker, 1985) report final compaction density as 92.1% TMD corresponding to a particle velocity of 161 m/s and a shock velocity of 775 m/s. While the experimental input conditions are similar to the LANL gas gun and therefore CTH setup conditions, variations in final

compaction density are expected due to the nearly two orders of magnitude difference in mean particle size, 10-15 μm versus 870 μm.

Porosity Conclusions

Based on results presented for the five pronged validation approach, the following statements can be made regarding CTH modeling of granular HMX in the density range of 1.24-1.4 g/cm^3 via the P-α porosity model. These results are summarized in Table 11.

- Baseline 200 μm mesh results are subject to large error, calculation fluctuations, and diffusion issues on the overly coarse mesh. Consequently, summarized results comparison percentages are only provided relative to the 30 μm and 10 μm mesh simulations.
- Iterative analysis, in increments of 10 μm, determined that 30 μm is the largest mesh spacing to obtain good agreement with experimental results and analytical predictions. Results on the 30 μm and 10 μm meshes compare well both qualitatively and quantitatively.
- CTH calculates front plate stress within approximately 10% and front plate velocity within 6% of experiment for results at one density.
- Back plate velocity is predicted within 7% of experiment for results at two different HMX densities.
- Plastic compaction wave arrival time at the back plate is predicted within 6% of experiment for results at two different HMX densities.

- Elastic precursor wave speed is calculated in CTH within 2% of the published crystalline HMX longitudinal sound speed for results at two different HMX densities.
- CTH final compaction density is within 1% of analytically Hugoniot final compaction calculations for results at two different HMX densities.

Table 11: Comparison and Relative Error of Validation Approaches

Validation Approaches	$\rho = 1.24$ g/cm^3	*Error*	$\rho = 1.4$ g/cm^3	*Error*
1. Front Plate Stress, crest of empirical dip at t=0.39 μs	2.1 kBar	11%	N/A	N/A
2a. Front Plate Velocity Profiles, t=0-2.2 μs	Multiple Data Points	-6%	N/A	N/A
2b. Back Plate Velocity Rise Times	0.2 μs	100%†	0.2 μs	100%†
3. Shock Wave Arrival Time at Back Plate	4.9 μs	-4%	4.6 μs	-2%
4. Elastic Sound Speed	2,785 m/s	2%	2,785 m/s	2%
5. Final Compaction Density (Empirical calculation)	1.71 g/cm^3, 90% TMD	-1%	1.83 g/cm^3, 96% TMD	-1%

† The 100% relative error is indicative of the simulation data-write interval of 0.1 μs, thus the CTH rise times are not resolved on a sufficiently fine interval. This is an area for future refinement.

Extension of Porosity Model to DDT Tubes

Due to the determination that the 200 μm mesh was unable to approximate experimental gas gun porosity results, the author re-meshed the NSWC and LANL DDT tube representative test case CTH input decks for acceptable porosity thresholds, updated P-α porosity parameters, and re-ran the simulations. The NSWC simulation is more likely to rapidly initiate via DDT based on the use of the History Variable Reactive Burn EOS (Arrhenius EOS results were incorrect) and $BKNO_3$ high amplitude

pyrogenic initiation mechanism. The LANL DDT test tube simulation was run again because porosity model validation study results indicate that low amplitude piston driven impact initiation mechanisms require very fine mesh resolution. Results from the LANL DDT tube simulations will enable further consideration of that conclusion.

In the chapter entitled RESEARCH GAP IDENTIFICATION, the finest mesh spacing was utilize in the non-uniform mesh simulations with HVRB EOS and forced reaction with an augmented initiation mechanism as well as the Arrhenius EOS simulations. The finest mesh utilized to analyze the representative test case is a uniform spacing of 0.05 cm (500 μm). Very fine 30 μm mesh spacing necessitated a non-uniform mesh. Even with a non-uniform mesh, if only the column of granular HMX were modeled at 30 μm and the remaining 3-dimensional quarter symmetry computational domain at a coarse setting of 0.2 cm (2,000 μm) the total mesh cell count would still number in the billions of cells, making this problem prohibitively large for the available computational resources. Consequently, only the first two centimeters of the granular HMX column were modeled at a mesh resolution of 30 μm and then the mesh was tapered, over a distance of 1 cm, to a 0.2 cm uniform mesh for the remainder of the computational domain. With this mesh scheme the NSWC representative test case mesh increased from nearly 11 million to 90 million cells and LANL mesh from 4 million to 50 million cells. Run time correspondingly increased from 246 CPU hours to over 3,000 CPU hours.

From the time sequence contour plots of density included in Figure 26 for the representative NSWC initiation mechanism CTH simulation of inert HMX it is evident that compaction occurs within and beyond the first centimeter of granular HMX. The

inert Mie-Gruneisen EOS results are approximately equivalent to the HVRB composite EOS because the HMX extent of reaction in Table 10 is 0.0366 (maximum) at 0.1cm indicating minimal reactivity such that the unreacted HVRB EOS portion, the Mie-Gruneisen EOS, dominates. In this figure three Eulerian tracers, indicated by black dots, are clustered directly above the piston at depths of 0.1, 0.5 and 1 centimeter within the granular HMX. In Figure 54, density versus time at these three Eulerian tracer positions are compared. Plotted results include the 500 μm uniform mesh representative test case HVRB results discussed in the chapter entitled RESEARCH GAP IDENTIFICATION as well as the re-meshed and updated P-α parameters non-uniform mesh solution based on aforementioned porosity mesh threshold findings.

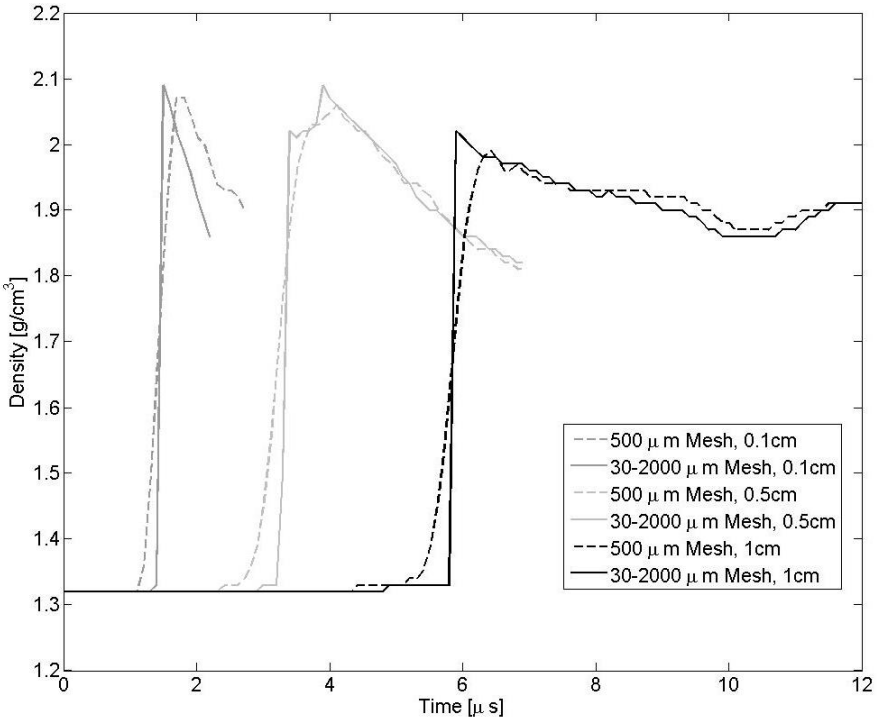

Figure 54: NSWC DDT Tube: Density Comparison with Updated P-α Parameters and Finer Mesh.

Despite the significant differences observed in the LANL gas gun P-α porosity parameter tuning study, the results in Figure 54 show that NSWC DDT tube simulations are quite similar for HMX with P-α porosity on a 500 μm mesh and a 30 μm mesh in the region near $BKNO_3$ initiation. Density versus time traces from Eulerian fixed tracers imbedded at 0.1 cm, 0.5 cm, and 1 cm within the granular HMX column near the initiator pellet show qualitatively similar trends. The author postulates that this markedly different behavior is due to fundamental differences in initiation mechanisms in the LANL gas gun experiments and NSWC DDT tube experiments. LANL gas gun trials of interest were conducted with flyer velocities in the range of 270-288 m/s, which imparted a planar pressure wave of approximately 2.3 kBar into the Kel-F front plate. However, NSWC DDT tube experiments employ a pyrogenic $BKNO_3$ ignitor pellet which imparts a pressure wave of approximately 27-29 kBar directly into the granular HMX (as measured from tracer particles at 0.1 cm depth in HMX). This order of magnitude increase in peak pressure wave input serves to diminish the mesh dependence of the P-α porosity model within the Mie-Gruneisen EOS.

In keeping with the aforementioned P-α study, results from the NSWC DDT tube CTH simulation coarser mesh have a longer rise time than the sharper peaks observed with a very fine mesh. Density specific only to the HMX material is plotted in the above figure for fixed tracers. Thus, the density data points at 0.1 cm and 0.5 cm end prior to the plotted timeline because $BKNO_3$ products eventually expand to entirely occupy the cells associated with the Eulerian tracers. Contamination of $BKNO_3$ products is also the reason that the peak density at each of the three tracer locations initially exceeds the theoretical maximum density of HMX. Applying Equation 30 to

calculate the Hugoniot based final compaction density, in a similar manner to the previous methodology, yields a predicted final compaction density of 98%. This compaction percentage corresponds to a shock arrival time of 5.8 μs at an Eulerian fixed tracer positioned at 1 cm depth in HMX, which translates to a shock velocity of 1724 m/s, as well as a particle velocity of 501 m/s obtained from a Lagrangian tracer at the same depth. In Figure 54 it is evident that at 1 cm HMX reaches a steady state compaction of 1.9 g/cm^3, 100% TMD. The error between Hugoniot based analytical final compaction density and CTH calculation is 2%, which compares well to the 1% error observed in LANL gas gun P-α porosity validation simulations.

LANL DDT tube experiments are conducted with a thick piston traveling at 100 m/s which imparts an approximately 0.6 kBar low amplitude pressure wave into the granular HMX, as measured at an Eulerian tracer positioned 0.5cm above the piston impact/HMX boundary in the 30 μm mesh. From the time sequence contour plots of density included in Figure 28 for the representative LANL initiation mechanism CTH simulation of inert HMX it is evident that compaction occurs primarily within the first half centimeter of HMX. For this reason the representative HVRB EOS test simulation was re-run with Eulerian tracers added at distances of 0.1, 0.2, 0.3 and 0.4 centimeters within the granular HMX boundary. As with the NSWC simulations, inert Mie-Gruneisen EOS results are approximately equivalent to the HVRB composite EOS because the HMX extent of reaction in Table 10 is zero at 0.1cm. Density versus time at Eulerian tracers positioned 0.1, 0.3 and 0.5 centimeters into HMX are compared in the figure below. Results are presented for both the 500 μm uniform mesh representative test case HVRB results discussed in the chapter entitled RESEARCH

GAP IDENTIFICATION as well as the re-meshed and updated P-α parameters non-uniform mesh solution.

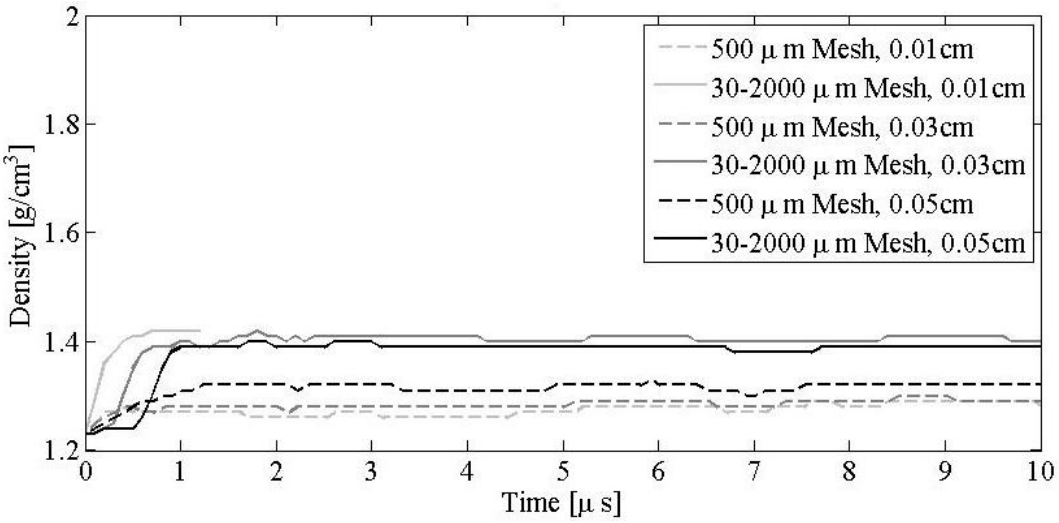

Figure 55: LANL DDT Tube: Density in Granular HMX Column

As theorized in the LANL gas gun experiment compaction validation parameter study, Figure 55 further supports the existence of very fine mesh dependence on low amplitude pressure pulse initiation mechanisms. The LANL DDT tube test configuration 100 m/s piston imparts a pressure of 0.6 kBar into the 1.2285 g/cm^3, 65% TMD, granular HMX whereas the P-α model validation gas gun experiments were performed with 1.24 g/cm^3 granular HMX with a 2.3 kBar pressure wave imparted by a 270-288 m/s piston impact event. Given that the low amplitude pressure pulse in the LANL DDT tube experiments is approximately 25% of the P-α parameter validation simulations, even more substantial mesh dependence is anticipated.

Density specific only to the HMX material is plotted in the above figure for fixed tracers. Thus, the density data points at 0.01 cm on the 30 μm mesh end prior to

the plotted timeline because the piston eventually travels upward to occupy the computational cells associated with the Eulerian tracers. The presence of the trend line of the 0.01cm tracer in the 500 μm mesh throughout the 10 μs duration implies piston position calculation differences. Furthermore, tracers in the 30 μm mesh simulation are shifted upward relative to the 500 μm mesh results. Steady state final compaction density from the 500 μm mesh occurs in the range of 1.28-1.32 g/cm^3. Results from the 30 μm non-uniform mesh indicate final compaction densities in the range of 1.39-1.41 g/cm^3. It was not possible to calculate a theoretical prediction of final compaction density for the LANL DDT tube scenario as the particle velocities within the 0.5 cm region of interest did not level off to a steady state value due to continued piston impingement in a confined region within the 10 microsecond simulation timescale. However, it is evident that the coarser mesh under-predicts localized compaction. Lower density granular HMX directly translates to a diminished likelihood of accurate deflagration or detonation initiation due to hotspot void collapse or closure.

A possible reason for the significant mesh dependence in the low pressure impact regime within the hydrocode CTH can be attributed to its inherent design as a shock propagation code. CTH is designed to model transmission of high velocity and high pressure phenomenon. The code does this in part by enforcing the Courant stability limits at the end of each iteration to control timesteps. One criteria is that material is not allowed to traverse more than one cell distance in a single timestep. Thus, finer meshes correspondingly result in smaller timesteps. However, when too coarse of a mesh is used in a relatively low velocity scenario, too many changes occur within the materials within a single cell over several timesteps and these changes are

not adequately tracked as CTH was designed for materials to move nearly every timestep. Consequently, finer meshes are much more accurate in resolving low velocity and pressure phenomena.

The author concludes that it is appropriate to use a relatively "coarse" mesh spacing of 500 μm for high amplitude initiation mechanisms imparting peak wave pressures on the order of tens of kBar into granular HMX. Conversely, for low amplitude initiation mechanisms, such as piston driven configurations, imparting pressures on the order 2.3 kBar or less requires a "very fine" mesh spacing of 10-30 μm to obtain experimentally representative results.

The determination of P-α parameters presented herein for granular HMX enable modeling of porosity in Eulerian hydrocodes via the P-α model. Porosity is a vital component of modeling precursory hotspots caused by hydrodynamic collapse of void regions and grain interactions. Formation of hot spots can lead to DDT of confined granular explosives, though experimental characterization of this phenomenon is currently limited. With the evolution of existing experimental techniques in conjunction with new emerging technologies, such as in-situ fiber Bragg grating sensors, a more complete data set will exist for validation of increasingly robust DDT computational models. Porosity models will therefore be of prime importance when coupled with enhanced hot spot models and deflagration EOS to predict the onset of DDT in explosives.

Analytics of Deflagration Model

With modeling of inert granular HMX resolved via the addition of a validated P-α porosity parameter set, the focus of the remainder of this dissertation will shift to

formulating and applying a hydrocode modeling methodology to addressing deflagration of HMX. Prior to delving into the addition of an explosive material deflagration model in CTH, a brief overview of HMX crystal phase transitions as well as the analytics of deflagration is included to clarify the pertinent physics. A detailed review of experimental deflagration studies on HMX is included in APPENDIX A in the subsection entitled DEFLAGRATION OF HIGH EXPLOSIVES. Analytical verification of burn rate data for the aforementioned NSWC and LANL DDT tube test cases is included in CHAPTER 3.

Granular HMX has four known crystal polymorph forms, listed in order of insensitive to sensitive: β, α, γ, and δ, (Saw, 2002). The sensitivity extreme forms, δ and β HMX, are the most well documented polymorph forms in the literature. Granular explosive material sensitivity and phase transition thresholds are grain size dependent. Large HMX grains are more sensitive than finer HMX grain size samples. *Saw* indicates that β to δ HMX phase transition occurs in the range of 160-170°C (433-443 K) for "coarse" 100 μm maximum grain size HMX and 170-190°C (443-463 K) for "fine" 3 μm grain size HMX. Additionally, a 7-8% increase in volume is observed in the phase transition from β to δ HMX resulting in a shift in crystalline density from 1.91 g/cm^3 for β HMX to 1.76 g/cm^3 for δ HMX. (Saw, 2002) Additional data on specific breakdown mechanisms for δ HMX are included in Reference (Berg & Dlott, 2014). Reference (Sewell & Menikoff, 2003) contains a thorough study of elastic properties pertaining to β, α, and δ HMX polymorphs.

As shock waves travel through granular energetic material, compaction of the inherent voids generates local temperature increases, known as hot spots. These hot

spots are of interest as they increase the sensitivity of the energetic material and may cause detonation - intentional or otherwise - at temperatures lower than deflagration thresholds. Reference (Walley, Field, & Greenaway, 2006) contains an excellent historical review of hot spot theories citing nearly two hundred sources in the literature. In this review article, *Walley* notes that there are two leading theoretical hot spot formation mechanisms: "adiabatic asymmetric collapse of gas spaces producing gas heating, jetting, and viscoplastic work" as well as "rubbing together of surfaces as in friction or adiabatic shear."

Granular HMX sensitivity increases with increasing grain size. Larger grain sizes imply larger void regions, also referred to as pores, between particles. Particle defects, such as open pores on a crystal surface, also contribute to sensitivity. Figure 2 contains an inverted microscope image of granular HMX demonstrating voids between grains. Figure 56 below from Reference (Bourne & Milne, 2004) contains an image of RDX grains with open pores visible as dark circles on the crystal surfaces. In this image the crystals are bound in a polymer binder which fills spaces between grains. *Walley* notes that the generally accepted minimum hot spot size is 5 μm. Table 12 below lists critical reaction threshold temperature as a function of hot spot radius. Given the minimum hot spot size and the general length scales listed in the table below, it is evident that hot spots are a mesoscale phenomenon.

Table 12: HMX Critical Hot Spot Temperature as a Function of Hot Spot Radius. (Walley, Field, & Greenaway, 2006)

Hot Spot Radius	Temperature
10^{-3} cm (10 μm)	405 °C (678 K)
10^{-4} cm (1 μm)	500 °C (773 K)
10^{-5} cm (0.1 μm)	625 °C (898 K)
10^{-6} cm (0.01 μm)	805 °C (1,078 K)

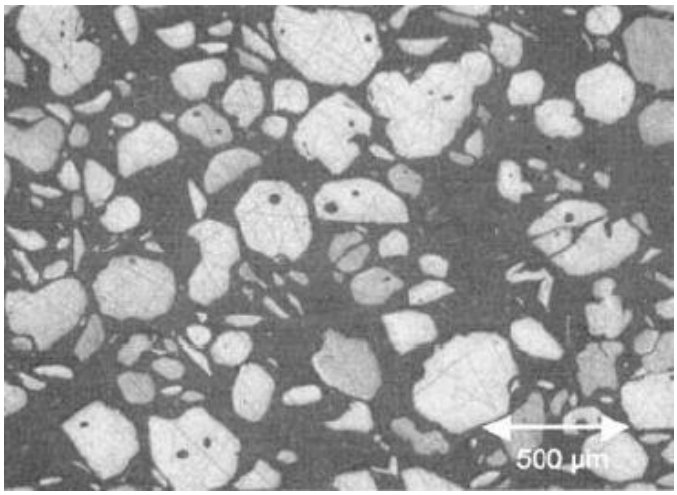

Figure 56: Open Pores on RDX Crystal Surfaces (Bourne & Milne, 2004)

The author is only aware of one hydrocode, ALE3D, with existing macroscale treatment of hot spots. Details of the ALE3D probabilistic hot spot model formulation are included in Reference (Nichols, et al., 2005). Modeling of hot spots in CTH is therefore beyond the scope of the present work, and any single PhD, and will not be considered within the subsequent deflagration study. However, data in Table 12 are

important for identifying temperatures at which hot spot reactivity can contribute to reaction initiation in experimental deflagration studies. Another useful reference that will be referred to in subsequent deflagration modeling efforts is the compilation plot of ignition time versus temperature for various experimental configurations included in Figure 57, originally from Reference (Henson, Asay, Smilowitz, & Dickson, 2001). This plot includes data compiled across the time range of hours to nanoseconds and the temperature range of approximately 450 - 2,500 K from the following types of experiments: thermal explosion, fast pyrolysis, laser ignition studies, frictional heating studies, and detonation experiments. Results in the upper right corner correspond to cook-off type events. Data in the lower left corner indicate detonation events. The primary points of interest for deflagration are the two black circles in the lower center in the millisecond time range, corresponding to deflagration reactions.

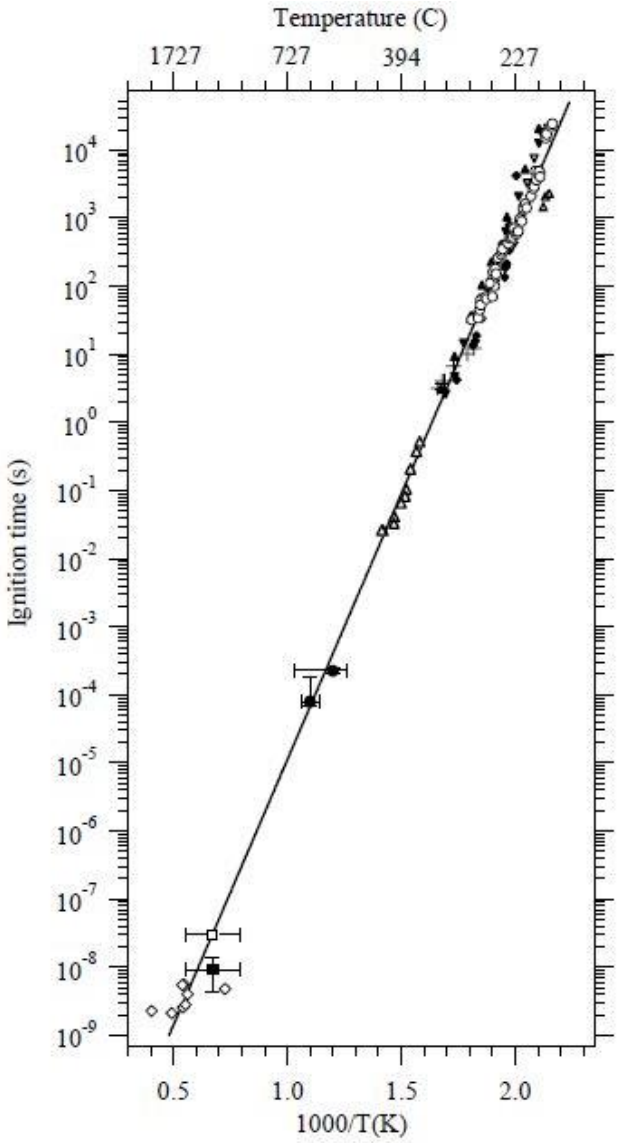

Figure 57: Experimental HMX Ignition Time versus Reaction Temperature (Henson, Asay, Smilowitz, & Dickson, 2001)

Within the limitations of CTH as an Eulerian hydrocode reliant on primarily pressure dependent EOS, it is possible to formulate a deflagration model expressly for explosive material deflagration in terms of pressure. As mentioned in CHAPTER 3 the burn rate for HMX is identical to the equation primarily used in solid rocket propellant,

Eqn. [16] (repeated below for clarity), which is a function of operating pressure and the empirical "a" and "n" values (repeating Table 3 for clarity).

$$\dot{r} = ap^n \qquad [16]$$

Table 3: HMX Combustion Indices for a Range of Pressures

Source	Pressure (MPa)	Combustion Index "n"
Sinditskii, et al	0.2 - 10	0.77-0.82
Sinditskii, et al	10 - 100	0.9-1.1
Esposito, et al	>5,000	1.27

The regression rate is of prime importance as it controls the rate of solid to gas phase transition of the propellant or explosive. The mass flow rate is then $\dot{m} = \dot{r}\rho A_b$ where ρ is the density of the solid reactant and A_b is the local surface burn area. In solid rocket motors, the burn area A_b is predictable and the propellant flame front burns perpendicularly outward from the surface. Solid rocket motor grains are often designed and cast with complex surface areas that change as a function of the burn time such that the mass flow rate and thus the thrust of the motor can be tailored to the mission profile appropriately.

Granular explosive surface burn areas are more complicated and indeed non-uniform due to porosity, compaction and pores inherent in the granular materials. Solid rocket motor grains do not suffer this issue as they are often cast with rubber binders whereas not all explosive formulations contain polymeric binders. The topic of this

dissertation deals with homogeneous (non-binder) granular materials. Confinement of an explosive material results in gaseous product flow back into unreacted porous energetic material which serves to increase the unreacted material temperature and pressure and thereby increase burn rate. (Margolis, Telengator, & Williams, 2001) As an example, a single ignited HMX crystal will immediately shatter into smaller crystals because of the large thermal stress on the crystalline structure. Pressed HMX will not have this same effect since the inherent voids will relieve this pressure (up to the TMD limit for HMX). (Kubota, 2002) However, *Nunziato* notes that during quasi-static compaction HMX crystals are known to fracture at input stress values beginning in the 1 MPa (10 Bar) range and that 900 μm large HMX crystals break into smaller crystals during compaction up to approximately 85% TMD. (Baer & Nunziato, 1989)

Figure 58 below clearly shows the flame structure of deflagrating HMX, with higher chamber pressures driving the flame front closer to the burning surface. The close proximity of the flame front increases the local heat transfer in the condensed phase reaction zone, thus yielding higher burn rates according to Eqn. [16], similar in process to the deflagration of solid rocket motor propellants.

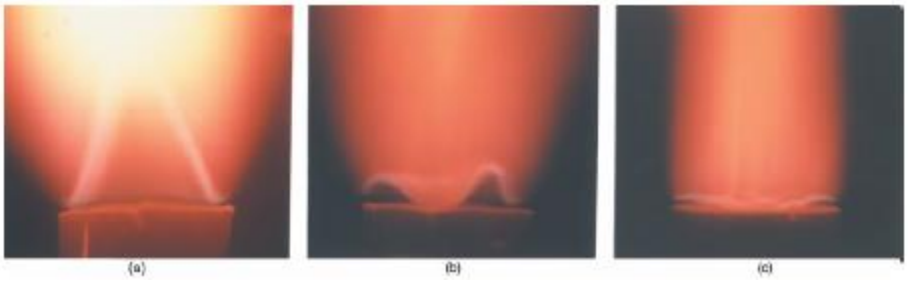

Figure 58: Flame Photographs of HMX at Three Different Pressures: (a) 0.18MPa, (b) 0.25 MPa, and (c) 0.30MPa (Kubota, 2002)

It is therefore important to model the volumetric burning area of granular material in addition to the surface burning area of the exposed material. Volumetric burning area captures the interior surface area due to damage and porosity of the material as they both change the surface area to mass ratio (A_v/m) for a finite piece of granular material.

Using a regression rate from HMX burn rate data at a single reference pressure, we can resolve the $\dot{m} = \dot{r}\rho A_b$ mass flow rate equation for solid to gas transition for deflagration material as specific volumetric mass flow rate:

$$Volumetric\ Burn = \left[\frac{\dot{r}_{ref}}{p_{ref}^{n}}\right] P_o^n \left(\frac{A_v}{m}\right)\rho \qquad [31]$$

Where "n" includes slope breaks according to Table 3. This form of volumetric burning is discussed further in (Kubota, 2002).

CTH contains an existing propellant model designed to simulate propellant damage and reactivity due to shock loading. This model provided the framework for subsequent modifications to implement a volumetric burning model specifically applicable to granular homogeneous explosives. The existing model was modified to remove the possibility of bulk material tensile cracking (which would not occur due to the lack of polymeric binder) and redefine compressive burning such that volumetric burning is modeling according to the above equation, where A_v is defined as a constant based on grain size assumptions. Additional required parameters include those to define the burning regime such as start pressure, reference burn rate and exponent, slope break pressure, second burn rate exponent, reaction energy, and density thresholds which

serve as reactivity bounds. It is not permissible to go into greater detail regarding the equations as the CTH source code is considered Export Controlled.

As in the existing propellant damage model implementation, CTH calculates deflagration outside of the EOS section in order to allow for conversion of solid reactants to gaseous products. Thus, unreacted explosive material is assigned a material number, EOS, strength model and fracture criteria and the gaseous deflagration products are assigned a separate material number and EOS. This post-EOS deflagration calculation formulation is necessary in order to work within the existing material state specific variable tracking limitations of the current CTH code architecture. By allowing for volumetric burning as a function of specific grain surface area (per mass) in conjunction with a P-α porosity model, this deflagration model is a macroscopic attempt at treatment of hotspots because the gaseous detonation products are allowed to propagate into the unreacted porous material and the additional surface area in this region is accounted for. The approach utilized in CTH is based on continuum mechanics. An alternative kinetics based set of equations for modeling deflagration via an Arrhenius EOS might include a thermal decomposition model for HMX, such as the four-step, five species reaction for HMX as defined by (Yoh & Kim, 2008).

The next chapter validates this deflagration model and choice of constants with empirical burn rate data to demonstrate a working implementation of deflagration in CTH inclusive of compaction. The results can be later extended to include statistical formation of hotspots which is a key contributor to the onset of DDT. Originally, the author had intended to simulate DDT by utilizing stable deflagration simulation output as input for the HVRB detonation EOS in a subsequent simulation (two separate runs

where output of the first feeds into the second). However, preliminary simulation attempts indicated that HVRB requires a larger pressure pulse beyond that provided by pressurized deflagration products to initiate detonation and as such simulating DDT in this two run approach is not possible. Consequently, deflagration results are viewed as an integral component in a trio of simulations (inert, detonation EOS, deflagration model) to assess the likelihood of DDT. The compendium of these approaches will yield a robust practical and applicable methodology to determine if granular HMX will undergo DDT.

CHAPTER 6

DEFLAGRATION RESULTS AND PROPOSED DDT APPROACH

Strand Burner Deflagration Simulation

The previous chapter ended by addressing analytics of the reformulated volumetric burning model in CTH. As discussed, deflagrating explosives at low pressures behave in a manner similar to solid rocket motor propellant: as a first-order function of pressure. Common propellant characterization techniques include obtaining burn rate data, generally in units of cm/s or inch/s, by varying the pressure in a large closed volume and igniting a strand of propellant (inhibited on the sides) to record the linear distance burned as a function of time. The apparatus volume is large enough that the pressure rise due to burning energetic material is negligible such that the burning pressure can be assumed equal to the pressurized volume. Furthermore, the volume is pressurized with an inert gas to avoid biasing the results with additional oxygen in air. Such an experimental apparatus is commonly referred to as a Crawford bomb. Repeating experimental trials in the Crawford bomb over a range of pressures enables the generation of a burn rate versus pressure plot for a propellant or energetic material, as shown in Figure 16 and Figure 17 for granular HMX. Pressure dependent burn rate equation constants “a” and “n” can then be extracted from a power fit on the log-log plot for comparison with other energetic materials. The subsequent section describes the CTH simulation configuration of a strand burner modeled according to Reference (Sinditskii, Egorshev, Berezin, & Serushkin, 2009) followed by results with a burn rate

versus pressure plot comparing CTH simulation output to experimental strand burner data summarizing the findings.

Hydrocode Model Description

Sinditskii et al performed granular HMX strand burner experiments at the Mendeleev University of Chemical Technology in Moscow, Russia. Their Crawford bomb trials were conducted over the pressure range of approximately 0.1 to 100 MPa (1 Bar to 1 kBar) and compared to results for three sets of published data available in the literature across the pressure range of interest. The Russian experiments were configured such that a 1.5 Liter BPD-400 constant pressure bomb pressurized with nitrogen housed 7 mm diameter pressed HMX samples at a density of 1.76 g/cm^3, 92.5% TMD. Samples were inhibited with an epoxy coating and encased in Plexiglas (acrylic, also known as polymethyl methacrylate, PMMA) tubes with 12 mm outer diameter. Burn rate data was determined from test event videos. No description of granular HMX strand length or initiation mechanism is provided in the primary reference (Sinditskii, Egorshev, Berezin, & Serushkin, 2009).

CTH strand burner simulations ran on a high speed parallel cluster on up to 36 processors. Mesh sizes with non-uniform spacing of 0.01 cm (100 μm) in the strand burner region coarsened to 0.05 cm (500 μm) in the Crawford bomb far field were utilized as the baseline coarse mesh. Based on P-α compaction model validation findings, the non-uniform fine mesh spacing employed a mesh of 0.003 cm (30 μm) in the strand burner region coarsened to 0.05 cm (500 μm) in the Crawford bomb far field. The problem domain was bounded by the 1.5 Liter Crawford bomb specification. For simplicity the interior bomb geometry was assumed to be cylindrical. Original CTH

simulations with the plastic inhibitor material modeled with a Mie-Gruneisen EOS for PMMA encountered numerical issues causing the simulation to encounter very small timesteps. Un-physical states can occur with Mie-Gruneisen EOS when local pressure values are beyond the bounds of the defining shock velocity versus particle velocity Hugoniot curve. Consequently, the inhibitor material was ultimately modeled as a 1 mm thick tube of 4340 Steel with a more robust SESAME tabular EOS. This material substitution resolved previously encountered numerical issues. The driving thin feature in this model is the 1 mm 4340 Steel inhibitor tube, which contains 10 cells through the radial thickness on the coarse mesh and 33.33 cells on the fine mesh.

Total cell counts for the two-dimensional axisymmetric coarse and fine mesh simulations were 140,000 and 640,000 cells, respectively. To reach the simulation stop time of 250 μs the coarse mesh run time was 17 CPU hours and the fine mesh was 360 CPU hours per set of iterations. In order to capture burn rates at much finer time intervals data write occurred every 10^{-8} seconds (100 records per microsecond). All simulations were performed in a two-dimensional cylindrical coordinates system with a symmetry boundary condition at the axis of symmetry. Specifically, the boundary condition at the bottom of the X axis was set to symmetry and boundary conditions at the bottom and top of the Y axis as well as the top of the X axis were set to an outflow boundary condition such that mass is allowed to exit (but not re-enter) the mesh.

Figure 59 contains a 2D image of the strand burner materials plot with mirroring across the axis of symmetry, the Y axis. In this figure, A indicates low density explosive material initiator. The 4340 Steel side burning inhibitor tube is denoted as B. HMX is identified with marker C. Pressurized nitrogen fill is included in the white region filling

the remainder of the computational domain and denoted with marker D. SESAME tabular EOS were utilized for the 4340 Steel inhibitor tube, nitrogen gas pressurized fill, and HMX gaseous reaction products (approximated as HMX detonation products). Low density explosive initiator was modeled with a Jones Wilkins Lee (JWL) EOS and initiated via programmed burn at time zero.

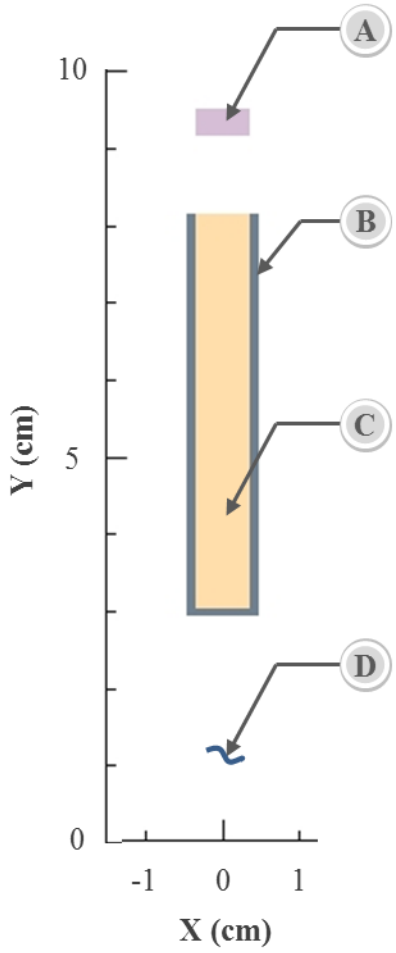

(A) - Initiator (low density explosive)
(B) - Sidewall Inhibitor (4340 steel)
(C) - Granular HMX Fill (92.6% TMD)
(D) - Ambient High Pressure (nitrogen)

Figure 59: CTH 2-D Axisymmetric Material Plot of Strand Burner

SESAME and JWL EOS and programmed burn parameters were obtained from the following references for 4340 Steel, Nitrogen, HMX detonation products, and the low density explosive initiator: [(Sandia, CTH 10.2: Equation of State Data File, 2006), and (Hall & Holden, 1988)]. Unreacted solid granular HMX Mie-Gruneisen EOS parameters were compiled from the references listed in Table 8 and Table 9 with the notable exception P-α porosity parameters discussed in the above chapter and detailed in (Mahon, 2015). With the exception of 4340 Steel using a Johnson Cook strength model, all remaining material strength models were assigned as Elastic Perfectly Plastic Von Mises models with yield strength, Poisson ratio, and fracture pressure obtained from (Matweb, 2014), (Baer, Kipp, & van Swol, 1998), or standard energetic material approximations.

Strand burner simulations in CTH were initiated with a low density, low output explosive material detonated a distance of 1 cm above the end of the HMX strand. Though (Sinditskii, Egorshev, Berezin, & Serushkin, 2009) do not specifically state the initiation method employed in their experiments, it is common to use a bridgewire type mechanism to induce the onset of burning via Joule heating or a small squib charge. The vast majority of EOS in CTH are pressure, not temperature, dependent. Thus, initiating via a bridgewire mechanism cannot be accurately modeled in CTH. However, CTH is designed as a shock transmission code and therefore excellent at propagating pressure wave disturbances. Consequently, the CTH modeled strand burner simulations were initiated via shock transfer (sympathetic reaction) of an adjacent explosive charge. The buffer distance of 1 cm was iteratively added to decrease the magnitude of the pressure wave imparted onto the strand burner by damping the detonation wave through

a 1 cm thickness of nitrogen gas. With this initiation mechanism the pressure dependent burn rate equation was no longer a function of the pressurized nitrogen setting (50 Bar in all simulations), rather the pressure in the burn rate equation became a function of the local average pressure acting above the burning region. One additional necessary augmentation to the experimental setup was to also inhibit the bottom of the HMX strand sample. Pressure wave propagation from the low density explosive initiator induced a secondary reaction front on the lower strand surface in preliminary CTH simulations.

An augmented volumetric burning model was formulated specifically to model granular explosive material deflagration according to Equation [31]. In this equation the grain size dependent burning surface area constant A_v is of primary importance as it controls macroscopic simulation of propagation of the burn front into interstitial voids between the porous material. Appropriate values were determined through iterative simulation of the restructured volumetric burning model and are specific to the grain size of the intended simulation. Burn rate control parameters were input from experimental data compiled in (Sinditskii, Egorshev, Berezin, & Serushkin, 2009). The table below contains a list of augmented volumetric burning input parameters. CTH calculates deflagration outside of the EOS section in order to allow for conversion of solid reactants to gaseous products. In subsequent results the unreacted explosive material is shown with a material color of light tan and the gaseous deflagration products are shown in dark pink once deflagration begins in the post-EOS volumetric burning model.

Table 13: HMX Volumetric Burn Model Variables

Burn Rate Variable	**Value**
Granular HMX Initial Density:	1.76 g/cm^3
Minimum Burning Pressure:	0.1 MPa (1 Bar)
Maximum Allowable Density (stability condition):	2.5 g/cm^3
Burning surface area constant $A_{v:}$	4 cm^2/g
Maximum allowable burning surface area:	500 cm^2/g
Volumetric Burn Reaction Energy:	(Sandia, CTH 10.2: Equation of State Data File, 2006)
Slope Break One; P = 5 MPa :	$\dot{r}_{ref}$ = 9 cm/s, n = 0.82
Slope Break Two: P = 10 MPa :	n = 1.1

Only Eulerian fixed tracers in the center of the HMX strand (and low density initiator) were included in the strand burner simulations to facilitate burn rate calculation at a known fixed geometric position. Tracers were positioned every 0.01 cm for the first centimeter of the HMX strand (100 tracers in the first centimeter) followed by every 0.25 centimeters until reaching the end of the 5.1 cm (2 inch) long strand. This strand length was assumed by the author and not stated in *Sinditskii et al*. A Matlab data reduction and post-processing script was written by the author to calculate burn rate and determine the corresponding pressure acting on the burning surface as a function of position within the HMX strand. Burn rate was calculated by examining material specific density results for the solid unreacted HMX. When solid unreacted HMX is converted to gaseous HMX products the density of the solid HMX material goes to zero. This proved to be an accurate means of tracking the burn front position. Thus, movement of the burn front enabled calculation of burn rates at adjacent

linearly aligned central tracers by subtracting the positional tracer difference (0.01cm within the first centimeter of HMX) and dividing by the difference in wave arrival times at the corresponding tracers. Pressure acting on the burn surface was calculated by averaging the pressure records at the tracer above the burn front from the time the detonation moved past the upper tracer to one time record before the burn front reached the lower tracer. CTH simulation results from the coarse and fine mesh simulations are presented in the following sub-section.

Volumetric Burning Results

Results presented in this sub-section correspond to simulations of the aforementioned strand burner experimental set-up described in (Sinditskii, Egorshev, Berezin, & Serushkin, 2009). The simulated 1.5 liter 2-dimesional axisymmetric geometry was filled with Nitrogen pressurized to 50 Bar (5 MPa) in an attempt to replicate the corresponding 0.9 cm/s experimental burn rate plotted in *Sinditskii et al*. However, through data analysis of numerous simulations it became apparent that volumetric burn rate was not only a direct function of the Crawford bomb constant pressurization setting, as with solid rocket propellant, but rather largely a function of the local pressure acting above the burning region. This is due to the presence and effect of the initiator shock wave and the reflected waves in the confined HMX burn rate sample. Thus, it was possible to obtain multiple burn rate measurements from post-processing a single CTH simulation. The lack of burn rate stability for granular HMX is expected given that the second slope break "n" exponent in the pressure dependent burn rate equation is greater than unity.

CTH strand burner simulations begin with detonation of the low density initiator charge positioned one centimeter above the porous HMX strand at time zero. The detonation wave from the low density initiator traverses the one centimeter Nitrogen gas gap and the magnitude of the pressure wave decreases substantially. Pressure recorded by an Eulerian tracer in the geometric center of the low density initiator pellet (fine mesh results) recorded a maximum detonation wave pressure of 29.8 kBar (for comparison the CJ pressure of 100% TMD HMX is 390 kBar). An Eulerian tracer positioned at the top of the porous HMX strand recorded a maximum pressure of 3.23 kBar (323 MPa) 4.1 μs after the low density initiator peak pressure record. This 90% reduction in pressure impinging on the porous HMX sample was necessary to obtain burn rate data within the order of magnitude of the experimental data range and impose a pressure lower than the Pop-Plot prompt initiation pressure threshold of HMX. Dramatic pressure decrease across the one centimeter Nitrogen gap is due to impedance mismatch discussed in the CHAPTER 4 subsection entitled CHARACTERISTICS OF SHOCK PHYSICS. It is worth noting that the 3.23 kBar, or 3,230 Bar pressure, due to the initiator shock wave is far above the 50 Bar nitrogen pressurization of the Crawford bomb.

Once the initiator generated detonation wave reaches and begins transmission through the porous HMX strand, compaction modeled with P-α parameters calculated within the EOS occurs. Figure 60 contains a density contour plot of the HMX strand top end 0.9 μs after pressure wave impingement begins. All contour and material plots in this subsection were obtained from simulation results run on the coarser 0.01 cm mesh. In the contour plot below it is evident that the initially 92.5% TMD HMX has

compacted to 100% TMD in a pattern consistent with a spherical detonation wave. Diffusion represented by a flattening of the leading edge of the wave is consistent with the theory that plastic compaction wave velocity changes as a function of depth through the granular compact and that granular materials are not able to propagate sharp discontinuities. Tracers positioned within the first few millimeters of the strand burner end indicate that deflagration occurs at approximately 100% TMD, as indicated by the solid HMX material density changing from roughly 1.9 g/cm^3 to 0.0 in a single time record. Zeroing of solid HMX density is indicative of a transition from solid reactant to gaseous product. Further into the strand, porous HMX density decreases from 100% TMD prior to deflagration due to rarefaction wave interaction with the grain inhibitor steel sidewalls, which causes HMX expansion beyond the initial porous density of 1.76 g/cm^3. HMX density gradually decreases from initial compaction 100% TMD down to approximately 1.6 g/cm^3 prior to deflagration. This density decrease is another reason that stable burn rates were not observed in computational results. Although CTH is not capable of modeling the transition from β to δ HMX, the literature indicates that during crystal polymorphs phase transition a 7-8% volume increase occurs dropping density from 100% TMD to 1.76 g/cm^3. (Saw, 2002) Though the simulated expansion is likely due to shock wave propagation and coalescence in CTH, the phenomena of CTH density decrease prior to deflagration is consistent with the literature.

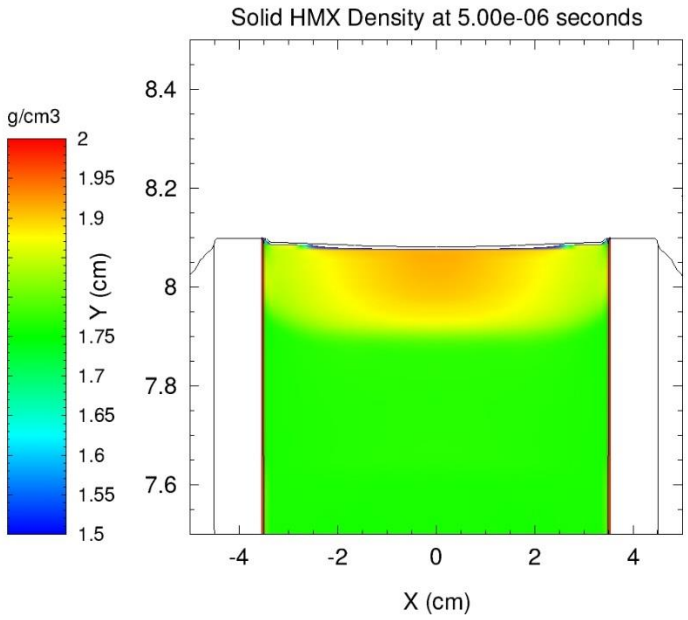

Figure 60: Strand Burner Density Profile of Compacting HMX at 5 Microseconds Following Initiation

Porous HMX strand burner simulations show initial un-sustained deflagration of HMX at the HMX – Nitrogen interface. Sustained strand deflagration commenced a finite distance into the explosive sample, as shown in Figure 61 by localized red dots in the pressure contour plot and in Figure 63 by dark pink regions in the material plot at t = 112 µs. Coarse 0.01 cm mesh plots were utilized in this discussion as the corresponding localized pressure on the 0.003 cm fine mesh occurred in between plot record intervals just prior to 103 µs and thus the coarse mesh results show a clearer depiction of phenomena. Restructuring of the volumetric burn equation as a function of the constant burning surface area, A_v, enabled CTH to account for increased burning surface area of the granular energetic material. P-α porosity further enabled simulation of propagation of high pressure generated by un-sustained burning on the strand surface

into interstitial voids in the porous material. This combination of porosity, compaction and increased burn area results in a macroscopic approximation of hot spots, though more accurately called high pressure spots in the present work. Pressure in the red localized spots in Figure 61 is in excess of 15 kBar (1.5 GPa). Tracers are not present at these locations and thus the precise pressure value of these spots could not be determined from stored simulation data.

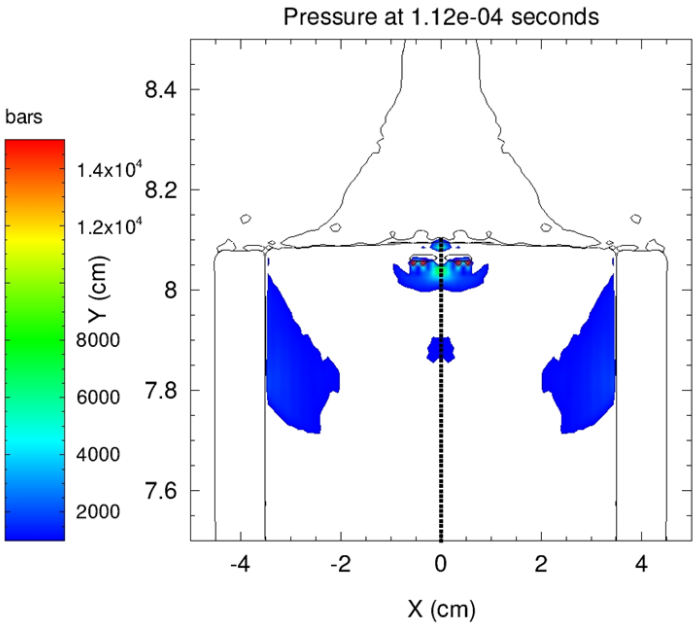

Figure 61: Strand Burner Pressure Profile at Start of Burn at 112 Microseconds

Figure 62 below further supports the macroscopic high pressure spot theory. Temperatures in the central red region just below the strand surface are well above those specified in Table 12 for hot spot initiation. Again, due to the theoretically uniform granular spacing imposed by P-α porosity model assumptions it is likely that macroscopically simulated hotspots or high pressure spots would require initiation temperature thresholds corresponding to very small hot spot pore sizes.

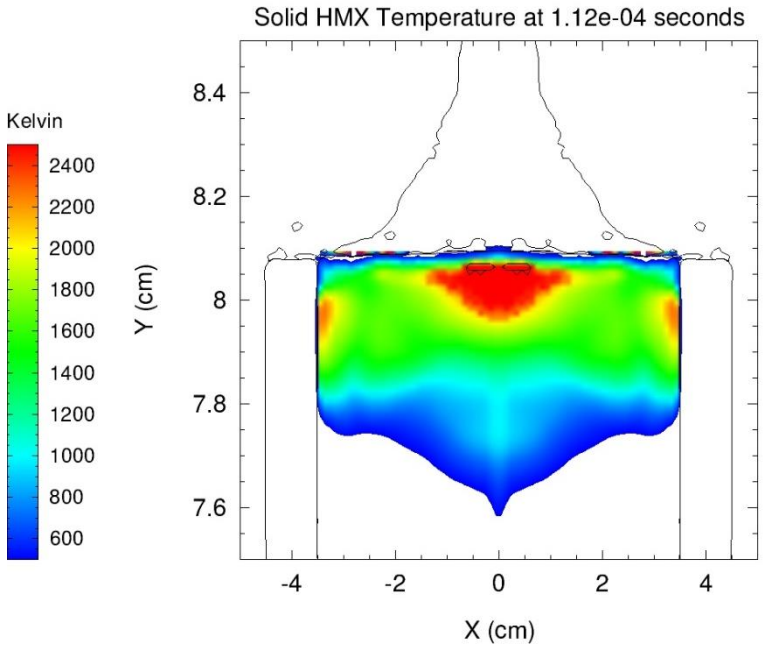

Figure 62: Strand Burner Temperature Profile at Start of Burn at 112 Microseconds

Lastly, Figure 63 contains time sequence material plots of the strand burner coarse mesh simulation results from the time of sustained initiation at 112 µs through formation of a nearly planar burn front at 117 µs. In all strand burner simulations with appropriately tuned volumetric burning parameters the burn rate was very high at the onset of deflagration due to pressure buildup above the 100% TMD strand end plug and subsequently due to propagation into the expanded porous energetic material. However, burning rate calculated values did decrease to values consistent with experimental results once the early high burn rate deflagration products expanded above the deflagrating strand. Pressure fluctuations did occur and consequently a stable burn rate per simulation was not obtained, rather a series of recorded burn rates were calculated depending on the pressure acting above the deflagration front.

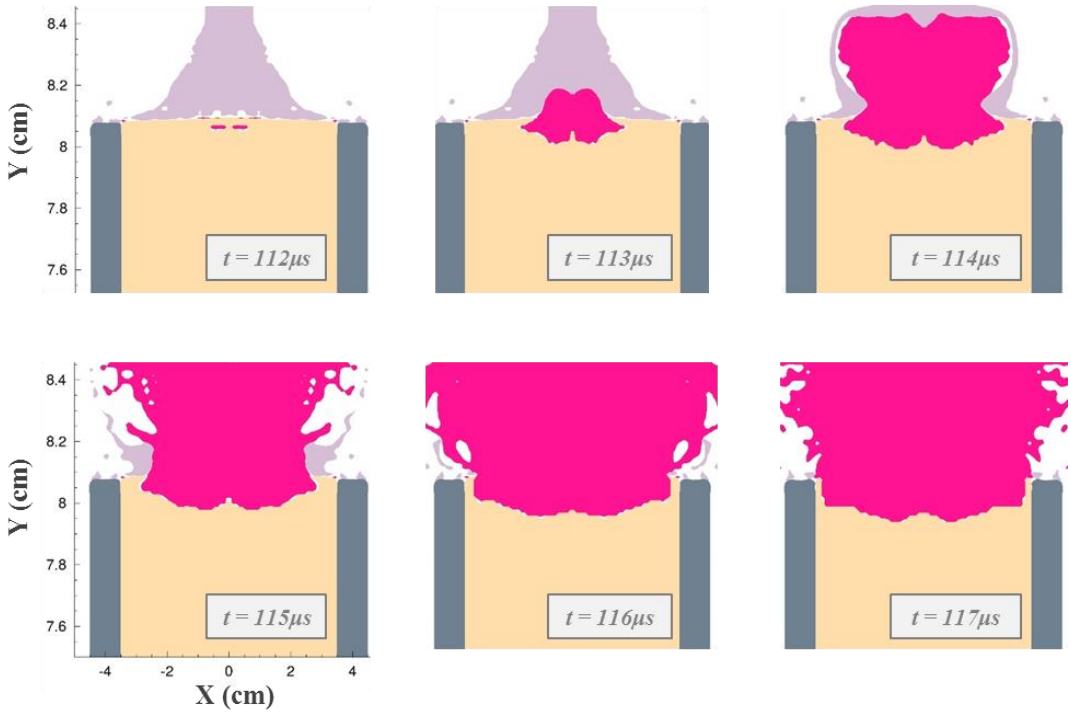

Figure 63: Example Burn Profile from 112 to 117 Microseconds

The below comparison in Figure 64 includes experimental results digitized from (Sinditskii, Egorshev, Berezin, & Serushkin, 2009), (Esposito, Farber, Reaugh, & Zaug, 2003), and (Atwood, et al., 1999). *Atwood et al.* was the primary source cited in both *Sinditskii et al. and Esposito et al* for burn rate data in the 0.24 – 345 MPa pressure range. *Atwood* is directly cited in the plot below because the original reference contained tabulated experimental data (plotted for 298 K results) utilized to decrease error incurred from plot digitization in secondary sources. Crawford bomb experiments conducted by *Atwood* and his colleagues at the China Lake Naval base (U.S. Naval Air Warfare Center) were performed on three variations of HMX. At lower pressures large single HMX crystals and pressed pellets were tested. At higher pressures fine powder screened for uniform particle size distribution was utilized in burn rate testing. Sample

densities or grain sizes were not provided in the primary source. Data from these experiments are denoted by black circles on Figure 64. In this plot experimental data are shown with black points and computational hydrocode results are plotted with grey points. Trendlines on the *Atwood et al.* data show the two slope breaks at "n" values of 0.82 followed by 1.1. A second set of experimental data is plotted with black triangles from data provided in *Esposito et al.* for "large grain" samples defined as having particle size distributions where 90% of the sample contains crystals above 10 μm and the median crystal size is 33 μm. Compared to NSWC DDT tube, LANL DDT tube, and LANL gas gun data where coarse grains are in excess of 100 μm, a median grain size of 33 μm is considered fine relatively to the other data sets discussed in this work. *Esposito* utilized a diamond anvil test configuration as opposed to a Crawford bomb.

CTH coarse and fine mesh strand burner simulation results across a range of pressures are plotted with grey diamond and X markers, respectively. CTH results are slightly above those obtained by *Atwood et al*, yet bounded by the *Esposito et al.* results. Excellent correlation occurred for coarse and fine mesh results. The author theorizes that this correlation occurred due to high pressures generated from deflagration events. As noted in the NSWC and LANL P-α porosity coarse and fine mesh results comparison, CTH is able to capture high amplitude phenomena quite well on meshes as coarse as 0.05 cm and has difficulty with low amplitude events. Given the increased run time penalty associated with volumetric burning calculations, the correlation between coarse and fine mesh results is encouraging for future practical and applicable model implementations.

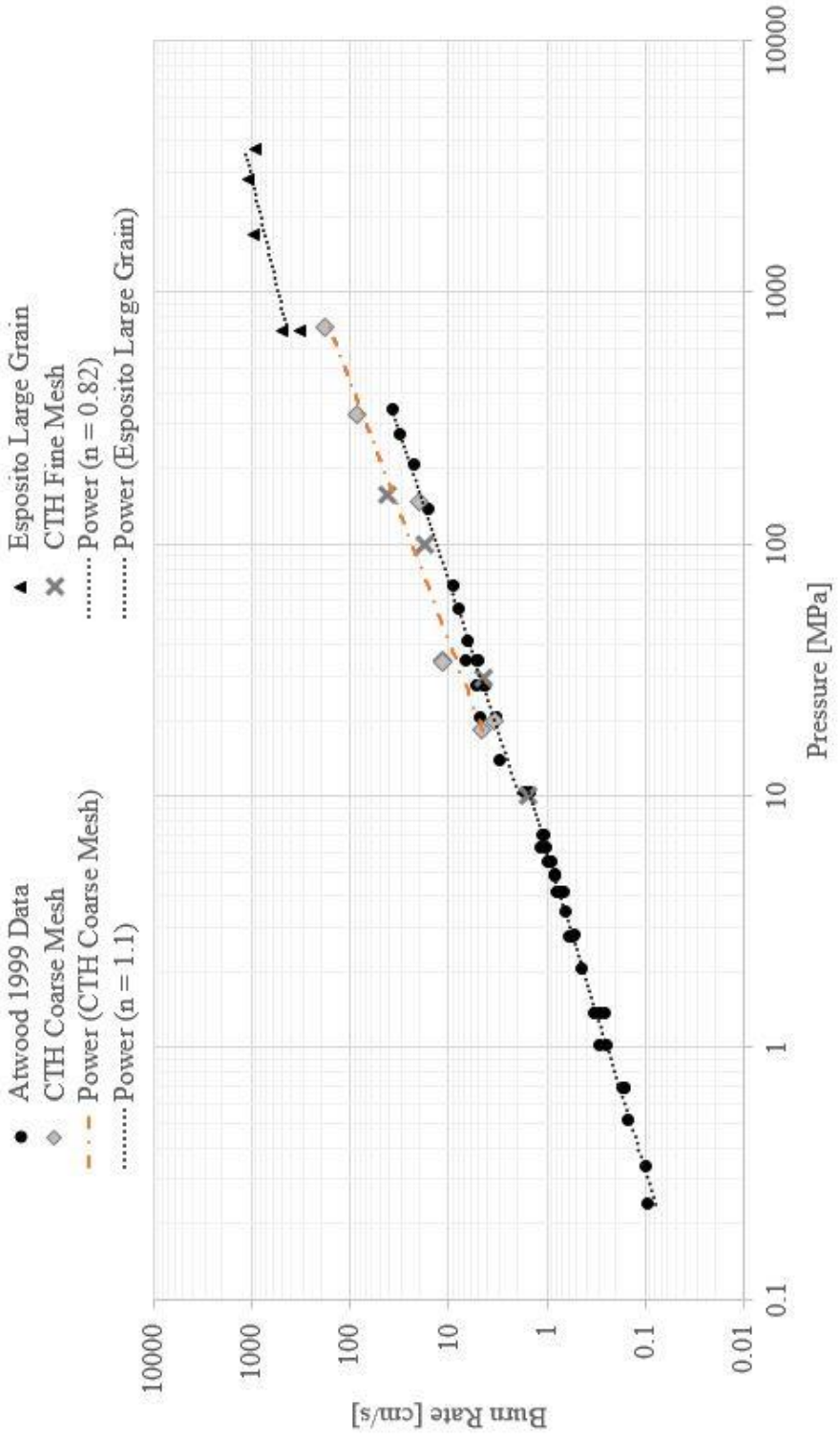

Figure 64: CTH Strand Burner Burn Rate Results Compared to Experimental Data

DDT Tube Deflagration Simulations

NSWC and LANL DDT tube simulations are reconsidered in the present section for simulations inclusive of the lessons learned and models developed throughout this dissertation. Simulations in the following section contain updated P-α porosity parameters detailed in (Mahon, 2015) and well as the reformulated volumetric burning implementation. Both DDT tube computational domains were re-meshed in two-dimensional axisymmetric coordinates to account for significant run time increases incurred by the addition of volumetric burning with P-α porosity for the energetic material. In both instances, non-uniform meshes were structured such that the initiation mechanism, porous HMX, and DDT tube side walls are modeled with a uniform 0.003 cm (30 μm) mesh tapered out to 0.05 cm over 0.3-0.5 cm to a uniform 0.05 cm mesh in the far field. With the exception of the three-dimensional rectangular to two-dimensional cylindrical coordinates conversion, P-α porosity parameter update, and inclusion of the augmented volumetric burning model following EOS calculations, all material properties are the same as specified in Table 8 and Table 9 in order to assess the impact of changes proposed in this body of work.

Reviewing results summarized in the research gap identification studies presented in Figure 40 and Figure 41 highlights that CTH simulations are able to model detonation accurately with HVRB EOS when the DDT tube initiation mechanisms are altered accordingly, but this detonation occurs with no prior burning. Table 10 and Figure 42 further expand upon the research gap finding by showing that XRN values for inert cases are all equal to zero (as expected), XRN for all forced detonation simulations are equal to one (again, as expected). The anomalous representative

experimental setup simulation with HVRB EOS for NSWC geometry XRN value of 0.0366 indicates that the HVRB model initiates minimal reactions, but is not formulated to sustain this type of reaction propagation. Based on these early results, the goal is to demonstrate that P-α porosity parameter correction and addition of a reformulated volumetric burning model are capable of predicting the onset of deflagration in known DDT scenarios with both low and high amplitude initiation mechanisms.

NSWC DDT Tube with Volumetric Burning

NSWC experimental data for shot numbers 1605 (approximately 115 micrometer granular HMX) and 1616 (class A approximately 200 micrometer granular HMX) are summarized in Table 2. In these experiments, time zero is defined as the time at which the first ionization pin location at 16 mm triggers. All referenced ionization pin locations are stated as a function of distance along the length of the granular HMX column. In Reference (Price & Bernecker, 1977) the authors note that the longer time delays to detonation observed in the 200 micron HMX sample as compared to the 115 micron HMX sample are in opposition to the trend in the literature and may be due to removal of fine grains from the larger granular sample. Data in the literature continues to support the trend that smaller average grain size samples correspond to larger pre-detonation column lengths. Hotspot theory reviewed in (Walley, Field, & Greenaway, 2006) dictates that smaller grain sizes require higher hotspot initiation temperatures. HMX granularity is included in the CTH simulations with the P-α porosity model, which corresponded well to fine grain 10-15 micron HMX

samples in the compaction validation study. Given that CTH models macroscopic porosity corresponding to fine grain samples, it is expected that the pre-detonation column length, and therefore time to reach detonation thresholds, is increased in the present simulations. However, because the NSWC apparatus setup did not record the time from $BKNO_3$ initiation to first ionization pin activation, it is not possible to compare deflagration start time and early burning region CTH results with experimental data. The NSWC DDT tube CTH simulation presented in this section ran approximately 7,000 CPU hours in 2D axisymmetric coordinates to a stop time of 479 µs.

CTH simulation of the NSWC DDT tube scenario begin with initiation of the $BKNO_3$ ignitor at time zero. Subsequently, $BKNO_3$ products propagate upward through the porous HMX solid and a compaction wave forms. Figure 65 contains time sequence images of CTH simulation material plots. $BKNO_3$ solid reactant and gaseous products are depicted in purple, porous solid HMX in tan, and HMX gaseous products in deep pink. Deflagration begins at a simulation time of 81.5 microseconds along the HMX to DDT tube wall interface. The initial burning location is shown by two small pink dots on the t = 85 µs image. Burning then continues to follow the DDT tube wall downward as BKNO3 products dissipate into porous HMX and HMX expands to fill the volume once occupied by the initiator. P-α porosity and reformulated volumetric burning models enable high pressure generated by the confined BKNO3 ignitor and initial HMX burning along the tube sidewalls to propagate into interstitial voids in the porous material and create localized burning regions in the lower DDT tube end. These burning regions are visible in the t = 137, 150, and 157 µs images. By 165 µs the lower DDT

tube end HMX is entirely reacted and the deflagration front shape stabilizes as it progresses further up the tube center, though the burn rate is not constant.

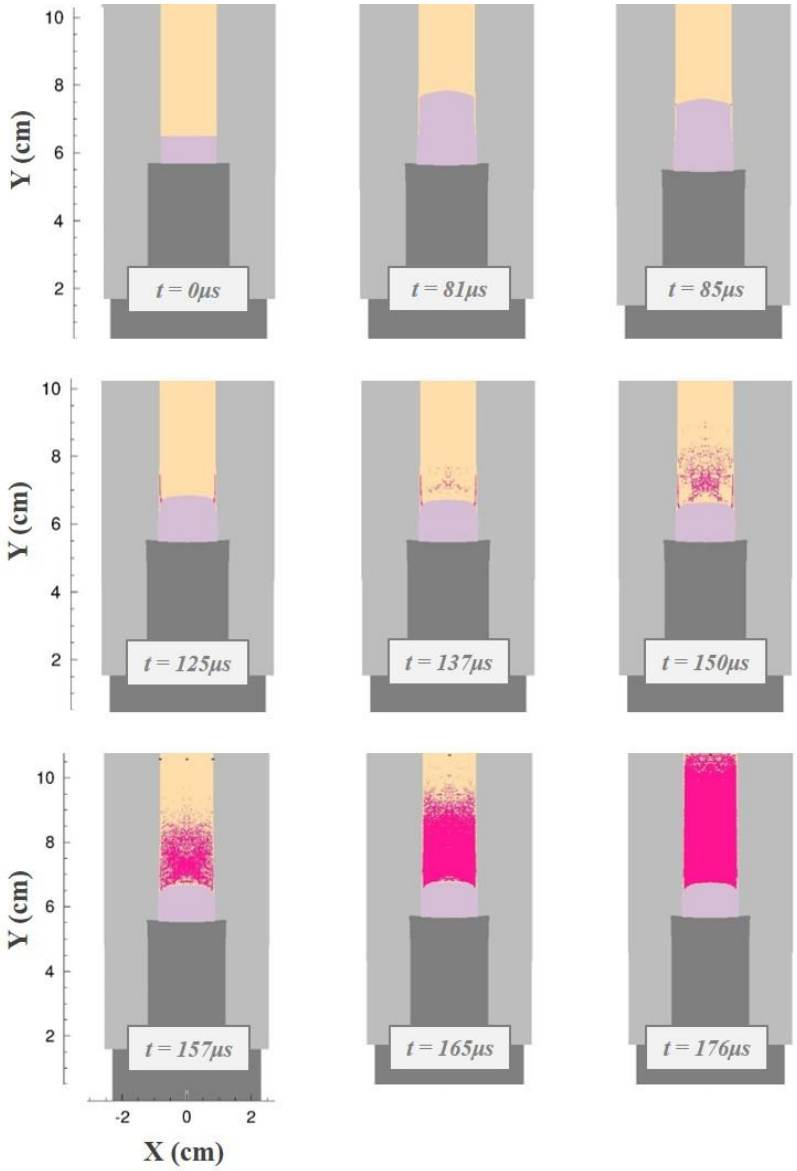

Figure 65: NSWC DDT Tube: Deflagrating Material Images

Figure 66 contains zoomed out material images at later times. These material plots show the burn front progressing upward to consume all granular HMX, ultimately reaching the tube end at 435 μs. Tube sidewall deformation due to confinement of high

pressure gaseous products is visible at the final simulation time of 479 μs. In reality, experimental results indicate transition to detonation at 35 mm and 45 mm for shot numbers 1605 and 1616, respectively. The current CTH volumetric burning reformulation is incapable of accurately modeling this transition and consequently results at later times are deemed unphysical.

Based on the experimental NSWC data presented in Table 2, the initial burn rates from ionization pins located at 16 mm and 28.8 mm are 888 m/s for shot 1605 and 427 m/s for shot 1616. An averaged burn rate can be calculated across the length of the DDT tube for a known sample length of 29.49 cm and a deflagration time range of 81.5-435 μs. With these known start and end deflagration parameters, the averaged burn rate is 834 m/s. It is acknowledged that the burn rate changes as a function of time and position within the DDT tube and this average burn rate is only included for general comparison purposes. As expected, the burn rates begin slow (sub m/s range) and transition to higher burn rates as the pressures increase, ultimately ending in high unphysical burn rates owing to the absence of a DDT model.

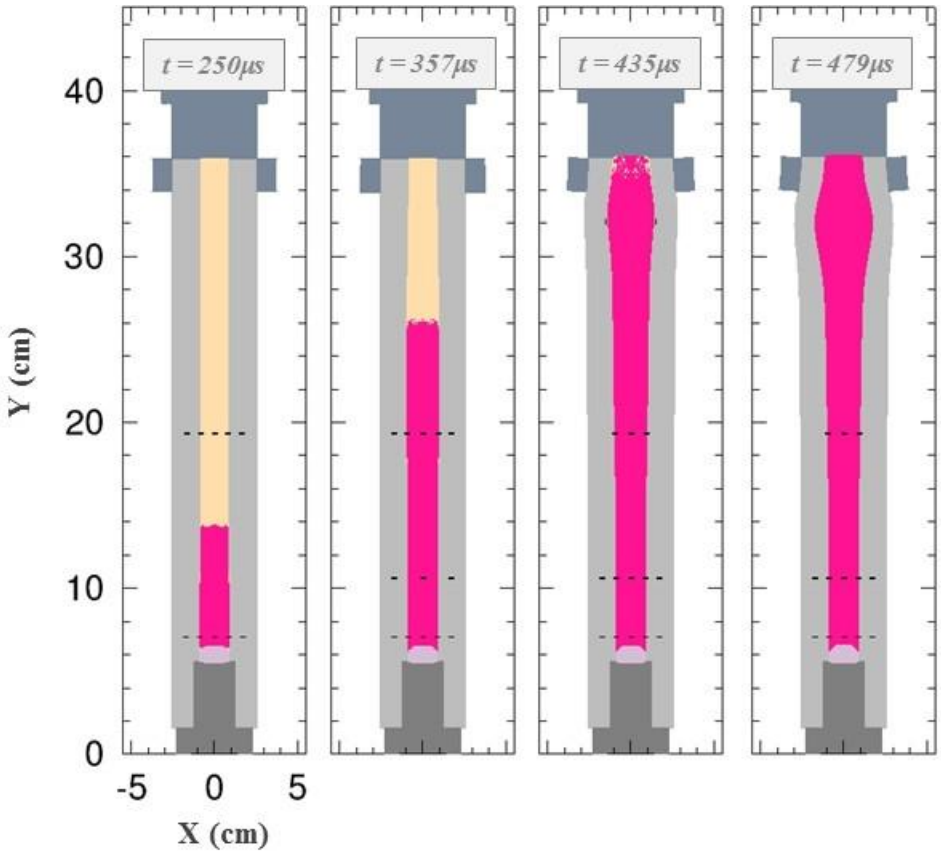

Figure 66: NSWC DDT Tube: Deflagrating Material Images Far Field View

Figure 67 contains time sequence images of solid HMX density contour plots in the initiator region and Figure 68 contains corresponding zoomed out density contour plots at later times. Near field density results show formation of a high density compaction region, referred to as a plug in the Los Alamos TMD Plug DDT theory. Consistent with the material images above, the density contours indicate that a 100% TMD initially propagates upward, but the aft end of this plug later expands to fill the initiator gas region reducing density from TMD to approximately 1.3 g/cm^3. The time snapshot at t = 85 μs shows this porous HMX expansion during early deflagration. These density contours are only colored for solid HMX. The final time image in Figure 67 is primarily white in the central tube area as solid HMX has been converted to

gaseous HMX products, confirmed through comparison with the last image in Figure 65.

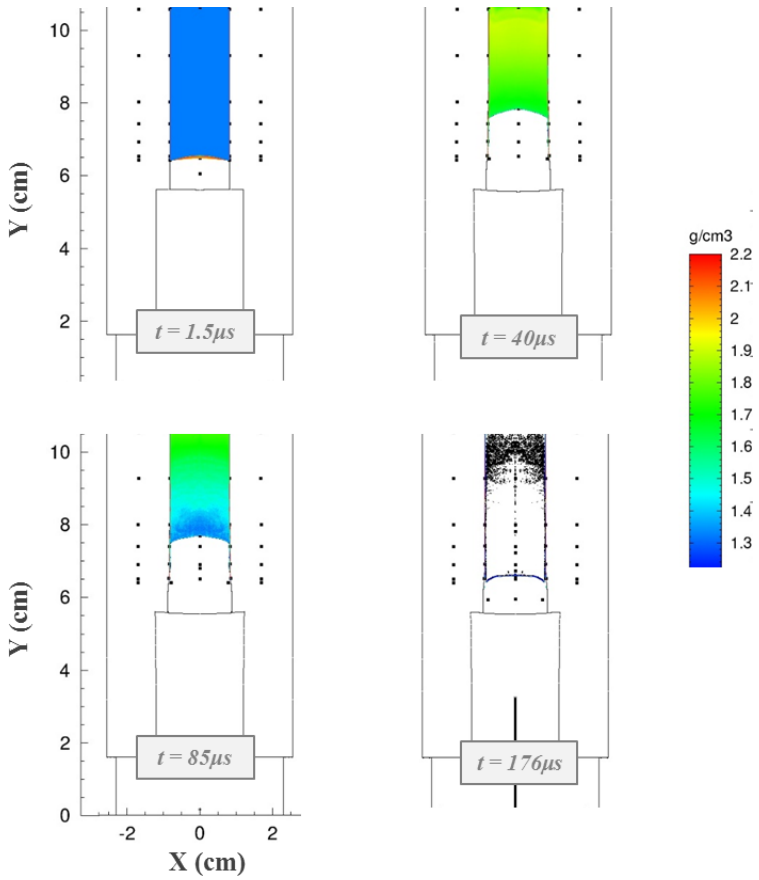

Figure 67: NSWC DDT Tube: Deflagrating Density Contour Plots

Contour plots in the zoomed out view show the TMD plug reaching the far end of the DDT tube at 357 μs, compared to the deflagration front arrival time of 435 μs. Assuming an average compaction wave speed throughout the duration of compaction in the time interval from 1.5 to 358 μs across the 29.49 cm long column of granular HMX, the plastic compaction wave velocity is determined to be 830.7 m/s for the sample with and initial density of 1.322 g/cm^3. P-α porosity model validation results yielded plastic compaction wave velocities of 780 m/s for an initial sample density of

1.24 g/cm^3 and 848 m/s for an initial sample density of 1.4 g/cm^3. Thus, the NSWC average plastic compaction wave speed is consistent with porosity model validation results. Furthermore, the average burn rate and compaction wave speed are very similar, where compaction begins 80 µs prior to deflagration.

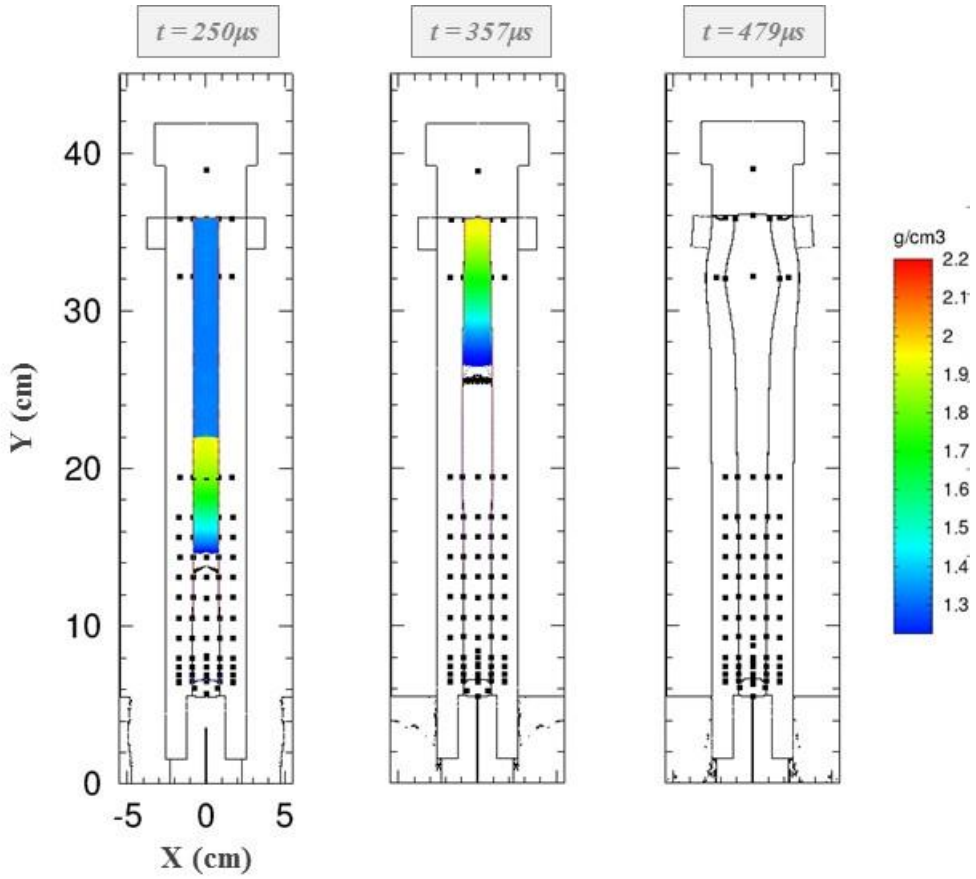

Figure 68: NSWC DDT Tube: Deflagrating Density Contour Plots Far Field View

Figure 69 and Figure 70 contain time sequence images of pressure contour plots with a linear pressure scale from 1-10 kBar (0.1-1 GPa, 100-1000 MPa). Detonation pressures are on the order of hundreds of kBar (tens of GPa). In the figure below, pressure contours at t = 85 µs immediately following onset of deflagration show pressures of approximately 3 kBar (300 MPa, 0.3 GPa) in the vicinity of the burning region. These pressures are similar to the pressure wave imposed on the strand burner

end by the low density initiator in the reformulated volumetric burning model validation. Less than 100 μs later, the pressure in this localized ignitor region has increase to above 10 kBar due to confinement.

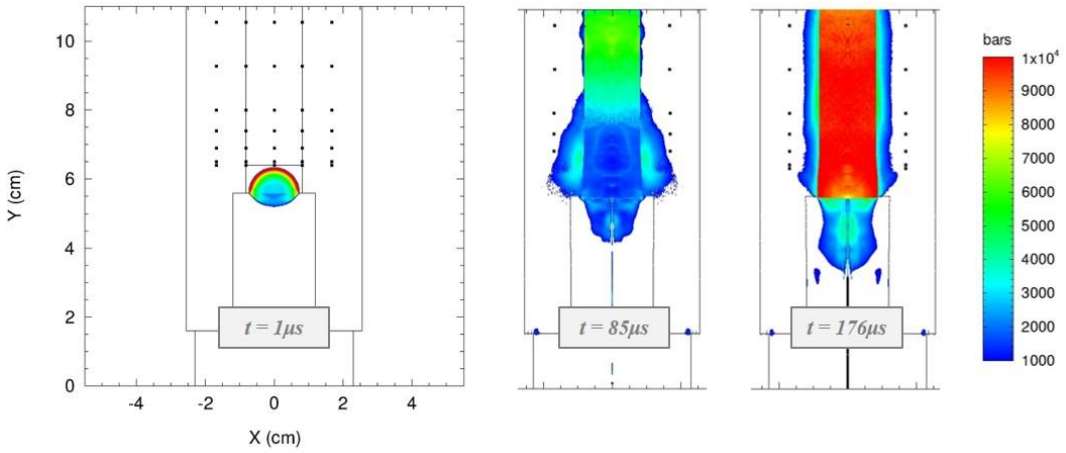

Figure 69: NSWC DDT Tube: Deflagrating Pressure Contour Plots

Farther up the DDT tube porous HMX column, wave front pressures occur in the range of 6-10 kBar, again likely increasing due to confinement. Comparing Figure 70 to zoomed out density contours in Figure 68 and material plots in Figure 66, it is evident that the pressure wave front location corresponds to the compaction wave front and not the deflagration wave front. Thus it can be concluded that the burn front does not overtake the compaction wave, rather it lags the compaction wave by a value roughly equal to the induction time of 80 μs. APPENDIX D entitled VOLUMETRIC BURNING: DDT TUBE TRACER OUTPUT contains pressure traces (and density traces) at simulated ionization pin locations similar to those presented in APPENDIX C for the CTH HYDROCODE: RESEARCH GAP IDENTIFICATION chapter. Detonation velocity at the initial HMX density of 1.322 g/cm^3, 69.4% TMD, is 6.83

km/s further demonstrating that this reformulated volumetric burning model is incapable of capturing DDT.

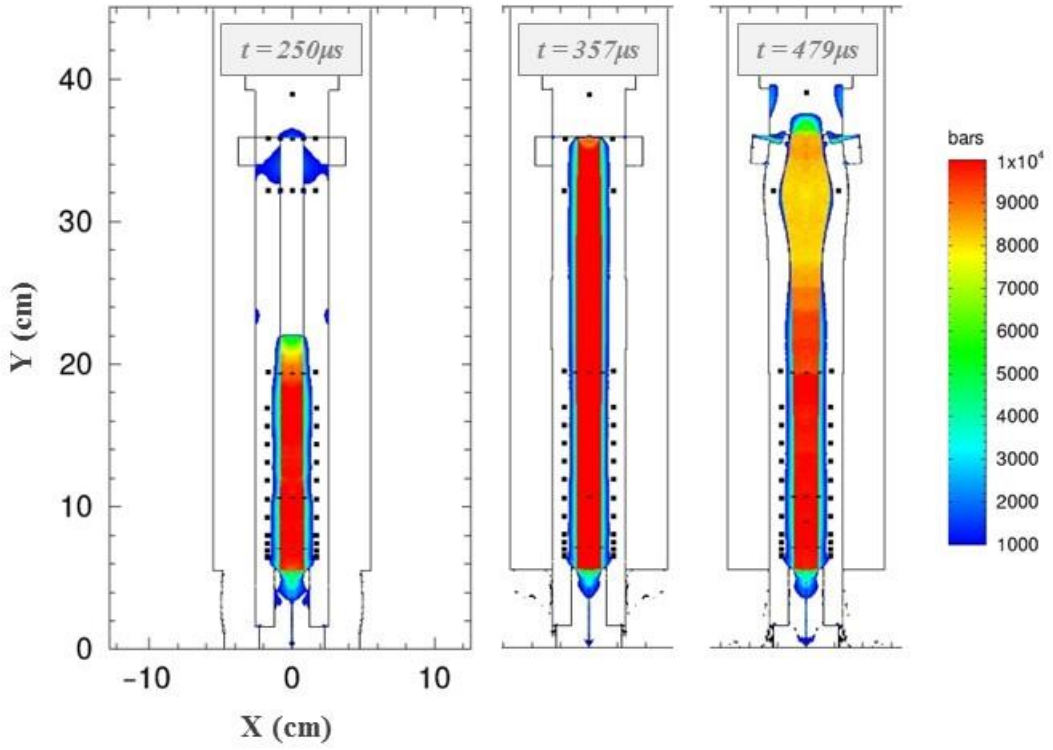

Figure 70: NSWC DDT Tube: Deflagrating Pressure Contour Plots Far View

Figure 71 contains an updated version to the plot in Figure 40 summarizing burn front location versus time for NSWC experimental shot number 1605 and 1616 results, HVRB forced detonation results, as well as the reformulated volumetric burning model computational results. Again, experimental results are plotted with black markers and CTH results are plotted in grey. Experimental results indicate that the pre-detonation column length for shot 1605 is 35mm and 45 mm for shot 1616, implying that DDT is supposed to occur in a similar range for the present simulation. However, the current reformulated volumetric burn rate model is currently only capable

of modeling deflagration. DDT mechanism modeling is the subject of future work. CTH results in the plot below have been shifted in time to correspond to the experimental convention of time zero at first ionization pin activation. As previously discussed, experimental data did not record the time from BKNO3 ignition to triggering of the first ionization pin, thus it is not possible to compare CTH results for deflagration induction time.

CTH results at the first four simulated ionization pin locations (16, 28.7, 41.4, and 54.1 mm) fall within the region bounded by the two sets of experimental data. Beyond the tracer at 54.1 mm CTH results and experimental data diverge. This is likely due to CTH producing unphysical results in the absence of a DDT mechanism to transition from deflagration to detonation in a single simulation. Were CTH capable of modeling the full DDT regime, it is anticipated that the pre-detonation distance would be larger than those in experimental results as the P-α porosity model more closely replicates compaction of very fine grain (10-15 micron) explosives.

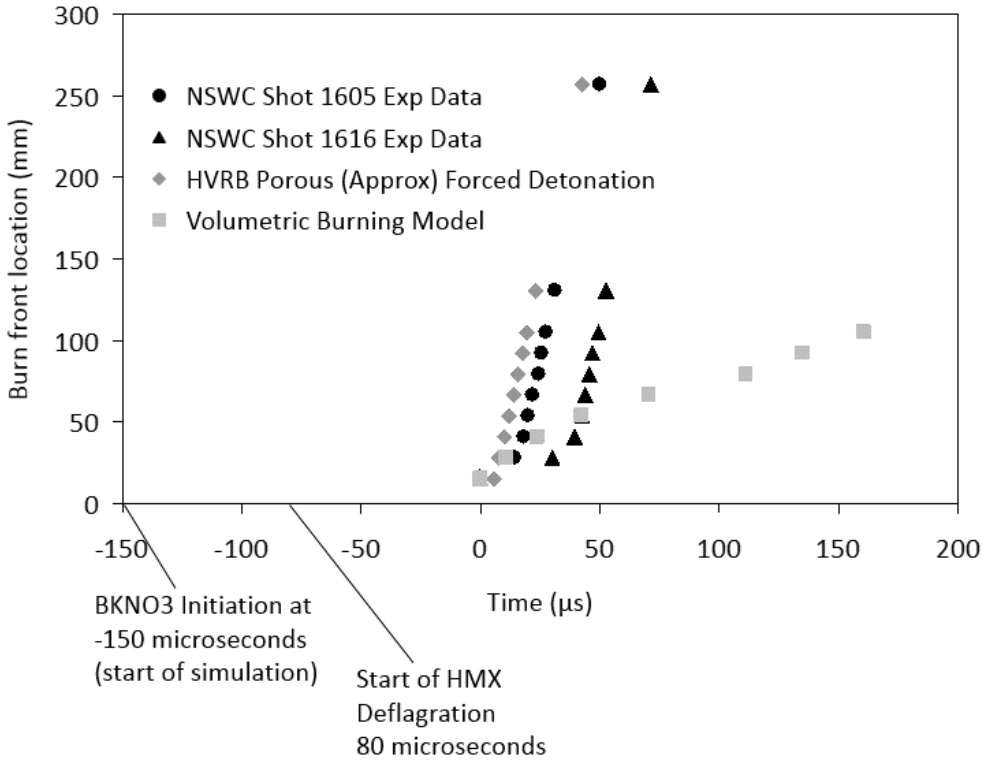

Figure 71: NSWC Volumetric Burning Model Outputs vs Experimental and HVRB Forced Detonation

LANL DDT Tube with Volumetric Burning

LANL experimental data for shot number B-9036 (approximately 170 micrometer granular HMX) are summarized in Figure 14 and Figure 15. Time zero in the LANL DDT tube experiments is defined as the first current detected by the capacitance discharge unit to ignite the fuze, gas generated in turn causes the piston to move upward at 100 m/s. CTH simulation time zero begins immediately prior to piston impact with porous HMX. Thus, the LANL time zero occurs prior to CTH time zero. As with the NSWC simulation, all referenced ionization pin locations are stated as a function of distance along the length of the granular HMX column. This simulation

differs greatly from the NSWC high amplitude initiation mechanism with a BKNO3 pyrogenic ignitor. The low velocity piston utilized in the LANL DDT tube experiments imparts a low amplitude pressure wave of approximately 0.6 kBar into the granular HMX sample. Results for numerous experimental trials are included in Reference (McAfee, Asay, & Campbell, 1989) for 65% and 75% TMD HMX, though the authors do not specify the density corresponding to specific data sets. The LANL DDT tube CTH simulation presented in this section ran approximately 2,000 CPU hours in 2D axisymmetric coordinates to a stop time of 337 μs.

Figure 72 contains time sequence images of CTH simulation material plots. DDT tube side walls are shown in light grey, the piston impactor is dark grey, porous solid HMX is tan, and HMX gaseous products are deep pink. Deflagration begins at a simulation time of 288 microseconds at the piston edges along the DDT tube wall to porous HMX interface. The initial burning location is shown by two small pink dots on the t = 290 μs image. Burning continues to progress both inward and upward in the material images shown at t = 328 and 337 μs. The simulation was manually stopped at 337 μs due to relatively small time steps on the order of low 10^{-10} seconds. CTH simulation results at present cannot be compared to the LANL burn rate indicated in Figure 15 region "b" as 1.28 km/s because the CTH results did not form a planar progressive burn front. However, it is worth noting the burn rate range documented in (McAfee, Asay, & Campbell, 1989). Throughout their paper *McAfee et al.* provide experimental data with burn rates of: 431 m/s for shot number C-5947 (calculated by the author from plotted data), 520 m/s for shot number E-5586, and the aforementioned 1.28 km/s for shot number B-9036. Additionally, comparison of deflagration onset is

not straightforward as the CTH and LANL definitions of time zero differ. However, *McAfee et al.* note an induction time delay of approximately 300 μs for shot number B-9036 in their paper. This compares very well with the CTH induction time delay of 288 μs. Zoomed out views of material images as well as contour plots of density, pressure, and temperature are not included due to the localized burn results obtained in this simulation.

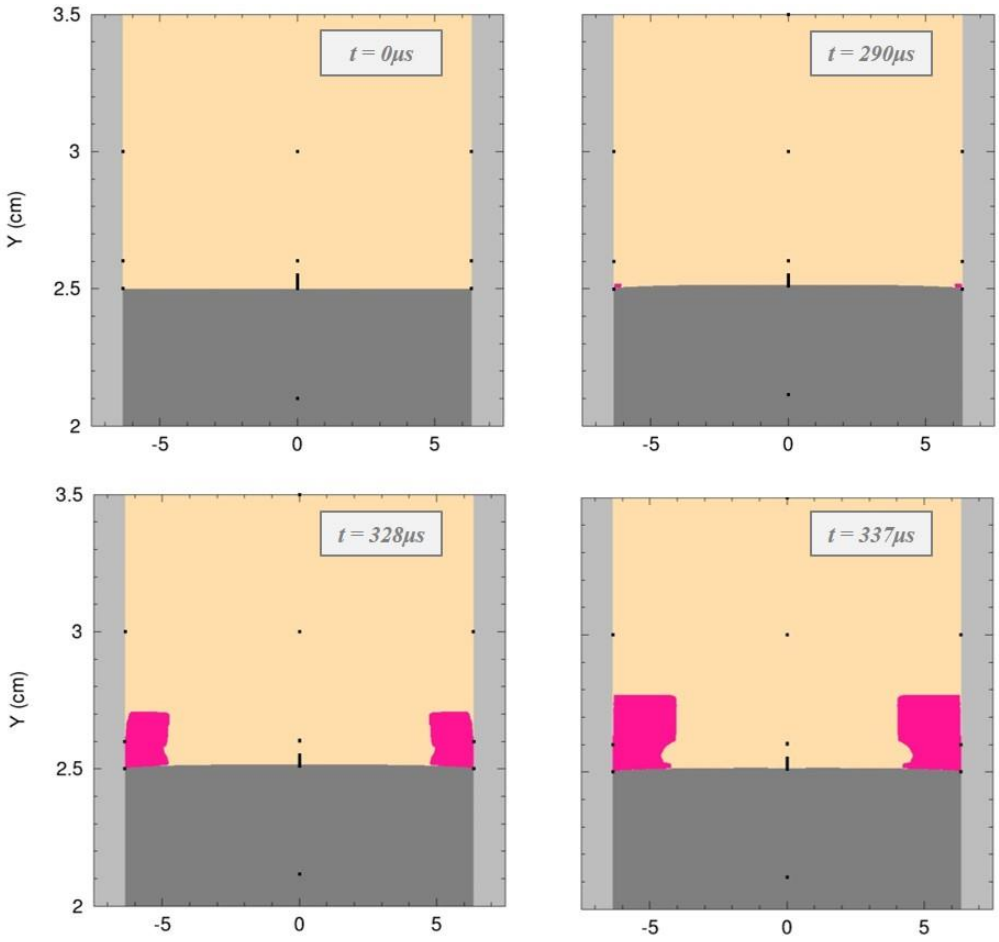

Figure 72: LANL DDT Tube: Material View

Figure 73 contains time sequence images of solid HMX density contour plots in the piston impact region. Compaction occurs primarily within the first 1 mm of the piston impact to HMX boundary. Maximum compaction occurs at a density of approximately 1.4 g/cm^3, as compared to the assumed simulation initial density of 1.2285 g/cm^3, or 65% TMD. Given the minimal localized compaction due to low velocity piston impact, the author assumes that the dominant mode of reaction initiation is due to hotspots. Density contours below are colored only for solid HMX, consequently the last image frame below shows a white region consistent with the gaseous HMX zone in the previous material images.

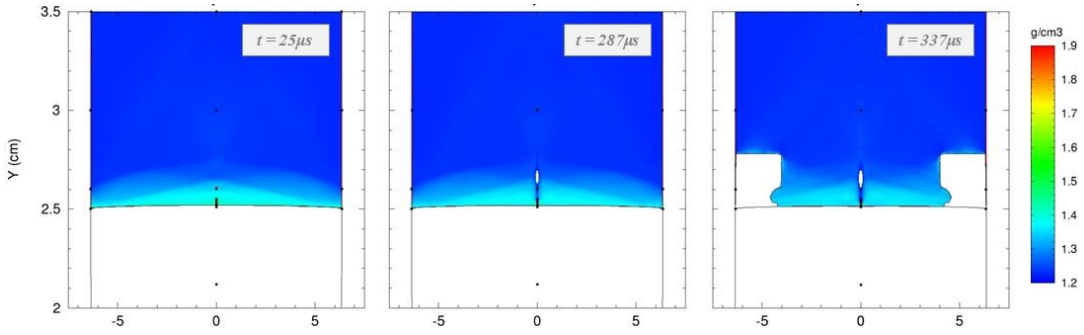

Figure 73: LANL DDT Tube: Deflagrating Density Contour Plots

Figure 74 contain time sequence images of pressure contour plots with a linear pressure scale from 100-1,000 Bar (0.1-1 kBar, 10-100 MPa). Immediately prior to reaction, a high pressure region at the intersection of the piston ends, tube wall, and porous HMX is evident in the plot at t = 287 μs. The presence of these pressure concentrations is consistent with the high pressure regions discussed in the strand burner reformulated volumetric burning model validation section. A subsequent

pressure contour plot at t = 337 μs captures pressure contours in the gaseous HMX product burning region and further shows pressure increase along the piston – HMX boundary. APPENDIX D entitled VOLUMETRIC BURNING: DDT TUBE TRACER OUTPUT contains pressure traces (and density traces) at simulated ionization pin locations (25-225 mm along the HMX column in increments on 25 mm) similar to those presented in APPENDIX C for the CTH HYDROCODE: RESEARCH GAP IDENTIFICATION chapter.

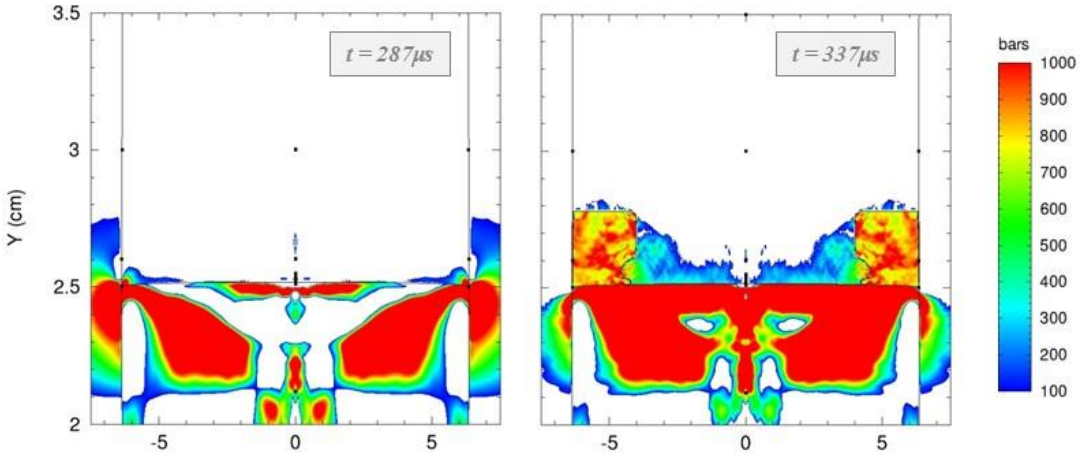

Figure 74: LANL DDT Tube: Deflagrating Pressure Contour Plots

Figure 75 provides a temperature contour at the microsecond before deflagration, t = 287 μs. This temperature contour further supports the localized high pressure region observed at the same time in the pressure contour plots above. A zoomed in view of the initiation zone shows temperature in excess of 2500 Kelvin, well above the hot spot ignition thresholds in Table 12. This figure is especially exciting as it demonstrates that the reformulated volumetric burning model is capable of modeling

macroscopic hotspot initiation for low amplitude initiation mechanisms, a major accomplishment in this dissertation.

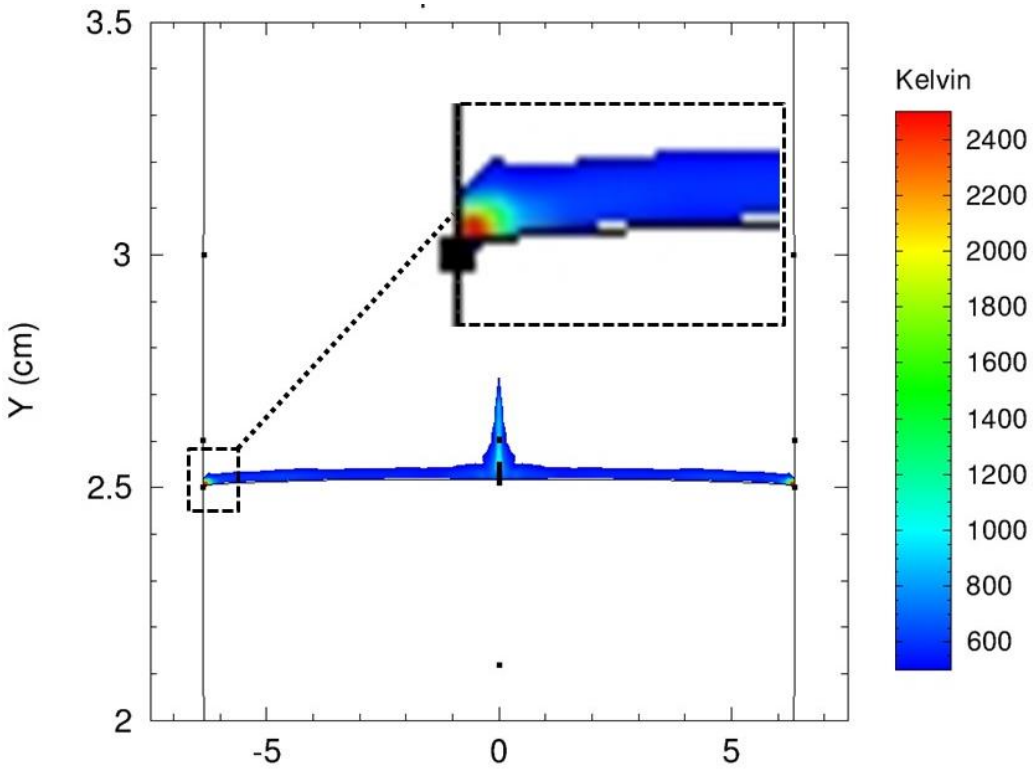

Figure 75: LANL DDT Tube: Temperature Contour Plot Immediately Prior to Deflagration.

The final figure in this section contains an updated version the plot in Figure 41 with burn front location versus time for LANL experimental shot number B-9036 results, HVRB forced detonation results, as well as the reformulated volumetric burning model computational results indicated with axis notes. The first black dot circle of experimental data corresponds to digitized results beginning with the burn region "b" in Figure 15 and progressing through "D1" and "D2" regions. LANL DDT plug theory postulates that confined granular explosives transition to detonation when shock pressure reach the 90% TMD prompt initiation limit. Additionally, this theory proposes

the propagation of a detonation wave at two distinct detonation velocities (D1 and D2) occurring by the mechanism described thusly. A compaction wave ("c" in Figure 15) travels up a DDT tube at a rate dependent on the initiation mechanism strength. Trailing this compaction wave a detonation wave forms subsequent to the DDT event. Once this detonation wave overtakes the initial plastic compaction wave the detonation wave is now consuming un-compacted granular explosive. Detonation properties such as velocity and CJ pressure are a function of local density. Lower density compacts have lower detonation velocities and pressures, thus the detonation wave slows to a second steady velocity in the un-compacted region. (McAfee, Asay, & Campbell, 1989) With the present simulation results it is not possible to make comparisons to experimental data beyond the induction time of 288 μs in CTH, stated as approximately 300 μs in (McAfee, Asay, & Campbell, 1989). The position of the axis note of the figure below could be considered misleading due to the time zero definition differences between CTH simulation and LANL experimental setup.

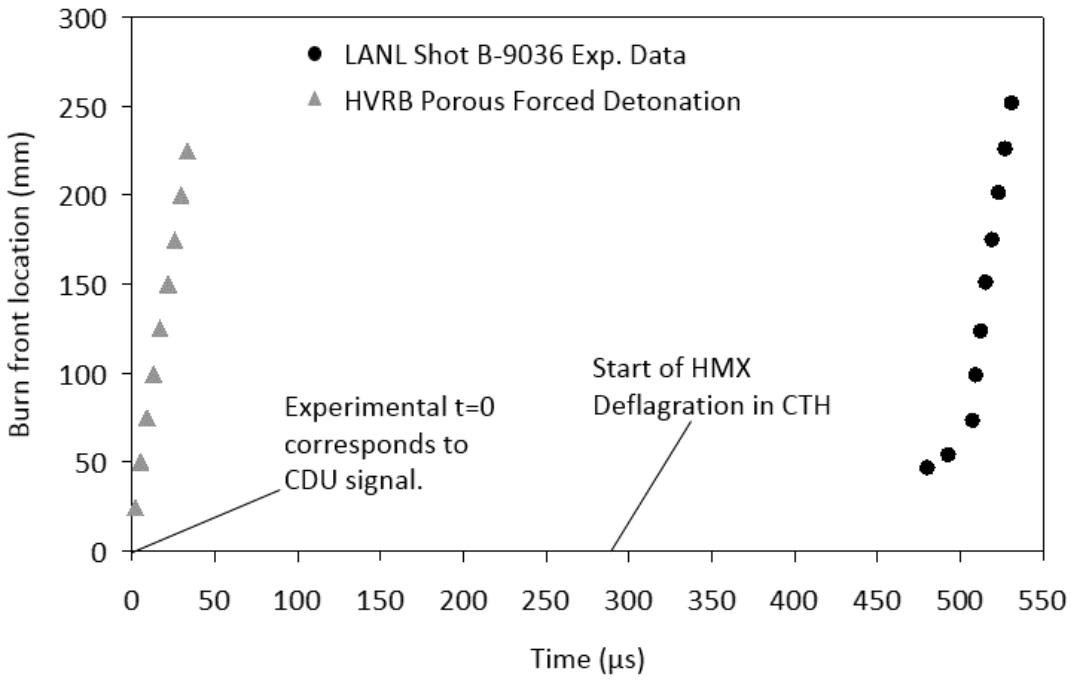

Figure 76: LANL Volumetric Burning Model Outputs vs Experimental and HVRB Forced Detonation.

Based on the CTH results for updated NSWC and LANL DDT tube simulations with validated models discussed in the present work a revised approach to DDT shock impact scenarios is proposed in the following section. It is noted however, that CTH is capable of modeling both the deflagration onset and subsequent detonation physics essential to DDT, just not (yet) within the same simulation. A combined approach is suggested.

Proposed DDT Approach

The current analytical approach for modeling a suspected shock impact DDT scenario is summarized in Figure 77. As shown in the diagram below, the process starts by first creating a computational model utilizing a reactive burn composite HVRB EOS for the energetic material. If initiation occurs in this model no further analysis is required. However, if detonation is not achieved directly with an HVRB EOS, the simulation is repeated with a Mie-Gruneisen EOS to obtain representative inert results. Data in the form of pressure as a function of penetration distance into the energetic material recorded at tracer points positioned known distances into the energetic material are compared to a Pop-plot at the closest density available in the literature. Risk assessment at this phase is heavily dependent on where CTH inert results fall when plotted with experimental Pop-plot data. If input pressure is very near the initiation line at a specified penetration distance the danger of rapid DDT scenarios is great. If input pressures are far below the initiation line at a given penetration distance the risk decreases. However, the LANL DDT tube results in the section above demonstrate that low input pressures are very much still capable of causing DDT in confined energetic material if long induction times are feasible in the specific scenario. Thus, the present analysis method is really only useful for risk level assessment, though the risk is ever present. It is not possible to rule out a DDT event with the current analysis approach.

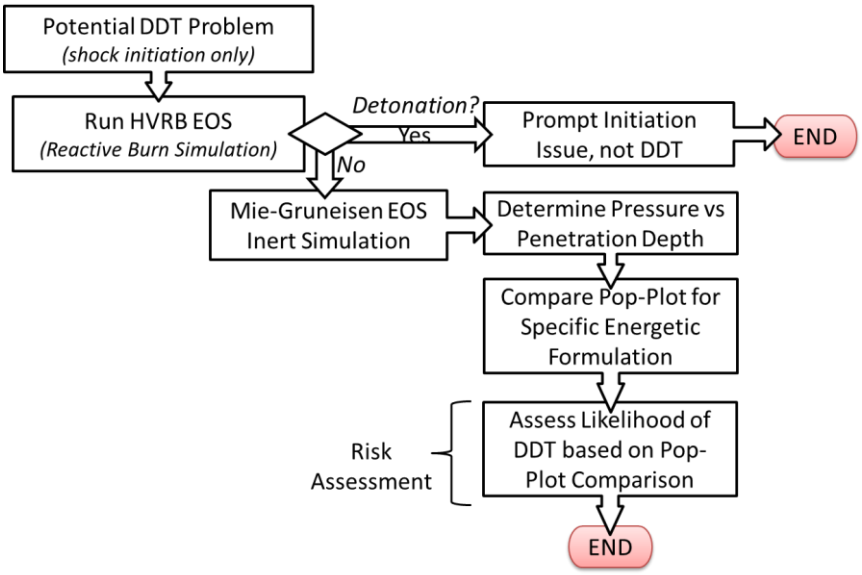

Figure 77: Current DDT Hydrocode Analysis Approach

Based on the above existing DDT CTH simulation methodology, it is evident that one primary component in Deflagration to Detonation Transition modeling, namely deflagration, is not currently included. The generation of a revised CTH hydrocode modeling methodology that addresses deflagration of granular HMX, inclusive of the lessons learned and models developed throughout this dissertation, is presented in Figure 78 with the ultimate goal of increasing simulation reliability and decreasing the need for DDT experimental testing in shock initiation scenarios. The revised approach presented in the figure below includes the addition of a method to run a simulation with the reformulated volumetric burning model (and P-α porosity, if applicable) following successful determination that detonation is not achieved with an HVRB EOS for the energetic material. Due to the computational resource intensiveness of the model revisions proposed in this body of work, it is still advisable to run a quick HVRB EOS simulation first to rule out the possibility of direct detonation. However,

if the reformulated volumetric burning model successfully identifies a deflagration risk it is not necessary to run a representative inert simulation unless comparison to a Pop-plot initiation line is desired. However, hot spot initiation is generally not captured on a Pop-plot and therefore the inert simulation may be unnecessary for risk assessment.

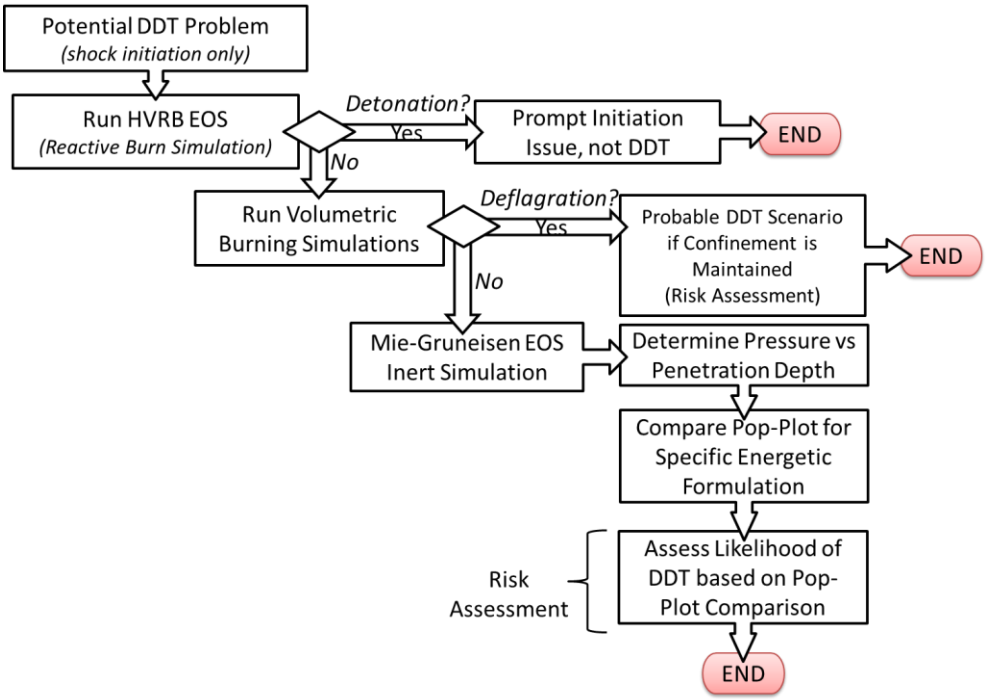

Figure 78: Revised DDT Hydrocode Analysis Methodology

This new methodology enables further predictive capability for risk assessment, decreases design lead time and increases confidence that the design will meet IM requirements. This methodology acts as a necessary bridge in the interim until a complete unified DDT modeling approach is formulated.

CHAPTER 7

CONCLUSIONS AND FUTURE WORK

CONCLUSIONS

The premise of this work was to aid in the computational prediction of IM response due to shock stimulus of granular explosives. This might include bullet impact, fragment impact or sympathetic reaction of adjacent explosives. To date, there is no successful DDT model to predict these responses owing to the challenging multi-phase physics, disparate timescales, and as discussed in this dissertation, the absence of suitable models to predict hotspot formation and growth. Instead, it is the scope of this work to delineate a practical and applicable approach that addresses the primary elements to determine if granular HMX is vulnerable to a DDT event. The impact of this work is great as it has direct applicability to current and future munitions and the very real need for insensitive munitions in our nation's (and allies) weapon's stores.

This work was successful in implementing new models and parameters that aid in the field of granular explosive DDT prediction, an active field of research since the 1950s. The focus of this research included the addition of new models to the existing equations of state in the massively parallel Linux based hydrocode CTH, after proving the existing models were not sufficient to address the whole of the DDT challenge. CTH, developed and maintained by Sandia National Laboratory, is a three-dimensional multi-material Eulerian hydrocode capable of modeling high strain rates characterized by high velocity impact, shock wave transmission through dissimilar materials and shock wave coalescence.

Much attention was paid to the analytical treatment and experimental validation of the models formulated in this dissertation. All data sets for gas gun and DDT tube experiments were not only validated, but several conditions for each experiment (when available) were run in CTH including different physical confinement configurations, different initiation methods, and different HMX densities. The sum of which demonstrates the validity of the new models and parameters and lends credence to the statement that CTH can be used as an IM predicative tool for shock initiation scenarios.

In all, this dissertation provides a clear picture of the complexities of DDT, the past excellent work that has been done in this field, and which topics should be addressed in future work. The work introduces new models and parameters that will be useful in this endeavor towards a consolidated and validated DDT model. The primary summaries, conclusions and insights can be drawn from this work are thus stated:

I. A thorough literature review is provided which highlights the challenges in DDT. The pivotal 1986 Baer-Nunziato multi-phase flow model for DDT and derived works are discussed in detail. The general understanding is that DDT occurs in four complex interacting regimes: conductive burning, convective burning, compressive burning, and detonation. The interaction of these regimes occurs with "greatly disparate time-scales" and leads to mathematical stiff solutions which are untenable in CTH.

II. Twenty-two (22) CTH simulations totaling 965 CPU-hours were run for NSWC and LANL DDT test configurations (11 for each configuration) to characterize the existing limitations of multiple EOS' including inert simulations using the Mie-Gruneisen equation of state for HMX, History

Variable Reaction Burn (HVRB) simulations and Arrhenius Reaction Burn (ARB). Multiple meshes (coarse, fine, non-uniform) and HMX densities were simulated to determine mesh size independence and confirmed with experimental data. Results for each EOS are tabulated below:

- Inert: Accurate simulation of the pyrogenic material $BKNO_3$ was demonstrated and porous energetic material compaction has been modeled (porosity and compaction will be discussed further). A 300% increase in pressure is observed when comparing the porous versus 100% TMD maximum pressure values demonstrating the effect of the porosity model.
- HVRB forced detonation: CTH is able to approximately match the slopes of the detonating portion of NSWC and LANL DDT tube data with porous compaction represented in the composite pressure dependent EOS. Figure 40 and Figure 41 on pages 89-90 note a simulated detonation velocity of 6.5 km/s for HVRB versus the experimental 6.8-6.9 km/s data for NSWC, an error of 4.4 to 5.8%. For LANL, the simulation detonation velocity was 6.3 km/s which slightly under-predicted the measured 6.36 km/s for an error of less than 1%. In all cases, especially LANL, only the detonation slope is matched, not the prior deflagration period.
- HVRB representative test cases: minimal reaction observed, EOS not suited to sustain burning.

- ARB: CTH is able to initiate reactions for high amplitude pressure wave impulses, but not for low amplitude piston driven mechanisms (likely due to lack of hot spot physics within the model). ARB simulated results were 7.1 km/s and 7.6 km/s for the deflagration porous and detonation porous simulations, respectively, versus the experimental data of 6.8-6.9 km/s for NSWC only. This over-predicts the NSWC experiments by 2.9 to 11.8% and is not able to model the LANL DDT tube experiments.

In summary, it is noted that CTH is indeed capable of modeling detonation (as it was designed for) and matches very well with existing open source experimental data once a suitable set of parameters is determined. CTH also tracks inert pressures well which is an important variable for later burning models. Moving forward, the research gap was first identified as a lack of suitable burning models to couple with detonation in a meaningful way to explore DDT. The kinetics model shows CTH cannot, as of yet, capture burning with single step Arrhenius deflagration. In the course of exploring other burning models, it was found that porosity, and hence compaction of the granular materials, plays a key role in both detonation and deflagration. This is because convective burning permeates into the HMX bed and further compacts until a TMD plug is formed. This TMD plug (caused by the burning) helped in part by the initial shock/compaction wave, will form a virtual non-permeable piston which is driven by the burning pressure until shock formation and subsequent detonation. Thus, while burning models are

important, it is equally if not more so important to first appropriately match the compaction properties of granular explosives. Likewise, detonation properties of HMX are intrinsically linked to density, and thus porosity as well.

III. Porosity was identified as a prime variable to capture for this dissertation as it enables compaction of the granular explosive which is a vital component of modeling precursory hotspots caused by hydrodynamic collapse of void regions and grain interactions. Formation of hot spots can lead to DDT of confined granular explosives. Compaction waves traveling through porous HMX were computationally modeled and validated with LANL gas gun experimental data. The method employed use of a newly generated set of P-α parameters for granular HMX in a Mie-Gruneisen equation of state. The P-α model adds a separate parameter to differentiate between the volume changes of a solid material due to compression from the volume change due to compaction, void collapse in a granular material. Computational results are compared via five validation schema for two different initial-porosity experiments. These schema include stress measurements, velocity rise times and arrival times, elastic sound speeds though the material and final compaction densities for a series of two different %TMD HMX sets of experimental data. There is a good agreement between the simulations and the experimental gas gun data with the largest source of error being an 11% overestimate of the peak stress which may be due to impedance mismatch on the experimental gauge interface.

IV. Detailed validation of the compaction model for HMX enabled use of a reformulated volumetric burning model for granular materials. Restructuring of the volumetric burn equation as a function of the constant burning surface area enabled CTH to account for increased burning surface area of the granular energetic material. P-α porosity further enabled simulation of propagation of high pressure generated by un-sustained burning on the strand surface into interstitial voids in the porous material. This combination of porosity, compaction and increased burn area results in a macroscopic approximation of hot spots, though more accurately called high pressure spots in the present work. Experimental HMX burn rate data were used to tune the new CTH model, which was validated across a range of pressures in a strand burning configuration. The CTH results match well with experimental data and are bounded by separate sources for differing HMX grain sizes up to very high pressures.

V. Lastly, the compendium of both burning and detonation was applied to the previous NSWC and LANL DDT tube experiments. Detonation was already shown to be in good agreement for both configurations, but the reformulation of a propellant damage model for granular explosive deflagration adds a new capability to CTH in the field of DDT. While a composite burning/detonation model is not tenable in the current code architecture of CTH owing to disparate timescales, it is possible to independently predict the onset of deflagration. For NSWC, which encompasses high amplitude initiation from a $BKNO_3$ charge and is characterized by high input peak pressures, CTH

shows high average deflagration rates and a compaction rate consistent with P-α porosity model plastic deformation wave speeds. The LANL DDT tube test case, which is a low amplitude initiation from a moving piston, was more surprising in that CTH was indeed able to capture high localized pressure regions characteristic of preliminary macroscopic hotspots, which later transitioned to deflagration regions. Both simulations took substantial computational resources, totaling nearly 10,000 CPU hours in two-dimensional axisymmetric coordinates. It was prohibitively large, with current resource limitations, to include the full three-dimensional simulations because of the additional computational overhead owing to the P-α porosity and volumetric burning models. Regardless, a working deflagration model for HMX was successfully reformulated and demonstrated in CTH.

VI. The current analytical methodology for DDT risk assessment was discussed which includes use of reactive burn composite HVRB EOS simulations, Mie-Gruneisen EOS to obtain representative inert results and final comparisons to Pop-plots. A revised approach was presented which supplemented the current methodology with the addition of a task to run a simulation with the reformulated volumetric burning model (and P-α porosity, if applicable) following successful determination that detonation is not achieved with an HVRB EOS for the energetic material. In this way it is possible to redesign until the criteria for both detonation and deflagration onset are satisfied. This robust hydrocode methodology was proposed to make use of the deflagration,

compaction, and detonation models as a means to predict IM response to shock stimulus of granular explosive materials.

In closing, it was demonstrated that CTH is a useful predictive tool for related shock initiation scenarios. Both detonation and deflagration of the well-known granular explosive HMX were simulated and validated with empirical data from multiple sources. The models and parameters presented herein will be useful in the ultimate goal of a unified DDT model. Results are applicable to both pressed pellet and damaged explosive approximations. Future work remains for further validation, especially with regards to different configurations and explosive materials. This dissertation proposed new computational methodologies and validated models that will aid in predicting shock stimulus IM response and drive the designer to safer and more reliable products.

REFERENCES

Aldis, D. F., Lee, E. L., Simpson, R. L., & Weston, A. M. (1989). Model Calculations and Experimental Measurements of the Response of HMX Porous Beds to Deflagration and Shock. *Ninth Symposium on Detonation*.

Atwood, A. I., Boggs, T. L., Curran, P. O., Parr, T. P., Hanson-Parr, D. M., Price, C. F., & Wiknich, J. (1999). Burning Rate of Solid Propellant Ingredients, Part I: Pressure and Initial Temperature Effects. *Journal of Propulsion and Power*, 740-747.

Baer, M. R., & Nunziato, J. W. (1986). A Two-Phase Mixture Theory for the Deflagration-to-Detonation Transition (DDT) in Reactive Granular Materials. *International Journal of Multiphase Flow,* Vol 12. No. 6. pp 861-889.

Baer, M. R., & Nunziato, J. W. (1989). Compressive Combustion of Granular Materials Induced by Low-Velocity Impact. *9th International Symposium on Detonation,* (pp. 293-305). Portland, Oregon.

Baer, M. R., Gross, R. J., & Nunziato, J. W. (1986). An Experimental and Theoetical Study of Deflagration to Detonation Transition in the Granular Explosive. *Combustion and Flame,* 15-30.

Baer, M. R., Hertel, E. S., & Bell, R. L. (1996). Multidimensional DDT Modeling of Energetic Materials. *American Institute of Physics*, 433-436.

Baer, M. R., Kipp, M. E., & van Swol, F. (1998). Micromechanical Modeling of Heterogeneous Energetic Materials. *11th Symposium on Detonation.* Snowmass, CO.

Bdzil, J. B., Menikoff, R., Son, S. F., Kapila, A. K., & Stewart, D. S. (1999). Two-Phase Modeling of Deflagration to Detonation Transition in Granular Materials: A Critical Examination of Modeling Issues. *Physics of Fluids,* 378-402.

Beauregard, R. (n.d.). *The History of Insensitive Munitions*. Retrieved August 2014, from Insensitive Munitions: http://www.insensitivemunitions.org

Beckstead, M. W., Peterson, N. L., Pilcher, D. T., Hopkins, B. D., & Krier, H. (1977). Convective Combustion Modeling Applied to Deflagration to Detonation Transition of HMX. *Combustion and Flame*, 231-241.

Berg, C. M., & Dlott, D. D. (2014). Picosecond Dynamics of Shock Compressed and Flash-Heated Nanometer Thick Films of Delta-HMX. *Journal of Physics: Conference Series 500 (2014) 142004.* IOP Publishing.

Bernecker, R. R., & Price, D. (1972). *Transition from Deflagration to Detonation in Granular Explosives.* White Oak, Maryland: Naval Ordnance Laboratory.

Bernecker, R. R., & Price, D. (1974). Studies in the Transition from Deflagration to Detonation in Granular Explosives - I. Experimental Arrangement and Behavior of Explosives Which Fail to Exhibit Detonation. *Combustion and Flame*, 111-118.

Bernecker, R. R., & Price, D. (1974). Studies in the Transition from Deflagration to Detonation in Granular Explosives - II. Transitional Characteristics and Mechanisms Observed in 91/9 RDX/Wax. *Combustion and Flame*, 119-129.

Bernecker, R. R., & Price, D. (1974). Studies in the Transition from Deflagration to Detonation in Granular Explosives - III. Proposed Mechanisms for Transition and Comparison with Other Proposals in the Literature. *Combustion and Flame*, 161-170.

Bourne, N. K., & Milne, A. M. (2004). Shock to Detonation Transition in a Plastic Bonded Explosive. *Journal of Applied Physics*, 2379-2385.

Butler, P. B., & Kriar, H. (1984). *Analysis of Deflagration to Detonation Transition in High-Energy Solid Propellants.* Urbana, IL: University of Illinois at Urbana-Champaign.

Carleone, J. (1993). *Tactical Missile Warheads.* AIAA Progress in Aeronautics and Astronautics.

Carroll, M. M., & Holt, A. C. (1971). Static and Dynamic Pore-Collapse Relations for Ductile Porous Materials. *Journal of Applied Physics*, 1626-1636.

Cooper, P. W. (1996). *Explosives Engineering.* New York: Wiley-VCH.

Crawford, Brundage, Harstad, Ruggirello, Schmitt, Schumacher, & Simmons. (2012). *CTH User's Manual and Input Instructions.* Albuquerque, New Mexico: CTH Development Project, Sandia National Laboratories.

Crawford, D. (2011). *CTH Course Notes.* Albuquerque, New Mexico: Sandia National Laboratories.

Dick, J. J. (1983). Measurement of the Shock Initiation Sensitivity of Low Density HMX. *Combustion and Flame*, 121-129.

Dobratz, B. M., & Crawford, P. C. (1985). *LLNL Explosives Handbook.* Livermore, CA: Lawrence Livermore National Laboratory.

Dudley, E., Damm, D., & Welle, E. (2010). Characterization of Physical Processes during Thin-Pulse Initiation of HNS. *14th International Detonation Symposium*, 622-630.

Elban, W. L., & Chiarito, M. A. (1986). Quasi-Static Study of Coarse HMX Explosive. *Powder Technology*, 181-193.

Erikson, W. W. (2000). *Implementation of Time Dependent form of JWL equation of state into CTH.* Albuquerque, New Mexico: Sandia National Labs.

Esposito, A. P., Farber, D. L., Reaugh, J. E., & Zaug, J. M. (2003). Reaction Propagation Rates in HMX at High Pressure. *Propellants, Explosives, Pyrotechnics*, 83-87.

Grebenkin, K. F., Taranik, M. V., Tsarenkova, S. K., & Shnitko, A. S. (2008). Physical Model of Low-Velocity Detonation in Plasticized HMX. *Combustion, Explosion, and Shock Waves*, 92-100.

Griffiths, N., & Groocock, J. M. (1960). The Burning to Detonation of Solid Explosives. *Journal of the Chemical Society*, 4154-4162.

Hall, T. N., & Holden, J. R. (1988). *Navy Explosives Handbook.* Silver Spring, MD: Naval Surface Warfare Center.

Henson, B. F., Asay, B. W., Smilowitz, L. B., & Dickson, P. M. (2001). *Ignition Chemistry in HMX from Thermal Explosion to Detonation.* Los Alamos, NM: Los Alamos National Laboratory.

Herrmann, W. (1969). Constitutive Equation for the Dynamic Compaction of Ductile Porous Materials. *Journal of Applied Physics*, 2490-2499.

Hertel, E. S. (1998). *CTH Reference Manual: The Equation of State Package.* Albuquerque, New Mexico: CTH Development Project Sandia National Labs.

Hertel, E., & Kerley, G. (1998). *CTH EOS Package; Introductory Tutorial.* Albuquerque, New Mexico: Sandia National Laboratories.

Hertel, E., & Kerley, G. (1999). *Recent Improvements to the CTH EOS Package.* Albuquerque, New Mexico: Sandia National Laboratories.

Hubbard, H. W., & Johnson, M. H. (1959). Initiation of Detonations. *Journal of Applied Physics*, 765-769.

Jaspers, S. F., & Dautzenberg, J. H. (2001). Material Behaviour in Conditions Similar to Metal Cutting: Flow Stress in the Primary Shear Zone. *Journals of Materials Processing Technology*, 322-330.

Kamlet, M. J., & Jacobs, S. J. (1967). *The Chemistry of Detonations; A Simple Method for Calculating Detonation Properties of C-H-N-O Explosives.* White Oak, MD: United States Naval Ordance Laboratory.

Kamlet, M. J., & Short, J. K. (1980). The Chemistry of Detonations. VI. A "Rule for Gamma" as a Criterion for Choice Among Conflicting Detonation Pressure Measurements. *Combustion and Flame*, 221-230.

Kapila, A. K., Menikoff, R., Bdzil, J. B., Son, S. F., & Stewart, D. S. (2001). Two-Phase Modeling of Deflagration to Detonation Transition in Granular Materials: Reduced Equations. *Physics of Fluids*, 3002-3024.

Kennedy, D. (1993). Warheads: An Historical Perspective. In J. Carleone, *Tactical Missile Warheads* (pp. 14, 27, 82). AIAA Progress in Aeronautics and Astronautics.

Kerley, G. (1992). *CTH Equation of State Package: Porosity and Reactive Burn Models.* Albuquerque. New Mexico: Sandia National Laboratories.

Kerley, G. I. (2006). *The Linear Us-Up Relation in Shock-Wave Physics.* Appomattox, VA: Kerley Technical Services.

Kubota, N. (2002). *Propellants and Explosives: Thermochemical Aspects of Combustion.* Weinheim, Germany: Wiley-VCH GmbH.

Lawrence Livermore. (2012). *Cheetah 7.0.* Livermore, CA: Lawrence Livermore National Laboratories.

Lee, E. L., & Tarver, C. M. (1980). Phenomenological Model of Shock Initiation in Heterogeneous Explosives. *Physics of Fluids*, 2362-2372.

Mahon, K. S. (2014). Temperature Dependent Hydrocode Analysis of Explosives. *Mechanical, Materials and Structures Technology Network Symposium.* Tewksbury, MA.

Mahon, K. S. (2015). Compaction of Granular HMX: A P-alpha Porosity Model in CTH Hydrocode. *Submitted to AIP Advances*.

Mahon, K. S., & Paine, G. H. (2014). Hydrocode Analysis of Explosive Shock Damping Materials. *Mechanical, Materials and Structures Technology Network Symposium.* Tewksbury, MA: Raytheon Company.

Maienschein, J. L. (2014). Research Topics in Explosives - A Look at Explosive Binders. *Journal of Physics*, 1-8.

Margolis, S. B., & Williams, F. A. (1996). Effect of Gas-Phase Thermal Expansion on Stability of Deflagration in Porous Energetic Materials. *International Journal of Multiphase Flow*, 69-91.

Margolis, S. B., Telengator, A. M., & Williams, F. A. (2001). *Influences of Confinement on the Structure and Stability of Deflagrations in Confined Porous Energetic Materials.* Sandia National Laboratories.

Marsh, S. P. (1980). *LASL Shock Hugoniot Data.* Berkeley and Los Angeles, CA: University of California Press.

Marshall, W. W. (1970). The Role of Interstitial Gas in the Detonation Build-up Characteristics of Low Density Granular HMX. *5th Symposium on Detonation* (pp. 247-249). Arlington, Virginia: Office of Naval Research.

Marshall, W. W. (1970). The Role of the Matrix in Determining the Shock Initiation Characteristics of Compositions Containing 60% by Volume of HMX. *5th Symposium on Detonation* (pp. 185-189). Arlington, Virginia: Office of Naval Research.

Matweb. (2014). *Matweb.com*. Retrieved from www.matweb.com

McAfee, J. M., Asay, B. W., & Bdzil, J. B. (1993). Deflagration-to-Detonation in Granular HMX: Ignition, Kinetics, and Shock Formation. *10th International Detonation Symposium*, (pp. 716-723). Boson, MA.

McAfee, J. M., Asay, B. W., & Campbell, A. W. (1989). Deflagration to Detonation in Granular HMX. *9th Symposium on Detonation* (pp. 265-279). Portland, Oregon: Office of Naval Research.

Menikoff, R. (2001). Compaction Wave Profiles: Simulations of Gas Gun Experiments. *Journal of Applied Physics*, 1754-1760.

Menikoff, R., & Kober, E. (1999). *Compaction Waves in Granular HMX.* Los Alamos, NM: Los Alamos National Laboratory.

Miller, P. J., & Guirguis, R. H. (1993). Experimental Study and MOdel Calculations f Metal Combustion in Al/AP Underwater Explosives. *Material Research Society Symposium*, (pp. 299-304).

Miller, P. J., & Guirguis, R. H. (1993). Experimental Study and Model Calculations of Metal Combustion in Al/AP Underwater Explosives. *Material Research Society Symposium*, (pp. 299-304).

(2011). *MIL-STD-2105D: Hazard Assessment Tests for Non-Nuclear Munitions.* Department of Defense.

Mitani, T., & Williams, F. A. (1986). A Model for the Deflagration of Nitramines. *Twenty-first Symposium on Combustion*, 1965-1974.

Nichols, A. L., Wallin, B. K., Maienschein, J. L., Reaugh, J. E., Yoh, J. J., & McClelland, M. E. (2005). Hazards Response of Energetic Materials - Developing a Predictative Capability for Initiation and Reaction under Multiple Stimuli. *36th International ICT-Conference & 32nd International Pyrotechnics Seminar.* Karlsruhe, Germany.

Power, J. M., Stewart, D. S., & Krier, H. (1989). Analysis of Steady Compaction Waves in Porous Materials. *Journal of Applied Mechanics*, 15-24.

Price, D., & Bernecker, R. R. (1975). Sensitivity of Porous Explosives to Transition from Deflagration to Detonation. *Combustion and Flame*, 91-100.

Price, D., & Bernecker, R. R. (1977). *DDT Behavior of Waxed Mixtures of RDX, HMX, and TETRYL.* Dahlgren, Virginia: Naval Surface Weapons Center.

Sandia. (1995). *CTH 10.2: VP Data File.* Albuquerque, NM: Sandia National Laboratories.

Sandia. (2006). *CTH 10.2: Equation of State Data File.* Albuquerque, NM: Sandia National Labs.

Sandusky, H. W., & Bernecker, R. R. (1985). Compressive Reaction in Porous Beds of Energetic Materials. *8th International Symposium on Detonation*, (pp. 881-891). Alburquerque, NM.

Sandusky, H. W., & Liddiard, T. P. (1985). *Dynamic Compaction of Porous Beds.* Dahlgren, Virginia: Naval Surface Weapons Center.

Saw, C. K. (2002). Kinetics of HMX and Phase Transitions: Effects of Grain Size at Elevated Temperature. *12th IDS 2002.*

Segletes, S. B. (1991). *An Analysis on the Stability of The Mie-Gruneisen Equation of State for Describing the Behavior of Shock-Loaded Materials.* Aberdeen Proving Ground, Maryland: Ballistic Research Laboratory.

Sewell, T. D., & Menikoff, R. (2003). A Molecular Dynamics Simulation Study of Elastic Properties of HMX. *Journal of Chemical Physics*, 7417-7426.

Sheffield, S. A., Gustavsen, R. L., & Anderson, M. U. (1997). Shock Loading of Porous High Explosives. In L. Davison, Y. Horie, & M. Shahinpoor, *High-Pressure Shock Compression of Solids IV - Response of Highly Porous Solids to Shock Loading* (pp. 23-61). New York: Springer-Verlag.

Silling, S. (1996). *Use of the Johnson-Cook Fracture Model in CTH.* Albuquerque, New Mexico: Sandia National Laboratories.

Sinditskii, V. P., Egorshev, V. Y., Berezin, M. V., & Serushkin, V. V. (2009). Mechanism of HMX Combustion in a Wide Range of Pressures. *Combustion, Explosion, and Shock Waves*, 461-477.

Sinditskii, V. P., Egorshev, V. Y., Serushkin, V. V., Levshenkov, A. I., Berezin, M. V., Filatov, S. A., & Smirnov, S. P. (2009). Evaluation of Decomposition Kinetics of Energetics Materials in the Combustion Wave. *Thermochimica Acta*.

Son, S. F., Kober, E. M., & Bdzil, J. B. (1997). *DDT in Reactive Granular Materials: Model Comparison with Experiments.* Los Alamos, New Mexico: Los Alamos National Laboratory.

Starkenberg, J. (2002). Modeling Detonation Propagation and Failure Using Explosive Initiation Models in a Conventional Hydrocode. *12th Symposium on Detonation*, (pp. 219-227). San Diego CA.

Stewart, D. S., Asay, B. W., & Prasad, K. (1994). Simplified Modeling of Transition to Detonation in Porous Energetic Materials. *Physics of Fluids*, 2515-2534.

Sulimov, A. A., Ermolaev, B. S., Borisov, A. A., Korotkov, A. I., Khasainov, B. A., & Khrapovksy, V. E. (1976). On the Mechanism of Deflagration to Detonation Transition in Gas-Permeable High Explosive. *Sixth Symposium on Detonation*, 250-257.

Sutton, G. P., & Biblarz, O. (2010). *Rocket Propulsion Elements, 8th Edition.* Hoboken, New Jersey: John Wiley & Sons.

Tarver, C. M., & Green, L. G. (1989). Using Small Scale Tests to Estimate the Failure Diameter of a Propellant. *Ninth Symposium on Detonation*, 701-710.

Tarver, C. M., & Tran, T. D. (2004). Thermal Decomposition Models for HMX-based Plastic Bonded Explosives. *Combustion and Flame*, 50-62.

Tarver, C. M., Hallquist, J. O., & Erickson, L. M. (1985). Modeling Short Pulse Duration Shock Initiation of Solid Explosives. *Eight Symposium on Detonation*, 951-961.

Taylor, P. (1992). *CTH Reference Manual: The Steinberg-Guinan-Lund Viscoplastic Model.* Albuquerque, New Mexico: Sandia National Laboratories.

Thanh, M. D., Kroner, D., & Chalons, C. (2012). A Robust Numberical Method for Approximating Solutions of a Model of Two-Phase Flows and its Properties. *Applied Mathematics and Computation*, 320-344.

Tindle, J. R., & Zeman, A. R. (1991). *A Historical Perspective of Insensitive Munitions and Their Estimated Contribution to CV Safety.* Center for Naval Analyses: CRM 90-260.

Udd, E., Dunaway, D., Biegert, L., & Johnson, E. (2011). Innovative Sensor to Measure Detonation Properties of Propellants. *JANNAF*.

Walley, S. M., Field, J. E., & Greenaway, M. W. (2006). Crystal Sensitivities of Energetic Materials. *Materials Science and Technology*, 402-413.

Wang, S. Y., Butler, P. B., & Krier, H. (1985). Non-Ideal Equations of State for Combusting and Detonating Explosives. *Prog. Energy Combust. Sci.*, 311-331.

Wang, Z., & Chen, Z. (1991). Deflagration to Detonation Transition Study in Mixed HMX Bed. *Combustion and Reaction Kinetics*, (pp. 91:1 - 91:10). Karlsruhe, Germany.

Ward, M. J., Son, S. F., & Brewster, M. Q. (1998). Steady Deflagration of HMX with Simple Kinetics: A Gas Phase Chain Reaction Model. *Combustion and Flame*, 556-568.

Xu, S., & Stewart, D. S. (1997). Deflagration to Detonation Transition in Porous Energetic Materials: A Comparative Model Study. *Journal of Engineering Mathematics*, 143-172.

Yang, L. C. (2008). Deflagration to Detonation Transition in Detonation Energetic Components. *AIAA Joint Propulsion Conference.* Hartford, CT.

Yang, L. C. (2009). Frequency Factor in Arrhenius Decomposition Kinetics for Insensitive Energetic Materials. *AIAA Joint Propulsion Conference.* Denver, Colorado.

Yoh, J. J., & Kim, K.-h. (2008). Shock Compression of Condensed Matter using Eulerian Multimaterial Method: Applications to Multidimensional Shocks, Deflagration, Detonation, and Laser Ablation. *Journal of Applied Physics*.

Yoh, J. J., McClelland, M. A., Maienschein, J. L., Wardell, J. F., & Tarver, C. M. (2005). Simulating Thermal Explosion of Cyclotrimethylenetrinitramine-based Explosives: Model Comparison with Experiment. *American Institute of Physics*, 083504-1 to 11.

Yoh, J. J.-i., McClelland, M. A., Maienschein, J. L., & Tarver, C. M. (2005). Test-based Thermal Explosion Model for HMX. *Combustion Institute*, 2353-2359.

Zel'dovich, Y. B. (1966). *Physics of Shock Waves and High-Temperature Hydrodynamics Phenomena.* Mineola, New York: Dover Publications, Inc.

Zenin, A. A., & Finjakov, S. V. (2007). Response Functions of HMX and RDX Burning Rates with Allowance for Melting. *Combustion, Explosions, and Shock Waves*, 309-319.

Zerilli, F. J. (1981). *Notes from Lectures on Detonation Physics.* Dahlgren, Virginia: Naval Surface Weapons Center.

APPENDIX A

THOROUGH LITERATURE REVIEW

As discussed in the introduction, DDT is a research problem that has been in continuous study since the late 1950s. The aim of this literature review is to summarize key milestones and research approaches to DDT as it relates to granular secondary explosives, specifically HMX, both in terms of modeling and experiment. DDT can, in very simplified terms, be broken into three fundamental topics: deflagration, a transition mechanism from deflagration to detonation, and subsequent detonation. These topics will be explored in greater detail throughout the following three sub-sections.

DETONATION OF HIGH EXPLOSIVES

Given that the primary design intent behind the synthesis of granular explosives is to achieve detonation, of the three aforementioned DDT problem segments, detonation of granular secondary explosives is by far the best characterized. Only the implementation of numerical detonation models in existing hydrocodes will be discussed in this portion of the literature review as the aim of this dissertation is to develop a robust DDT model in an Eulerian hydrocode. Numerous detonation models of varying fidelity exist within the literature and are currently implemented in widely used hydrocodes today. The most commonly used hydrocode detonation models include: the Jones Wilkins Lee (JWL) model, Ignition and Growth model, History Variable Reactive Burn (HVRB) model, and the Arrhenius decomposition kinetics based reactive burn model. These models were primarily developed at Sandia National Laboratory or Lawrence Livermore National Laboratory, with the notable exception of the Arrhenius rate equation. Hydrocode detonation models can be subdivided into two categories, either idealized detonation or reactive burn. The difference between the two modeling approaches lies in the treatment of the detonation wave reaction zone.

Idealized detonation models assume the detonation wave front is modeled as a jump discontinuity, reaction products are in chemical and thermodynamic equilibrium, a steady-state detonation condition exists, and the detonation velocity is constant. These assumptions imply that the detonation wave shape remains constant throughout propagation of the computational domain until boundary conditions, additional detonation waves, or rarefaction waves are encountered. The P-v plane Hugoniot curves from (Cooper, 1996, p. 254) in Figure 79 offer a graphical depiction of the jump discontinuity from unreacted to reacted states in a detonation. A model for steady state detonation conditions was developed by Chapman and Jouguet in the late 1800s and is commonly referred to as the CJ state. (Cooper, 1996) Alternatively, the CJ state is succinctly defined in (Kamlet & Jacobs, 1967) as the "minimum detonation velocity compatible with conservation conditions for sonic flow behind the discontinuity in a reference frame where the discontinuity is at rest."

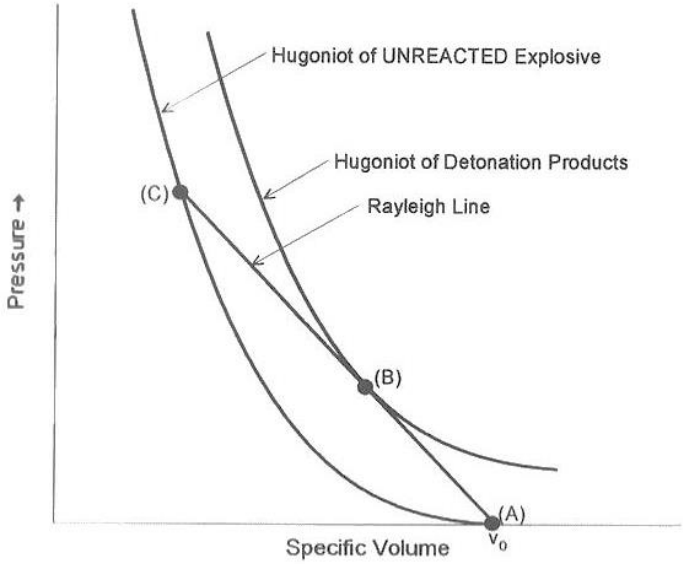

Figure 79: P-v Plane Hugoniot Curves of Detonation (Cooper, 1996, p. 254)

Simplified first order one dimensional approaches to idealized detonation were simultaneously formulated by Zel'dovich, Von Neumann, and Deering in the 1940s. (Cooper, 1996, p. 253) In Zel'dovich's 1946 model he applies assumptions of reversible chemical reactions and molecular vibrational mode excitation to a shock front propagating through a gas. He defines two regions of gas excitation, where one region has quickly excited gas dynamic degrees of freedom and a second region requires numerous kinetic collisions to achieve excited states. In this model the rapidly excited region represents the shock front and the slower chemistry region is the post-compression shock relaxation region. (Zel'dovich, 1966)

Jones, Wilkins and Lee developed one of the most widely implemented idealized detonation models while working at Lawrence Livermore National Laboratory. A version of the JWL equation with an additional λQ term added by the U.S. Navy's White Oaks Laboratory to account for the late energy release associated with aluminized explosives is given in the two equations below. The variables A and B are adjustable parameters, ω is the Gruneisen coefficient, and R_1 and R_2 are test cylinder radii. This equation is generally characterized with cylinder expansion data where a hollow metal cylinder is packed with an explosive core and initiated on one end. Data for the cylinder expansion as a function of time are recorded and used to calibrate JWL parameters. [(Miller & Guirguis, 1993) , (Crawford, et al., 2012) , (Hertel E. S., 1998) , (Erikson, 2000)]

$$P = A\left(1 - \frac{\omega}{R_1 v}\right)e^{-R_1 v} + B\left(1 - \frac{\omega}{R_2 v}\right)e^{-R_2 v} + \frac{\omega}{v}(E + \lambda Q) \qquad [1]$$

Where

$$\frac{d\lambda}{dt} = a(1-\lambda)^{1/2}\, p^{1/8} \qquad [2]$$

In general, idealized detonation models such as the JWL model are useful when the exact point of initiation and general detonation wave shape are known or can be reasonably assumed.

Unlike idealized detonation models, reactive burn models are capable of modeling detonation in reaction to surrounding computational stimuli, for example due to incoming shock waves from high velocity impact or local detonations. These models take into account a peak leading detonation wave pressure known as the Von Neumann spike followed by a thin reaction zone with a corresponding pressure gradient prior to detonation products reaching steady state. [(Cooper, 1996) , (Zerilli, 1981)] The presence of a Von Neumann spike requires a finite reaction zone thickness and is not accounted for in idealized detonation models. A generalized plot of pressure versus distance for a detonation wave is included in Figure 80 for clarity.

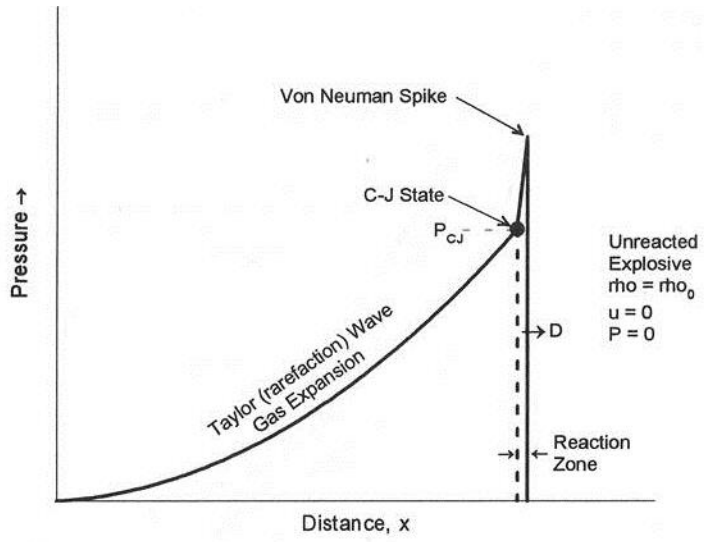

Figure 80: Pressure versus Distance CJ State Explanation. (Cooper, 1996, p. 256)

Arrhenius reactive burn is the oldest of the three most common reactive burn model types. This model is based on the Arrhenius equation developed by the Swedish chemist Svente Arrhenius in the early 1900s. The Arrhenius decomposition rate equation is given in its simplest

form in below, where k is the reaction rate constant, A is the pre-exponential factor, E_a is activation energy, R is the universal gas constant, and T is temperature. (Yang, 2009)

$$k = Ae^{-E_a/RT} \quad [3]$$

This equation has been adapted, to varying degrees of complexity, for implementation in modern day hydrocodes. Arrhenius decomposition reactions can be written in terms of global reactions where the pre-exponential factor is scaled to account for the rate of molecular collisions and the activation energy threshold is reaction mechanism specific. *Yang's* 2009 paper provides a thorough examination of the pre-exponential frequency factor in terms of statistical mechanics. (Yang, 2009) In terms of detonation modeling, the Arrhenius reactive burn model can be used to model a one-step global reaction from unreacted to final states, as in reference (Mahon, 2014) for RDX detonation. Alternatively, detonation reactions can be broken into multi-step global reaction models, as in the work of (Lee & Tarver, 1980). In *Tarver's* multi-step model he divides HMX detonation into four global decomposition reactions: β HMX crystal phase to δ HMX crystal phase, δ HMX crystal phase to solid intermediates, solid intermediates to gaseous intermediates, and gaseous intermediates to final products. (Tarver & Tran, 2004) While the multi-step global reaction models have higher fidelity, the only hydrocode the author is aware of that is capable of modeling multi-step global Arrhenius decomposition reactions is ALE3D developed and maintained by Lawrence Livermore National Laboratory.

The Ignition and Growth reactive burn model was developed by *Lee and Tarver* of Lawrence Livermore National Laboratory in the late 1970s and is also referred to in the literature as the Lee-Tarver model. (Hertel E. S., 1998) Lee and Tarver's original Ignition and Growth model shown in the following equation from (Lee & Tarver, 1980) contained two reaction steps: an ignition phase and a subsequent growth phase. In this equation F is the reacted explosive fraction,

η is the relative compression of unreacted explosive, G is a surface area to volume ratio constant, V_0 is the explosive initial specific volume, V_1 is the shocked yet unreacted explosive specific volume, p is pressure and I, x, y, and r are constants.

$$\frac{\delta F}{\delta t} = I(1-F)^x \left(\frac{V_0}{V_1} - 1\right)^r + G(1-F)^x F^y p^z, \qquad \eta = \frac{V_0}{V_1} - 1 \qquad [4]$$

The first term in the above equation represents ignition of hot spots during void collapse or closure and the second term models growth of the reaction throughout the unreacted explosive. (Lee & Tarver, 1980) Subsequent work by *Lee and Tarver* modified their original Ignition and Growth model to account for short pulse duration shock initiation and further extend the applicability of the model beyond explosives to propellants. [(Hertel E. S., 1998), (Tarver, Hallquist, & Erickson, 1985), (Tarver & Green, 1989)]

The History Variable Reactive Burn (HVRB) model is specific to the hydrocode CTH and frequently used in the analysis field to model detonations. [(Hertel E. S., 1998), (Kerley G. , 1992)] HVRB calculates an extent of reaction, λ, given as a function of a pressure dependent history variable, φ, as shown in the two subsequent equations. (Starkenberg, 2002) Parameter sets for the HVRB model can be generated from and tuned with Pop-plot data. *Dudley's* 2010 International Detonation Symposium paper discusses HVRB parameter tuning in greater detail. (Dudley, Damm, & Welle, 2010)

$$\lambda = 1 - \left(1 - \frac{\varphi^{n_\varphi}}{n_\lambda}\right)^{n_\lambda} \qquad [5]$$

Where:

$$\phi = \int_0^t \left(\frac{p - p_i}{p_s}\right)^{n_p} \frac{d\tau}{\tau_s} \qquad [6]$$

DEFLAGRATION OF HIGH EXPLOSIVES

Deflagration of high explosives has come into prominence as a field of study for two primary reasons. Further understanding of the deflagration properties of high explosives became desirable when explosives such as nitroglycerin, RDX, and HMX began being used in double base propellants to increase burn rate and energetic output. Additional concerns relating to explosive combustion are also due to Insensitive Munitions issues and qualification testing requirements addressed in the Introduction. Literature references for HMX deflagration begin in the 1970s and are still a popular area of publication.

Testing of explosive deflagration is similar to that of propellant characterization. Experiments are generally conducted to measure burn rate data, also known as reaction propagation rate, as a function of pressure in a closed bomb type apparatus. Results are reported based on the composition of the explosive test sample in terms of density percentage of theoretical maximum density (TMD) and energetic material grain size distribution. The literature contains several excellent references for HMX burn rate data, where references characterizing the pressure range of 0.01 MPa to 35 GPa are summarized below. *Esposito, et al's* 2003 paper presents experimentally determined HMX reaction propagation rates for both large grain sample (65% of grains larger than 10 μm) and small grain sample (90% of grains smaller than 10 μm) over a pressure range of 0.7 to 35 GPa. This testing was conducted at Lawrence Livermore National Laboratory. Over the experimental pressure range the reaction propagation rate increases nearly monotonically with pressure, where the high end bound of their pressure testing is near the value of HMX's CJ pressure. (Esposito, Farber, Reaugh, & Zaug, 2003) Further experimental study HMX's burn rate is presented in a 2009 publication by *Sinditskii* with testing conducted in conjunction with Mendeleev University of Chemical Technology in Moscow. Temperature and

burn rate data from constant pressure bomb studies were obtained over a pressure range from 0.01 MPa to 100 MPa with additional study of the influence of initial sample temperature on burn rate in the initial temperature range of 150 to approximately 425 K over a pressure range of 1 to 10.34 MPa. (Sinditskii, Egorshev, Berezin, & Serushkin, 2009) *Sinditskii* further applies these experimental results for both burning rate and grain surface temperature to derive decomposition kinetics of HMX in reference (Sinditskii, et al., 2009).

Throughout the period of study of HMX deflagration several combustion mechanisms have been proposed that make different assumptions about the convective and conductive burning phase propagation, the dominance of combustion mechanisms within the condensed phase, liquid melt layer and gaseous reaction layer as well as the importance of porosity. Notable proposed combustion mechanisms in the 1986 to 2009 time frame are summarized below in chronological order. The author acknowledges that this is by no means an exhaustive list, and is meant to summarize trends in the literature.

Mitani and Williams' 1986 paper proposes a combustion mechanism for Nitramines, explosives with NH-NO_2 in their bond structure as opposed to nitrate esters which are oxidized by ONO_2. (Cooper, 1996) Condensed phase decomposition occurs with a liquid melt layer between the condensed phase and gas layer. The condensed phase region reactions are treated as exothermic as are the gas combustion reactions. Vaporization reactions are assumed to occur in equilibrium. The impact of gas phase decomposition on burn rate is restricted to the gas layer near the burn front surface and not the entire gaseous product region. A one step Arrhenius decomposition of the combustion reaction is provided. (Mitani & Williams, 1986)

In 1995 *Margolis and Williams* proposed a deflagration mechanism for energetic materials with emphasis on diffusion and thermal instabilities observed in combustion. Figure 81 below

from this reference summarizes their conceptualization of the combustion problem as consisting of a porous unreacted region with a thin melting region containing gas bubbles due to porosity of the energetic material followed by a gaseous region.

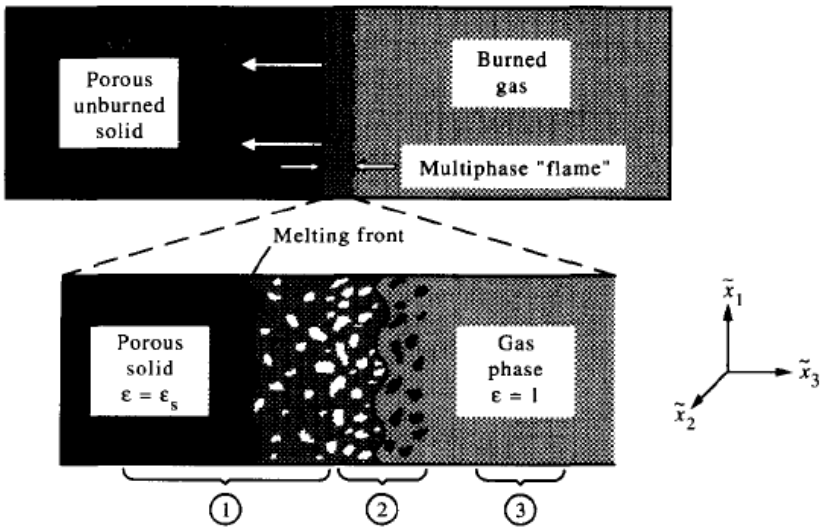

Figure 81: Deflagration Phase Diagram with Condensed Melting and Gaseous Phases. (Margolis & Williams, 1996, p. 71)

The computational model employs asymptotics to formulate an explicit solution to porous energetic material deflagration, where the gas phase is assumed to be quasi-steady and the model is applicable only for instances of large activation energies. Impacts to solution stability due to the inclusion of porosity and gaseous thermal expansion are addressed with a linear stability analysis. (Margolis & Williams, 1996)

The combustion mechanism proposed by *Ward* in reference (Ward, Son, & Brewster, 1998) similarly applies an activation energy asymptotics analytical approach to derive a solution for HMX deflagration with condensed and gas phases. This model does not include a melting region or porosity effects. The condensed phase reactions are calculated with a one-step global Arrhenius reaction assuming large activation energies. An expression for gaseous phase chain reactions is

calculated from governing equations assuming low activation energy in this region (unlike other models that assume high activation energy throughout the reactions zones). (Ward, Son, & Brewster, 1998)

A follow-on paper by *Margolis* in 2001 extends the study of deflagration of unconfined explosives in reference (Margolis & Williams, 1996) to the impact of confinement on deflagration stability. Confinement of an explosive material results in gaseous product flow back into unreacted porous energetic material, which serves to increase the unreacted material temperature and thereby increase burn rate. Increasing burn rate also increases reactive over-pressure and corresponding temperatures which increase the combustion solution stability. (Margolis, Telengator, & Williams, 2001) It should be noted that though the numerical solution stability is increased, confinement and subsequent combustion reaction pressure increase can lead to reaction thermal run-away and result in a transition from deflagration to detonation.

An empirical and analytical analysis of the impact of melt layer thickness on burning rates is conducted in reference. (Zenin & Finjakov, 2007) In this publication, burn rate data for both RDX and HMX are obtained and computational models for deflagration with and without melting in the condensed phase are formulated. It is determined that melt layer thickness does not appreciably impact burn rates and the presence of a melt layer in the condensed phase reduce the amplitude of pressure response fluctuations in the derived deflagration models. (Zenin & Finjakov, 2007)

The previously introduced work by *Sinditskii* in 2009 contains a descriptive combustion mechanism based on observations from experimental data. *Sinditskii* proposes that the heat release in the condensed phase goes into surface heating and the heat released during the gaseous combustion phase is “spent only on the non-decomposed portion of HMX” and thus does not alter

burn rate. However, changes in the initial temperature of energetic materials do increase the burn rate and therefore rate of heat release in the gaseous phase. Furthermore, *Sinditskii* postulates that temperature measurement oscillations recorded via thermocouples are attributed to the rupture of surface layer bubbles. (Sinditskii, Egorshev, Berezin, & Serushkin, 2009) This conclusion is supported in the analytical models of porosity effects by Margolis. [(Margolis & Williams, 1996), (Margolis, Telengator, & Williams, 2001)]

DEFLAGRATION TO DETONATION TRANSITION

As previously noted, the field of deflagration to detonation transition has been active since the late 1950s. The literature review of this prolific field is subsequently divided into three sections as they relate to the present work: early experimental DDT with an emphasis on published HMX data, the Baer-Nunziato model and suggested modifications, and non-Baer-Nunziato based analytical formulations. Numerous publications in the field contained both experimental data as well as proposed analytical models based on the collected data. These works will be divided into two categories: those based on the Baer-Nunziato DDT model and other proposed mechanisms, which are discussed in chronological order. In general, DDT in confined column type tests is thought to occur over four regimes: "conductive burning, convective burning, compressive burning, and detonation." (Baer & Nunziato, 1986) Discussions in the literature support the varying dominance of reactions within these four regimes. Typical experimental configurations include a hollow metal tube filled with porous explosive initiated on one end.

DDT Experimental

A thorough literature review of early DDT experimentation is available in reference (Butler & Kriar, 1984) with seminal contributions through 1983 summarized in the following paragraphs.

According to *Butler and & Kriar*, introductory experimental work in the field of DDT experimental testing began in 1959 with the work of *Macek* analyzing DDT of cast explosives. The following year in 1960 *Griffiths and Groocock* configured thick walled brass cylinders packed with a narrow center core of granular explosives to capture the burning to detonation transition of solid explosives including RDX, HMX and PETN. This is the earliest experimental DDT testing of HMX identified by the author. *Griffiths and Groocock* also note that their paper contains the first successful photographs of burning to detonation. (Griffiths & Groocock, 1960)

In the mid-1970s, *Bernecker and Price* published a series of papers on the empirical and analytical study of DDT in granular explosives. Their work was conducted at the Naval Surface Weapons Center (NSWC) in White Oaks, Maryland. The final installment of the 1974 three publication series will be discussed in the next DDT literature review section where non-Baer-Nunziato based modeling efforts are described. The first two *Bernecker and Price* 1974 publications detail experimental configuration setup, ionization probe distance versus time data where applicable, and mechanism theories for DDT steel tube type tests of ammonium picrate, 95% TNT and 5% wax mixtures, and 91% RDX and 9% wax mixtures at multiple densities relative to theoretical maximum density. [(Bernecker & Price, Studies in the Transition from Deflagration to Detonation in Granular Explosives - I. Experimental Arrangement and Behavior of Explosives Which Fail to Exhibit Detonation, 1974), (Bernecker & Price, Studies in the Transition from Deflagration to Detonation in Granular Explosives - II. Transitional Characteristics and Mechanisms Observed in 91/9 RDX/Wax, 1974)] *Bernecker and Price* had difficulty inducing a transition from deflagration to detonation with their original 1974 test apparatus and samples of ammonium picrate and TNT/wax mixtures. Their subsequent 1975 publication discusses a revised test apparatus where rapidly deflagrating 94% RDX and 6% wax is positioned between the ignitor

and ammonium picrate or TNT based test samples. The addition of a "gas loader" was utilized to confirm the theory that detonation transitions were not achieved in the 1974 experiments due to slow energetic material burning rates and thereby insufficient pressure buildup. (Price & Bernecker, 1975) *Price and Bernecker* summarize their testing data captured for RDX, HMX and Tetryl wax mixtures over the span of several years in NSWC report TR 77-96. (Price & Bernecker, 1977) HMX DDT experimental methods and data from this technical report will be discussed in greater detail in Chapter 3 of this dissertation.

Testing to study DDT of granular HMX, where gas permeability in samples was retarded by separating stacked grains with neoprene disks was presented in 1981 by *Campbell*. Los Alamos National Laboratory based work with low density HMX (65% TMD) shock initiation was conducted by J.J. Dick in 1983 to understand and statistically analyze the effect of particle size and density distributions on run distance and time to detonation. (Dick, 1983)

Two noteworthy proceedings from 1970 not included in the *Butler and Kriar* experimental DDT literature review references described above were presented by *Marshall* at the Fifth International Symposium on Detonation. *Marshall's* experimental apparatus consisted of a hollow thin walled brass tube packed with coarse granulated HMX and covered with a mild steel witness block. The HMX test sample was isolated from the PETN initiating charge to determine the previously postulated influence of interstitial gases on initiation time delay. Based on the results of this series of experiments, *Marshall* concludes that initiation time delay is not dependent on interstitial gas pressure. (Marshall, 1970) However, *Marshall* does conclude that shock initiation sensitivity is strongly influenced by temperature. (Marshall, 1970)

Wang and Chen experimentally assessed the influence of various additives to coarse and fine HMX mixtures on DDT responses in 1991. Using a standard hollow tube filled with explosive

test samples initiated on one end, they tested coarse HMX mixed with fine HMX, PMMA, graphite fluoride or Triaminotrinitrobenzene (TATB) in five and ten percent concentrations to determine the influence of both inert and reactive additives. Results show that fine HMX and PMMA additives decrease DDT run-up length while graphite fluoride, TATB and wax increase the DDT run-up length with wax additives resulting in the largest length increase. (Wang & Chen, 1991)

Detonation, deflagration and DDT test apparatus set-up are addressed as related to specific experimental data utilized for verification and validation of the present work in Chapter 3. However, it is noteworthy that a new type of experimental measurement technique has been developed by Columbia Gorge Research in collaboration with Lawrence Livermore National Laboratory utilizing chirped fiber grating sensors. Sensors imbedded in energetic material are capable of capturing velocity, position, temperature and pressure of energetic responses ranging from burning to deflagration to detonation. While the sensors remain intact during burning and possibly deflagration spectral measurements are used to record sensor response. Then, while the reaction progresses and the sensors are destroyed, the amplitude of reflection data is collected. This voltage data corresponds to calibrated responses for velocity, position, temperature and pressure. An example plot of voltage response captured during Russian DDT type testing of an RDX based energetic material is included in Figure 82, (Udd, Dunaway, Biegert, & Johnson, 2011). Further development of this emerging new technology has the potential to substantially aid the field of DDT research.

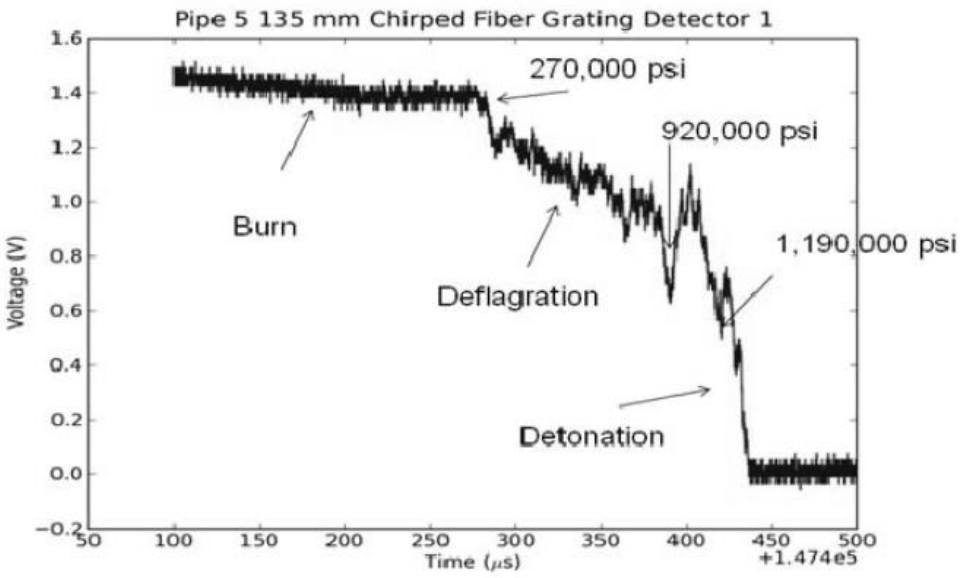

Figure 82: Chirped Fiber Optic Grating in a DDT Test Configuration Clearly Shows the Transition from Burning to Deflagration to Detonation. (Udd, Dunaway, Biegert, & Johnson, 2011)

Proposed Analytical Models Unrelated to Baer-Nunziato

In *Bernecker and Price's* mid-1970s series of publications on DDT research conducted at NSCW they evaluate both past experimental work in addition to their own experimental results for 91% RDX and 9% wax explosives in confined steel tubes. In their final installment of a three part 1974 publication work they propose that the pre-cursor shock to achieve successful DDT is not formed at the leading portion of the convective region, but rather near the initiation site further aft in the convective burning region. They hypothesize that the region near the initiator is a more likely pre-cursor shock formation site due to exponential pressure build-up leading to compression wave formation trailing the convective front. Studying explosives samples with a range of porosities, they proposed that as porosity increases and sample density decreases or for situations with low burn rates, the likelihood of achieving exponential pressure build-up of sufficient magnitude to induce formation of a pre-cursor shock diminishes. (Bernecker & Price, 1974)

Sumilov's 1976 work focused on the explosive pentaerythritol tetranitrate (PETN). Filled hollow tube type experiments conducted in conjunction with the USSR Academy of Sciences in Moscow yielded velocity and streak camera photography for PETN. With this data, *Sumilov* postulated that maintaining convective burning (without DDT) is possible for explosives below a threshold porosity if the combustion region pressure is able to stay roughly constant (within 10%) and with a subsonic convection front. As compression wave amplitude increases a transition from convective burning to Low Velocity Detonation (LVD) occurs. Low velocity detonation can be differentiated from standard detonation in that only 10-20% of reaction products are formed near the reaction propagation front with the balance forming in the downstream reaction zone. (Butler & Kriar, 1984) Unlike (Bernecker & Price, 1974), *Sumilov* contends that the leading zone pressure is the dominant factor in reaction propagation velocity and not the rate of pressure increase. (Sulimov, et al., 1976)

The two-phase flow computational model for granular HMX proposed by *Beckstead et al* in 1977 describes DDT in terms of a continuum mechanics approach utilizing a 1-D convective combustion computer code. A parametric study was conducted to assess variables that dominantly influence run-up to detonation lengths. Figure 83 from this reference contains a visual explanation of run-up length as the distance from the initiating end of a cylinder to the plane where a sustained detonation wave forms.

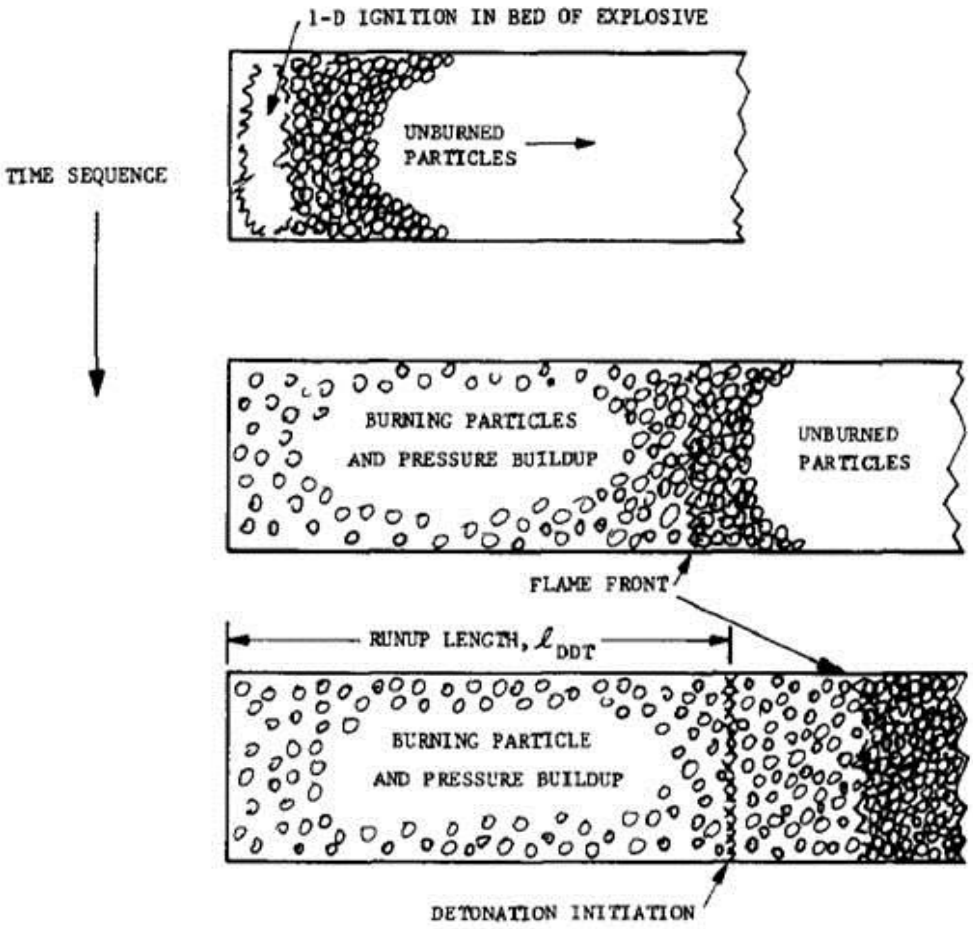

Figure 83: Run-up Distance of a Porous Explosive Undergoing DDT. (Beckstead, Peterson, Pilcher, Hopkins, & Krier, 1977, p. 234)

The most important variable identified in their parametric study was particle diameter, followed by porosity, burn rate and chemical energy content of the simulated explosives. (Beckstead, Peterson, Pilcher, Hopkins, & Krier, 1977)

Wang et al applies a computational analysis approach to burning or detonation (where applicable based on code limitations) of HMX in their 1985 publication. A variety of existing Equations of State (EOS) were employed and modified to account for pertinent physics in manners applicable to each unique EOS. The EOS evaluated in this paper include: the virial EOS, Haar-

Shenker EOS, Becker-Kistiakowsky-Wilson EOS, and Jacobs-Cowperthwaite-Zwisler EOS. A non-ideal EOS is proposed to handle DDT of HMX. (Wang, Butler, & Krier, 1985)

The 1989 Lawrence Livermore National Laboratory paper by *Aldis* describes a plethora of experimental DDT results obtained for HMX used to validate development of one and two dimensional hydrocodes. Experiments include a polycarbonate flyer plate impacting a porous HMX bed separated from the flyer with an Aluminum buffer plate, explosive lens experiments, a piston driven into HMX in a merging steel tube experiments as well as experiments where gas generated from an ignited Boron Potassium Nitrate ($BKNO_3$) pellet is used to generate a compression wave in HMX and induce DDT. Results from these experiments were used to validate the one dimensional Lagrangian hydrocode capable of modeling gas permeation through solids and the two dimensional hydrocode DYNA2D. The one dimensional model described in this paper utilized a JWL EOS and the two dimensional model applied an Ignition and Growth model EOS. (Aldis, Lee, Simpson, & Weston, 1989)

The concept of a high density plug in the DDT formation field was introduced by Los Alamos National Laboratory. This model differs from the more traditional conduction, convection, and compressive burning followed by detonation schema generally assumed in DDT scenarios. *Stewart et al* describe the Los Alamos high density plug model in Figure 84.

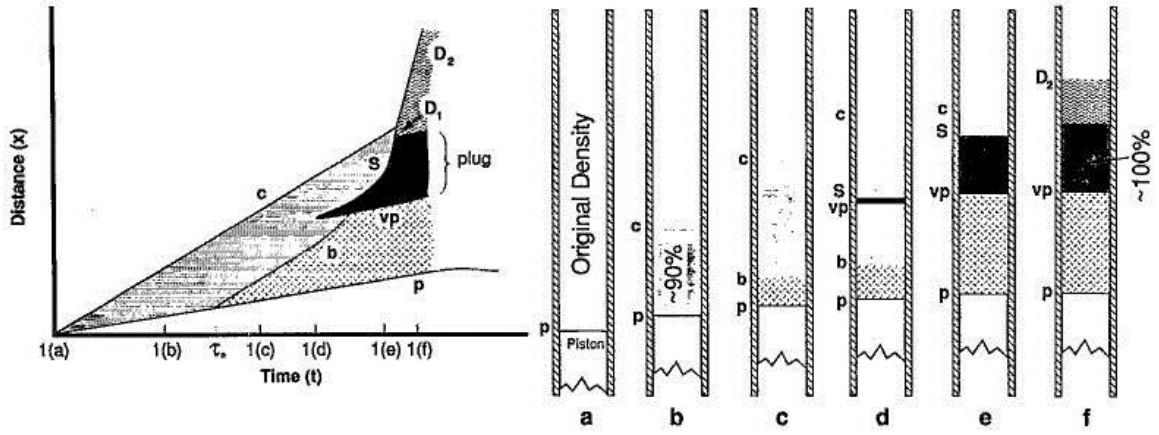

Figure 84: Los Alamos National Laboratory High Density Plug Model Description. (Stewart, Asay, & Prasad, 1994)

This model beginning with a piston driven into an explosive sample during testing, denoted as (p) in Figure 84. Piston impact generates a leading compaction wave, labeled (c). This compaction wave increases test sample density from 70% of theoretical maximum and results in the formation of a reactive combustion wave, labeled (b), near the trailing wave due to piston impact. The reactive combustion wave works its way forward and burns the compacted material. The reactive combustion front burn rate increase causes a shock, labeled (s), to coalesce in front of the combustion front and further compact the remaining unconsumed explosive to one hundred percent theoretical maximum density (TMD). This TMD "plug" region increases to consume all remaining unreacted material and then shock initiation occurs resulting in detonation of remaining material. The aft end of the plug is referred to as a "virtual piston" and labeled (vp). (Stewart, Asay, & Prasad, 1994)

Experimental work in support of the Los Alamos National Laboratory high density plug DDT model was presented by *McAfee* at the 1989 Ninth International Symposium on Detonation. In this work, *McAfee* emphasized the importance of utilizing a piston driven energetic material initiation mechanism to avoid introduction of contaminating detonation products as well as the

usefulness of being able to approximate 1-dimmensional reaction initiation at the piston impact site. *McAffee's* multi-faceted instrumentation approach included x-rays, stress gauges, light emission techniques and ionization pins. (McAfee, Asay, & Campbell, 1989)

Stewart et al propose a simplified single phase computational model to represent the aforementioned plug phenomenon behavior encompassing an Equation of State with allowance for compaction mechanisms. (Stewart, Asay, & Prasad, 1994) This model is referred to in the following publication as the Gas Interpolated Solid Stewart-Asay-Prasad (GISPA) model.

Xu's 1996 publication studies the phenomenon of HMX DDT by assessing the applicability of one, two and three phase flow non-ideal Equation of State models as compared to experimental tube type DDT data in conjunction with the high density plug theory advocated by Los Alamos National Laboratory. The aforementioned GISPA single phase model is applied in addition to a two phase gas and solid model by *Bdzil, Kapila, and Stewart* as well as the ultimately recommended three phase model encompassing solid, void and gas, termed the SVG model. The two phase gas solid model applied by *Xu* is based on the Baer-Nunziato model to be discussed in the following section. However, this work is included in the non-Baer-Nunziato model section as the primary focus of the paper was the SVG model. (Xu & Stewart, 1997)

Development of a physical model for low velocity detonation is the subject of *Grebenkin et al* in 2008. This phenomenon is important to understand conceptually as it is theorized to contribute to the transition mechanism in DDT in some instances. *Grebenkin* uses a hot spot initiation model in conjunction with macrokinetic equations to describe a weak shock front trailed by a compression wave. This model is formulated specifically for plasticized HMX formulations, which implies low sample porosity. (Grebenkin, Taranik, Tsarenkova, & Shnitko, 2008)

Yang's 2008 paper contains an overview of the various types of reactions HMX can undergo. This paper is relevant to the present work as it contains a review of HMX Arrhenius decomposition rate equation parameters found in the literature with critique on the conditions at which they are applicable and a tabulation of temperatures at which experiments were conducted to obtain the Arrhenius parameters. (Yang, 2008) This is the last of the non-Baer-Nunziato related works to be discussed in this literature review.

Baer-Nunziato Based Analytical DDT Models

The following section contains a detailed literature review of the pivotal 1986 Baer-Nunziato multi-phase flow model for DDT formulated at Sandia National Laboratory and subsequent derived works. This model is one of the most referenced and well known of the multi-phase DDT models. Implementation of model improvements in an Eulerian hydrocode is the focus of the present dissertation work.

The Baer-Nunziato (BN) model is based on the physical assumption of four regimes, including conductive burning, convective burning, compressive burning, and detonation as depicted in Figure 85. *Baer and Nunziato* emphasize the important coupling that occurs between thermal and mechanical processes during DDT, where the thermal process involves convective heating of upstream unreacted explosive material and mechanical processes involve compaction of the granular particles upstream thereby increasing material density and inducing pressure build-up. Shock wave formation to full-fledged detonation is supported by "hot spot" regions. (Baer & Nunziato, 1986)

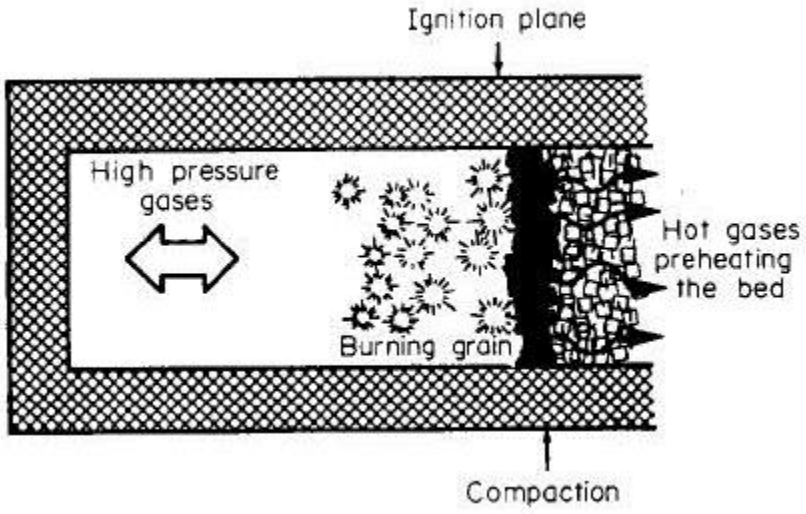

Figure 85: Baer-Nunziato Depiction of DDT Regimes. (Baer & Nunziato, 1986, p. 861)

Baer and Nunziato employ a continuum approach to the reactive two phase flow problem of HMX DDT in total non-equilibrium. They assert that the primary complication with the continuum approach in past solution attempts has been the problem of "closure" as it pertains to the volume fraction. For a one dimensional two phase problem there are ten unknown variables: "pressure, temperature, density, velocity, and volume fraction" in each of the two phases. Mass, momentum and energy conservation in each phase solve for six variables with an additional two from phase based state relations, and one from volume constraint. Thus, one equation is still needed in order for the problem to be fully determined. The BN model "proposes an evolutionary equation for the volume fraction consistent with thermodynamics" to resolve the closure issue. (Baer & Nunziato, 1986)

Baer and Nunziato derive the following set of one dimensional governing equations, where the subscripts s and g denote solid and gas phases.

Conservation of mass:

$$\frac{\partial \rho_s}{\partial t} + \frac{\partial}{\partial x}(\rho_s v_s) = c_s^+ \quad [7]$$

and

$$\frac{\partial \rho_g}{\partial t} + \frac{\partial}{\partial x}(\rho_g v_g) = -c_s^+ \quad [8]$$

Conservation of momentum:

$$\rho_s \left[\frac{\partial v_s}{\partial t} + v_s \frac{\partial v_s}{\partial x}\right] = -\alpha_s \frac{\partial p_s}{\partial x} + (p_g - p_s)\frac{\partial \alpha_s}{\partial x} - \left(\delta + \frac{1}{2}c_s^+\right)(v_s - v_g) \quad [9]$$

and

$$\rho_g \left[\frac{\partial v_g}{\partial t} + v_g \frac{\partial v_g}{\partial x}\right] = -\alpha_g \frac{\partial p_g}{\partial x} - \left(\delta - \frac{1}{2}c_s^+\right)(v_g - v_s) \quad [10]$$

Conservation of energy:

$$\rho_s \left[\frac{\partial e_s}{\partial t} + v_s \frac{\partial e_s}{\partial x}\right] = -\alpha_s p_s \frac{\partial v_s}{\partial x} + \frac{\partial}{\partial x}\left(k_s \frac{\partial T_s}{\partial x}\right) + h(T_g - T_s) - (p_s - T\beta_s)\left(\alpha_s' - \frac{c_s^+}{\gamma_s}\right) \quad [11]$$

and

$$\rho_g \left[\frac{\partial e_g}{\partial t} + v_g \frac{\partial e_g}{\partial x}\right] = -\alpha_g p_g \frac{\partial v_g}{\partial x} + \frac{\partial}{\partial x}\left(k_g \frac{\partial T_g}{\partial x}\right) - h(T_g - T_s) - \left[p_g \frac{\partial \alpha_s}{\partial x} - \delta(v_s - v_g)\right](v_s - v_g) + (p_s - \beta_s)\left(\alpha_s' - \frac{c_s^+}{\gamma_s}\right) + c_s^+(e_g - e_s) \quad [12]$$

Compaction:

$$\frac{\partial \alpha_s}{\partial t} + v_s \frac{\partial \alpha_s}{\partial x} = \frac{\alpha_s \alpha_g}{\mu_c}\left[p_s - (p_g + \beta_s)\right] + \frac{c_s^+}{\gamma_s} \quad [13]$$

and

$$\alpha_g = 1 - \alpha_s \quad [14]$$

The BN model as applied to HMX DDT further utilizes a thermo-elastic variation of the Helmholtz free energy for the unreacted energetic material, a JWL Equation of State for the gaseous reaction products, a thermodynamic based equation for gas temperature, and a burn law given in the equation below. Theta is a function of both phases and epsilon is the kinetic shape factor.

$$c_{solid}^{+} = -\epsilon\left(\theta + p_{gas}\right) \quad [15]$$

In the validation case of HMX DDT, a reflection boundary condition is used at the ignition end of the cylinder and an outflow boundary condition is applied at the opposite cylinder end. Initial conditions are consistent with the ignition of HMX. The aforementioned BN model equations are solved via application of the Method of Lines and yield results shown below in Figure 86. (Baer & Nunziato, 1986)

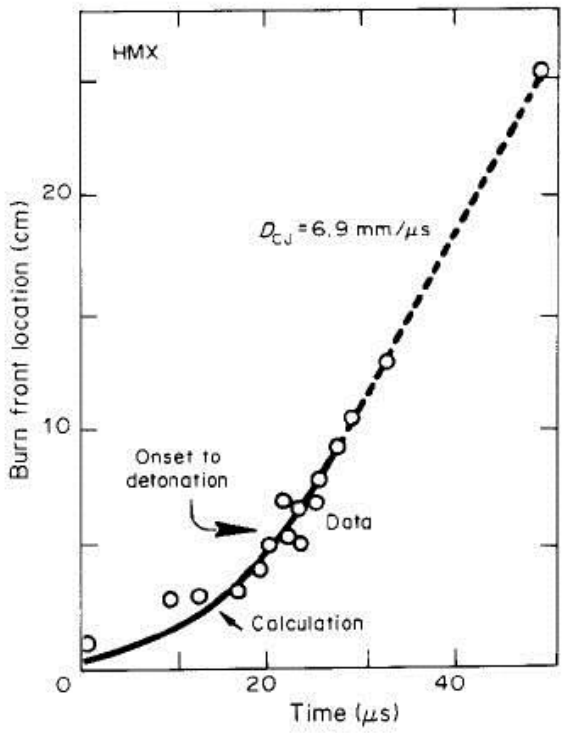

Figure 86: Baer-Nunziato Model Solution Ratio from 1986.

(Baer & Nunziato, 1986, p. 877)

A second paper by *Baer and Nunziato*, with *Robert Gross*, also published in 1986 applies the BN multi-phase flow model developed in (Baer & Nunziato, 1986) to the explosive cyanotetrazolato pentaaminecobalt perchlorate, known by the abbreviation CP. Computational results for CP DDT compared fairly well to streak data. Experimental methods conducted by *Baer, Nunziato, and Gross* are also discussed. (Baer, Gross, & Nunziato, 1986)

Los Alamos National Laboratory, notably authors S. F. Son and J. B. Bdzil, have produced numerous papers on the topic of improvements to the BN model. In (Son, Kober, & Bdzil, 1997) the BN model kinetic scheme is implemented into the two dimensional hydrocode MESA and a variety of benchmark comparisons to experimental results for granular HMX tests are made. Son et al determine that the hydrocode model as implemented does not qualitatively match

experimental observations. (Son, Kober, & Bdzil, 1997) A subsequent Los Alamos paper critically reviewed the original BN model derivation and suggested modifications to increase fidelity. The many recommendations for areas of improvement to the BN model include: modification of subsonic dispersed compaction wave treatment to correct the unreacted energetic material Equation of State, inclusion of irreversible slow compaction mechanisms, and hot spots. Additional suggestions largely pertain to greater attention to detail on the microscopic granular level such that the BN model can be extended to damaged energetic material. (Bdzil, Menikoff, Son, Kapila, & Stewart, 1999) A third Los Alamos publication focuses on proposing a reduced set of modified BN modeling equations in order to circumvent stiffness issues arising from small equilibrating time scales. *Kapila et al.* proposed a method to reduce the original BN equations and implement either a one velocity or one velocity and one pressure outer model. Jump conditions are recommended as the reduced equations cannot be fully characterized in a set of conservation equations, alternatively the use of artificial viscosity is suggested. (Kapila, Menikoff, Bdzil, Son, & Stewart, 2001)

Most recently, a 2011 publication by *Thanh et al.* discusses a more "numerically stable and robust solution" to two phase flow problems of the type proposed for DDT of granular energetic materials by Baer and Nunziato. *Thanh et al.* propose a numerical method that divides the existing model into three problem regimes with separate governing equations: the gas phase, mixture phase and compaction dynamics phase. Each of the three phases utilizes different numerical methods in order to avoid stiffness issues encountered with the BN model. This approach yields results that are much more accurate in the detonation portion, with results deemed unacceptable by *Thanh et al.* in the subsonic reaction regime. (Thanh, Kroner, & Chalons, 2012) While this numerical

method approach is unique and interesting, robust models for detonation physics are already in existence and widely used in hydrocodes today.

APPENDIX B

INSENSITIVE MUNITIONS

Insensitive Munitions (IM) is a very real and important endeavor by the U.S. Armed Forces. A definition for munitions that are "IM compliant" are ones that are safe for handle and use in their intended designs, while resistant to adverse stimuli that would induce premature reactions. More specifically, the government military standard definition is:

> "Munitions which reliably fulfill (specified) performance, readiness, and operational requirements on demand but which minimize the probability of inadvertent initiation and severity of subsequent collateral damage to the weapon platforms, logistic systems, and personnel when subjected to unplanned stimuli." (MIL-STD-2105D: Hazard Assessment Tests for Non-Nuclear Munitions, 2011)

Examples of this would include responses to thermal cook-off events and shock (e.g. bullet impact) stimuli. This might include accidental initiation or deliberate attacks on rocket motors and warheads that might normally end with an explosive or detonable response. It is therefore an important engineering design constraint to build such rocket motors, warheads, initiators, etc. that are IM compliant. As will be discussed, IM compliance is no longer a "nice to have" for new ordnance developments. In the past few years the US Armed Forces have mandated that no new waivers will be issued for failure to meet IM requirements.

The genesis of this IM compliance requirement is driven by the sad history of losses of life and billions of adjusted dollars in ship, aircraft, vehicle and facilities loss or damage. The infamous example is that of the USS Forrestal on 29 July 1967, when the flight deck caught on fire after a missile accidently fired and hit a fuel tank of an adjacent aircraft. This started an initial deck fire that was not destructive in itself, but rather the fire started a series of detonations from adjacent ordnances. Some would recall the story of the USS Forrestal because of the later famous Arizona Senator and Vietnam War POW John S McCain III, who was then a LCdr. and was briefly trapped in his aircraft when the initial fire broke out. (Beauregard, n.d.)

Figure 87: Damage on the USS Forrestal. US Navy Photo.

The damage of the USS Forrestal cost over $1 billion in adjusted US Dollars, which included 43 damaged aircraft and 21 that were destroyed. Sadly, it also cost the lives of 74 sailors with an additional 141 injured. Similar stories can be told for the USS Oriskany in 1966, USS Enterprise in 1969, SS Badger State in 1969, and the USS Nimitz in 1981. In total, they account for 174 lost lives and nearly $2 billion in adjusted US Dollars. (Tindle & Zeman, 1991)

These are just infamous IM related accidents at sea. There are many further accounts of ordnance detonations at supply depots, in vehicles, and elsewhere, that have resulted in more loss of life and significant costs. Deliberate attacks on supply depots are a still a very real threat; though accidental fires causing depot fires and subsequent explosions are equally destructive - an example is Camp Doha, Kuwait in July 1991.

As previously mentioned, there are no new waivers being granted for IM compliance. New rocket motor and warhead developments are now required to pass a certain series of tests that are designed to demonstrate a product's ability to withstand adverse stimuli. The governing document for these IM tests and passing criteria is MIL-STD-2105: Department of Defense Test Method Standard Hazard Assessment Tests for Non-Nuclear Munitions. (MIL-STD-2105D: Hazard Assessment Tests for Non-Nuclear Munitions, 2011)

In addition to basic environmental and safety tests, the IM tests include:

- 12-meter (40-foot) drop
- Fast cook-off & Slow cook-off
- Bullet impact
- Fragment impact
- Shaped charge jet impact
- Sympathetic detonation

These tests can be loosely grouped into two categories: thermal and shock stimulus. Thermal based tests include the two cook-off requirements, with the remaining tests falling into the shock stimulus category. Usually there are multiple trials used for each IM test, each one being in a different configuration. For example: two test articles for the bullet impact test would include one in an open configuration, such as a missile hanging on a wing of an aircraft in captive carry mode, and the other in the shipping container. Bullet impact would include three 50 caliber bullets being simultaneously passed through the bulk of the propellant in a rocket motor IM test or the most likely initiation site in a warhead IM test. The specifics and passing criteria for each test are governed by the respective NATO Standardization Agreements (STANAGs) listed in MIL-STD-2105 for each IM test.

There is much interest in IM modeling capabilities. The premise is simple: if we can predict it, we can design for it. That is to say that IM modeling can be worked into the pre-design phase. This is currently not done. Designs in the recent past have used “best IM practices” or devices intended to aid in IM, but these are in no way an indicator of IM success. In fact, they are not often enough to pass the gambit of tests. Redesigns are very costly, on the order of a redeveloping the entire rocket motor or warhead, which often takes two to four years. It should be mentioned that the IM tests in themselves are very costly as they nominally require the products to be tested in the “all up round” (AUR) configuration which includes the forward missile assembly - often much, much more expensive than the ordnances which are the intended subjects of the IM tests. This dissertation proposes new computational practices that can be used to predict shock stimulus IM response, and thusly can be used in lieu of a subset of the IM tests.

APPENDIX C

EXISTING EOS: TRACER PRESSURE OUTPUT

NSWC:

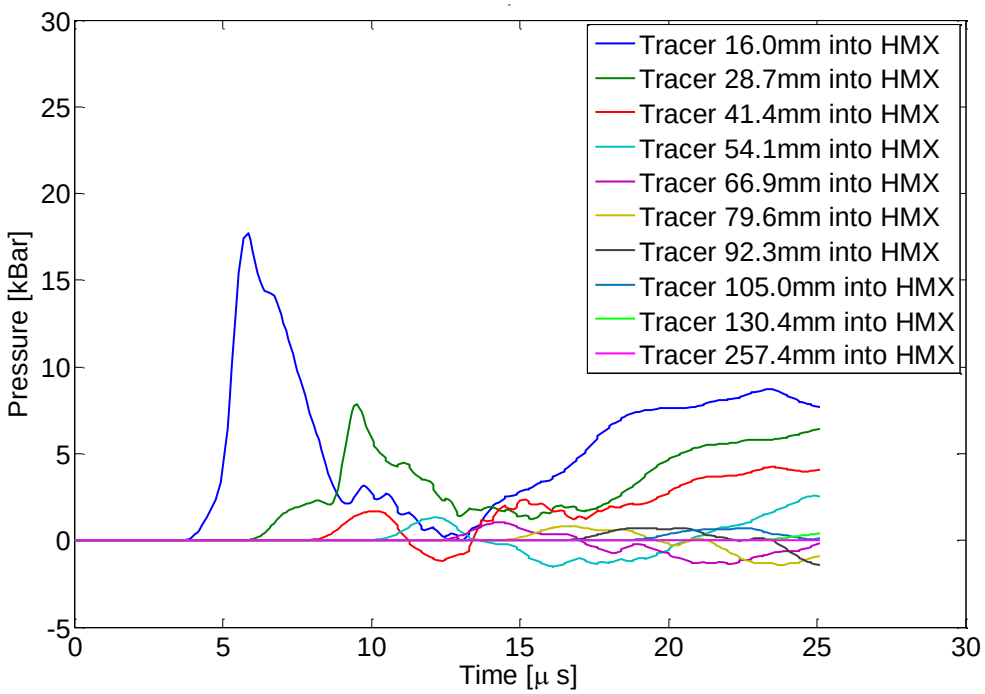

Figure 88: NSWC Inert 100% TMD HMX Pressure Trace Data

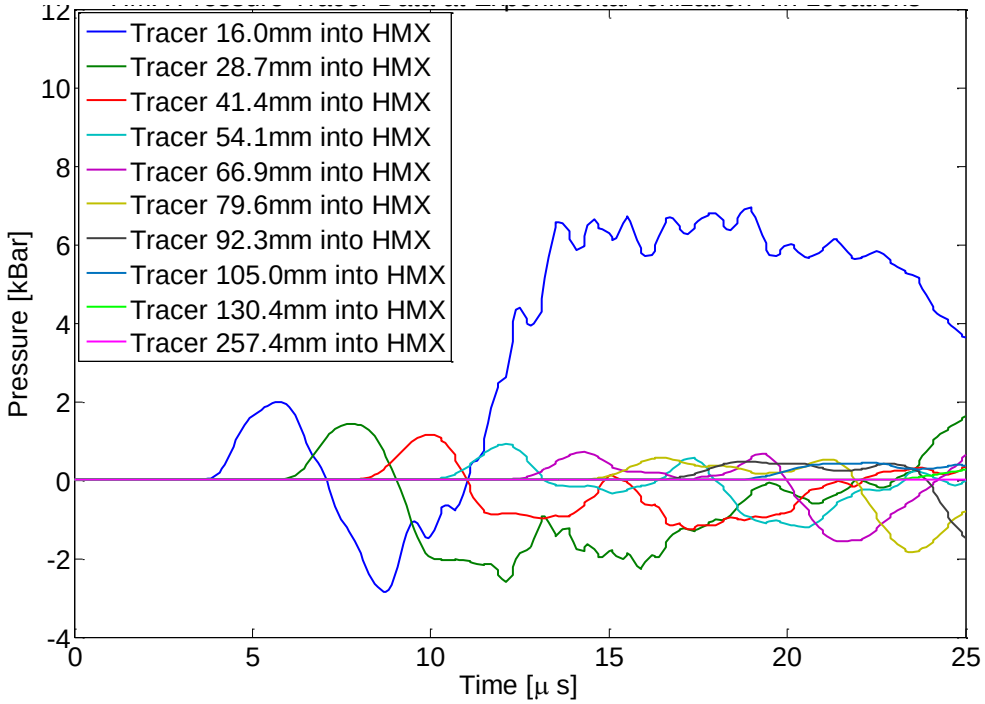

Figure 89: NSWC Inert Granular HMX Pressure Trace Data

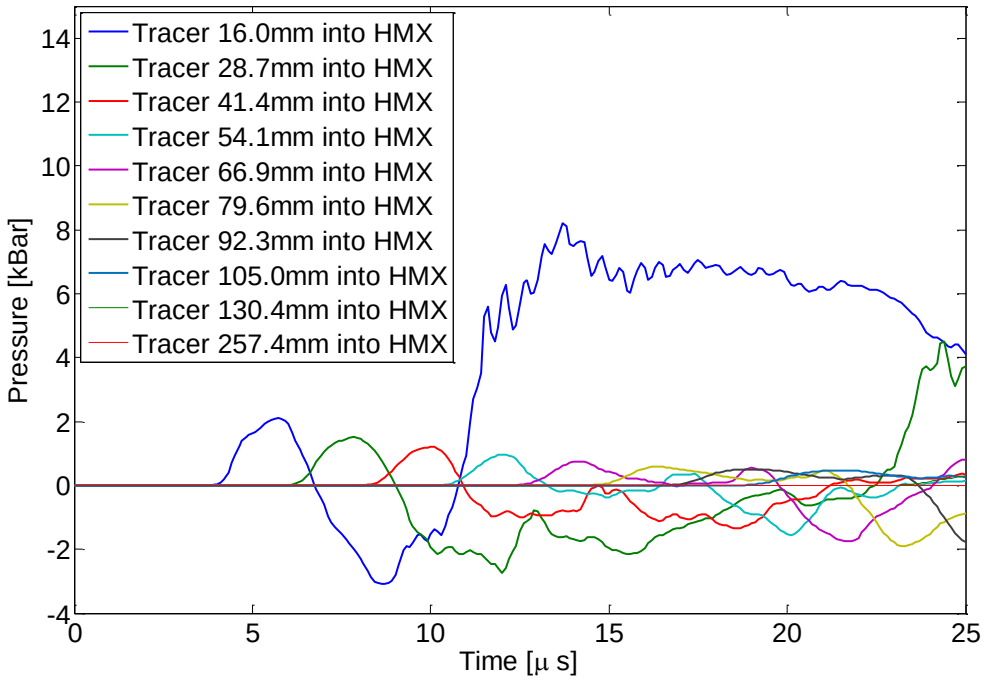

Figure 90: NSWC Inert Fine Mesh Granular HMX Pressure Trace Data

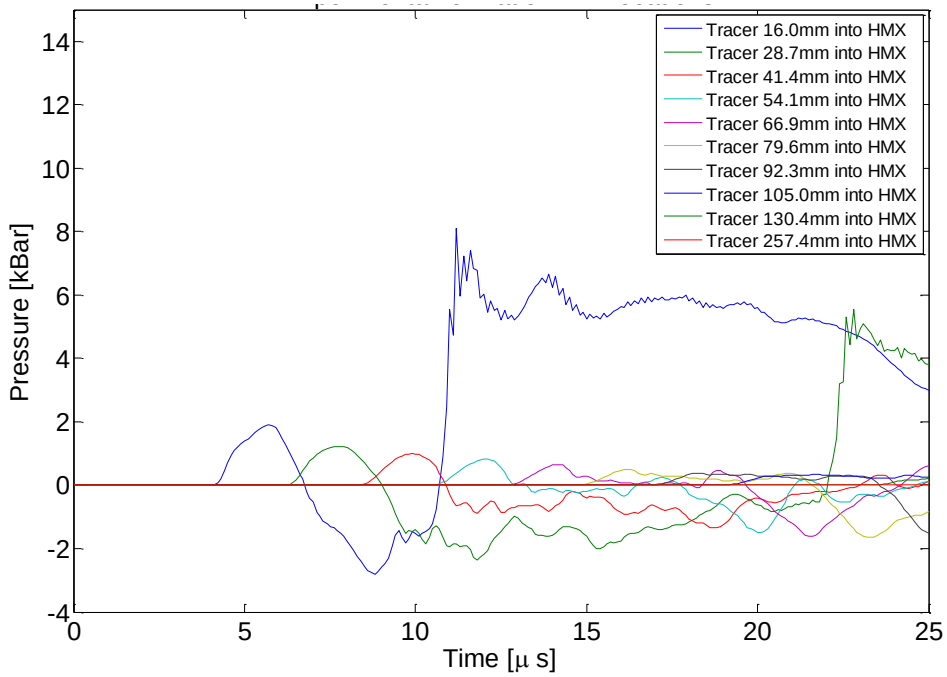

Figure 91: NSWC Inert Non-Uniform Mesh Granular HMX Pressure Trace Data

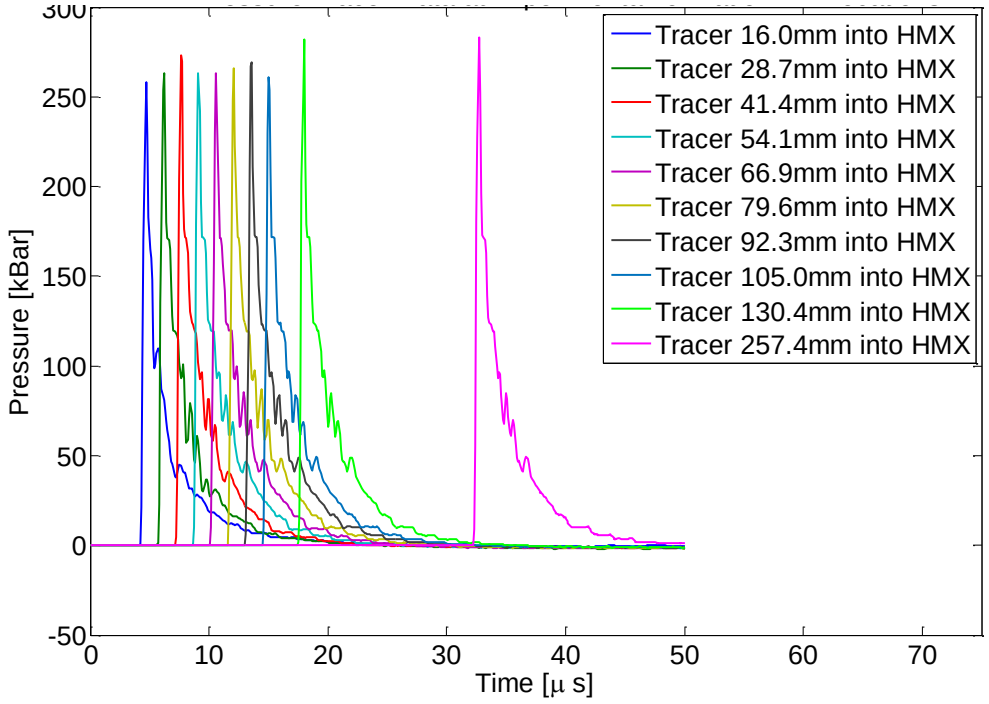

Figure 92: NSWC HVRB Forced Detonation 100% TMD HMX Pressure Trace Data

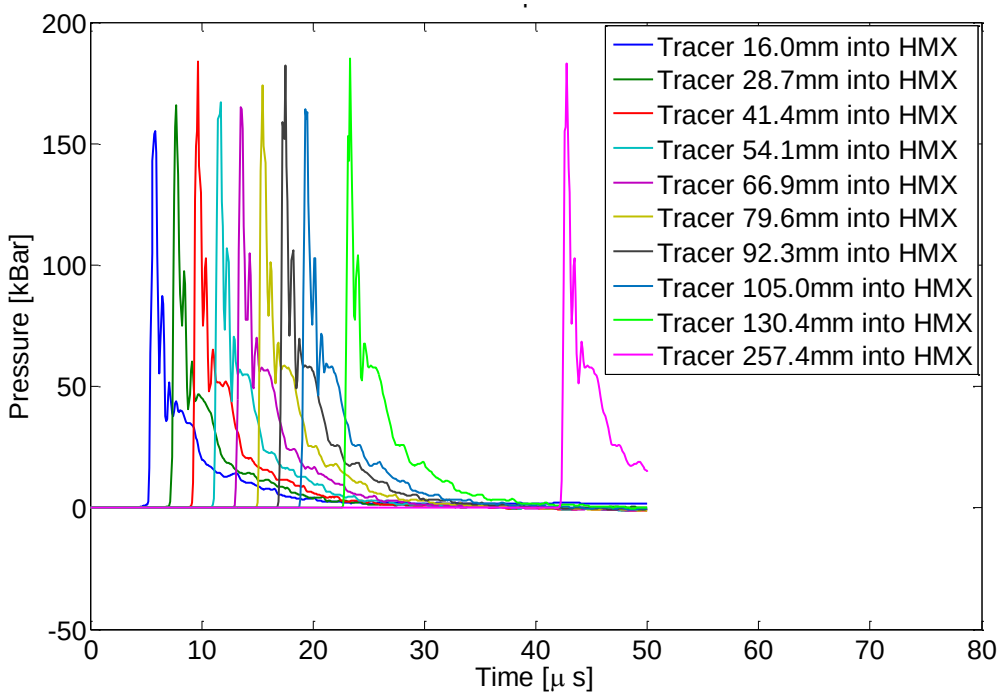

Figure 93: NSWC HVRB Forced Detonation Granular HMX Pressure Trace Data

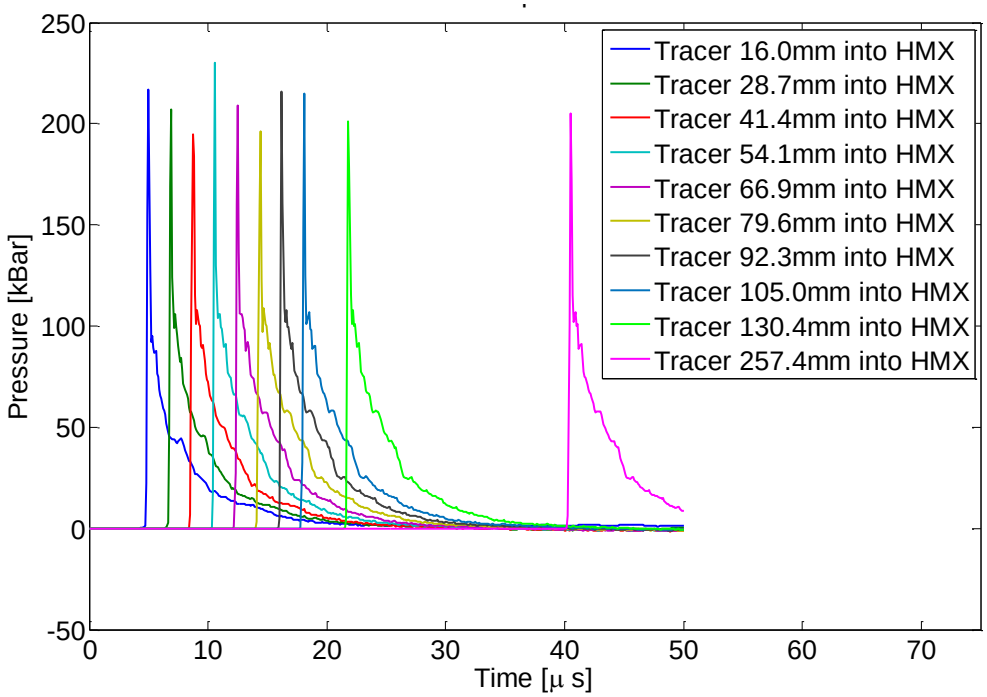

Figure 94: NSWC HVRB Forced Detonation Fine Mesh Granular HMX Pressure Trace Data

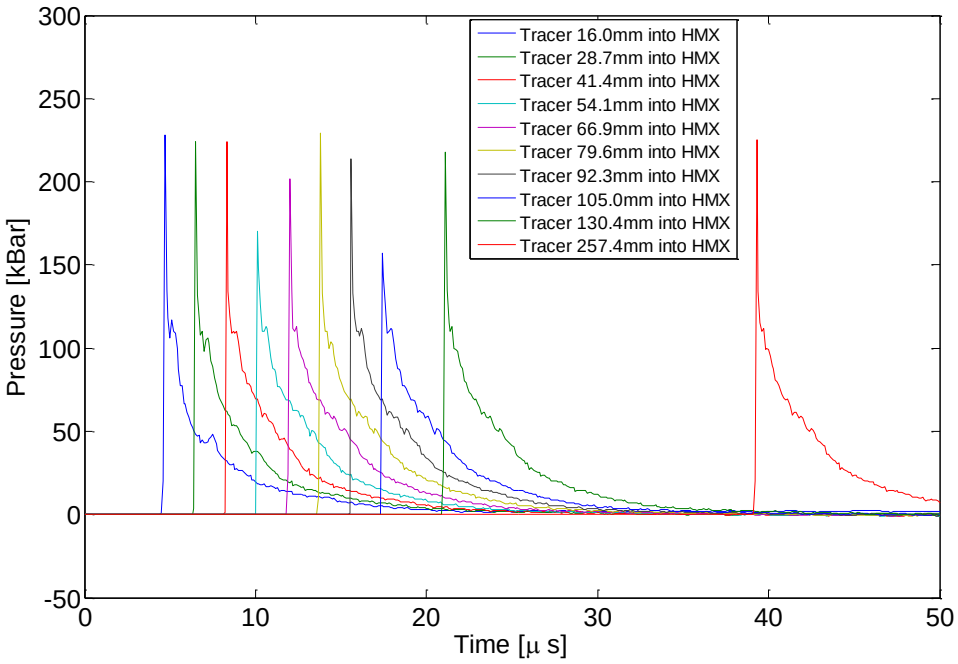

Figure 95: NSWC HVRB Forced Detonation Non-Uniform Mesh Granular HMX Pressure Trace Data

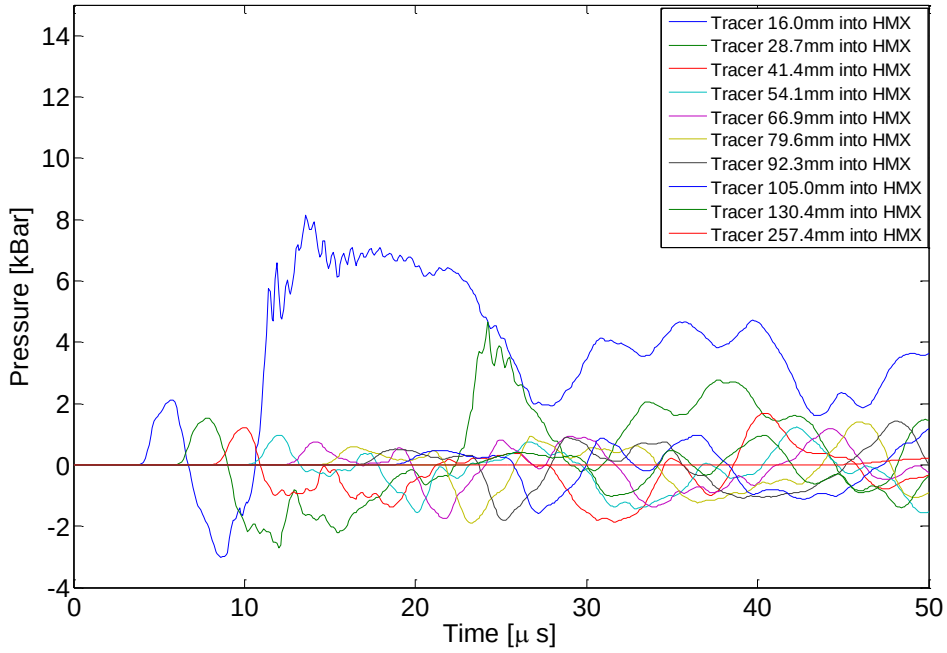

Figure 96: NSWC HVRB Representative Test Case Fine Mesh Granular HMX Pressure Trace Data

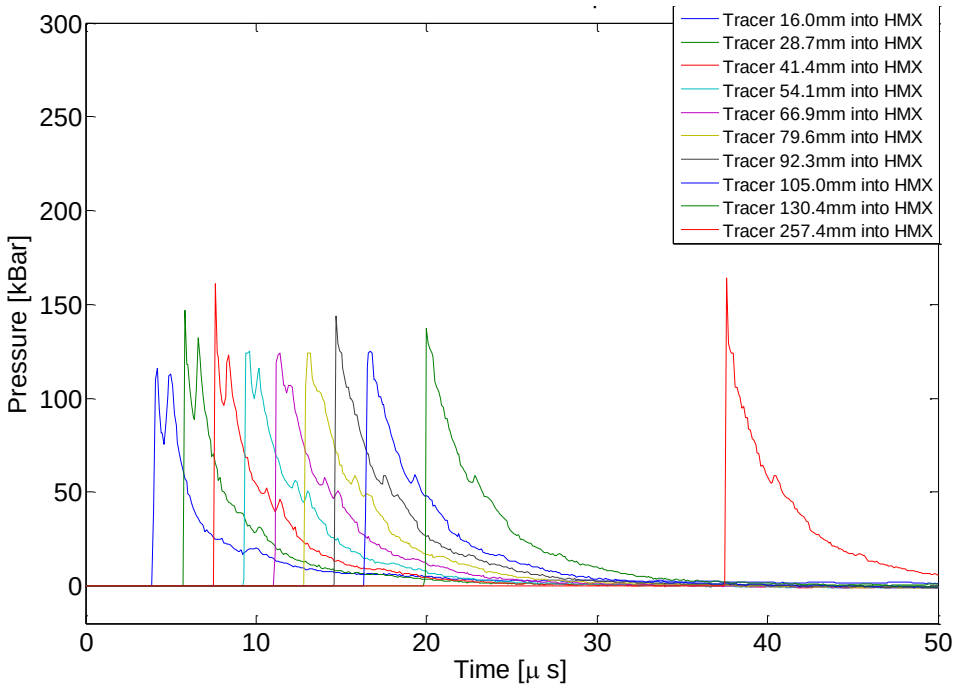

Figure 97: NSWC Arrhenius EOS with Deflagration Parameters Representative Test Case Non-Uniform Mesh Granular HMX Pressure Trace Data

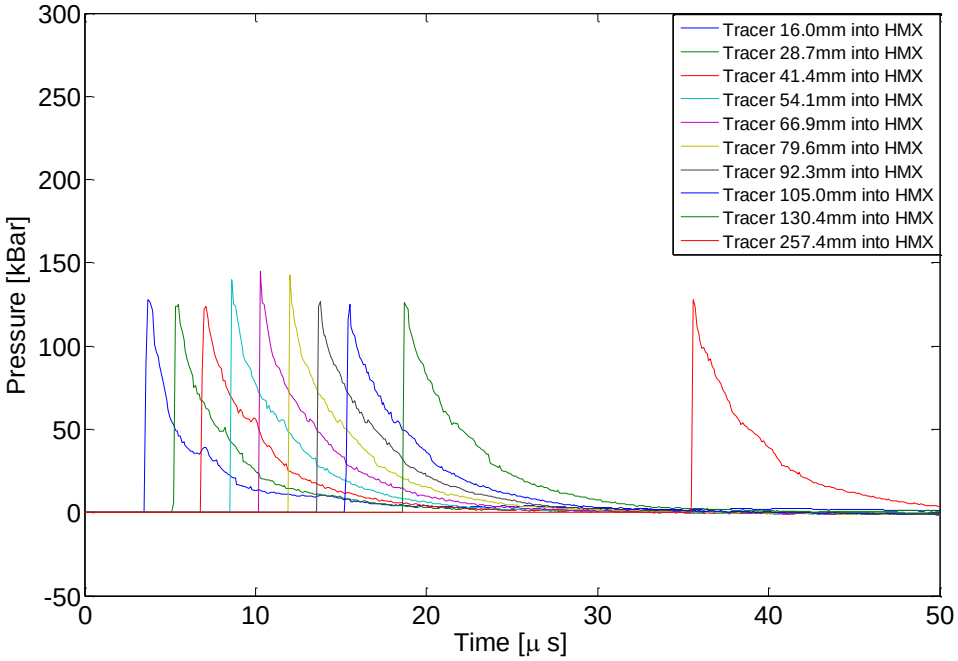

Figure 98: NSWC Arrhenius EOS with Detonation Parameters Representative Test Case Non-Uniform Mesh Granular HMX Pressure Trace Data

LANL:

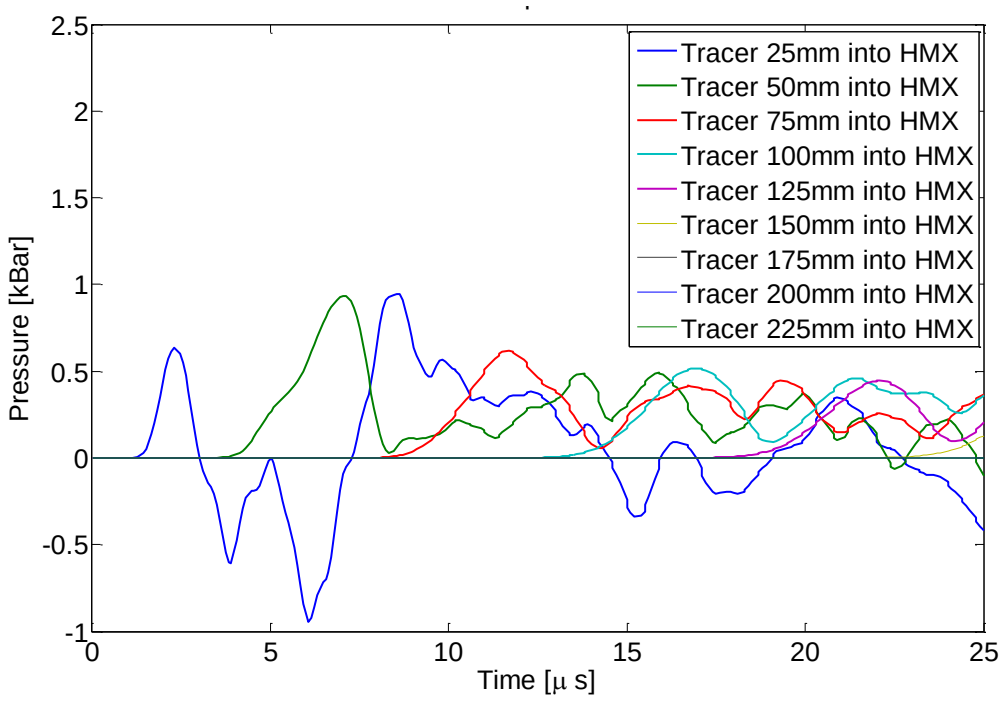

Figure 99: LANL Inert 100% TMD HMX Pressure Trace Data

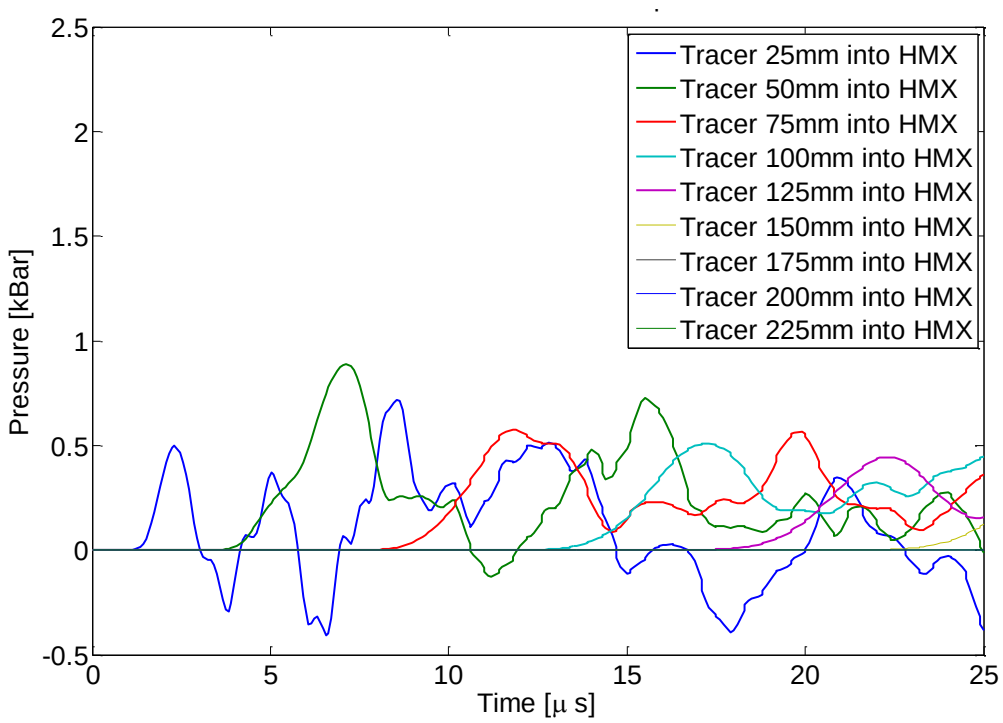

Figure 100: LANL Inert Granular HMX Pressure Trace Data

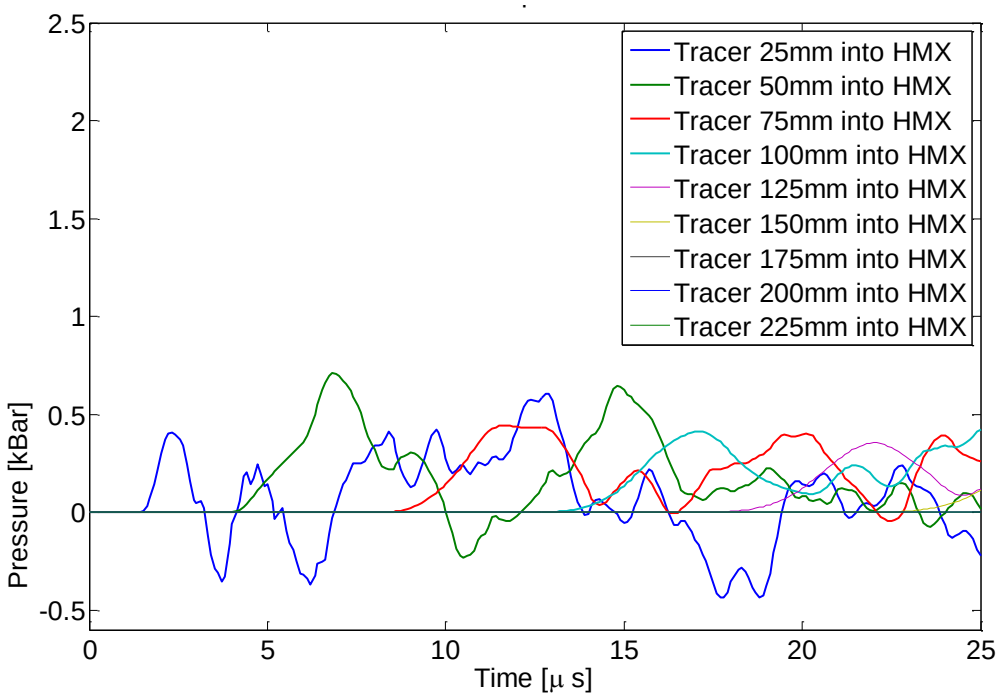

Figure 101: LANL Inert Fine Mesh Granular HMX Pressure Trace Data

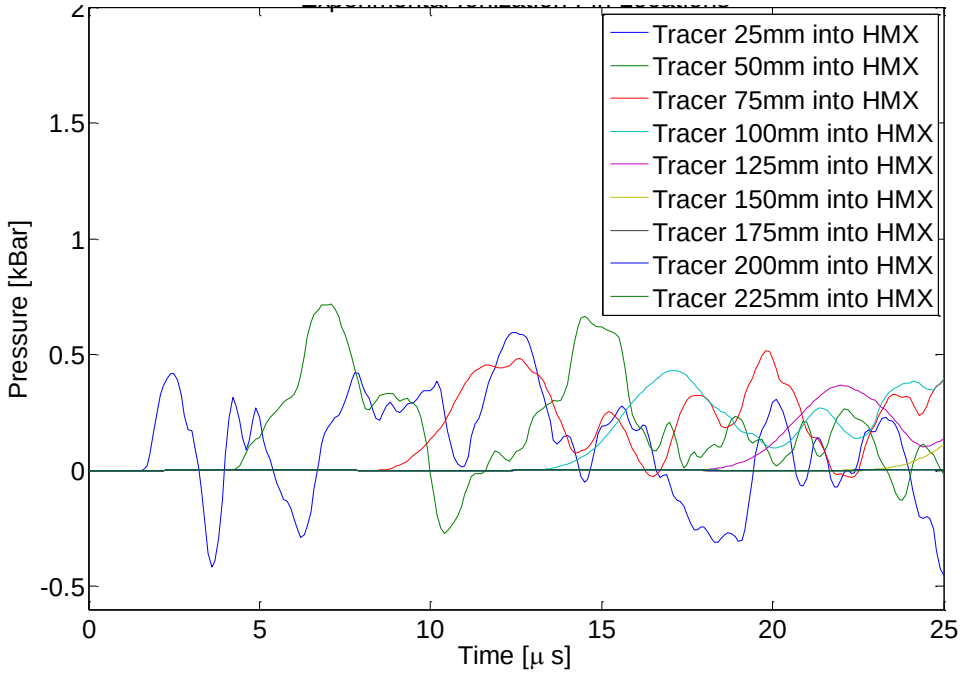

Figure 102: LANL Inert Non-Uniform Mesh Granular HMX Pressure Trace Data

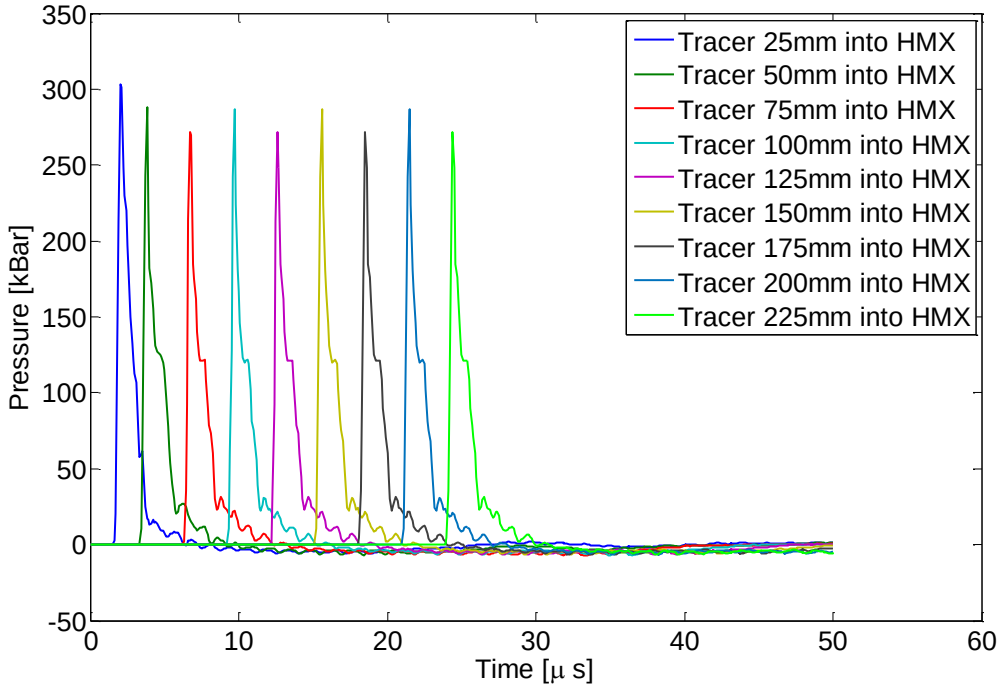

Figure 103: LANL HVRB Forced Detonation 100% TMD HMX Pressure Trace Data

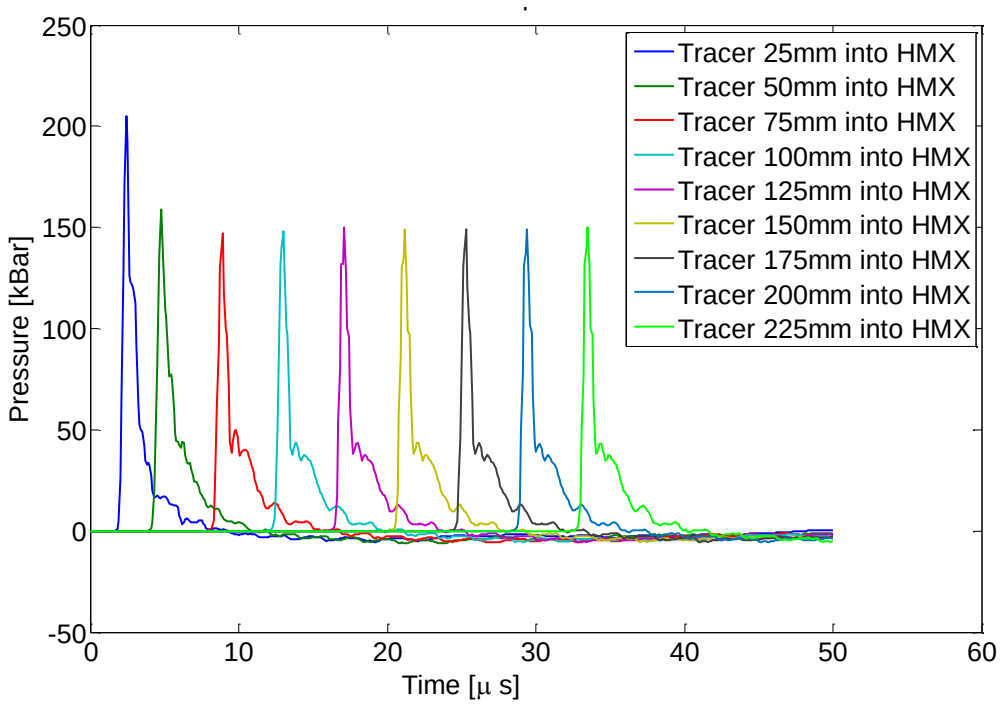

Figure 104: LANL HVRB Forced Detonation Granular HMX Pressure Trace Data

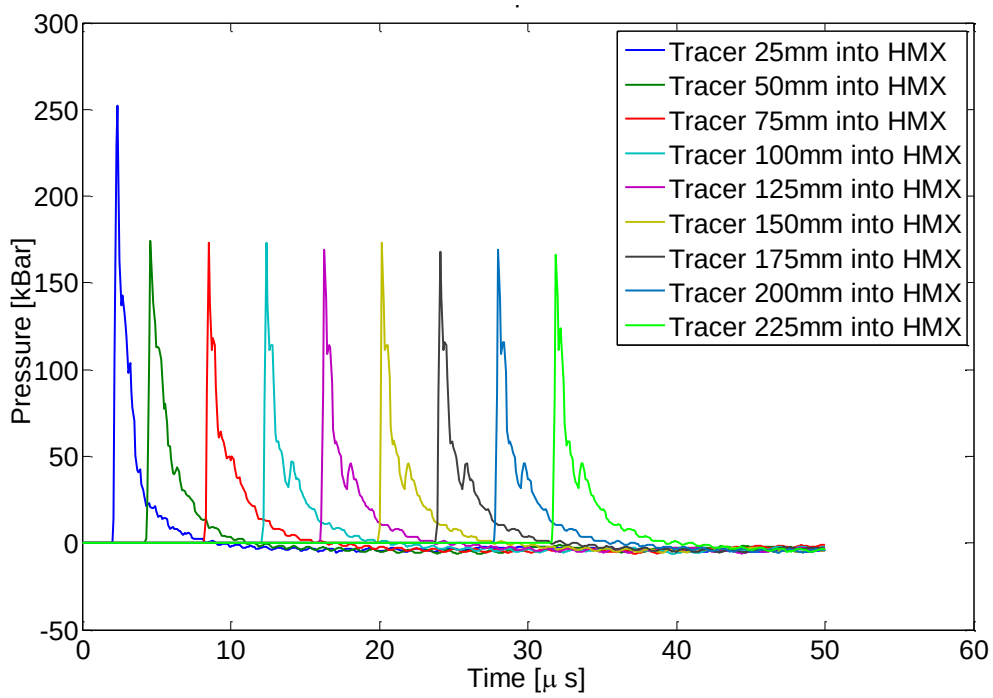

Figure 105: LANL HVRB Forced Detonation Fine Mesh Granular HMX Pressure Trace Data

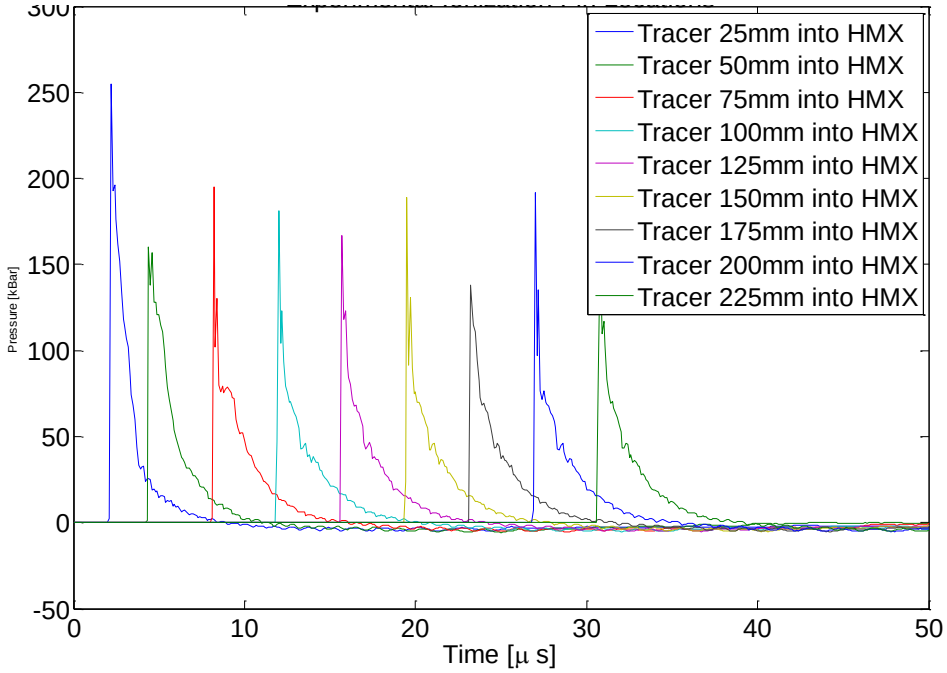

Figure 106: LANL HVRB Forced Detonation Non-Uniform Mesh Granular HMX Pressure Trace Data

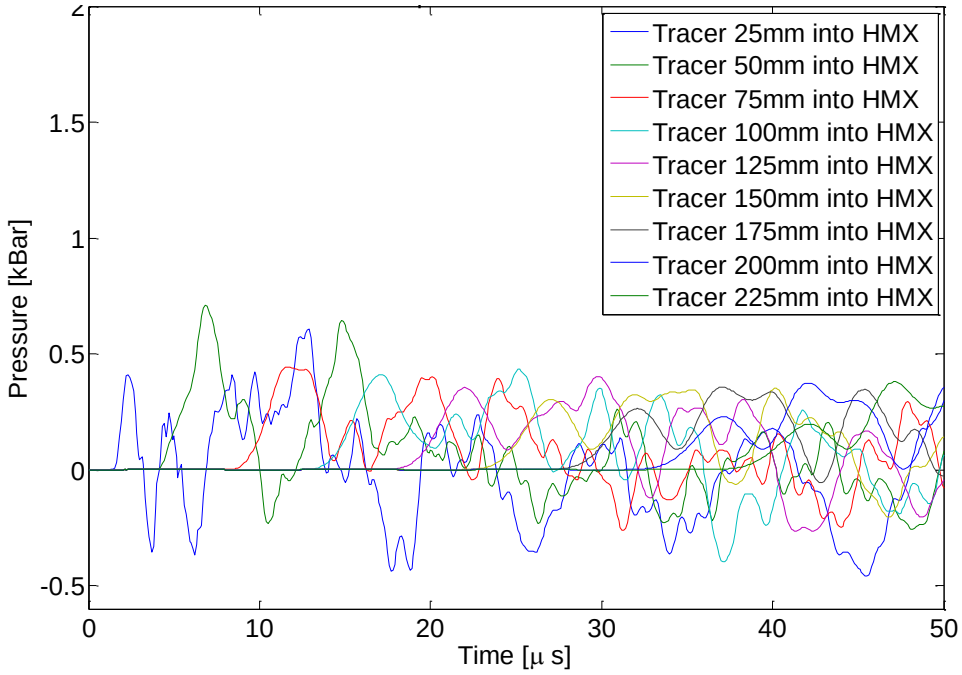

Figure 107: LANL HVRB Representative Test Case Fine Mesh Granular HMX Pressure Trace Data

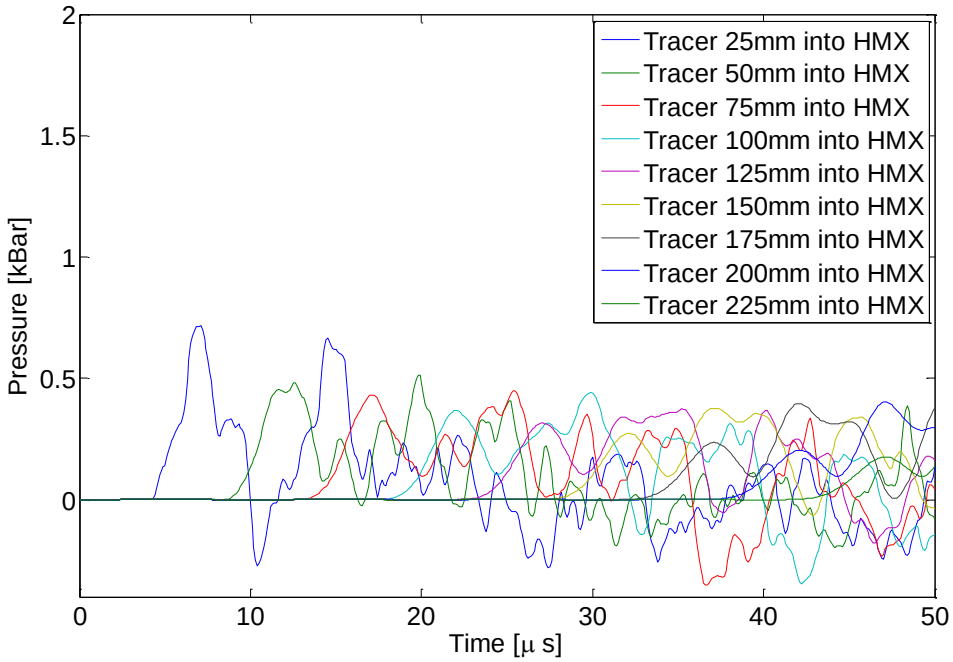

Figure 108: LANL Arrhenius EOS with Deflagration Parameters Representative Test Case Non-Uniform Mesh Granular HMX Pressure Trace Data

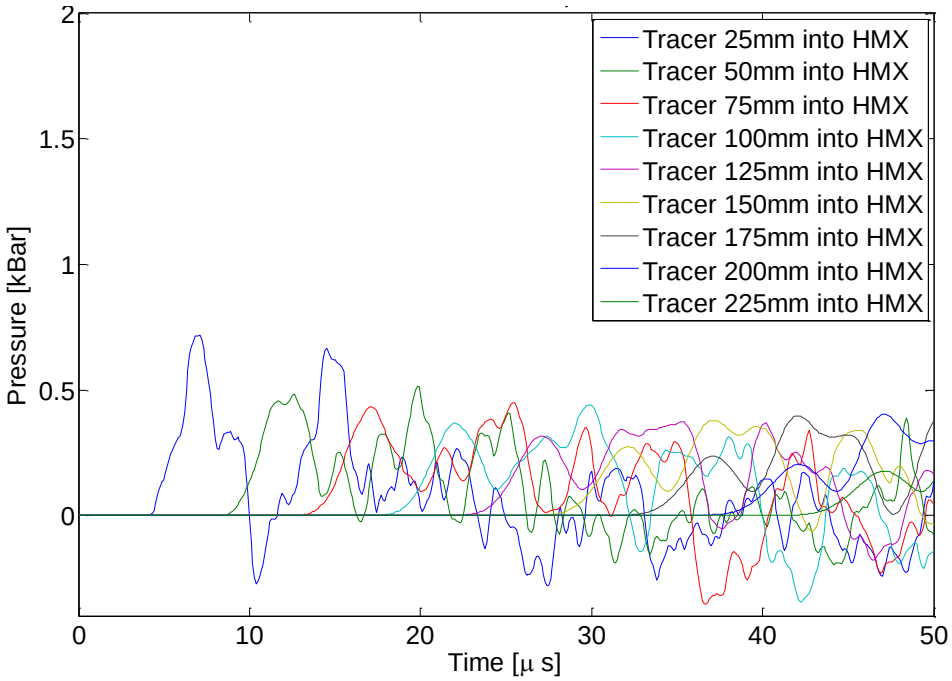

Figure 109: LANL Arrhenius EOS with Detonation Parameters Representative Test Case Non-Uniform Mesh Granular HMX Pressure Trace Data

APPENDIX D

VOLUMETRIC BURNING: DDT TUBE TRACER OUTPUT

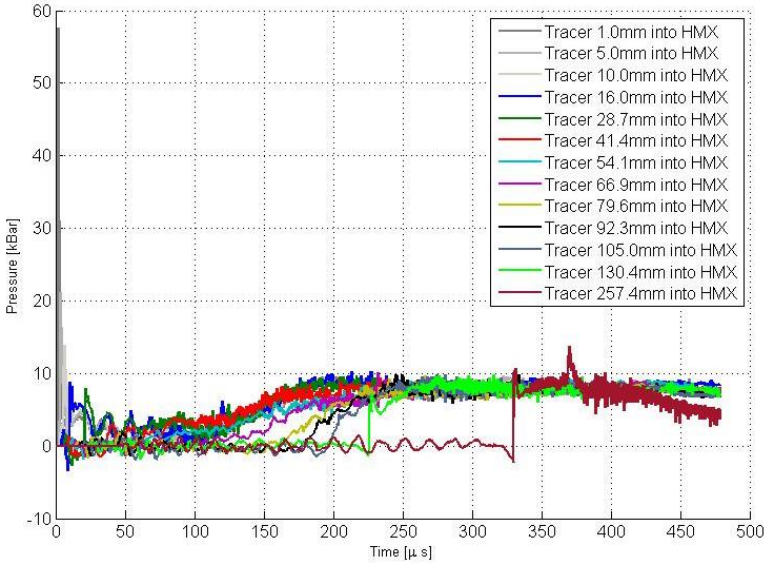

Figure 110: NSWC DDT Tube: Reformulated Volumetric Burning Model

Pressure at HMX - DDT Tube Wall Interface

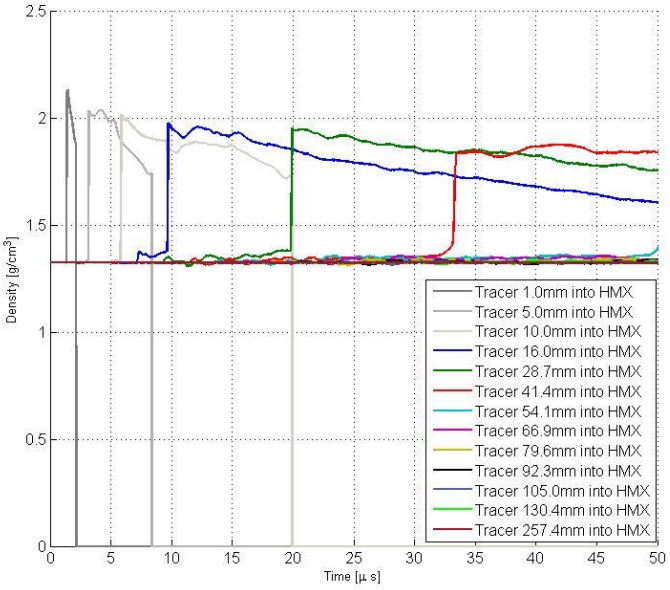

Figure 111: NSWC DDT Tube: Reformulated Volumetric Burning Model

Density at Solid HMX Center.

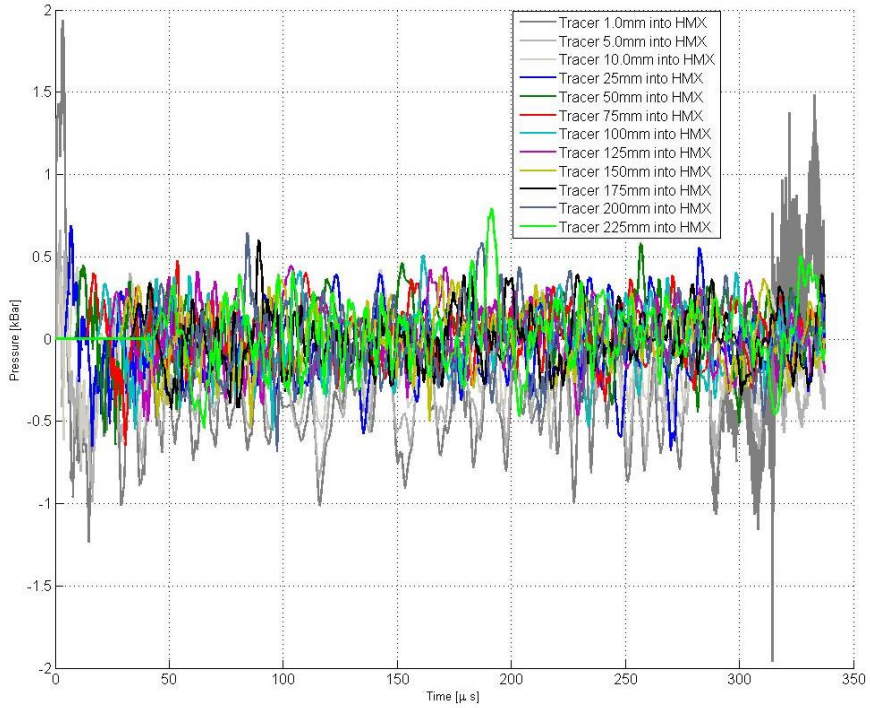

Figure 112: LANL DDT Tube: Reformulated Volumetric Burning Model Pressure at HMX - DDT Tube Wall Interface

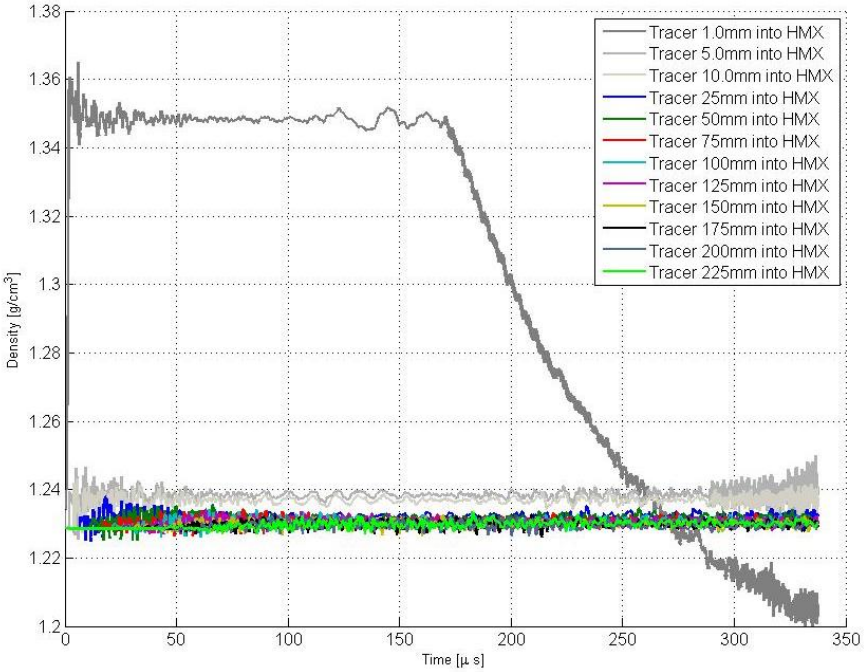

Figure 113: LANL DDT Tube: Reformulated Volumetric Burning Model Density